



Skolkovo Institute of Science and Technology

Skolkovo Institute of Science and Technology

EVALUATION OF HIGH-PRESSURE AIR INJECTION POTENTIAL FOR IN SITU
SYNTHETIC OIL GENERATION FROM OIL SHALE: BAZHENOV FORMATION

Doctoral Thesis

by

TATIANA BONDARENKO

DOCTORAL PROGRAM IN PETROLEUM ENGINEERING

Supervisor

Associate Professor of the Practice, Alexey Cheremisin

Moscow – 2018

© Tatiana Bondarenko 2018

Abstract

An integrated approach was used in this work to study high-pressure air injection in oil shales for *in situ* synthetic oil generation, during which oxidation, pyrolysis and hydrolysis of oil and organic matter coexist. These processes should be investigated separately and jointly in order to understand the mechanisms of synthetic oil generation and displacement during high-pressure air injection in oil shales.

Despite the abundance of research and field pilots, air injection remains one of the most complex enhanced oil recovery techniques due to the difficulty in designing a field project and predicting *in situ* processes. Besides, extensive laboratory studies should precede field implementation. Air injection into oil shale has been considered as a promising method from the very beginning of the *in situ* retorting research thanks to availability of air and the possibility of spontaneous ignition, and therefore, high temperatures that enable generating oil and gas from kerogen without costly external heating. However, this method has not been widely used in oil shales due to the complex chemical nature of kerogen, low permeability of shales and limited knowledge of the oxidation processes in this type of formations.

Kerogen-bearing rock samples of different degrees of maturity picked from the Bazhenov Formation were subjected to a series of tests, including unique laboratory oxidation, pyrolysis and hydrolysis experiments and a combustion tube test.

This study helped to define the processes taking place in the reservoir in different temperature ranges and present a block of chemical reactions for numerical simulation. New pseudo-components of organic matter were proposed for the reactions block to reflect the degree of thermal decomposition and oxidation of kerogen and explain the slow propagation of the combustion front in oil shale. Oxidation produced a substantial amount of supercritical water, such supercritical state being the result of high reservoir pressure and high temperature at the combustion front.

The potential of high-pressure air injection for generating synthetic oil in Bazhenov Formation oil shales was evaluated by assessing the degree of kerogen conversion and

hydrocarbon yields during three coexisting processes: oxidation, pyrolysis, and hydrolypyrolysis. The oxidation of crushed core samples enabled recovering 23.7 wt% of organic matter that can be pyrolyzed into hydrocarbons, as compared to 79.6 wt% for pyrolysis. Treating the consolidated samples by hydrolypyrolysis resulted in a 31 wt% recovery rate which can be higher if the treatment time is shortened and the generated hydrocarbons are forced from the sample by pressure-down.

This work has enhanced the knowledge and our understanding of the kerogen conversion mechanisms and their influence on the rock properties. The findings obtained bring into focus the importance of choosing the right air injection mode for achieving high hydrocarbons yields. The measurements of gas composition and the properties of produced oil can serve as benchmarks for monitoring field projects. A new experimental methodology was designed for high-pressure air injection testing in oil shales and applied to a specific reservoir. The methodology is based on the investigation of kerogen thermal decomposition, oxidation and hydrolypyrolysis processes that coexist during air injection in oil shale. The results obtained provided directional insights into air injection mechanisms in oil shales. Recommendations were made on how to proceed to a large-scale pilot test using high-pressure air injection in oil shales. Cyclic wet combustion was proposed for optimizing the coking process and synthetic oil extraction and reducing the air requirement.

Keywords: high-pressure air injection, *in situ* retorting, enhanced oil recovery, benchmarks, Bazhenov Formation, oxidation, pyrolysis, hydrolypyrolysis, chemical reactions, thermomicroscopy, thermal analysis, oxidation studies, high-pressure ramped temperature oxidation, combustion tube test, autoclaves experiments.

Publications

While this Thesis was being written, several scientific papers were published:

1. Bondarenko, T.M., Popov, E.Yu., Cheremisin, A.N., Karpov, I.A., Morozov, N.V., “Experimental assessment of the hydrocarbons yields from Bazhenov shale formation by kerogen conversion in the presence of supercritical water”, Proceedings of the International Symposium of the Society of Core Analysts, Snowmass, Colorado, USA, 21-26 August 2016.
2. Bondarenko, T.M., Cheremisin, A.N., Kozlova, E.V., Zvereva, I.A., Chislov, M.V., Myshenkov, M.S., Novakowski, V.A., “Experimental investigation of thermal decomposition of Bazhenov formation kerogen: Mechanism and application for thermal enhanced oil recovery”, *Journal of Petroleum Science and Engineering* 150 (2017) 288–296. <http://dx.doi.org/10.1016/j.petrol.2016.12.011>.
3. Bondarenko, T.M., Popov, E.Yu., Cheremisin, A.N., Kozlova, E.V., Karpov, I.A., Morozov, N.V., “Laboratory modeling of high-pressure air injection in oil fields of Bazhenov formation” (In Russ.), *Neftyanoe khozyaystvo = Oil Industry*, 2017, no. 3, pp. 34-39, DOI: 10.24887/0028-2448-2017-3-34-39.
4. Bondarenko, T.M., Mukhametdinova, A.Z., Popov, E.Yu., Cheremisin, A.N., Kalmykov, A.G., Karpov, I.A., “Analysis of changes in Bazhenov formation rock properties as a result of high-pressure air injection based on laboratory modelling data” (In Russ.), *Neftyanoe khozyaystvo = Oil Industry*, 2017, no. 3., pp. 40-44, DOI: 10.24887/0028-2448-2017-3-40-44.
5. Popov, E.Yu., Bondarenko, T.M., Dobrovolskaya, S.A., Kalmykov, A.G., Morozov, N.V., Erofeev, A.A., “The potential of tertiary methods application for unconventional hydrocarbon systems exposure on the example of Bazhenov formation” (In Russ.), *Neftyanoe khozyaystvo = Oil Industry*, 2017, no. 3, pp. 54-57, DOI: 10.24887/0028-2448-2017-3-54-57.
6. Khakimova, L.A., Mysnikov, A.V., Bondarenko, T.M., Popov, E.Yu., Cheremisin, A.N., Karpov, I.A., “Validation of computational model of high-pressure air injection for Bazhenov formations by laboratory modelling results” (In Russ.), *Neftyanoe khozyaystvo = Oil Industry*, 2017, no. 4, pp. 85-89, DOI: 10.24887/0028-2448-2017-4-85-89.
7. Popov, E., Kalmykov, K., Cheremisin, A., Bychkov, A., Bondarenko, T., Morozov, N., Karpov, I. 2017. Laboratory investigations of hydrous pyrolysis as ternary enhanced oil recovery method for Bazhenov Formation. *Journal of*

8. Bondarenko, T., Khakimova, L., Cheremisin, A., Spasennykh, M. 2017. High-pressure air injection laboratory and numerical modeling in Bazhenov source rocks. Paper SPE-187849-MS prepared for presentation at SPE Russian Petroleum Technology Conference, Moscow, Russia, 16–18 October 2017.
9. Khakimova, L., Bondarenko, T., Cheremisin, A., Mysnikov, A., Varfolomeev, M. 2018. High-pressure air injection kinetic model for Bazhenov Shale Formation based on a set of oxidation studies. *Journal of Petroleum Science and Engineering* 172:1120–1132. <https://doi.org/10.1016/j.petrol.2018.09.021>.

Acknowledgments

This thesis would not have been possible without the generous contributions of many people who readily shared their knowledge and experience and offered guidance and moral support.

I wish to express my very great appreciation to my supervisor, Alexey Cheremisin, for his unceasing support, unreserved encouragement and patient guidance throughout my Ph.D program.

A very special recognition should be given to my Individual Doctoral Committee members, Mikhail Spasennykh and Elena Kozlova, for their extremely helpful comments and substantive suggestions.

I would like to acknowledge the extraordinary help and support of Sergey Antonov, Alexander Mishin, Evgenia Leushina, Evgeny Popov, Inna Chapanova, Polina Mikhailova, Igor Balakin, Egor Savelev, Sergei Buzov, Nikolai Taraskin, Kirill Maerle, Pavel Zobov, and Denis Bakulin. Without their passionate involvement, the experiments could not have been a success. With a special mention to Lyudmila Khakimova, who did the history matching of experiments. It was fantastic to have the opportunity to work with this big team of multidisciplinary experts.

I am deeply thankful to Irina Zvereva, Mikhail Chislov, Mikhail Myshenkov and Vadim Novakowski of the Thermogravimetric and Calorimetric Research Centre at Saint Petersburg State University for performing the thermal analysis tests.

My heartfelt thanks to Evgenia Nikitina, Alexander Vasilyevsky, Sergei Charuyev, Elena Zhidkova, Sergei Tolokonsky, and Pavel Grishin of VNIINEft for their cooperation and efficiency in preparing and conducting the combustion tube test.

I am very grateful to the team of Kazan Federal University for their invaluable help in performing the oxidation studies, especially to Mikhail Varfolomeev, Dmitrii Emelianov, Artashes Khachatryan, and Andrey Galukhin.

I also would like to express thanks to Anton Kalmykov of Moscow State University for his suggestions and constructive comments. I am thankful to Artem Erofeev and Alexey Pachezhertsev of MIPT Center for Engineering and Technologies for microtomography analysis of the samples from the combustion tube test.

This work has been performed with the financial support of the Russian Ministry of Education and Science (unique identification number RFMEFI58114X0008) and Gaspromneft Oil Company. I would like to express my gratitude to Igor Karpov, Nikita Morozov, Anton Kasyanenko and Vladislav Zhukov for their guidance throughout the industrial project.

Finally, I wish to express my very profound gratitude to my family and friends for their continued moral support. You've been an endless source of strength and inspiration in this challenging endeavor. Thank you for supporting me throughout the process of this thesis and beyond.

Table of Contents

Abstract.....	ii
Publications.....	iv
Acknowledgments.....	vi
Table of Contents.....	viii
List of Symbols, Abbreviations	xiv
List of Figures.....	xvi
List of Tables	xxiv
Chapter 1. Introduction.....	1
1.1. Background	1
1.1.1 Statement of the problem.....	3
1.1.2 Goal and objectives.....	4
1.1.3 Outline of the Thesis.....	5
Chapter 2. Literature Review.....	7
2.1. Air injection.....	7
2.1.1 Air injection mechanisms	7
2.1.2 HPAI projects in low permeability reservoirs	8
2.1.3 Cyclic air injection projects	15
2.2. <i>In situ</i> synthetic oil generation from oil shales	16
2.2.1 True in situ retorting process	17
2.2.2 Thermogas (RITEK Oil Company, Sredne-Nazymkoye field, Russia)	19
2.2.3 «ElectroFrac» technology (ExxonMobil Corporation).....	22

2.2.4	In situ Conversion Process «ICP» (Shell Oil Company)	23
2.2.5	Conduction, Convection and Reflux process, «AMSO CCR» (American Shale Oil)	23
2.2.6	Chevron's Technology for the Recovery and Upgrading of Oil from Shale (CRUSH in situ process), Chevron	24
2.2.7	Radio Frequency / Critical Fluid Technology (RF/CF)	25
2.3.	Laboratory and numerical investigations of air injection processes in oil shales	26
2.3.1	Pyrolysis and hydrolysis studies	26
2.3.2	Oxidation/air injection studies	32
2.3.3	Chemical reactions model of air injection in oil shales/Bazhenov Formation	36
2.3.4	Conclusions	39
Chapter 3.	Laboratory investigation of oil shale oxidation, pyrolysis, and hydrolysis	41
3.1.	Laboratory plan for HPAI testing in oil shale	41
3.2.	Samples selection and tests design strategy	48
3.3.	Thermal analysis	50
3.3.1	Samples selection and test design strategy	50
3.3.2	Thermal microscopy	51
3.3.3	Simultaneous thermal analysis	57
3.3.4	Conclusions	59

3.4.	Pyrolysis and oxidation: kinetic studies	60
3.4.1	Samples selection and test design strategy	60
3.4.2	Kerogen thermal decomposition kinetics.....	61
3.4.3	Pressurized Differential Scanning Calorimetry (PDSC).....	69
3.4.4	Accelerating Rate Calorimetry (ARC).....	74
3.4.5	Ramped-temperature oxidation experiment (RTO).....	76
3.4.6	Conclusions.....	79
3.5.	Oxidation: High-pressure ramped temperature oxidation (HPRTO).....	80
3.5.1	Samples selection and test design strategy	80
3.5.2	Methodology	80
3.5.3	Results: temperature profiles	82
3.5.4	Results: gas analysis	83
3.5.5	Results: core analysis	88
3.5.6	Results: oil analysis.....	92
3.5.7	Material balance calculation	96
3.5.8	Conclusions.....	96
3.6.	Pyrolysis: High-pressure ramped temperature cracking (HPRTC).....	97
3.6.1	Samples selection and test design strategy	97
3.6.2	Methodology.....	97
3.6.3	Results: core analysis	97
3.6.4	Results: oil analysis.....	101
3.6.5	Results: gas analysis	103

3.6.6	Material balance calculation	105
3.6.7	Conclusions.....	105
3.7.	Hydropyrolysis: closed-system test.....	106
3.7.1	Samples selection and test design strategy	106
3.7.2	Methodology	106
3.7.3	Results: core analysis	108
3.7.4	Results: gas and oil analysis	109
3.7.5	Conclusions.....	110
3.8.	Hydropyrolysis: open-system test	111
3.8.1	Samples selection and test design strategy	111
3.8.2	Methodology	111
3.8.3	Experimental results.....	112
3.8.4	Results: oil analysis.....	113
3.8.5	Results: core analysis.....	114
3.8.6	Results: gas analysis	124
3.8.7	Material balance estimation	125
3.8.8	Conclusions.....	126
3.9.	Comparison of three processes: pyrolysis, oxidation, and hydropyrolysis	127
3.9.1	Results: oil analysis.....	128
3.9.2	Results: gas analysis	130
3.9.3	Results: elemental analysis	130
3.9.4	Conclusions.....	131

Chapter 4. Laboratory investigation of high-pressure air injection in oil shale via combustion tube test	136
4.1. Samples selection and test design strategy.....	136
4.2. Methodology	137
4.3. Results: temperature profiles.....	142
4.4. Results: oil analysis	145
4.5. Results: gas analysis.....	148
4.6. Results: core analysis	150
4.6.1 Core samples appearance after the test	150
4.6.2 Pyrolysis study of crushed core	151
4.6.3 2D pyrolysis of consolidated samples.....	157
4.6.4 Kerogen thermal decomposition kinetics after the exposure	163
4.6.5 Elemental analysis of crushed core samples from different combustion tube zones	165
4.6.6 Permeability and porosity of consolidated core samples from different combustion tube zones	166
4.6.7 Thermal properties of consolidated core samples from different combustion tube zones.....	169
4.6.8 Microtomography of samples from different combustion tube zones	172
4.7. Conclusions	174
Chapter 5. An integrated approach to developing a HPAI kinetic model for the oil shale	176

5.1. Aspects of an air injection kinetic model development	176
5.2. Complex nature of oil shale and oxygen and pyrolysis behavior of its components	177
5.3. Choice of pseudo-components and schematic representation of the reactions	180
5.4. Results of history matching of conducted experiments and proposed kinetic model	182
5.5. Recommendations for multistage development and validation of HPAI kinetic model for oil shales.....	187
5.6. Conclusions	191
Chapter 6. Summary, conclusions and recommendations	192
6.1. Summary	192
6.2. Conclusions	196
6.3. Contributions to Knowledge	197
6.4. Recommendations	198
References.....	201
Appendix A: Photographs of samples after combustion tube test	207

List of Symbols, Abbreviations

A	frequency factor
ARC	accelerating rate calorimetry
BF	Bazhenov Formation
BRRU	Buffalo Red River unit
CMG	Computer Modeling Group
CT	combustion tube
E_a	activation energy
EOS	equation of state
EOR	enhanced oil recovery
GC	gas chromatography
GC-MS	gas chromatography-mass spectrometry
GOC	generative organic carbon
HPAI	high-pressure air injection
HPRTO	high-pressure ramped-temperature oxidation
H_r	reaction enthalpy
HTO	high-temperature oxidation
HTR	high-temperature oxidation region
ISC	<i>in situ</i> combustion
LTO	low-temperature oxidation
LTR	low-temperature oxidation region

MC	mesocatagenesis substage
NGOC	non-generative organic carbon
NMR	nuclear magnetic resonance
NTGR	negative temperature gradient region
OM	organic matter
PC	protocatagenetic substage
PDSC	pressurized differential scanning calorimetry
RF	radio frequency
RTO	ramped temperature oxidation
SBRRU	South Buffalo Red River Unit
SCW	supercritical water
STA	simultaneous thermal analysis
TC	thermocouple
TGA	thermogravimetry analysis
TG–FTIR	thermogravimetry–Fourier transform infrared spectroscopy
WBRRU	West Buffalo Red River Unit

List of Figures

Figure 1. Bazhenov Formation on the map (<i>USGS World Energy Assessment Team, 2000</i>).	3
Figure 2. Red River Formation structure map (<i>Gutierrez et al., 2008</i>).	10
Figure 3. BRRU injection and production performance (1954-2006) (<i>Gutierrez et al., 2008</i>).	10
Figure 4. SBRRU injection and production performance (1959-2006) (<i>Gutierrez et al., 2008</i>).	11
Figure 5. WBRRU injection and production performance (1958-2006) (<i>Gutierrez et al., 2008</i>).	11
Figure 6. Schematics of «True in situ retorting process» (<i>Johnson et al., 2004</i>).	17
Figure 7. Cross-section of the core material drilled from the zone	18
Figure 8. Thermogas technology schematics, RITEK (<i>Bokserman and Kokorev, 2013</i>).	19
Figure 9. Field pilot area #1 around Well #219, Sredne-Nazymkoye Field (<i>Kokorev et al., 2014</i>).	19
Figure 10. Change in oil composition during the air injection (Well #3000, January 2009 and January 2010) (<i>Darischev et al., 2017</i>).	20
Figure 11. Associated gas composition during the air injection (<i>Darischev et al., 2017</i>).	20
Figure 12. Change in produced oil viscosity and density during air injection (<i>Darischev et al., 2017</i>).	21
Figure 13. Photo of the core from the Well #219bis drilled 70m away from the injection well, giving evidence of oxidation reactions occurrence (<i>Darischev et al., 2017</i>).	21
Figure 14. Field pilot area #2 around Well #3003, Sredne-Nazymkoye Field (<i>Darischev et al., 2017</i>).	22
Figure 15. Field pilot area #3 around Well #3019, Sredne-Nazymkoye Field (<i>Darischev et al., 2017</i>).	22
Figure 16. «ElectroFrac» technology, ExxonMobil (<i>INTEK, 2011</i>).	23
Figure 17. <i>In situ</i> Conversion Process (ICP), Shell (<i>INTEK, 2011</i>).	23
Figure 18. AMSO CCR (<i>Allix et al., 2010</i>).	25

Figure 19. CRUSH <i>In Situ</i> Process, Chevron (<i>INTEK, 2011</i>).	25
Figure 20. Raytheon and CF Technology (<i>Pan et al., 2012</i>).	26
Figure 21. Comparison of thin section images of oil shale before and after heating (<i>Kobchenko et al., 2011</i>).	27
Figure 22. Comparison of crack formation results from laboratory and numerical modeling (<i>Kobchenko et al., 2011</i>).	27
Figure 23. Tri-planar image of the core sample heated at 500°C for 24 hours. Estimated porosity is 21% (<i>Tiwari et al., 2013</i>).	28
Figure 24. Simulation of a low porosity sample <i>in situ</i> conversion (<i>Kibodeaux, 2014</i>)...	30
Figure 25. Permeability and porosity measurements in ICP field pilot (<i>Kibodeaux, 2014</i>).	31
Figure 26. Temperature profile along the combustion tube (<i>Kök et al., 2008b</i>).....	34
Figure 27. Produced gas versus time (<i>Kök et al., 2008b</i>).	35
Figure 28. Bazhenov shale rock and fluids schematic model (modified from <i>Manuilova et al. (2017)</i>).	42
Figure 29. Test design strategy.	50
Figure 30. Sample #6. Photo before heating with helium purge	52
Figure 31. Sample #6. Photo after heating with helium purge up to 720°C (50µm) (<i>Bondarenko et al., 2017</i>).	53
Figure 32. Sample #6. Photo after heating with helium purge up to 720°C (10µm) (<i>Bondarenko et al., 2017</i>).	53
Figure 33. Sample #7. Photo before heating with air purge up to 720°C (20µm) (<i>Bondarenko et al., 2017</i>).	54
Figure 34. Sample #7. Photo after heating with air purge up to 720°C (20µm) (<i>Bondarenko et al., 2017</i>).	54
Figure 35. Sample #7. Size of organic matter spot is 23.43 µm. Mechanism of kerogen conversion over time during heating at a rate of 10°C/min with air purge up to 600°C (<i>Bondarenko et al., 2017</i>).	56
Figure 36. Sample #7. Cracking formation during heating with air purge	56

Figure 37. Heating effect and TOC relationship. Samples 1-4 from Oil Field 4 (<i>Bondarenko et al., 2017</i>).	58
Figure 38. DSC curves for four samples from Oil Field 4 (<i>Bondarenko et al., 2017</i>).	58
Figure 39. STA curves for Sample #5 from Oil Field 1 (PC ₃ grade).....	59
Figure 40. STA curves for Sample #3 from Oil Field 4 (MC ₁ – MC ₂ grade).....	59
Figure 41. Pyrogram of Sample #1 (<i>Bondarenko et al., 2017</i>).	63
Figure 42. Pyrogram of Sample #2 (<i>Bondarenko et al., 2017</i>).	63
Figure 43. Pyrogram of Sample #3 (<i>Bondarenko et al., 2017</i>).	64
Figure 44. Pyrogram of Sample #4 (<i>Bondarenko et al., 2017</i>).	64
Figure 45. Pyrogram of Sample #5 (<i>Bondarenko et al., 2017</i>).	64
Figure 46. Pyrogram of Sample #6 (<i>Bondarenko et al., 2017</i>).	64
Figure 47. Pyrogram of Sample #7 (<i>Bondarenko et al., 2017</i>).	64
Figure 48. Logs of A factors shown in histogram form for hydrocarbon-generation kinetics published for 259 source rocks. All these A factors were determined by allowing both A and E _a to vary freely during derivation of kinetic parameters from raw pyrolysis data (<i>Waples and Nowaczewski, 2014</i>).	66
Figure 49. E _a distribution with a spacing of 1 kcal/mole (4,184 J/mol) between groups and A = 1.1674×10 ¹⁵ s ⁻¹ . Sample #1 (<i>Bondarenko et al., 2017</i>).	68
Figure 50. E _a distribution with a spacing of 1 kcal/mole (4,184 J/mol) between groups and fixed A = 2×10 ¹⁴ s ⁻¹ . Sample #1 (<i>Bondarenko et al., 2017</i>).	68
Figure 51. E _a distribution with a spacing of 1 kcal/mole (4,184 J/mol) between groups and A = 4.8325×10 ¹³ s ⁻¹ . Sample #2 (<i>Bondarenko et al., 2017</i>).	68
Figure 52. E _a distribution with a spacing of 1 kcal/mole (4,184 J/mol) between groups and fixed A = 2×10 ¹⁴ s ⁻¹ . Sample #2 (<i>Bondarenko et al., 2017</i>).	68
Figure 53. E _a distribution with a spacing of 1 kcal/mole (4,184 J/mol) between groups and A = 8.3616×10 ¹⁵ s ⁻¹ . Sample #3 (<i>Bondarenko et al., 2017</i>).	68
Figure 54. E _a distribution with a spacing of 1 kcal/mole (4,184 J/mol) between groups and fixed A = 2×10 ¹⁴ s ⁻¹ . Sample #3 (<i>Bondarenko et al., 2017</i>).	68

Figure 55. Figure 56. Ea distribution with a spacing of 1 kcal/mole (4,184 J/mol) between groups and $A = 4.5061 \times 10^{15} \text{ s}^{-1}$. Sample #4 (<i>Bondarenko et al., 2017</i>).....	69
Figure 57. Ea distribution with a spacing of 1 kcal/mole (4,184 J/mol) between groups and fixed $A = 2 \times 10^{14} \text{ s}^{-1}$. Sample #4 (<i>Bondarenko et al., 2017</i>).	69
Figure 58. Ea distribution with a spacing of 1 kcal/mole (4,184 J/mol) between groups and $A = 4.5061 \times 10^{15} \text{ s}^{-1}$	69
Figure 59. Ea distribution with a spacing of 1 kcal/mole (4,184 J/mol) between groups and fixed $A = 2 \times 10^{14} \text{ s}^{-1}$. Sample #5 (isolated kerogen) (<i>Bondarenko et al., 2017</i>).	69
Figure 60. Pyrogram for Sample #8 (<i>Khakimova et al., 2018</i>).....	70
Figure 61. Sample #8. DSC oxidation curves, pressure 8 MPa. Upper right corner curve represents a heating rate of $1^\circ\text{C}/\text{min}$ (<i>Khakimova et al., 2018</i>).	72
Figure 62. Sample #8. Example of DSC curve breakdown into individual peaks, heating rate $10^\circ\text{C}/\text{min}$ (<i>Khakimova et al., 2018</i>).	72
Figure 63. Pressure profile (purple line) and temperature profile (red line) during oxidation (<i>Khakimova et al., 2018</i>).....	76
Figure 64. Schematics of RTO set-up (<i>Khakimova et al., 2018</i>).....	76
Figure 65. Sample 8. Rate of oxygen uptake (1.50, 1.75, 2.00 and $2.25^\circ\text{C}/\text{min}$) (<i>Khakimova et al., 2018</i>).....	77
Figure 66. Sample #8. Gas mixture composition versus temperature ($1.50^\circ\text{C}/\text{min}$) (<i>Khakimova et al., 2018</i>).....	78
Figure 67. Flow schematics of HPRTO set-up.	81
Figure 68. Temperature profiles and gas compositions (CO , CO_2 , N_2 , O_2). GC delay time – 1.47 hours.....	85
Figure 69. Temperature profiles and hydrocarbon gas compositions. GC delay time – 1.47 hours.....	86
Figure 70. Unpacking the core from the reactor (<i>Bondarenko et al., 2017b</i>).....	89
Figure 71. Pyrogram (hydrocarbon yield) of initial core sample and unpacked core samples (HPRTO air injection test).	89

Figure 72. Pyrogram (S4CO ₂) of initial core sample and unpacked core samples with temperature schedule (HPRTO air injection test).....	89
Figure 73. Results of elemental analysis of crushed core samples before and after exposure (HPRTO test: oxidation test).....	91
Figure 74. Photos of traps after the experiment – oxidation test.....	93
Figure 75. Cannon Cassou diagram – sample after oxidation treatment.....	94
Figure 76. Pyrogram (hydrocarbon yield) of initial core sample and unpacked core samples.....	98
Figure 77. Pyrogram (S4CO ₂) of initial core sample and unpacked core samples with temperature schedule.....	98
Figure 78. Results of elemental analysis of crushed core samples before and after exposure (HPRTC test: nitrogen injection test).....	100
Figure 79. Photos of traps after the experiment – pyrolysis test (HPRTC).....	101
Figure 80. Cannon Cassou diagram – sample after pyrolysis treatment.....	103
Figure 81. Temperature profiles and gas compositions. GC delay time - 1.47 hours. ...	103
Figure 82. Experimental set-up for closed-system hydrolysis testing (<i>Bondarenko et al., 2016</i>).....	108
Figure 83. A disintegrated core sample of Bazhenov oil shale.....	108
Figure 84. Produced gas compositional analysis.....	110
Figure 85. Temperature and pressure profiles.....	112
Figure 86. Cannon Cassou diagram – samples after hydrolysis treatment.....	114
Figure 87. Photo of the core sample after exposure (Oil Field 4).....	114
Figure 88. Photo of the sample used for 2D pyrolysis study.....	116
Figure 89. Distribution of S1, S2 and S4CO ₂ parameters in the consolidated sample ..	116
Figure 90. Distribution of S1, S2 and S4CO ₂ parameters in the consolidated sample ..	117
Figure 91. Distribution of S1, S2 and S4CO ₂ parameters in the consolidated sample ..	117
Figure 92. Pyrogram (hydrocarbon yield) of the initial core sample 1 and samples from the Sections 10 and 15.....	121

Figure 93. Pyrogram (S4CO ₂) of the initial core sample 1 and samples from all the 20 sections.....	122
Figure 94. Pyrogram of coke-like material.....	122
Figure 95. Elemental analysis of the original core sample and samples after exposure.	124
Figure 96. Molar gas composition.....	125
Figure 97. Material balance estimation.....	126
Figure 98. Cannon Cassou diagram – all the collected oil samples and extracts.	129
Figure 99. Results of elemental analysis of crushed core samples before and after exposure (HPRTO tests: oxidation and pyrolysis).....	131
Figure 100. Rock samples packed in CT.	139
Figure 101. Photos and schematics of core samples packing.	140
Figure 102. Temperature profiles.	143
Figure 103. Combustion front locations.	145
Figure 104. Cannon Cassou diagram – extracted oil samples and original oil.....	147
Figure 105. Evolved gas composition (N ₂ , CO, CO ₂).	149
Figure 106. Evolved gas composition (hydrocarbon gases and hydrogen sulfide).	150
Figure 107. Photos of core samples after exposure.	151
Figure 108. Pyrograms of non-extracted crushed core samples from different zones (combustion tube test). Oil Field 4.	154
Figure 109. Comparison of pyrograms of extracted core and non-extracted core from Zone 4.2 (combustion tube test).....	154
Figure 110. Comparison of pyrograms of extracted core and non-extracted core from Zone 5.1 (combustion tube test).....	155
Figure 111. Comparison of pyrograms of extracted core and non-extracted core from Zone 5.2 (combustion tube test).....	155
Figure 112. Comparison of pyrograms of extracted core and non-extracted core from Zone 6.1 (combustion tube test).....	156
Figure 113. Comparison of pyrograms of extracted core and non-extracted core from Zone 6.2 (combustion tube test).....	156

Figure 114. Comparison of core from Zone 3.4 (bold line) and Zone 4.1.....	157
Figure 115. Results of 2D pyrolysis study – Sample #15 (consolidated core).	158
Figure 116. Results of 2D pyrolysis study – Sample #10 (consolidated core).	159
Figure 117. E _a distribution with a spacing of 1 kcal/mole (4,184 J/mol) between groups and.....	163
Figure 118. E _a distribution with a spacing of 1 kcal/mole (4,184 J/mol) between groups and.....	163
Figure 119. E _a distribution with a spacing of 1 kcal/mole (4,184 J/mol) between groups and.....	164
Figure 120. E _a distribution with a spacing of 1 kcal/mole (4,184 J/mol) between groups and.....	164
Figure 121. E _a distribution with a spacing of 1 kcal/mole (4,184 J/mol) between groups and.....	164
Figure 122. E _a distribution with a spacing of 1 kcal/mole (4,184 J/mol) between groups and.....	164
Figure 123. E _a distribution with a spacing of 1 kcal/mole (4,184 J/mol) between groups and.....	165
Figure 124. E _a distribution with a spacing of 1 kcal/mole (4,184 J/mol) between groups and.....	165
Figure 125. Results of elemental analysis of crushed core samples after exposure (combustion tube test).....	165
Figure 126. Relationship between sample mass loss and increase in permeability.....	167
Figure 127. Relationship between maximum temperatures reached at the sample location and increase in porosity (Oil Field 1).	169
Figure 128. Changes in thermal conductivity and anisotropy coefficient as a result of exposure.	170
Figure 129. Microtomography results (samples from different zones).	173
Figure 130. Comparison of two DSC curves of isolated kerogen and oil shale sample saturated with oil.....	179

Figure 131. Comparison of two DSC curves of oil shale samples with different degrees of maturity.....	180
Figure 132. Schematic model of oxidation and thermal decomposition processes during HPAI (modified from <i>Khakimova et al. (2018)</i>).....	182
Figure 133. Experimental and numerical oxygen uptake in RTO test (<i>Khakimova et al., 2018</i>).....	184
Figure 134. Kerogen and coke components conversion representation (<i>Khakimova et al., 2018</i>).....	186
Figure 135. Experimental and numerical results of PDSC test (<i>Khakimova et al., 2018</i>).....	186
Figure 136. Proposed schematics of multistage development and validation of HPAI kinetic model for oil shale.....	190
Figure 137. Schematics of high-pressure air injection in the oil shale (<i>modified from John Belgrave Skoltech Thermal EOR lecture notes, 2016</i>).....	193
Figure 138. Sample #1 (Zone 2.1). Peak temperature: 319°C.....	207
Figure 139. Sample #2 (Zone 2.2). Peak temperature: 319°C.....	208
Figure 140. Sample #3 (Zone 3.1). Peak temperature: 460°C.....	209
Figure 141. Sample #4 (Zone 3.4). Peak temperature: 460°C.....	210
Figure 142. Sample #5 (Zone 4.1). Peak temperature: 463°C.....	211
Figure 143. Sample 6 (Zone 4.2). Peak temperature: 463°C.....	212
Figure 144. Sample #7 (Zone 5.1). Peak temperature: 273°C.....	213
Figure 145. Sample #8 (Zone 5.1). Peak temperature: 273°C.....	214
Figure 146. Sample #13 (Zone 2.2). Peak temperature: 319°C. Oil Field 3.....	215
Figure 147. Sample #14 (Zone 3.4). Peak temperature: 460°C. Oil Field 3.....	217
Figure 148. Sample #16 (Zone 2.1). Peak temperature: 319°C. Oil Field 2.....	218
Figure 149. Sample #18 (Zone 3.1). Peak temperature: 460°C. Oil Field 2.....	218

List of Tables

Table 1. Reservoir properties of deep light-oil reservoirs where HPAI was implemented.	12
Table 2. Summary of all the experiments conducted.....	49
Table 3. Test design strategy.	51
Table 4. STA results for four samples from Oil Field 4.	57
Table 5. Test design strategy and materials used (<i>Bondarenko et al., 2017</i>).	61
Table 6. Samples selection for open-system pyrolysis.	61
Table 7. Open-system pyrolysis experiment data (<i>Bondarenko et al., 2017</i>).....	63
Table 8. Kinetics data (activation energy and frequency factor).	66
Table 9. Open-system pyrolysis experiment data for Sample 8.	70
Table 10. PDSC individual peaks analysis results (<i>Khakimova et al., 2018</i>).	73
Table 11. Kinetic characteristics of sample oxidation at 8 MPa.....	74
Table 12. Temperature parameters of LTR and HTR (<i>Khakimova et al., 2018</i>).....	78
Table 13. Kinetic parameters in LTR and HTR (<i>Khakimova et al., 2018</i>).....	79
Table 14. Location of thermocouples (TC) along the HPRTO reactor.....	82
Table 15. Peak/maximum temperatures of the reactor intervals.....	83
Table 16. Total volumes and masses of evolved gases – HPRTO oxidation test.	85
Table 17. Combustion parameters.	88
Table 18. Pyrolysis study results (HPRTO test: oxidation test).	90
Table 19. Results of elemental analysis of crushed core samples before and after exposure (HPRTO test: oxidation test).	91
Table 20. Description of liquid samples in traps – oxidation test.....	92
Table 21. GC×GC-MS results of the original core extract and oil sample collected in trap 3.....	95
Table 22. Material balance. Air injection test (HPRTO).	96
Table 23. Pyrolysis study results (HPRTC nitrogen injection test).	99
Table 24. Results of elemental analysis of crushed core samples before and after exposure (HPRTC test: nitrogen injection test)	100

Table 25. Results of elemental analysis of crushed core samples before and after exposure (HPRTO tests: oxidation and pyrolysis).	101
Table 26. Description of liquid samples in traps – pyrolysis test.	102
Table 27. GC×GC-MS results of the extracts from original core and liquid samples collected.	102
Table 28. Total volumes and masses of evolved gases – HPRTC pyrolysis test.....	104
Table 29. Material balance. Comparison of oxidation (HPRTO) and pyrolysis (HPRTC) tests.	105
Table 30. S1 and S2 parameters before and after hydrolysis exposure.	109
Table 31. GRI analysis results: porosity and permeability.	109
Table 32. Samples selection.....	111
Table 33. GC×GC-MS results for the oil sample extracted from the sand and oil sample collected.	113
Table 34. Results of Sample #1 Rock-Eval pyrolysis study.....	118
Table 35. Results of Sample #2 Rock-Eval pyrolysis study.	119
Table 36. Results of Sample #3 Rock-Eval pyrolysis study.....	120
Table 37. Results of Sample 4 (crushed core) pyrolysis study.	123
Table 38. Results of Sample 4 (crushed core) pyrolysis study.	123
Table 39. Elemental analysis of the original core sample and samples after exposure. .	124
Table 40. GC×GC-MS results for the oil extract and oil samples collected.....	128
Table 41. Sample selection and test design strategy.....	136
Table 42. Peak temperatures.	143
Table 43. Original and produced oil composition.	146
Table 44. Original and produced oil properties.	146
Table 45. GC×GC-MS results for the oil sample extracted from the sand and core and original oil.	147
Table 46. Evolved gas composition.	148
Table 47. Crushed rock samples open-system pyrolysis results.....	153
Table 48. Results of 2D pyrolysis study – Sample #15 (consolidated core).	160

Table 49. Results of 2D pyrolysis study – Sample #10 (consolidated core).	161
Table 50. Consolidated rock samples open-system pyrolysis results (15 mm from the contact area).	162
Table 51. Results of elemental analysis of crushed core samples after exposure (combustion tube test).	166
Table 52. Core samples porosity and permeability measured before and after exposure.	168
Table 53. Thermal conductivity and anisotropy coefficient data before and after exposure.	171
Table 54. Microtomography results.	172
Table 55. Pseudo-components of the original oil (<i>Khakimova et al., 2018</i>).	183
Table 56. Pseudo-components of kerogen (<i>Khakimova et al., 2018</i>).	183
Table 57. Kinetic data for proposed chemical reaction model (<i>Khakimova et al., 2018</i>).	187

Chapter 1. Introduction

1.1. Background

The research on heavy oil combustion began as soon as the method started to be implemented. High-pressure air injection (HPAI) in deep, tight, light oil reservoirs brought into focus the importance of a gas drive mechanism in oil displacement during oxidation. Despite the growing amount of laboratory studies and field pilots, high-pressure air injection is still one of the most complex enhanced oil recovery techniques due to the difficulty in designing field operations and predicting the processes that occur in a reservoir. Moreover, it requires extensive experimental studies.

Oil shale is a tremendous source of fuel, therefore searching for a suitable technology is a priority, especially when conventional oil reserves decrease. Nowadays, oil shale is mined using surface or underground mining, and oil and gas are generated by surface retorting. These methods are not environmentally friendly, and companies are looking for a way to reach kerogen by drilling wells, heating the reservoir and bringing the generated fluids to the surface. Heating kerogen *in situ* is called *in situ* retorting. Air injection in oil shales from the start of the *in situ* retorting research was one of the most promising techniques thanks to availability of air and ability to create high temperatures that can lead to oil and gas generation from kerogen without expensive artificial heating. However, this technique has not been extensively used in shale formations due to the complex chemical structure of kerogen, low permeability of oil shales and limited expertise in the oxidation processes in this type of formations. Low permeability

obstructs air injection and generated fluids production, as well as reduces heat transfer to the formation. In order to efficiently produce oil from oil shale, regressive chemical and thermal reactions must be minimized. However, there is not enough data on the processes that occur underground during air injection and the regimes that can be reached.

The largest Russian shale formation with 55 billion barrels of oil in place is the Bazhenov Formation (BF) (**Figure 1**). Testing the air injection technology and finding the right regime can unlock these huge reserves. It should be mentioned that a field pilot has already been initiated by RITEK oil company (*Kokorev et al., 2014*). However, there are still not enough experimental data to evaluate the effectiveness of the field project, such as synthetic oil and gas benchmarks to monitor the *in situ* processes. It has been proved that the development of the chemical reactions model and the knowledge of its kinetics are essential for the success of the air-injection-based processes (*Gutierrez et al., 2011; Gutierrez et al., 2009*). The classical heavy oil model includes pyrolysis, low-temperature oxidation (LTO) or oxygen addition reactions and high-temperature oxidation (HTO) or bond scission reactions (*Moore et al., 1999; Gutierrez et al., 2011*). In the case of oil shales, kerogen increases the complexity of the chemical reactions scheme. Moreover, oxidation, pyrolysis, and hydrolysis of native oil, synthetic oil, and organic matter coexist during the high-pressure air injection in oil shale.



Figure 1. Bazhenov Formation on the map (USGS World Energy Assessment Team, 2000).

1.1.1 Statement of the problem

Oil shales contain substantial potential resources that can be unlocked by implementing the high-pressure air injection technique. The potential of this method for *in situ* synthetic oil generation needs to be evaluated. There is not enough experimental work conducted to assess the amount of synthetic shale oil that can be generated under reservoir conditions.

It was stated that gas composition, air requirements and fuel requirements obtained in the lab correlate fairly well with those observed in the field for light and

heavy oils, while gas composition may serve as an underground thermometer (*Gutierrez et al., 2009; Gutierrez et al., 2008; Moore et al., 2002*). However, there is no such data for oil shale projects to monitor the *in situ* process. It is also crucial to enhance the knowledge and understanding of the kerogen conversion mechanisms and their influence on rock properties.

Multiple reactions, such as pyrolysis/thermolysis, oxidation, and hydrolysis of original oil, synthetic oil, and kerogen should be investigated in order to establish which of them prevail in terms of performance. In classical combustion, several dominant mechanisms that accompany the burning are studied. One of them is the steam distillation process. However, in the case of heavy oils, combustion water and formation water will be in the presence of steam and hot water. In oil shales, the temperatures obtained during air injection and the high reservoir pressure result in supercritical water appearing ahead of the combustion front. That is why this work also focuses on pyrolysis with the presence of supercritical water.

1.1.2 Goal and objectives

Goal: to evaluate the potential for *in situ* synthetic oil generation from oil shale by using high-pressure air injection technique.

Objectives:

1. To evaluate and justify the high-pressure air injection potential in generating synthetic oil in oil shales based on the Bazhenov Formation example by assessing the degree of kerogen conversion and hydrocarbon yields.
2. To develop an experimental methodology for testing high-pressure air injection in oil shales based on an investigation of the kerogen thermal decomposition, oxidation and hydrolysis processes that coexist during air injection in oil shale.
3. To provide benchmarks for monitoring future field operations, such as produced gas composition and produced oil properties.
4. To develop a chemical reaction model and reaction kinetics for the numerical simulation of high-pressure air injection in oil shales.
5. To develop recommendations on how to move on to the large-scale pilot test of oil generation using high-pressure air injection in oil shales.

1.1.3 Outline of the Thesis

Chapter 2 offers a review of the previous experimental research/studies conducted to test oil shale oxidation, pyrolysis and hydrolysis processes and describes recent research and field pilots of the *in situ* retorting methods for synthetic oil generation in oil shales.

Chapter 3 provides a recommended laboratory plan for oil shale HPAI investigation; describes the laboratory methodology designed for the purpose of this

study and the results of the investigations, namely: thermal analysis, high-pressure ramped temperature oxidation and cracking tests, and hydrolysis tests in autoclaves.

Chapter 4 presents the methodology and results of the high-pressure air injection combustion tube test in oil shales.

Chapter 5 describes an integrated approach to building a kinetic model.

Chapter 6 contains a discussion of the findings, conclusions, and recommendations.

Chapter 2. Literature Review

2.1. Air injection

2.1.1 Air injection mechanisms

This technology was proposed by Soviet scientists A.B. Sheinman and K.K. Dubrovay in the early 1930s. Air injection is an enhanced oil recovery (EOR) method, where the air injected into the oil reservoir initiates the propagation of the oxidation zone through the reservoir that displaces the oil to the production wells. However, a small fraction of oil is consumed as a fuel by the combustion front. The main oil displacement mechanisms of high-pressure air injection (HPAI) are enhanced mobility ratio, oil vaporization, miscible displacement, steam, and flue gas drive (*Moore et al., 2002*). It should be mentioned that these mechanisms differ from the *in situ* combustion (ISC) displacement mechanisms in heavy oils reservoirs. For heavy oils, the primary mechanism for oil displacement is steam and heat generation, as well as the resulting viscosity reduction. In addition, ISC in heavy oils must be operated in high-temperature oxidation mode. Advantages of HPAI are good displacement efficiency, flue gases, and hydrocarbon gases displacement capability under near-miscibility pressure, the ability of spontaneous ignition, almost complete oxygen utilization, and the possibility to operate under high pressure, in other words, above the critical point of water, which leads to supercritical water extraction benefits (*Fassihi et al., 1996*).

To date, there has been little agreement on the nature of the fuel for combustion. One opinion is that low-temperature oxidation reactions are the source of coke, which serves as a fuel (*Alexander, 1962*). Another opinion is that the majority of coke for

combustion is generated via cracking reactions. Still another hypothesis is that the hydrocarbon vapors produced from oil cracking or liberated due to the vaporization can serve as fuel (*Bhattacharya et al., 2016; Mallory et al., 2018*). Oil shale oxidation adds complexity to this debate because of the complex nature of kerogen, which includes generative organic carbon (GOC) and non-generative organic carbon (NGOC) parts that can be consumed as a fuel as well. Moreover, it is known from the pyrolysis study that kerogen decomposition starts at high temperatures (*Behar et al., 2010*), which leads to continuous generation of hydrocarbons that can undergo cracking to produce coke and oxidation at the same time.

2.1.2 HPAI projects in low permeability reservoirs

Alfarge et al. (2017) conducted a comprehensive review of improved oil recovery methods in unconventional reservoirs in North America, where the authors focused on shale oil recovery processes excluding thermal methods. They stated that surfactants could improve shale oil recovery by changing the shale rock wettability from oil wet to water wet. However, low imbibition rate, small depth of penetration into the matrix and high adsorption rate might be obstacles for implementing surfactant flooding in this type of reservoirs and need to be investigated. The review (*Alfarge et al., 2017*) suggests that polymer flooding is not suitable due to the injectivity problems, and polymer can plug the pores. The authors mention that alkaline flooding was not studied due to possible incompatibility between the chemicals and rock minerals. One of the best-studied EOR techniques in shale oil reservoirs is gas injection, especially CO₂ flooding. Carbon dioxide can dissolve in shale oil, swell it and decrease oil viscosity. Also, miscibility

pressure is lower than that of nitrogen and methane (Zhang, 2016). In the authors' view (Alfarge *et al.*, 2017), thermal recovery processes are only applicable in heavy oil reservoirs, while shale oil is very light. That is why they think that there is no motivation for further investigation. However, it should be pointed out that there are some successful high-pressure air injection field pilots in deep light-oil reservoirs with low permeability (Manrique *et al.*, 2004; Gutierrez *et al.*, 2008). Moreover, shale oil reservoirs have some characteristics in common with the mentioned HPAI field pilot reservoirs, namely: high reservoir temperature, high reservoir pressure, low oil density and viscosity, and very low permeability.

One of the most successful examples of HPAI pilots in the deep light-oil reservoir is Buffalo field, which is still running (Gutierrez *et al.*, 2008). This reservoir is located on the southeastern slope of the Williston basin in the northwestern part of South Dakota, USA. A carbonate reservoir with a light (865 - 871 kg/m³) and highly undersaturated oil (saturation pressure 2 MPa) is located at a significant depth (about 2,560 m) with thin net-pay (about 4.5 m), high reservoir temperature (102°C), an average porosity of 16% and a low permeability (about 10 mD). The reservoir oil viscosity is 2.4 mPa·s. The initial reservoir pressure was 24.82 MPa, and the average water saturation was 50%. The deposit was discovered in 1954. By 1963, the reservoir pressure began to decline rapidly. The water infectivity test was conducted, but it showed a low rate of well response to water. In mid-1977, the operator initiated a field pilot to increase oil recovery after numerous laboratory studies, including a combustion tube test. Due to the excellent test results, in September 1978, the first air injection field pilot block, Buffalo Red River unit

(BRRU), was launched on an area of 906 hectares (3.5 sections). The field pilot was a success too, and the test area was increased in 1980 and 1981. After the successful BRRU project in June 1983, the southern block, the South Buffalo Red River Unit (SBRRU), was launched on an area of 7,900 hectares (30.5 sections), which in 1985 showed a growth in the production rate after the start of air injection. Later, in November 1987, the Western Block, the West Buffalo Red River Unit (WBRRU), was launched.

Figure 2 presents a structural map of the Red River Formation with development blocks. **Figure 3**, **Figure 4**, and **Figure 5** show the dynamics of oil and water production and air injection, as well as the number of production and injection wells. It can be seen from the graphs that oil production increased after the start of air injection. Production data after 2006 have not yet been published.

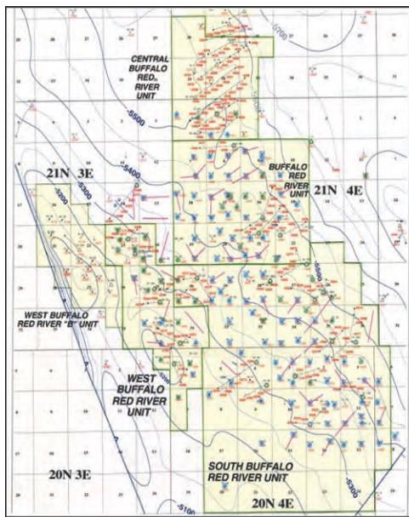


Figure 2. Red River Formation structure map (Gutierrez et al., 2008).

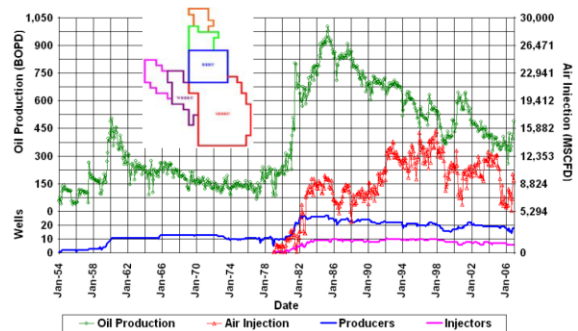


Figure 3. BRRU injection and production performance (1954-2006) (Gutierrez et al., 2008).

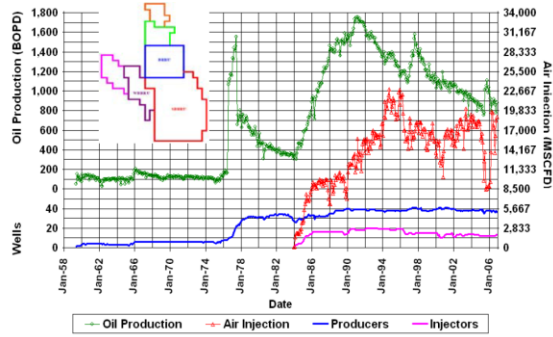


Figure 4. SBRRU injection and production performance (1959-2006)
(Gutierrez et al., 2008).

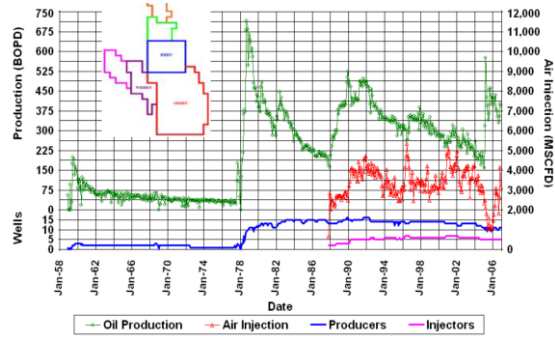


Figure 5. WBRRU injection and production performance (1958-2006)
(Gutierrez et al., 2008).

Another example of using air injection in low-permeability oil deposits is the Coral Creek deposit (*Glandt et al., 1999*), where the technology has been successfully used since the mid-1980s. The deposit was discovered in 1954. The production history started with primary depletion, followed by a water flood in 1967. Oil recovery after water-flooding in a low permeable porous carbonate reservoir was in the range of 20 - 35%, depending on the well spacing, the thickness of the formation and the number of pore volumes of water injected. The depth of the reservoir is 2,652 - 2,743 m. The oil density is 860 kg/m³. The productive layer is dolomite, surrounded by an impermeable limestone. The success in applying the method at this field has proved that high-pressure air injection (HPAI) can become an effective method of increasing oil recovery in water-flooded carbonate reservoirs. **Table 1** presents the characteristics of the deep light-oil reservoirs in the United States where HPAI was implemented successfully. Medicine Pole Hill (*Glandt et al., 1999*) and Horse Creek (*Manrique et al., 2004*) HPAI projects were fairly effective too.

Table 1. Reservoir properties of deep light-oil reservoirs where HPAI was implemented.

Oil Field /Location	Rock type	Pressure, psi	ϕ , %	K, mD	Depth, m	Oil density, kg/m ³	Oil viscosity, cP	Temperature, °C	Net pay, m
Hourse Creek (Williston Basin)/North Dakota, USA	dolomites	3,500-4,200	16	20	2,895.6	865	1.4	92.2	6
Medicine Pole Hills (Williston Basin)/North Dakota, USA	dolomites	3,500-4,200	18,9	15	2,895.6	835	1.0	110	6
Cedar Hills North Unit (Williston Basin)/North Dakota, USA	dolomites	3,500-4,200	16	6	2,529.8	876	2.9	93.3	6
West Cedar Hills Unit/Montana, USA	dolomites	3,500-4,200	17	10	2,743.2	860.2	2	101.7	6
Buffalo (Williston Basin)/South Dakota, USA	dolomites	3,600	18	10	2,575.6	865.4	2.4	101.7	4.6

It should be noted that the above-listed projects are similar in some respects to the Bazhenov Formation layers: all of them have large depth (up to 3,800 m), low permeability (less than one millidarcy), low oil density and viscosity, and high reservoir temperature (around 100°C). In a detailed review (*Jia and Sheng, 2017*), the authors make arguments for and against the use of the air injection technology in oil shale and compare the characteristics of the deposits where this method was successfully applied to those of the shale oil deposits in the United States. The authors (*Jia and Sheng, 2017*) choose high-pressure air injection over gas and chemical EOR methods due to the air availability, low cost as compared to other gases (hydrocarbon gases, CO₂) and the "bulldozer effect", all of which contributes to sweep efficiency. The article emphasizes the difference between classical *in situ* combustion used as a technology for heavy oil production and high-pressure air injection to produce light oil. This difference lies in the absence of preheating of the bottom-hole zone of the well before oxidant injection. In oil shales, oil reactivity and relatively high reservoir temperature contribute to self-ignition of oil, which has a favorable effect on the cost of oil production.

Jia and Sheng (2017) also list the risks of implementing this technology, including the risks of explosion and corrosion of both the surface and downhole equipment. However, in the authors' opinion, corrosion can be prevented by proper well completion. The choice of synthetic lubricants is crucial for preventing explosions in compressors and wells. However, the created pressure drop will cause the inflow of hydrocarbons and unreacted oxygen to the well and may result in additional risks and

uncertainties associated with the creation of dangerous concentrations of oil and oxygen leading to ignition.

The authors (*Jia and Sheng, 2017*) provide geological characteristics of the formation that are favorable for effective implementation, including the dipping which is typical for deposits where this method is successfully implemented. Usually the gas is injected into the upper part of the reservoir in order to maximize the effect of gravity. However, the geological continuity and reservoir thickness also need to be considered. A sufficient amount of air is needed to maintain a stable oxidation process. Another important parameter is reservoir pressure. By analyzing experimental data from thermal analysis and combustion tube tests at different pressures, the authors (*Jia and Sheng, 2017*) concluded that the higher the pressure, the more heat is generated during the oxidation reactions, which increases the maximum temperatures of the exothermic reactions by decreasing the activation energy. When the pressure is increased, a greater degree of oxygen consumption and a higher concentration of such emitted gases, such as methane and carbon dioxide, are also observed, which is suggestive of a gradual transition to the high-temperature oxidation regime. Shale oil deposits, in turn, are characterized by abnormally high reservoir pressures, which will contribute to higher temperatures and faster transition to an efficient oxidation mode.

Ultra-low formation permeability will adversely affect the injectivity of the well, but a large surface area of the grains will result in good oil reactivity with oxygen. In addition, low reservoir porosity will lead to large thermal losses due to the rock matrix heating, which will interfere with the formation of a high-temperature combustion front.

A high concentration of clays, in turn, has a catalytic effect on combustion, lowering the activation energy. The above arguments point to the high potential of the method for bringing residual and adsorbed hydrocarbon reserves into production. At the same time, the technology implies warming up the reservoir to temperatures of thermal decomposition of kerogen, which will help to bring solid unconventional hydrocarbon reserves into production too.

2.1.3 Cyclic air injection projects

As stated earlier, due to the low permeability of oil shale, it is worth exploring the possibility of using cyclic air injection as an option. As an example of a successful pilot project to test this technology, one can consider cyclic treatments of 8 wells in Patos-Marinza, Albania's largest heavy oil field (*Gjini et al., 2013*). Before cyclic application, *in situ* combustion had been applied at the field for 20 years since 1973. The purpose of using cyclic injection was to solve problems of sand production and low oil rates from the wells that were closed for four years before the pilot project began. With the reservoir's oil-saturated thickness of 5 - 11 meters, the estimated combustion front advance radius was 5 - 7 meters. Air injection continued for 43 - 126 days, and the soaking time was 3 to 6 days, after which oil production from the wells was resumed. The increase in oil production was observed only for a couple of weeks. The average production rate for the deposit was 1 m³/day per well. The increase in production from 0.3 to 1.5 m³/day can be considered as a significant improvement. The increase in production was 650 tons. The sand content in the produced products dropped from 8% to 0.7 - 2%. Cyclic air injection has proved to be a successful technology for sand control

and oil production intensification. According to the authors (*Gjini et al., 2013*), a pilot project should be set up based on the calculation of sufficient heat to increase the temperature of the formation, which will help to mobilize oil and generate fuel for combustion. After the completion of air injection and closure of the well, combustion will stop as a result of a lack of oxygen, and the generated heat will continue to heat the formation.

Another example of the successful application of the cyclic air injection technology is a pilot project at the Pleito Creek heavy oil field in the United States (*McGee et al., 2011*). Within the framework of the tests, 22 treatment cycles were performed in nine wells, with coke deposition and liners blockage problems encountered in all the wells. In the Well B-8, the oil production rate increased by 19 times, and the oil density decreased from 993 to 806 kg/m³. In the Well B-7, the oil production rate increased by seven times.

2.2. *In situ* synthetic oil generation from oil shales

The methods of producing oil from oil shale typically fall into one of two groups: underground or surface mining followed by surface processing and *in situ* retorting, which implies heating kerogen in place, extracting the generated fluids from the underground, and transporting them to the surface. Nowadays, oil companies all over the world are trying to develop these technologies which use different techniques to introduce heat *in situ*. However, the oil shale potential is still locked.

2.2.1 True in situ retorting process

The report (Johnson *et al.*, 2004) noted that *in situ* kerogen conversion processes could be economically viable only in those strata that have sufficient permeability or where such permeability is created artificially through hydraulic fracturing of the formation. In the same report, the concept of a "true *in situ* process" was mentioned, which does not include the mining. This method involves the creation of fractures in the target formation, after which air is injected. As a result, the deposit ignites and the combustion front heats the entire formation, while synthetic oil formed through this retorting is displaced along the natural and artificial fractures to production wells. The report emphasizes that in such a "true *in situ* process" it is difficult to control the combustion front and the filtration of synthetic oil, which limits the degree of its extraction, leaving part of the reservoir unheated and part of the synthetic oil undeveloped. An example of such a process is schematically shown in **Figure 6** (Johnson *et al.*, 2004).

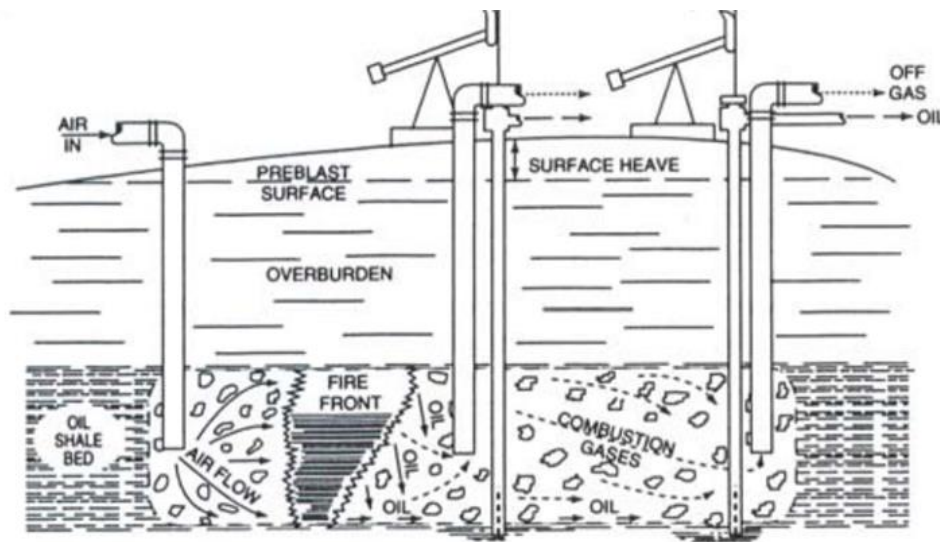


Figure 6. Schematics of «True in situ retorting process» (Johnson *et al.*, 2004).

The work of 1975 (*Raimondi, 1975*), presents the results of a pilot coal combustion project in western Kentucky. **Figure 7** shows the line separating the coked zone from the untouched part of the rock. The composition of the gases released during combustion is similar to the composition of gases corresponding to combustion in shales. The work also mentions transformation of minerals manifested by the rock changing color to brown and pink. At the combustion front, there are liquid hydrocarbons that have not been extracted from the reservoir by the end of the tests, highlighting the prospect of producing liquid hydrocarbons from coal seams and the importance of selecting the desired oxidation regime.

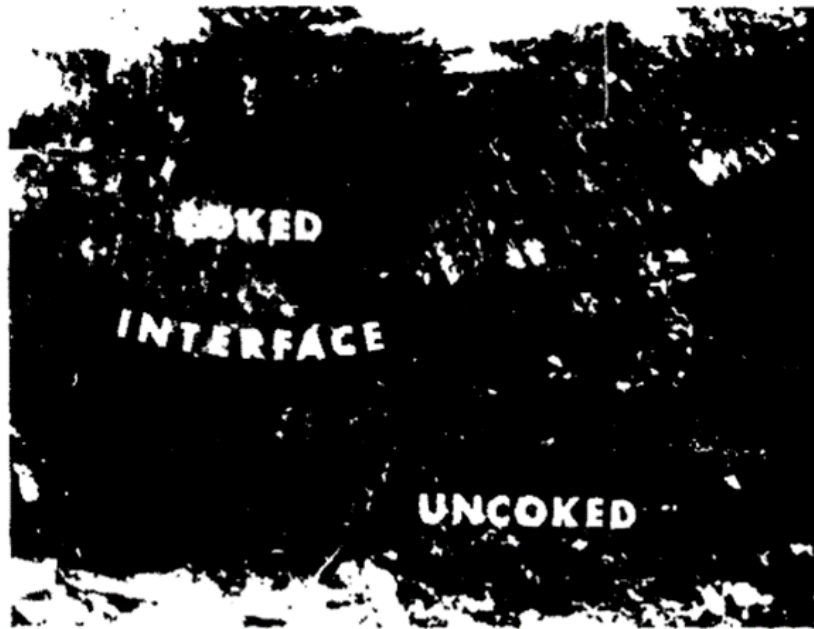


Figure 7. Cross-section of the core material drilled from the zone after combustion (*Raimondi, 1975*).

2.2.2 Thermogas (RITEK Oil Company, Sredne-Nazymkoye field, Russia)

The only pilot project involving high-pressure air injection or thermogas technology (Russian terminology) in oil shales is a project in Sredne-Nazymkoye oil field in Russia, conducted by RITEK oil company (**Figure 8**). This technology is about integrating thermal and gas EOR through injecting air and water into the formation (*Bokserman and Kokorev, 2013; Darischev et al., 2017*).

The area selected for the thermogas field pilot (**Figure 9**) had five operational wells prior to air injection (Wells #219, #401, #3000, #3001 and #3002). All the wells were vertical, except Well #401 which was a horizontal well, and were natural flowing wells. However, oil production rates dropped sharply from 45 to 5 tons per day in 2007 - 2009, while the reservoir pressure dropped from 309 atm (Well #219) to 160 atm. In 2009, the recovery factor was 3.8%, which testified to the low efficiency of oil depletion in such a reservoir.

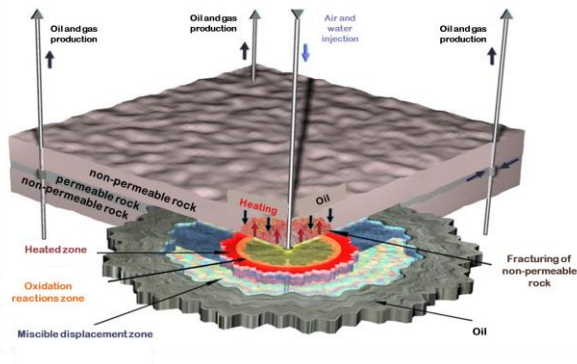


Figure 8. Thermogas technology schematics, RITEK (*Bokserman and Kokorev, 2013*).

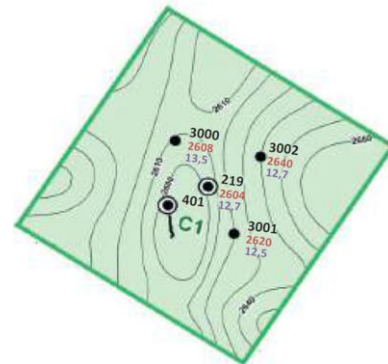


Figure 9. Field pilot area #1 around Well #219, Sredne-Nazymkoye Field (*Kokorev et al., 2014*).

Air injection in the pilot area near the Well #219 in the Sredne-Nazymskoye field was started in October 2009 and was carried out in stages. A total of over 10 million ST.m³ of air have been injected into the reservoir by now. Water was injected mainly during well testing (Darischev et al., 2017). As thermogas was applied, the reservoir pressure increased by 100 atm or more, which had a positive effect on oil production. It was found that the nitrogen content of the associated petroleum gas increased significantly during the thermogas period (from 5 - 10% to 80% and higher). An increase in the hydrocarbon gas production volume and CO₂ content was also observed in the pilot area during the thermogas technology implementation. Oil viscosity and oil density decreased (Figure 10, Figure 11, Figure 12) (Darischev et al., 2017).

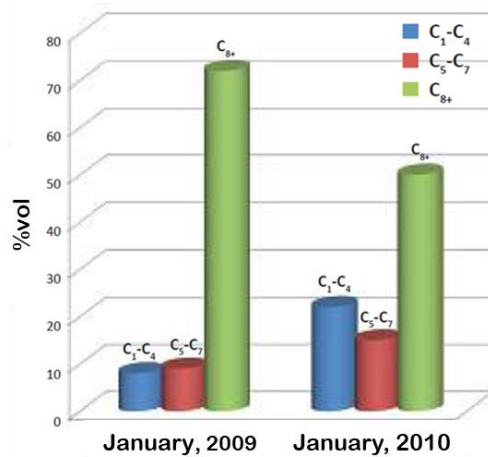


Figure 10. Change in oil composition during the air injection (Well #3000, January 2009 and January 2010) (Darischev et al., 2017).

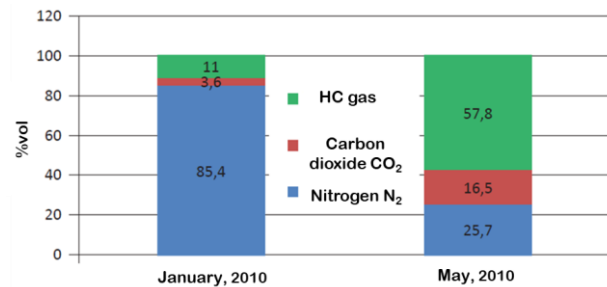


Figure 11. Associated gas composition during the air injection (Darischev et al., 2017).

An additional 40,000 tons of oil were produced in this area. Besides, the сушки drilling in the pilot site was completed in 2016 by selecting the core of the Well #219bis for the oxidation processes zone investigation. Well #219bis is located 71 m away from

Well #219. Based on the analysis of the unique core material, the intervals of oxidative reactions were established for thermogas. These intervals are distinguished by a change in the appearance of the rocks towards red color, the absence of smell and traces of hydrocarbons. The core of the thermogas interval is characterized by hydrophilic properties (**Figure 13**). The total thickness of the interval of thermogas was more than 2 m.

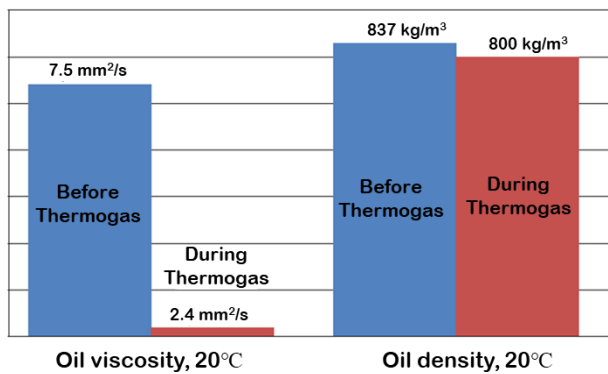


Figure 12. Change in produced oil viscosity and density during air injection (*Darischev et al., 2017*).



Figure 13. Photo of the core from the Well #219bis drilled 70m away from the injection well, giving evidence of oxidation reactions occurrence (*Darischev et al., 2017*).

The second thermogas test site was created in the area of the Well #3003 in the Sredne-Nazymkoye field. The pilot site consists of six wells: one injection and five production wells. The Wells #3008, #3009, #3005, #3007, and #100H are reacting in the experimental section. The site map is presented in **Figure 14**. The Well #210 has been shut down.

A total of 10×10^6 m³(ST) of air was injected into the formation during the period of thermogas in this section. The results confirm the occurrence of oxidation reactions. An increase in the nitrogen content in the associated gas from 1.5% to 18% was observed

in the Well #3007 in the absence of oxygen, along with an increase in CO₂ content from 7 to 16 m³/t per ton of oil. An increase in oil production is estimated at 5×10³ tons.

Currently, the third thermogas field pilot area is being prepared in the southern part of the Sredne-Nazymskoye field. The tentative diagram of this area is presented in **Figure 15**.

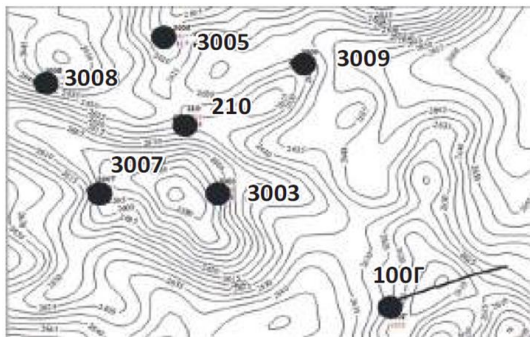


Figure 14. Field pilot area #2 around Well #3003, Sredne-Nazymskoye Field (Darischev et al., 2017).

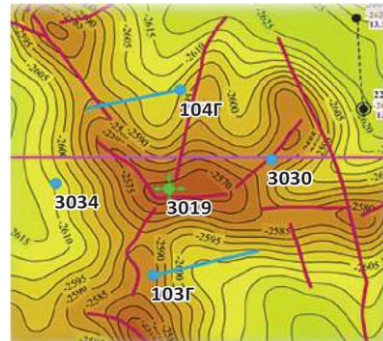


Figure 15. Field pilot area #3 around Well #3019, Sredne-Nazymskoye Field (Darischev et al., 2017).

2.2.3 «ElectroFrac» technology (ExxonMobil Corporation)

The Electrofrac technology (**Figure 16**) is designed to heat kerogen-bearing rock subsurface by conducting electricity along the induced fractures which form a resistive conductive material because they are actually filled with it. As a result, heat is transferred from the induced fracture into the oil shale and continuously converts kerogen into oil and gas which can be produced from the subsurface to the surface using conventional techniques. This technology has the potential to provide effective oil recovery in thick and deep reservoirs. Moreover, the field pilot has proved that electrically conductive induced fractures can be formed, they were operated at a low temperature for several months (Symington et al., 2009; INTEK, 2011; Allix et al., 2010).

2.2.4 In situ Conversion Process «ICP» (Shell Oil Company)

In situ Conversion Process (ICP) utilizes heaters *in situ* to convert oil shale organic matter (kerogen) into gaseous and liquid hydrocarbons (**Figure 17**). Electric heaters steadily heat oil shale beneath the surface, with the formation temperature increasing slowly over time to 350 to 379°C. The products of the heating applied are produced from underground using conventional production techniques and contain about 1/3 of gas and 2/3 of light oil. Therefore, fewer processing stages are needed to obtain high-quality fuels. Shell is carrying out the Freeze Wall Test in Rio Blanco County in order to optimize the technology designed to prevent groundwater contamination. Moreover, several field pilot tests have demonstrated effective performance of the ICP technology (Fowler and Vinegar, 2009, INTEK, 2011, Allix et al., 2010).

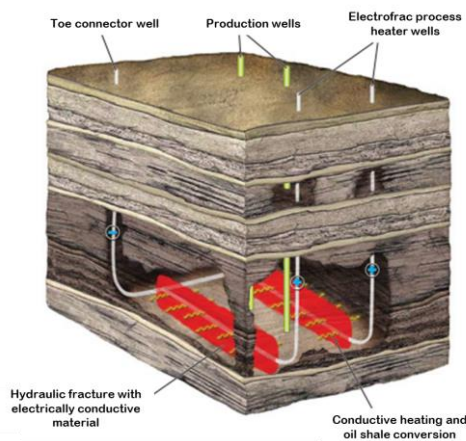


Figure 16. «ElectroFrac» technology, ExxonMobil (INTEK, 2011).

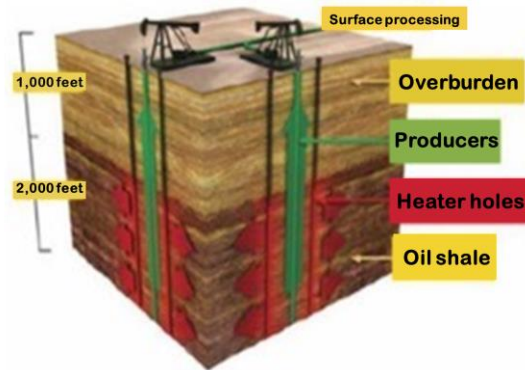


Figure 17. *In situ* Conversion Process (ICP), Shell (INTEK, 2011).

2.2.5 Conduction, Convection and Reflux process, «AMSO CCR» (American Shale Oil)

American Shale Oil company (AMSO) is designing a new technology for *in situ* oil shale retorting that involves advanced drilling and completion expertise coupled with

underground shale heating (**Figure 18**). Heat is introduced into the formation through two horizontal wells, where the heater is placed below the producer. Wells are drilled close to the oil shale bed base. This technology improves heat transfer through the oil shale formation by utilizing thermal micro-fracturing, convection, and refluxing. As kerogen converts into gases and light hydrocarbon components, they rise and reflux. It should be noted that the produced gases eventually will serve as a fuel for a downhole burner that is used for heating the formation. Moreover, a pilot retort experiment is under construction in the Piceance Basin in Rio Blanco County, USA (*Allix et al., 2010; INTEK, 2011*).

2.2.6 Chevron's Technology for the Recovery and Upgrading of Oil from Shale (CRUSH *in situ* process), Chevron

The Chevron technology for the recovery and upgrading of oil from shale (CRUSH *in situ* process) utilizes heated carbon dioxide for oil shale kerogen decomposition (**Figure 19**). This process requires drilling vertical wells and creating horizontal fractures that are induced through high-pressure CO₂ injection. In order to rubble the production zone, carbon dioxide is then circulated through the fractured zones. Explosives might be used for further rock rubblezation. The produced carbon dioxide is then sent to the gas generator for reheating and recycling. To enhance the economics of the process, the heated gases required to continue processing are generated through combustion of kerogen in the depleted zones (*INTEK, 2011*).

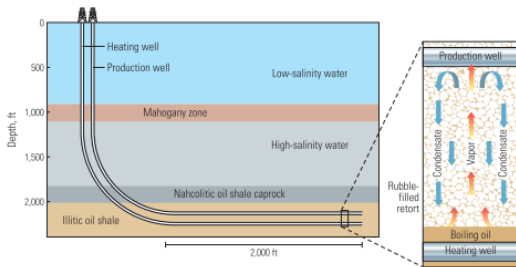


Figure 18. AMSO CCR (Allix et al., 2010).

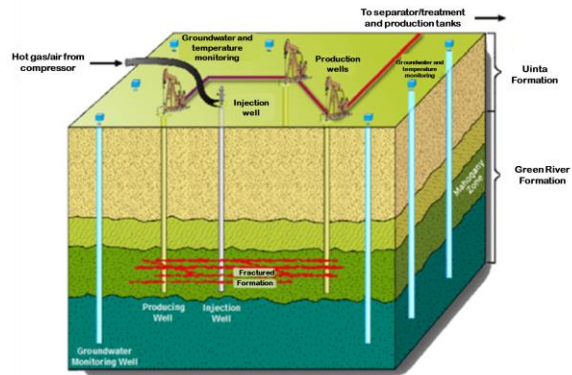


Figure 19. CRUSH In Situ Process, Chevron (INTEK, 2011).

2.2.7 Radio Frequency / Critical Fluid Technology (RF/CF)

According to this technique, radio frequency (RF) energy and supercritical carbon dioxide are used to heat the reservoir and extract the hydrocarbons (Figure 20). For this purpose, radio frequency antennae are lowered into the oil shale formation. Radio frequency energy distribution causes uniform heating and water volatilization, which results in the micro-fracturing of the rock and improvement of the hydrocarbons recovery. Afterward, supercritical CO₂ is injected into the oil shale to separate the petroleum from the rock and displace the hydrocarbons to the relevant production well. The produced CO₂ is reused afterwards.

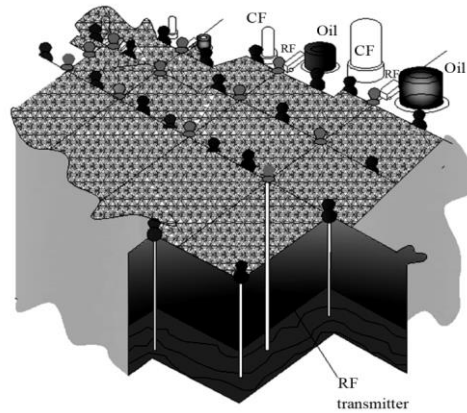


Figure 20. Raytheon and CF Technology (Pan et al., 2012).

2.3. Laboratory and numerical investigations of air injection processes in oil shales

Numerous experimental works dealing with oil shale pyrolysis tests, supercritical water (SCW) extraction and oxidation were conducted mostly to investigate the hydrocarbons yields that can be obtained through oil shale surface retorting. However, very few studies looked into the effectiveness of *in situ* air injection. The findings are useful for understanding the kerogen conversion mechanisms at different stages and distances from the combustion front. A brief review of the current findings is given below.

2.3.1 Pyrolysis and hydrolysis studies

Kobchenko et al. (2011) investigated the oil shale fracturing mechanism during heating, both experimentally and numerically, and discovered a swelling perpendicular to the bedding right before the fracture started to form. Moreover, petrography studies showed that the main fracturing starts in the fine-grained clay-rich layers with a high amount of kerogen, whereas thermogravimetry analysis (TGA) coupled with gas chromatography demonstrated significant mass loss and release of water, CO₂ and

hydrocarbon gases at around 350°C. The authors explained that this is a result of a scenario in which organic matter present in thin lenses begins to transform at around 350°C, causing an increase in volume and build-up of internal pressure. All of these processes lead to fracturing. **Figure 21** compares the thin section images before and after the heating and illustrates kerogen conversion. The modeling of the fracture formation revealed that prior to macroscopic fracturing, small low permeability fluid channels are formed in the oil shale (**Figure 22**).

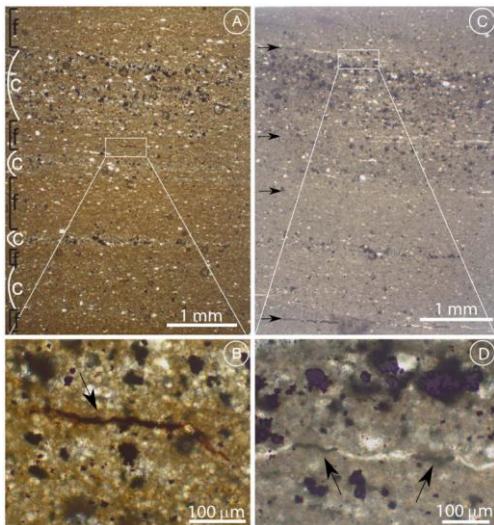


Figure 21. Comparison of thin section images of oil shale before and after heating (Kobchenko et al., 2011).

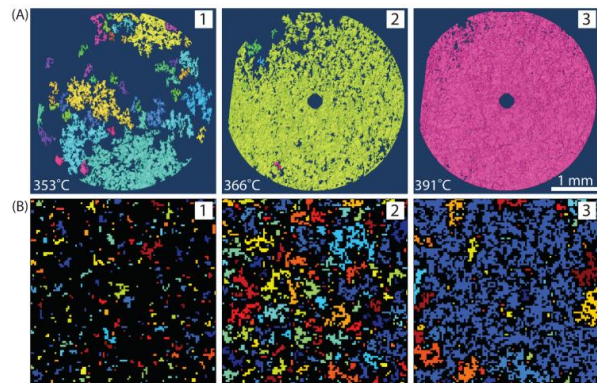


Figure 22. Comparison of crack formation results from laboratory and numerical modeling (Kobchenko et al., 2011).

Tiwari et al. (2013) studied the change in the pore structure before and after pyrolysis. The results showed that different core zones contain different amounts of kerogen, and as a result, different amounts of pore space were created during pyrolysis of one-inch cylindrical cores. The core sections were compared before and after pyrolysis at different treatment temperatures. The study showed that the higher the organic content,

the higher the void space formed during heating. The porosities measured after the treatment by high-resolution X-ray micro tomography scanning were 20 – 25%. However, the created channels may not be fully connected. Moreover, the porosity formed was very uneven and depended on the kerogen distribution in the core sample

Figure 23.

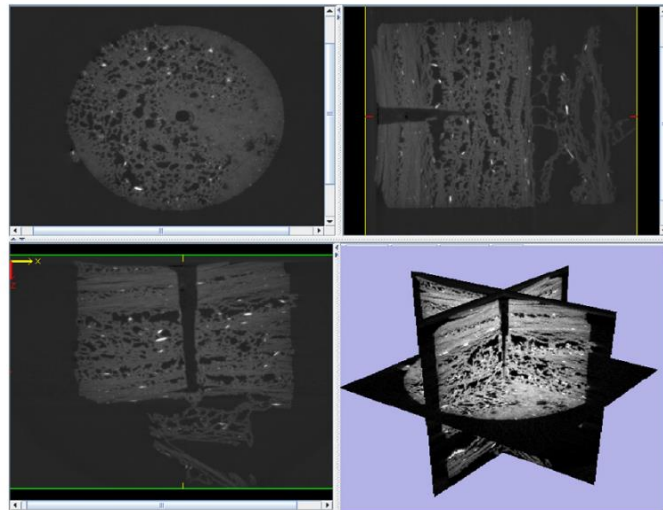


Figure 23. Tri-planar image of the core sample heated at 500°C for 24 hours. Estimated porosity is 21% (Tiwari et al., 2013).

Kibodeaux (2014) examined the changes in oil shale permeability, porosity, and fluid saturations during pyrolysis using an analytical model, laboratory investigation, and numerical simulation. The results of that study showed that oil shales from different depths and areas differ strongly in their thermal decomposition behavior. The authors describe the competing processes, such as coking and compaction, that occur during the oil shale pyrolysis and counteract an increase of porosity and permeability caused by kerogen conversion into gaseous and liquid hydrocarbons. This investigation established three reasons for compaction during *in situ* heating of the oil shale, namely: kerogen softening, a decrease in fluid pressure and grain loss. Increased porosity results in the

permeable region development. Moreover, it was found that the permeable region is formed at the early stages of the *in situ* conversion process (ICP), which suggests that the formation may not need to be pre-heated. **Figure 24** illustrates the results from a numerical simulation of the ICP field pilot for the low-porosity case. All the plots have a common x-axis and display a mass history, temperature and pressure change, a bulk volume history and saturation change during the heating. Kerogen conversion into gaseous and liquid hydrocarbons, pyro-bitumen and coke, as well as water vaporization, were simulated. Pressure decrease with temperature increase and kerogen conversion was calculated. **Figure 25** provides the data on porosity and permeability measurements of core samples from two wells in ICP field pilot. It can be seen from the graph that the porosity and permeability of the core samples picked from the heated zones shot up to 20 - 25% and 1-10 mD, respectively.

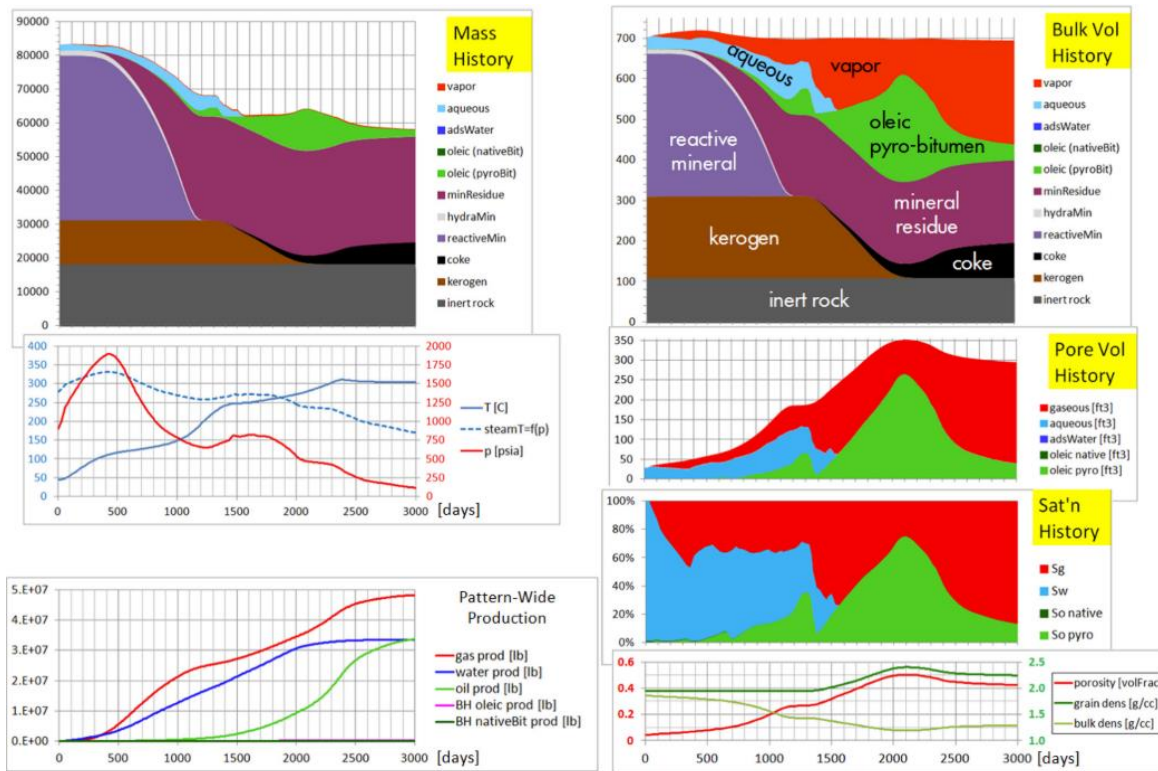


Figure 24. Simulation of a low porosity sample *in situ* conversion (Kibodeaux, 2014).

In their work, *Lee et al. (2015)* present the results obtained by simulating the oil shale *in situ* upgrading using the developed simulator. Six kinetic reactions, four phases and ten components were described in the simulator, which was validated against the production data from Shell's ICP field pilot. The authors studied the effect of fracture network permeability on liquid hydrocarbons production and showed that lower permeability of the fracture resulted in a bigger amount of cracked synthetic oil.

Ekinci et al. (1991) performed hydrolysis studies at 15 MPa and 520°C, as a result of which 72% of kerogen were converted into oil. In addition, treatment by hydrolysis yielded more aromatic oil. *Yanik et al. (1995)* presented the oil fractions characterization results obtained by oil shale pyrolysis and supercritical water extraction. The so-called slow pyrolysis with the heating to 550°C at a rate of 5°C/min resulted in a

low yield of hydrocarbon products which are highly aliphatic and have a low carbon number. Another test, fast pyrolysis, showed a higher yield of highly aromatic hydrocarbons. SCW extraction demonstrated the highest hydrocarbon yield, however, the generated oil is characterized by a high content of asphaltenes and polar compounds. This study underscored the importance of the heating rate for the analysis of kerogen conversion into oil and gas and proved that SCW does not only convert kerogen but also reacts with both kerogen and the products of its decomposition.

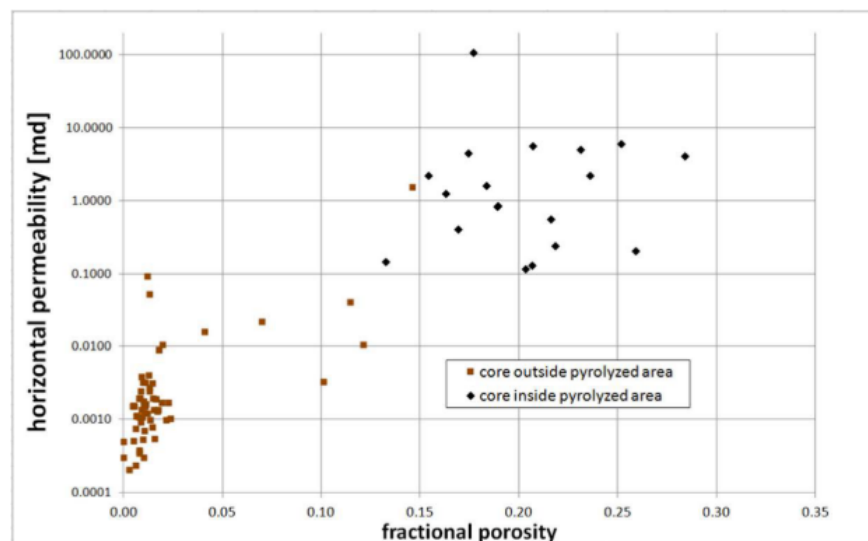


Figure 25. Permeability and porosity measurements in ICP field pilot (Kibodeaux, 2014).

Deng et al. (2011) tested supercritical water extraction of hydrocarbons from Huadian oil shale and were positive that SCW has an effect on kerogen thermal decomposition. The gas chromatography – mass spectrometry (GC–MS) analysis showed that SCW extraction resulted in the formation of many saturated and unsaturated HC from C₁ to C₆. The oil extracts contained many hydrocarbons along with aromatic

compound derivatives, thiophene, quinoline, cyclic ketones, phenol derivatives, indenenes, and other heteroatom compounds. In addition, a higher treatment temperature resulted in the decomposition of more high molecular weight HC. Moreover, the increase in temperature and pressure caused an increase in extract yields.

The paper by *Khlebnikov et al. (2011)* looks at the effect of hot water (100 - 250°C) on oil displacement from Bazhenov shale samples. The authors found that hot water altered rock wettability from oil wet to water wet. Hot water injection at 100°C and 150°C caused a permeability decrease due to the clay swelling – a problem that was not observed during hot water injection at 200°C. This observation indicated that hydrolysis at 200°C resulted in clay dispersion. In addition, higher treatment temperature resulted in a higher oil recovery factor. This work demonstrated that hydrolysis at high temperatures can be an effective process to extract generated hydrocarbons ahead of the combustion front.

2.3.2 Oxidation/air injection studies

Li et al. (2006) performed an experimental work via pressurized differential scanning calorimetry (PDSC) that showed the influence of pressure on the oxidation behavior of different oil types (light oil, medium oil, and heavy oil) and pure aromatic and saturated hydrocarbons. As a result, the increase in pressure boosted oil oxidation, whereas a different effect was observed for light oil and heavy oil. An increase in pressure resulted in more heat being released from oxidation reactions. The authors identified the effects of the composition and chemical structure of hydrocarbons on their oxidation behavior. The chemical structure of hydrocarbons was found to play an

essential role in their oxidation behavior. It was observed that paraffins generated more heat in the low-temperature range than in the high-temperature range. Aromatics displayed more intensive exothermic reactions and released more heat in the high-temperature range than in the low-temperature range. Light or medium oil with higher paraffin and/or lower asphaltene content displayed a stronger exothermic activity in the low-temperature range. In contrast, Athabasca bitumen exhibited a more intensive exothermic reaction in the high-temperature range than in the low-temperature range.

It should be pointed out that it is critical to perform lab testing under reservoir pressure to obtain the right characteristics of the processes that occur during air injection.

The study performed by *Kar and Hascakir, 2017* compares the oil shale oxidation and pyrolysis processes by means of thermal analysis. At the same time, the authors conclude that oxidation is more effective for generating synthetic oil from oil shales due to a lower activation energy of the process, which is more cost-effective. It is also indicated in the paper that water and catalysts can further enhance the attractiveness of the oxidation process.

The work by *Kök et al. (2008)* describes a test in a combustion tube with oil shale samples picked from Turkish oil shale formations, such as Seyitömer, Himmetoğlu, and Hatıldağ. The test results testify to a high potential of the HPAI technology for oil production from oil shales. The following results of oil generation are reported: 4.46 liters of oil per ton for the Seyitömer Formation, 32.22 liters of oil per ton for the Himmetoğlu Formation and 18.27 liters of oil per ton for the Hatılda Formation. In this case, the Himmetoğlu Formation is characterized by the highest content of organic matter.

The experiment was carried out in a combustion tube at a pressure of 0.24 MPa, with the ignition temperature set to 250 - 300°C, which was sufficient for initiating the combustion front and ensuring its steady propagation along the tube. **Figure 26** shows the temperature profiles as a result of the combustion front propagation, with peak temperatures of up to 900°C. The combustion front velocity was 0.2333 cm/h in the experiment with the Himmetoğlu core formation. **Figure 27** illustrates evolved gases composition versus time. It is worth noting the low oxygen concentration at the tube outlet, which is indicative of a high degree of oxygen consumption or, in other words, effective high-temperature oxidation reactions. The only drawback of this experiment is that the test was not carried out under reservoir conditions.

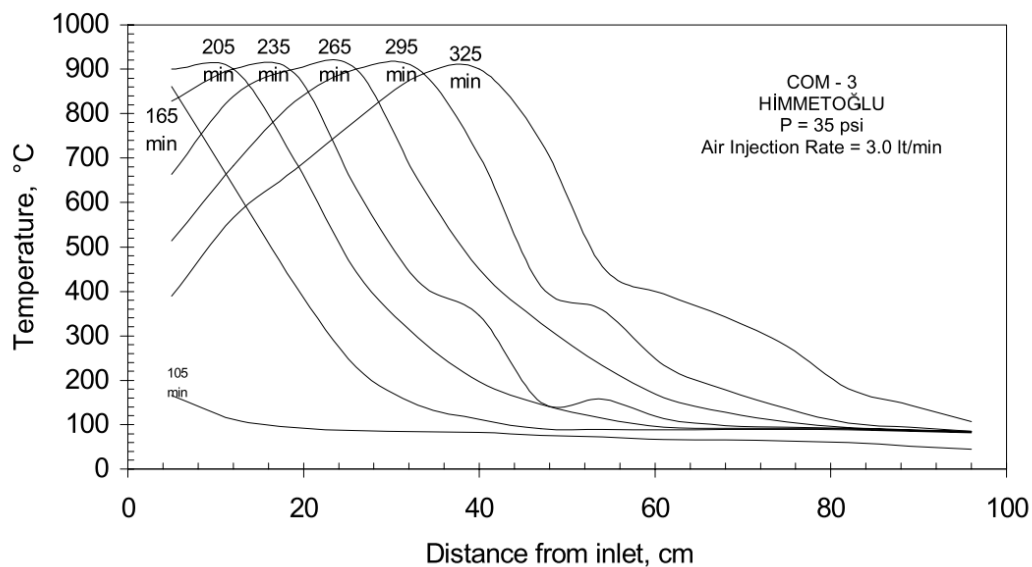


Figure 26. Temperature profile along the combustion tube (Kök et al., 2008b).

As indicated above, the pressure plays a significant role in the course of combustion reactions. By creating conditions that are as close as possible to the

conditions of the reservoir, we obtain the results that come closest to meeting the stated objective.

To date, there is no information in the open sources about field pilots of this technology in the oil shale in Turkey. However, several research projects in this direction were mentioned in the literature (*Abdurrahman, 2016*).

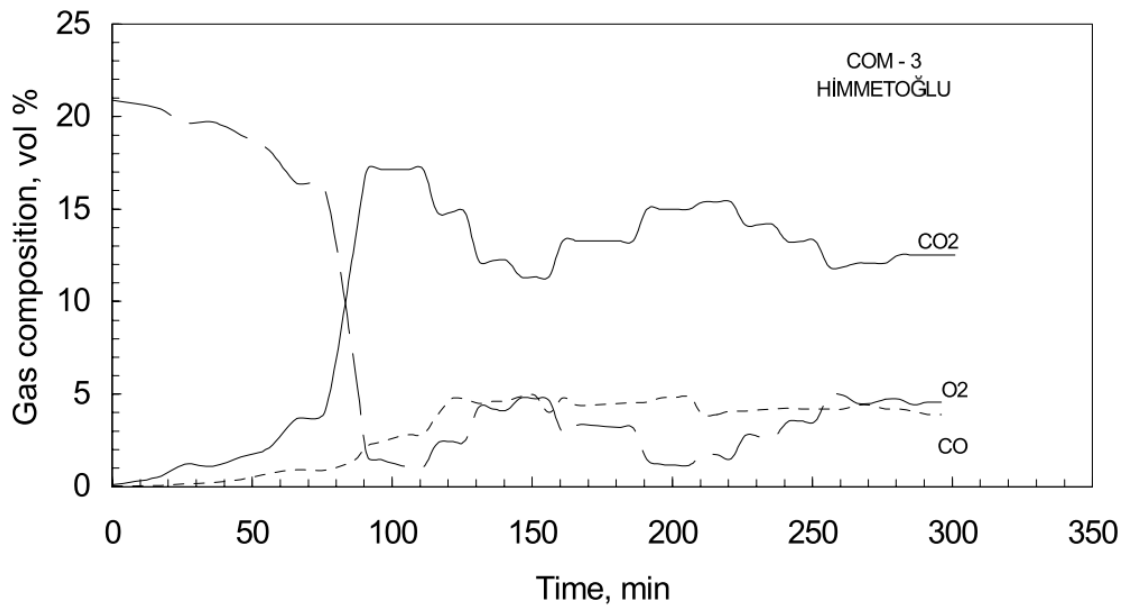


Figure 27. Produced gas versus time (*Kök et al., 2008b*).

It is worth noting that the oil shale rocks, and especially the Bazhenov shale, have a complex mineralogical composition. Minerals can have a catalytic and inhibitory effect on the oxidation, hydrolysis and pyrolysis reactions. *Spiro (1991)* investigates the effect of various minerals on the pyrolysis of kerogen by pyrolytic studies using the Rock-Eval pyrolysis method. The author shows a different effect of quartz, calcite, pyrite, limonite, kaolinite, bentonite and illite on the thermal decomposition of kerogen.

Deng et al. (2011) investigated the catalytic effect of minerals in oil shale on the oxidation and pyrolysis of kerogen via Thermogravimetry – Fourier-transform infrared spectroscopy (TG–FTIR) technique based on Huadian oil shale and isolated kerogen samples. The study reveals an increase in kerogen’s thermal decomposition activity and gases yield in the presence of the mineral matrix. The authors show that kerogen oxidation can be divided into two stages, with kerogen undergoing thermal oxidative degradation at the first stage and oxidation of the coke generated during the first stage occurring at the second stage. The results suggest that the minerals intensify the oxidation of kerogen, while the mineral matrix creates extra porosity during the first stage of oxidation, which significantly lowers the resistance of oxygen diffusivity to oxidize the coke. It was found that oxidation of the pyrite in the isolated kerogen and oil shale sample starts at nearly 470°C.

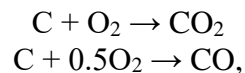
Kozłowski et al. (2015) studied the catalytic effect of clays on ISC performance and showed that clays change the oil oxidation characteristics. However, different oils show different combustion performance in the presence of clays, which points to the importance of using real reservoir rocks in combustion tube tests.

2.3.3 Chemical reactions model of air injection in oil shales/Bazhenov Formation

To see how effective the method would be for oil shales, one should run numerical simulation paying specific attention to the block of chemical reactions. The development of oil fields using *in situ* combustion methods leads to intensive phase transitions of the components of the reservoir systems and to a change in the number, compositions and properties of the coexisting phases, which must be taken into account

in carrying out experimental work and, in particular, studying the reaction products obtained under the influence of thermal effects on BF rocks. Incorrect description of chemical reactions makes the mathematical modeling predictions less reliable. However, the block of chemical reactions can be compiled only as a result of a multistage laboratory study of the cracking and oxidation of an oil sample, separately selected oil components and kerogen for a particular mineral rock composition that can act as a catalyst.

The results of the combustion experiment (*Kök et al., 2008a*) described above were used to adapt the numerical model of oil shale combustion, which is described in the paper (*Zheng et al., 2017*). The authors note the complexity of building a block of chemical reactions to describe a complex process such as combustion in oil shales, due to the parallel flow of several reactions and a large number of products of these reactions. In their model, they ignore the degradation kerogen reaction, the products of which are oil, gas and coke. Thermal destruction of the matrix is ignored too when creating a model that reduces to two reactions:

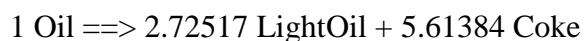


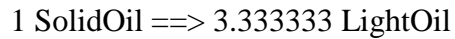
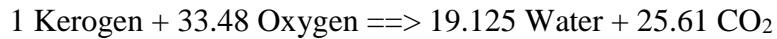
where C is coke which, according to the authors, is formed as a result of kerogen pyrolysis only.

In the simulation of the combustion tube experiment (*Kök et al., 2008a*), the simulation results for the temperature profiles and combustion front velocity fit experimental data. The conclusions also point to an expansion of the combustion front as the front edge moves through the tube, which is due to the slow cooling of the core

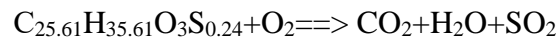
behind the front. This may also be due to the slow progress of the combustion reactions of kerogen and all the products of its thermal destruction, which is not mentioned in the article. In this paper, along with the base scenario, the authors studied the effects of the model's air injection rate, the model's permeability, the initial oil saturation, and the oxygen concentration in the injected air. As a result, they concluded that an increase in air consumption and oxygen concentration leads to oil recovery acceleration. The higher the flow, the higher the temperatures reached during combustion, in view of the greater supply of oxygen to the reaction zone in time to maintain combustion. Low permeability contributes to a longer duration of combustion reactions due to the slow displacement of oil and, as a consequence, its accumulation at the front. A large initial oil saturation results in more heat generated as a result of reactions. This work is useful for studying the modeling of the combustion process in shales, but the presented model of reactions does not reflect the full picture of the process.

The work by *Shchekoldin (2016)* supplements the chemical reaction block with two additional pseudo-components characterizing kerogen, including nine chemical reactions with eleven pseudo-components. However, kinetic parameters are not provided for these reactions. Kerogen's molecular weight is assumed to be 0.4 kg/mol. The proposed reactions are presented below:





An optional reaction is proposed for kerogen oxidation; however, it cannot be simulated at this point:



The modeling of air injection in shales has been given little attention in the literature, which points to the complexity of this process and the need for work in this direction.

2.3.4 Conclusions

According to the literature review, there is no clear methodology for testing HPAI in the oil shale and evaluating its effectiveness. Moreover, chemical reactions used for numerical simulation of air injection in the oil shale are not determined and proved as sufficient.

There is a lack of experimental studies into air injection in oil shales, especially in the Bazhenov Formation. It is necessary to confirm the air injection theory by conducting a set of individual studies. It should be noted that according to my knowledge, the field pilot project in the Sredne-Nazymkoye field was launched without sufficient laboratory research and its effectiveness has not been clearly determined yet. It is not well-understood whether the combustion front is able to propagate through low permeable

rock and convert kerogen into valuable products. There are no known synthetic oil and gas benchmarks that would help to assess the effectiveness of the method in the field and monitor the field operations.

Many works were aimed at examining various methods of oil shale surface retorting. However, it is necessary to check what is happening in the reservoir and understand how this process can be controlled underground. To date, extensive research has been performed into kerogen pyrolysis which is not the case with oil shale oxidation. Moreover, there is lack of detailed studies comparing the influence of the coexisting processes, such as pyrolysis, oxidation, and hydrolysis, in kerogen conversion. The majority of the studies were done under low pressures, which will affect the testing results.

As was noted in the literature review section, each of the oil shales differs in mineralogy and kerogen content and coming from different areas and depth has its own and unique kerogen conversion behavior, which means that core samples from the Bazhenov Formation oil field of interest must be investigated.

Chapter 3. Laboratory investigation of oil shale oxidation, pyrolysis, and hydrolysis

3.1. Laboratory plan for HPAI testing in oil shale

According to the literature review and the gaps identified in the knowledge of the air injection process in oil shale, a laboratory investigation aiming to test air injection is proposed in this Section. The methodology can be divided into two groups: primary and complementary studies. The primary experiments are studies that are necessary for evaluating the HPAI potential for *in situ* synthetic oil generation and combustion performance, assessing the process characteristics, oil and gas analysis and construction of a numerical simulation model, determining the kinetic parameters of oil and kerogen oxidation and pyrolysis. Complementary studies consist of experiments that help to assess the change in the reservoir properties caused by the chemical and thermal exposure, and obtain the correlations between the changes in permeability and porosity and temperature and time of exposure; to evaluate implicitly native and synthetic oil displacement and kerogen conversion into gaseous and liquid hydrocarbons along the anisotropic low permeable core; to determine the inhibitory/catalytic effect of different minerals on fuel laydown, kerogen decomposition, and oxidation reactions.

Air injection results in intensive phase transitions with a change in the compositions and properties of the coexisting phases and increase in the number of components (*Gutierrez et al., 2011*). That is why determining the chemical composition of generated products is essential for understanding the nature of the process, especially for a complex system, such as oil shale.

It should be emphasized that the Bazhenov Formation (BF) still needs to be studied thoroughly, especially in the modeling of oxidation. In addition, BF represents a hybrid hydrocarbons system that consists of several types of hydrocarbon resources, namely, free oil, adsorbed oil, resins/asphaltenes, and kerogen.

The work of *Manuilova et al. (2017)* presents a model of the Bazhenov shale rock and fluids (**Figure 28**). And those resources can be unlocked through different recovery techniques. However, it must be noted that high-pressure air injection has the ability to recover all of them.

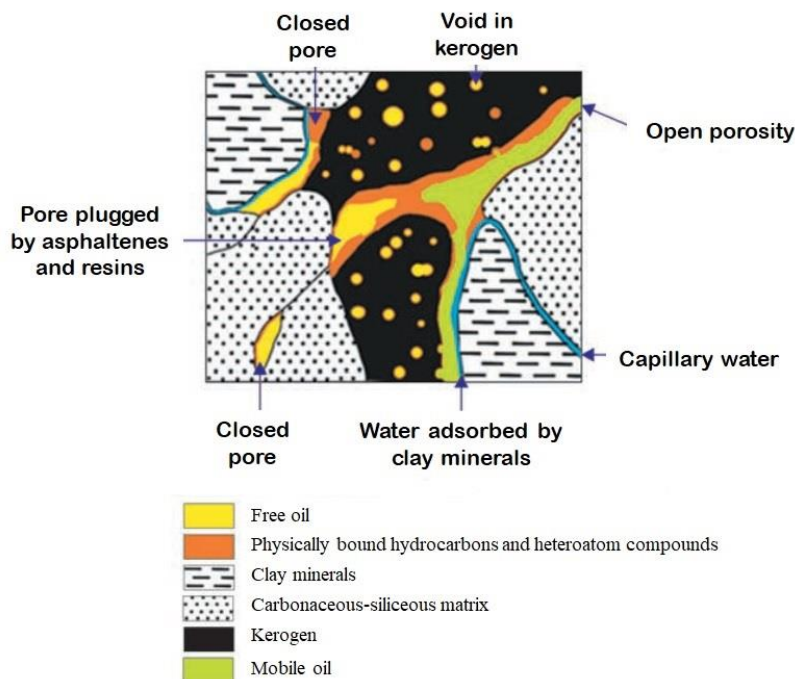


Figure 28. Bazhenov shale rock and fluids schematic model (modified from *Manuilova et al. (2017)*).

The following recommended laboratory plan lists a set of experiments and recommendations for thorough HPAI testing in the oil shale and gives some cautionary

remarks. The recommended integrated approach to investigating the thermal and chemical effects on oil shales during air injection includes the following primary studies:

1. Determining the properties and composition that will be used as the initial parameters for laboratory and numerical simulation.
2. Thermogravimetry analysis (TGA) at a minimum heating rate using nitrogen and air as purging gases to identify the temperature intervals and determine where native oil, synthetic oil, and kerogen react with oxygen (air purge) and where oil cracking and kerogen thermal decomposition (nitrogen purge) occur. Due to the complexity of the oil shale system, it is hard to identify the role of different fractions in chemical transformation, especially in oxidation processes. To link the course of thermal decomposition and oxidation reactions with a certain fraction, the sequence of experiments must be conducted on individual oil fractions, kerogen, extracted core, and a mixture of rock and oil. This will help to estimate temperature intervals of mass losses due to the reactions for individual fractions or hydrocarbon groups of the hybrid system.
3. Studying the thermal effects and kinetics of oxidation reactions by pressurized differential scanning calorimetry (PDSC) at reservoir pressure and determining the kinetic parameters of oxidation processes, the number of stages, their order and process mechanisms, and temperatures of the maximum reaction rate. These studies should be conducted separately for oil fractions, extracted core isolated kerogen and mixture of oil and rock for quantitative and qualitative evaluation of the fraction effects. Without this set of studies it is next to impossible to

- understand the nature of heat generation, in other words, understand what fractions react at what intervals and the kinetics of what reactions are calculated (*Akin et al., 2000; Gutierrez et al., 2011; Li et al., 2006*).
4. Investigating the thermal transformations by accelerating rate calorimetry (ARC) to determine the self-ignition temperature of native oil and isolated kerogen, temperature change and pressure response during the heating in an atmosphere of air, and the times corresponding to peak temperatures (*Yannimaras and Tiffin, 1995; Bhattacharya et al., 2015*).
 5. High-pressure ramped temperature oxidation (HPRTO) and cracking (HPRTC) study to understand the oil oxidation and thermolysis, kerogen thermal decomposition, and oxidation, cracking and oxidation of generated products in porous media. This test simulates reservoir conditions: porous media, oil saturation, and reservoir pressure. Also, this study helps to investigate reactions at the early stages of air injection. It is recommended to carry out at least two tests: one in air purge and one in the inert gas purge. This set of experiments is essential for separating the reactions which occur during HPAI (*Moore et al., 1999; Barzin et al., 2010; Chen et al., 2014; Mallory et al., 2018*). The more experiments are done at different air injection rates and heating schedule, the more data can be used to tune the chemical reactions model (*Chen et al., 2014*).
 6. Laboratory simulation of pyrolysis, hydrolyrolysis and oxidation reactions in bench reactors/autoclaves to study synthetic oil generation at different temperatures under reservoir pressure. This will help to determine synthetic oil

composition as a result of kerogen thermal decomposition at different temperatures. A closed-system allows studying secondary cracking reactions. The data obtained help to describe a chemical reactions scheme more accurately and to identify suitable pseudo-components, eliminating the simplifications. In reservoir simulation, it is commonly assumed that oil fractions reacted have the same composition and properties as the fractions generated. However, there is a continuous change in the fractions composition, primarily when we deal with such a complex by nature component as kerogen. This set of experiments also helps to construct a matrix of changes in synthetic oil composition with temperature and time of exposure, which can provide benchmarks for field operations.

7. A combustion tube test is carried out to evaluate ignition, combustion stability, and front velocity, evolved gas composition and combustion parameters. It is known that the amount of carbon dioxide can provide benchmarks for field operations monitoring (*Moore et al., 2002*). The material balance calculation must be interpreted with caution because core samples are characterized by heterogeneity in hydrocarbons and kerogen content, especially when non-extracted core samples are used for the study. Only the generative part of kerogen can be part of initial hydrocarbons content, while the non-generative part can be the fuel for combustion. To evaluate the combustion parameters, the core samples from the reservoir layers of interest should be selected and homogenized. The higher the heterogeneity of samples, the higher the error in the material balance calculations. Accurate extraction of separate combustion tube zones must be

carried out after the test in order to obtain the correct material balance results. It should be stressed again that these data must be analyzed with caution.

8. A slim-tube test to estimate flue gasses and hydrocarbon gases efficiency in displacing native and synthetic oil. As was stated before, gas drive in HPAI implementation in light oil reservoirs plays a significant role in oil displacement.
9. Geochemical, chemical and petrophysical studies of produced oil samples and core samples after the exposure. Special attention must be paid to the pyrolysis study in order to determine kerogen conversion mechanisms. Measurement of extracted oil properties is crucial for the assessment of possible oil upgrading and *in situ* oil generation as a result of *in situ* retorting. In addition, it allows identifying possible risks and problems during the field operations, for example, emulsions forming.

The following complementary studies can be considered:

1. Evaluating the changes in the rock geomechanical parameters after exposure in the combustion tube. This type of study can be carried out if the consolidated core samples are placed in the combustion tube (CT). In this case, duplicate samples are used: one will be investigated as is and the other will be tested on the geomechanical press system after exposure in CT.
2. Estimating the native and synthetic oil displacement, as well as kerogen conversion and water formation in consolidated samples using nuclear magnetic resonance (NMR) relaxometry.

3. Determining the thermal properties on chips and cylindrical samples: thermal conductivity on pressed chips and cylindrical samples; measuring a thermal coefficient of linear expansion of the rock on cylindrical samples before and after the combustion tube experiment. These measurements are necessary both for an implicit evaluation of kerogen conversion and for obtaining correlations of thermal properties for a correct description of the change in thermal conductivity in thermal simulators and evaluation of thermal exposure in the reservoir.
4. Determining the catalytic or inhibiting effects of the mineral matrix on the course of oil oxidation reactions for a correct assessment of the suitability of a particular field for the air injection implementation. Some interesting methodologies for such a study are described in *Spiro (1991)*, *Yan et al. (2013)*, *Kozłowski et al. (2015)*. This research must be done in a sequence in terms of the experimental scale. Firstly, thermal analysis can be used, such as TG-FTIR (*Yan et al., 2013*). Secondly, Rock-Eval pyrolysis study should be carried out by adding different minerals and analyzing their effect on hydrocarbons yield. Thirdly, autoclaves/bench reactor experiments and CT tests can help to evaluate the catalytic effects of minerals on pyrolysis, hydrolysis, and combustion performance.
5. Evaluating the changes in the rock wettability as a result of exposure.
6. Identifying the changes in the reservoir properties of the rock as a result of exposure in autoclaves and CT (on crushed core and cylinders) and obtaining the

necessary correlations. As noted above, permeability strongly affects the effectiveness of the method.

It should be noted that we should not confine ourselves to the above-described set of experimental studies. Such a complex and heterogeneous system as oil shale, especially the Bazhenov Formation, should be thoroughly studied.

The following section describes the samples selected for the research and test design strategy. In the scope of this study, only a part of the recommended experimental plan was included. However, this is an essential step towards understanding the air injection mechanisms in oil shale.

3.2. Samples selection and tests design strategy

This research proposes an integrated approach to investigating the high-pressure air injection (HPAI) in oil shales based on an investigation of coexisting processes separately and together. This approach is essential for better understanding the mechanisms of synthetic oil generation and displacement during HPAI. Those coexisting processes are pyrolysis, oxidation, and hydrolysis. As was stated previously, ahead of the combustion front, the formation water and water generated via the combustion process (combustion water) are in the hot, sub-critical and supercritical state depending on temperature, current reservoir pressure and gas content. That is why water extraction at different temperatures (hydrolysis) along with pyrolysis and oxidation were tested.

Table 2 lists all the experiments conducted with relation to the samples chosen and processes tested. As described in **Table 2**, kerogen-bearing rocks of the Bazhenov

Formation with different degrees of maturity were studied by conducting a series of laboratory experiments of oxidation, pyrolysis, and hydropyrolysis, as well as a CT test.

Figure 29 illustrates the tests design strategy and grouping of the experimental studies in terms of processes tested and experimental scale.

Table 2. Summary of all the experiments conducted.

Oil Field ID	Grade of catagenesis	Processes tested	Experiments conducted
Oil Field 1	Protocatagenetic substage (PC ₃ grade)	oxidation	STA, PDSC, ARC, RTO
		pyrolysis	open-system pyrolysis (kinetics)
		HPAI	combustion tube test
Oil Field 2	Mesocatagenesis substage (MC ₂ grade)	hydropyrolysis	autoclaves: open-system
		HPAI	combustion tube test
Oil Field 3	Mesocatagenesis substage (MC ₁ grade)	oxidation	thermal microscopy, STA
			HPRTO
		pyrolysis	thermal microscopy
			HPRTO
hydropyrolysis	autoclaves: closed-system		
HPAI	combustion tube test		
Oil Field 4	Mesocatagenesis substage (MC ₁ – MC ₂ grade)	oxidation	STA
		pyrolysis	open-system pyrolysis (kinetics)
		hydropyrolysis	autoclaves: open-system
		HPAI	combustion tube test

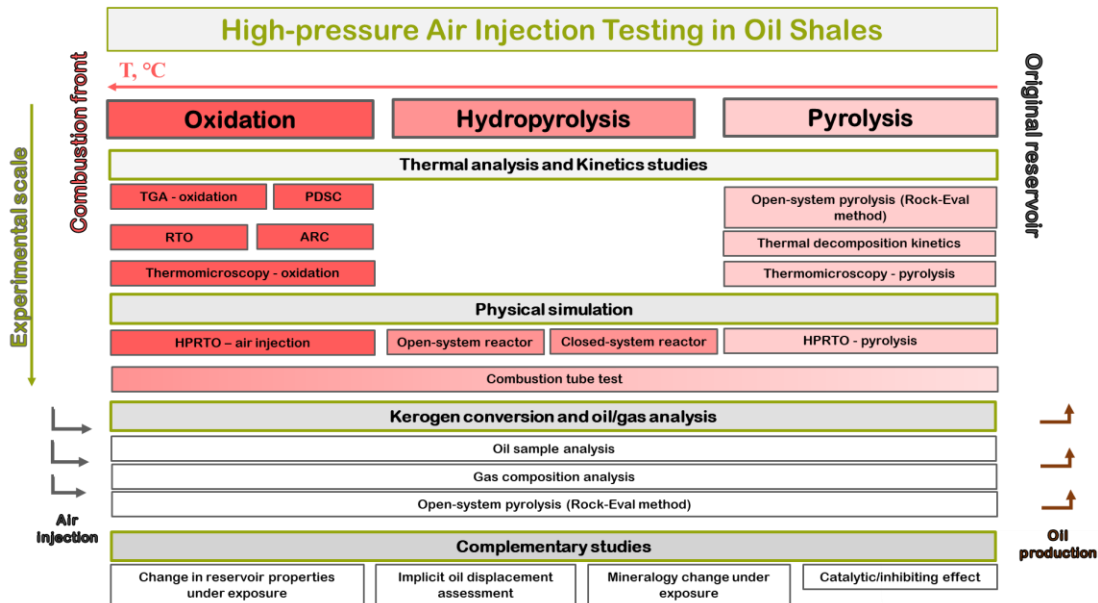


Figure 29. Test design strategy.

It should be noted that samples from four oil fields of the Bazhenov Formation were studied. Each section of Chapter 3 presents the results of testing different samples, unless specified otherwise. The samples' IDs are valid for the relevant section only.

3.3. Thermal analysis

3.3.1 Samples selection and test design strategy

For the thermal analysis, seven Bazhenov shale core samples from three oil fields of interest were chosen, namely: four samples (#1, #2, #3, #4) from Oil Field 4, one sample (#5) from Oil Field 1 and two samples (#6, #7) from Oil Field 3. Note that Sample #5 represents isolated kerogen.

To see a bigger picture of the mechanisms that occur during thermal decomposition and oxidation of kerogen, different techniques of thermal analysis were

applied. **Table 3** contains data on the selected samples and experiments which fall into the following categories:

- Thermomicroscopy Analysis: visually studying the kerogen conversion processes during oxidation and pyrolysis.
- Simultaneous Thermal Analysis (STA): investigating temperature intervals of mass losses and thermal effects corresponding to the low-temperature oxidation region and high-temperature oxidation region.

Table 3. Test design strategy.

Oil Field ID	Sample ID	Experiment conducted
3	6, 7	Thermomicroscopy
4	1, 2, 3, 4	Simultaneous thermal analysis (STA)
1	5 (isolated kerogen)	

Through implementing these analyses, one can investigate various aspects of the process: visual monitoring at micro-scale, mass losses, and heat output or energy consumption. In the following sub-sections, the experimental methodology is described in detail.

3.3.2 Thermal microscopy

Carl Zeiss Axio Scope A1 microscope coupled with a Linkam TS1500 heating stage was utilized for monitoring transformations in the morphology and the microstructure of the BF oil shale samples during heating with the heating rate of 10°C/min from room temperature up to 720°C in the helium and air purge at 100 ml/min rate. In order to visually study the organic matter conversion mechanisms during

oxidation and pyrolysis, two thin oil shale sections with the size of 5×5×1 mm were made from the Samples #6 and #7 (Oil Field 3). Thin sections of rock contain clays, dark gray silicates, pyrite, bitumen, and kerogen. Two experiments were performed, namely: one test designed to study the kerogen conversion mechanism during pyrolysis by purging helium, and the other aiming to study the kerogen conversion mechanism during oxidation by purging synthetic air (20% O₂ and 80% N₂).

Photo and video reports showing the pore space and minerals change dynamics were obtained. As a result, organic matter and mineral matrix conversion during heating of the thin rock section were monitored. **Figure 30**, **Figure 31** and **Figure 32** feature the photos of the thin rock section before and after pyrolysis. It can be seen from the photos that dark grey areas disappeared during heating, which could be explained by bitumen cracking. The sizes of some voids were also measured in the photos.

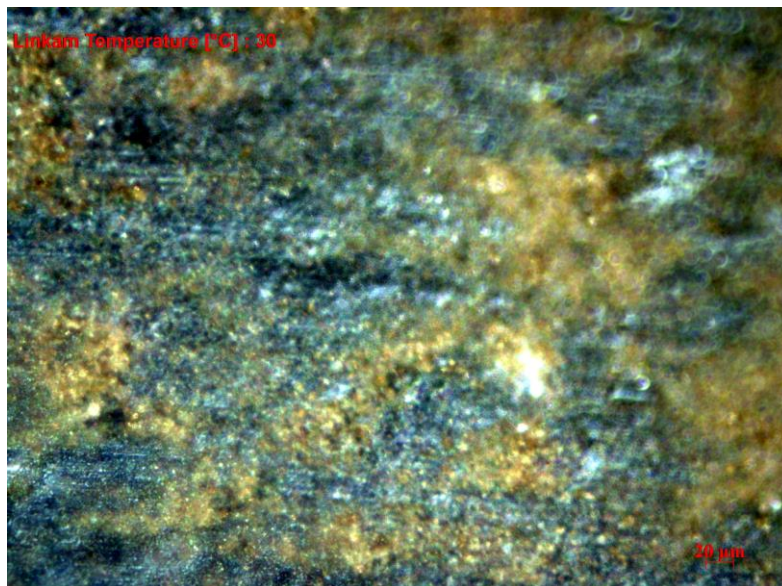


Figure 30. Sample #6. Photo before heating with helium purge (Bondarenko et al., 2017).

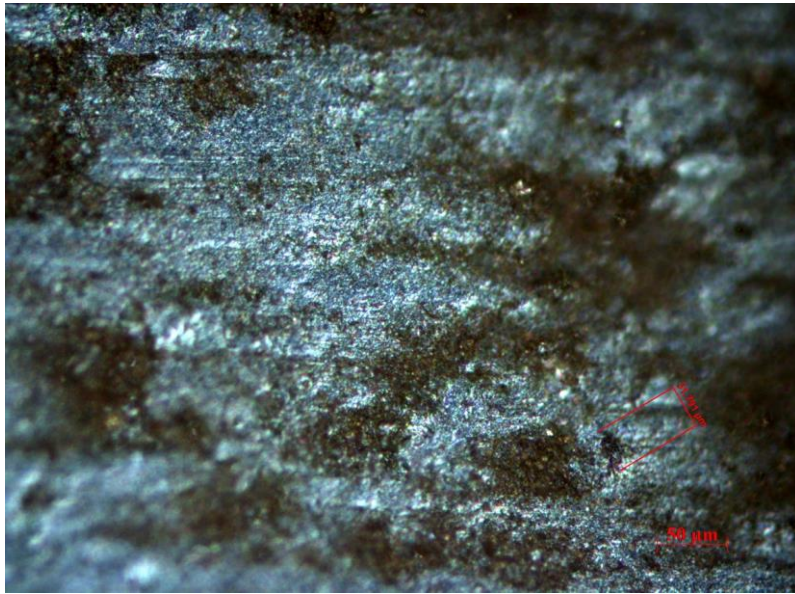


Figure 31. Sample #6. Photo after heating with helium purge up to 720°C (50µm)
(Bondarenko et al., 2017).

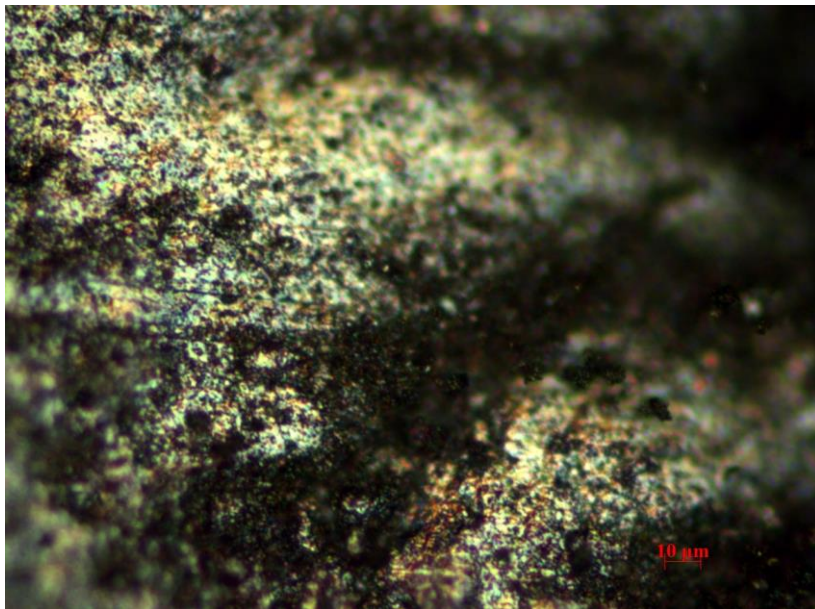


Figure 32. Sample #6. Photo after heating with helium purge up to 720°C (10µm)
(Bondarenko et al., 2017).

Figure 33 and **Figure 34** display the photos of the thin rock section before and after oxidation. In **Figure 34**, white minerals represent burnt core and red minerals look like iron oxides after pyrite oxidation.

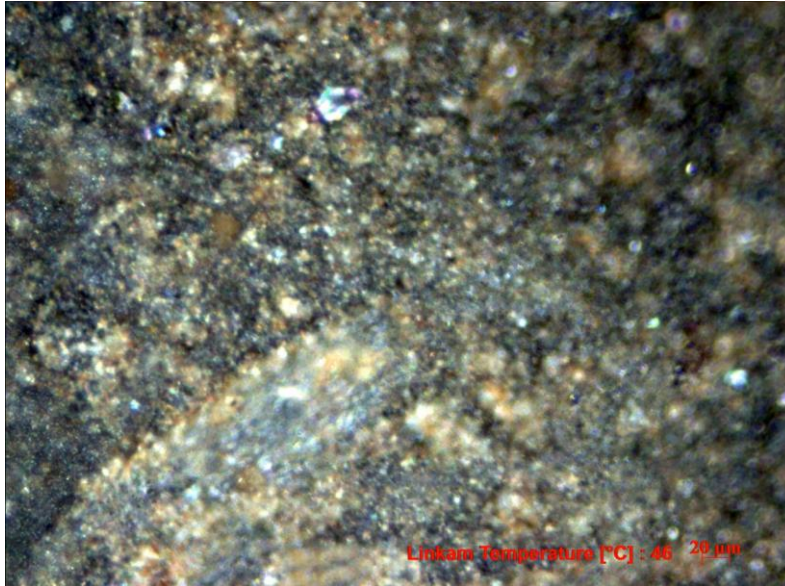


Figure 33. Sample #7. Photo before heating with air purge up to 720°C (20μm)
(Bondarenko et al., 2017).

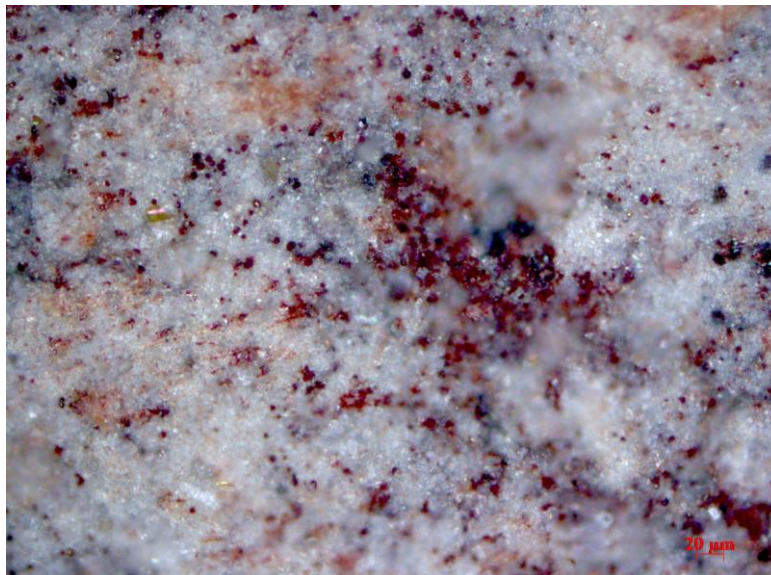


Figure 34. Sample #7. Photo after heating with air purge up to 720°C (20μm)
(Bondarenko et al., 2017).

In order to understand the kerogen and mineral matrix oxidation mechanism, the photos of an organic matter spot (23.43 μm in diameter) taken at different temperatures during oxidation were arranged into a sequence (**Figure 35**) which clearly displays a

change in color in the mineral matrix and release of gases and vapor. The color of the organic matter spot kept growing lighter up to nearly 200°C, which can be explained by the fact that this temperature marks the end of the first reactions group, which can be low-temperature oxidation reactions. As we know from the pyrolysis study of the oil shale, thermal oxidation and decomposition correspond to free oil and bitumen pyrolysis. The next intensive reactions range registered around 200 – 530°C might correspond to high-temperature oxidation reactions of the generative part of kerogen, while its non-generative part is still there, as well as coke generated from kerogen pyrolysis. It can be seen from the photos that thermal decomposition and oxidation of kerogen resulted in the formation of voids. Reactions at higher temperatures altered the minerals matrix, with dark gray siliceous minerals transformed into white, burnt minerals beyond 540°C. The reason for the color change might be formation of magnetic minerals as a result of pyrite oxidation. In addition, starting from around 540°C, coke-like material left in the voids started to be oxidized, and a change in color followed.

Intensive cracking that started at 450°C (**Figure 36**) is yet another important effect. The red circles mark the organic matter spots that underwent similar transformations. As was observed before, oxidation caused voids formation, and then fracture was induced through those voids.

The experiments described above helped to obtain useful information for the simulation of oil shale heating in terms of void space transformation and kerogen conversion mechanisms. In this work, thermomicroscopy was proved to be a useful tool for investigating organic matter conversion during heating. This method allows detecting

temperature-dependent changes using just one sample. Further investigation using thermomicroscopy coupled with mineralogy analysis is strongly recommended.

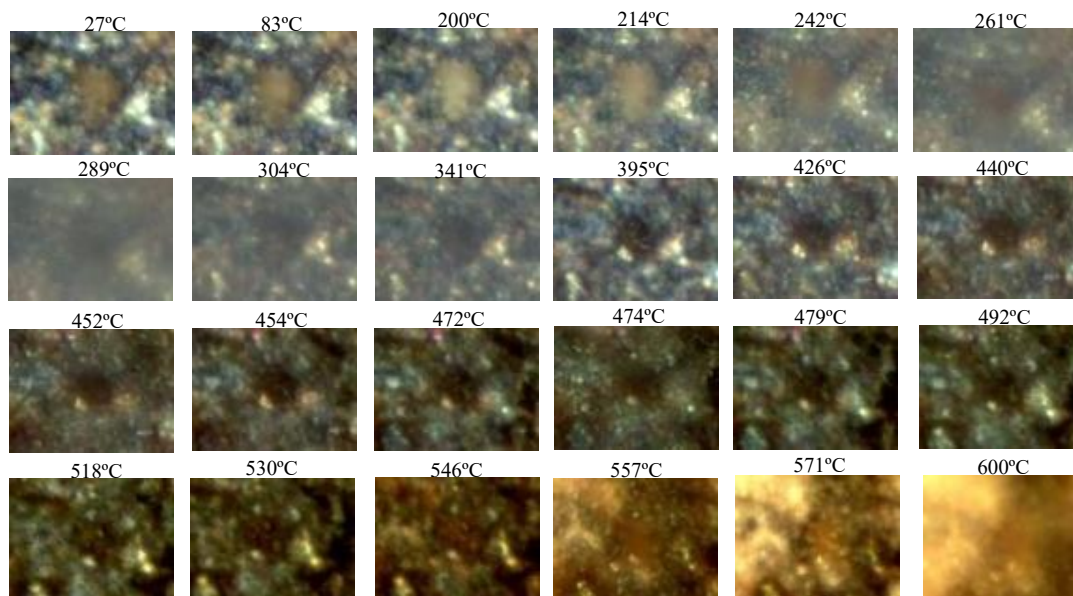


Figure 35. Sample #7. Size of organic matter spot is 23.43 μm . Mechanism of kerogen conversion over time during heating at a rate of 10°C/min with air purge up to 600°C (Bondarenko et al., 2017).

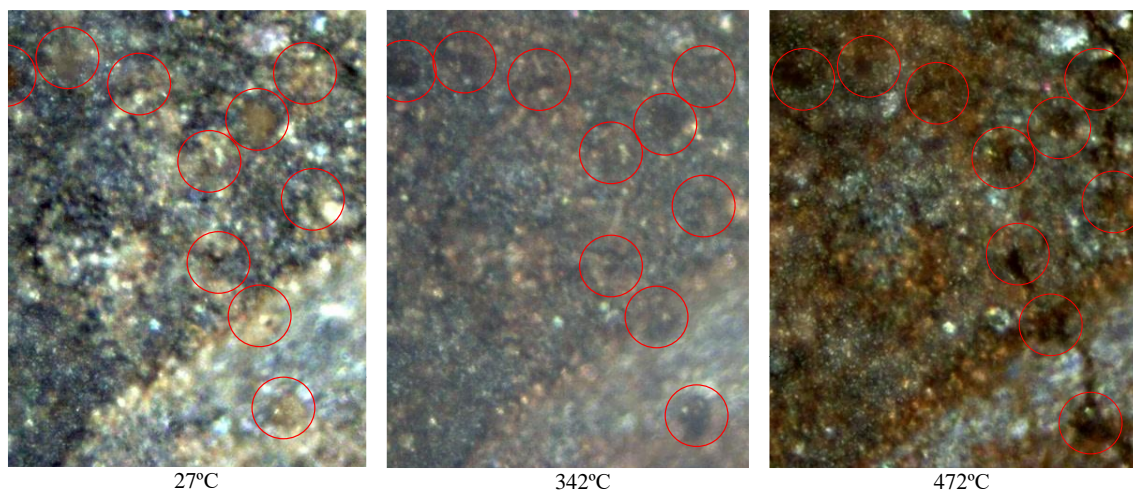


Figure 36. Sample #7. Cracking formation during heating with air purge (Bondarenko et al., 2017).

3.3.3 Simultaneous thermal analysis

Simultaneous thermal analysis (STA) means simultaneously applying two thermal analysis techniques to the same sample in one apparatus, namely: differential scanning calorimetry (DSC) and thermogravimetry analysis (TGA) (*Patrick, 1998*). In this study, Netzsch STA 449 F1 set-up was used to determine the sample's mass changes and heat effects. The analysis was carried out on 30 - 50 mg powdered extracted oil shale samples at a heating rate of 10°C/min from 40 to 720°C at an air rate of 100 ml/min.

Table 4 reports mass changes and heat effects due to oxidation. **Figure 37** displays the correlation between the Total Organic Carbon (TOC) value and the heat effect. There is a linear relationship between these two values, which means that the data might be interpolated for other samples of the same grade of catagenesis. Further research is needed.

Table 4. STA results for four samples from Oil Field 4.

Sample	TOC, %	Heat effect, J/g	Mass loss, %	
			40.69 ~ 262.50°C	262.50 ~ 731.91°C
1	16.98	5,350	0.77	27.77
			40.82 ~ 256.50°C	256.50 ~ 731.34°C
2	14.12	3,552	0.82	21.02
			40.74 ~ 241.90°C	241.90 ~ 731.39°C
3	8.51	1,695	0.41	11,08
			40.70 ~ 240.20°C	240.20 ~ 731.29°C
4	8.42	1,632	0.38	10.71
			40.72~218.00°C	218.00~641.20°C
5	Isolated kerogen	14,008	3.24	74.03

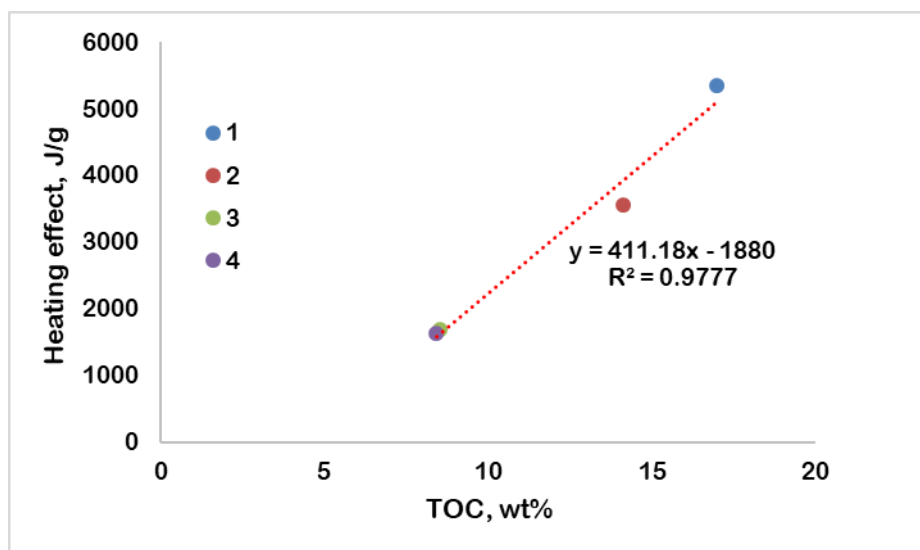


Figure 37. Heating effect and TOC relationship. Samples 1-4 from Oil Field 4 (Bondarenko et al., 2017).

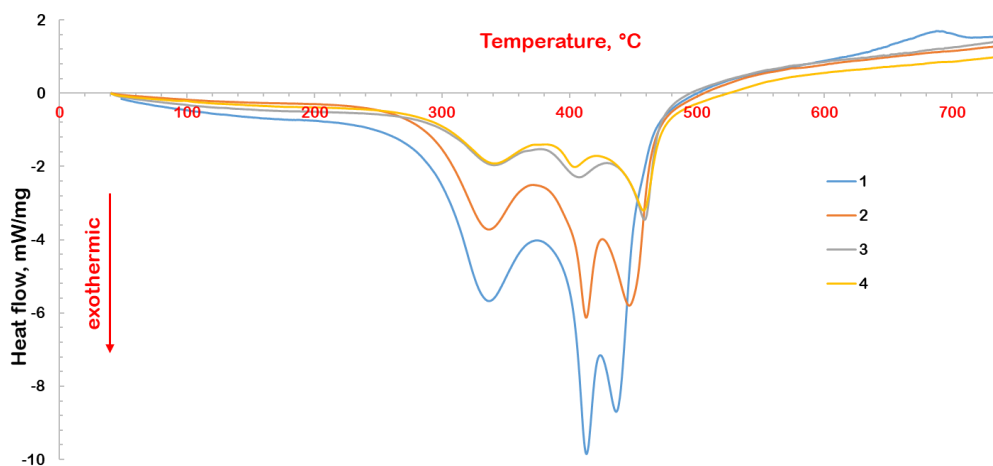


Figure 38. DSC curves for four samples from Oil Field 4 (Bondarenko et al., 2017).

Figure 39 and **Figure 40** give STA curves for isolated immature kerogen (Sample #5, Oil Field 1, PC₃) and an oil shale sample (Sample #3, Oil Field 4, MC₁₋₂). Comparing the two DSC curves suggests that the grade of catagenesis plays a certain role in heat

effects during oxidation. This difference will be discussed and explained in detail in Chapter 5.

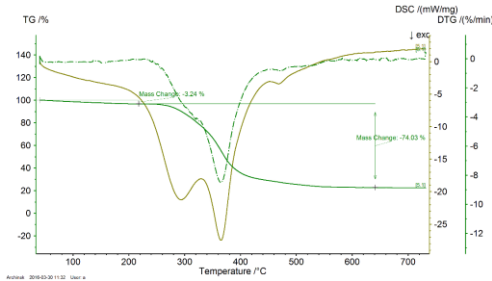


Figure 39. STA curves for Sample #5 from Oil Field 1 (PC₃ grade).

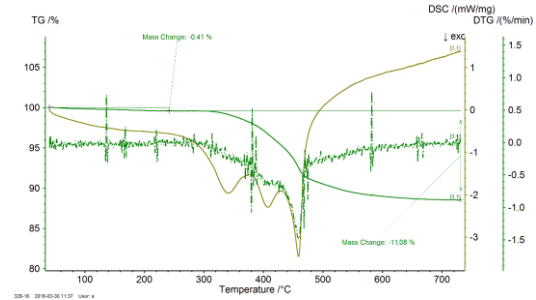


Figure 40. STA curves for Sample #3 from Oil Field 4 (MC₁ – MC₂ grade).

3.3.4 Conclusions

In this investigation, the aim was to determine kerogen conversion mechanisms due to thermal decomposition and oxidation using STA analysis and thermomicroscopy. As a result, a linear relationship was established between TOC and heat effect for oil shales with the same grade of catagenesis. Moreover, the grade of catagenesis might play an important role in the oxidation of organic matter. The mass loss and heat effect are indicative of the fact that the Bazhenov shale organic matter oxidation reactions occurred in the temperature range from 240 to 580°C.

Conversion of organic matter due to thermal decomposition and oxidation caused an increase in void space. The pyrolyzed thin section changed color to black due to the coking process. The analysis of video and photos of kerogen conversion in air purge revealed the existence of two temperature ranges of intensive oxidation reactions, namely 120 – 200°C and 220 – 570°C. Fracturing started at 450°C, induced through voids formed due to kerogen oxidation. Moreover, a change in the mineralogy of siliceous minerals manifested by a change in color from grey to white was observed at 540°C. Pink

and red magnetic minerals were generated via oxidation of pyrite. This study proved the thermomicroscopy thermal analysis method to be a useful tool for the investigation of organic matter conversion mechanisms.

3.4. Pyrolysis and oxidation: kinetic studies

3.4.1 Samples selection and test design strategy

The goal of this study was to investigate pyrolysis and oxidation of oil shale samples with and without oil saturation to improve the understanding of the complex nature of the reactions and to determine the role of different fractions in the above-mentioned processes.

Three series of tests composed of differential scanning calorimetry (PDSC), accelerating rate calorimetry (ARC) and ramped temperature oxidation (RTO) were proposed for this work. PDSC analysis was conducted at 8 MPa, which corresponded to the running pressure of the combustion tube test which will be described in Chapter 4. An additional test was conducted at 14 MPa (the highest operating pressure of the equipment). Other experiments, ARC and RTO, were performed at 15 and 14 MPa, respectively, which also represent the highest operating pressures. The reason for selecting the maximum pressures was to get much closer to a significantly higher reservoir pressure, 28 MPa. For this study, geochemical properties were measured by Rock-Eval open-system pyrolysis method. **Table 5** summarizes the objectives and test design strategy of these experiments.

Table 5. Test design strategy and materials used (Bondarenko et al., 2017).

Experiment	Material	Sample ID	Oil Field	Objectives and parameters to determine.
Open-system pyrolysis	Powered core	1, 2, 3, 4, 5, 6, 7	1, 3, 4	Geochemical parameters and pyrolysis kinetics.
PDSC	Oil pre-saturated core	8	1	Temperature regions where heat generation rates are significant and the kinetic parameter for each region.
ARC	Oil pre-saturated core	8	1	Ignition temperature and the temperature corresponding to the maximum self-heating rate.
RTO	Non-extracted core	8	1	Ignition temperature without oil saturation; temperature ranges over which oxygen uptake rates are high.

3.4.2 Kerogen thermal decomposition kinetics

Table 6. Samples selection for open-system pyrolysis.

Experiment	Oil Field ID	Sample ID
Open-system pyrolysis and kinetics	4	1, 2, 3, 4
	1	5
	3	6, 7

In this work, Rock-Eval pyrolysis method was applied to analyze the oil shale samples (Peters, 1986; Behar et al., 2001). This method involves thermal decomposition of the organic matter (OM) through programmed heating with and without oxygen to measure the hydrocarbons yield from pyrolysis and carbon dioxide yield from coke oxidation. In other words, the programmed heating (red line in **Figure 41**) can be divided into pyrolysis and oxidation stages, where the pyrolysis stage starts at 90°C and ends at

650°C or higher, followed by cooling down to 300°C, and oxidation at up to 750°C or higher. This programming can be changed to meet the purpose of the test. In this work, a classical pyrolysis study was implemented.

The pyrolysis study was conducted on 50 - 70 mg non-extracted powdered oil shale samples. According to the classical method, the amount of thermally decomposed hydrocarbons in milligrams of HC per gram of rock is designated as S0 peak at 120°C, and as S1 peak between 120 and 300°C which corresponds to free oil. It is known that kerogen decomposition starts at around 300°C and ends at 650°C, depending on the sample. For example, after oxidation or pyrolysis treatment, it might be necessary to investigate this sample at higher temperatures (this method will be shown in further sections of this Chapter). This temperature range corresponds to S2 kerogen yield in mg HC per gram of rock and represents the HC source potential. T_{max} is the temperature corresponding to the maximum HC yield at S2 peak and characterizing oil shale maturity, whereas Total Organic Carbon (TOC) is measured from both the pyrolysis and oxidation stages and characterizes a measure of the organic carbon richness of the rock.

Table 7 reports the results of Rock-Eval pyrolysis analysis, as well as lithological characteristics of the samples. **Figure 41 - Figure 47** illustrate temperature pyrograms of the samples selected. The black curve indicates hydrocarbons yield (S0, S1 and S2). According to the geochemical analysis, TOC values vary from 8.42 to 17.42 wt% across the samples selected, and T_{max} varies from 424°C to 446°C (*Bondarenko et al., 2017*). The results indicate that kerogen is of Type II in all the analyzed samples.

Table 7. Open-system pyrolysis experiment data (Bondarenko et al., 2017).

Sample	S1	S2	TOC	T _{max}	HI	Lithological type	OM type
	mg HC/g rock	mg HC/g rock	Total Organic Carbon, wt%	°C			
1	6.36	56.18	16.98	446	331	Kerogen-siliceous	II
2	6.67	44.08	14.12	445	312	Kerogen-clay-siliceous	II
3	8.60	23.03	8.51	444	270	Kerogen-siliceous- claystone	II
4	9.73	26.39	8.42	443	325	Kerogen-carbonaceous-claystone	II
5	3.96	100.20	14.01	424	750	Isolated kerogen	II
6	6.30	107.60	16.98	433	633	Bituminous kerogen-siliceous-claystone	II
7	6.90	117.07	17.42	433	672	Bituminous kerogen-siliceous-claystone	II

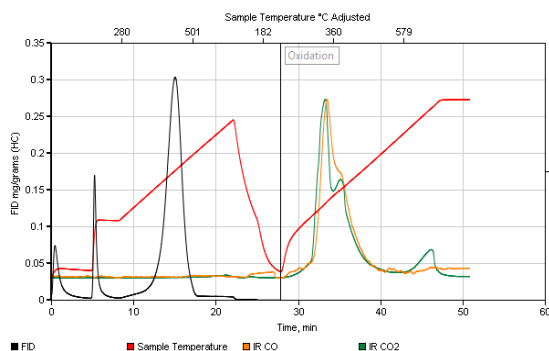


Figure 41. Pyrogram of Sample #1 (Bondarenko et al., 2017).

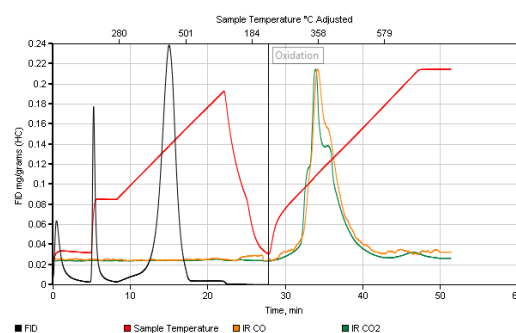


Figure 42. Pyrogram of Sample #2 (Bondarenko et al., 2017).

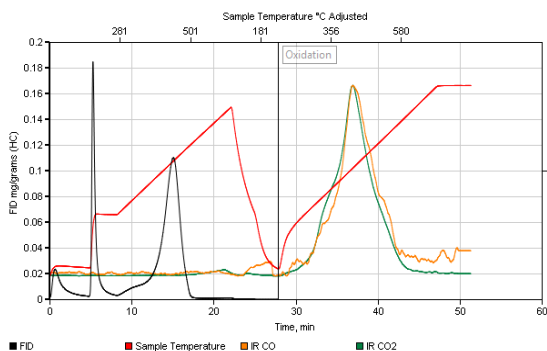


Figure 43. Pyrogram of Sample #3
(Bondarenko et al., 2017).

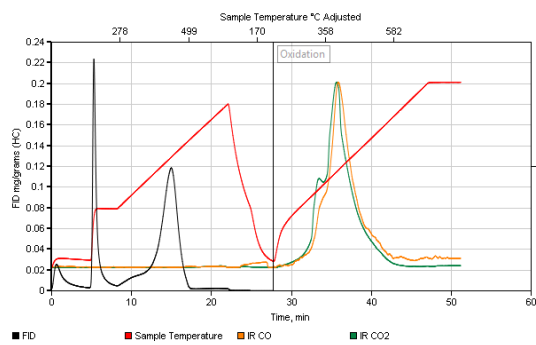


Figure 44. Pyrogram of Sample #4
(Bondarenko et al., 2017).

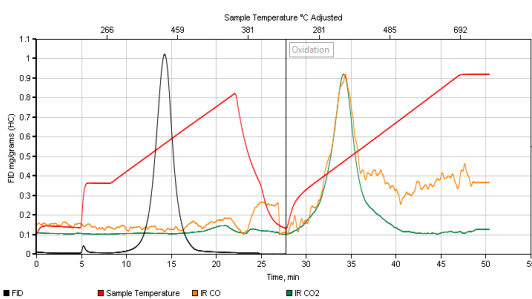


Figure 45. Pyrogram of Sample #5
(Bondarenko et al., 2017).

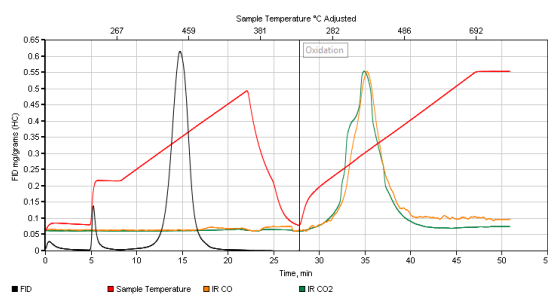


Figure 46. Pyrogram of Sample #6
(Bondarenko et al., 2017).

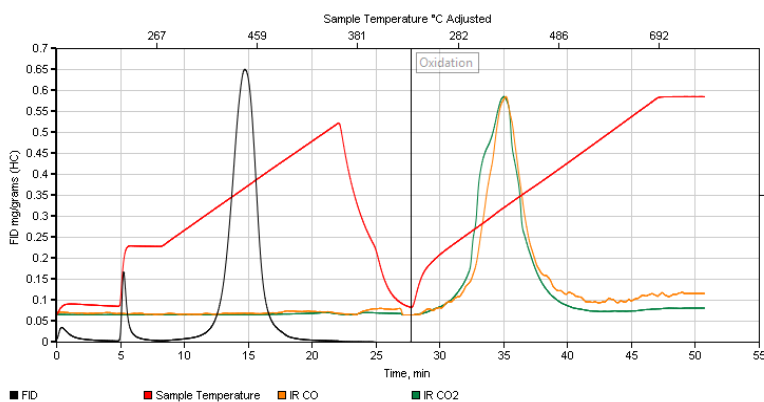


Figure 47. Pyrogram of Sample #7 (Bondarenko et al., 2017).

Two approaches were applied to generate the kinetic parameters from the pyrolysis study results. Firstly, three pyrolysis runs at different heating rates were conducted, in order to measure HC yield as a function of time/temperature. Then these

data were subjected to the numerical analysis using a software program that was designed to generate kinetic parameters, namely: frequency factor A and activation energy E_a distribution. The described approach lets them vary freely (*Benson, 1976; Braun et al., 1991*).

The alternative technique uses manual setting of a reasonable value for A to avoid unsuitable combinations of A and E_a distribution, which is often calculated when A can be varied freely. This approach was first proposed by *Waples (1996)* and then was applied and tested (*Waples et al., 2002; Waples et al., 2010*). Another reason for applying this technique is that using the same value of A for all the analyzed samples makes it easier to compare the samples in terms of E_a distributions. *Waples and Nowaczewski (2014)* recommended fixing the frequency factor at $2 \times 10^{14} \text{ s}^{-1}$ and deriving the activation energy distribution with a spacing of 1 kcal/mole (4,184 J/mol) after a single pyrolysis run. They made this conclusion after analyzing 259 oil shale samples. **Figure 48** illustrates the statistics analysis of the kinetic data. It should be noted that some researchers disagree with the described approach and suggest performing at least three ramps of an open-system pyrolysis study after testing a number of runs (*Peters et al., 2015*).

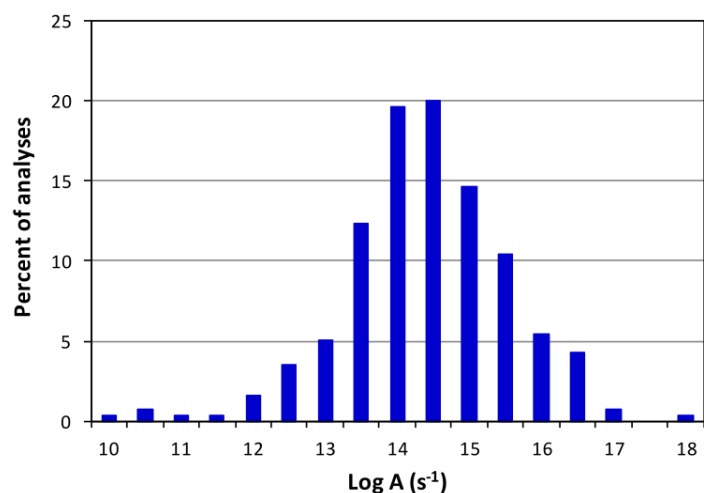


Figure 48. Logs of A factors shown in histogram form for hydrocarbon-generation kinetics published for 259 source rocks. All these A factors were determined by allowing both A and E_a to vary freely during derivation of kinetic parameters from raw pyrolysis data (Waples and Nowaczewski, 2014).

Kinetic runs were conducted on 30 - 50 mg powdered extracted samples at heating rates of 5, 10 and 30°C/min. After that, bulk-kinetic parameters were obtained using the Kinetics2015 optimization software (special software for interpreting HAWK pyrolysis station data). **Table 8** lists the kinetic parameters calculated.

Table 8. Kinetics data (activation energy and frequency factor).

Sample ID	Activation Energy E_a , J/mol	Frequency factor A, 10^{13} s^{-1}
1	237,568	93.337
2	216,648	2.559
3	244,848	3.781
4	245,936	93.337
5	220,622	1.549

Figure 49, Figure 51, Figure 53, Figure 55, and Figure 58 illustrate discrete activation energy distributions with 1 kcal/mole (4,184 J/mol) spacing between groups. **Figure 50, Figure 52, Figure 54, Figure 57, and Figure 59** show discrete activation

energy distributions with a fixed frequency factor $A = 2 \times 10^{14} \text{ s}^{-1}$ and 1 kcal/mole (4,184 J/mol) spacing between the groups (Bondarenko *et al.*, 2017).

It should be pointed out that pyrolysis kinetic parameters and E_a distribution should not vary a lot, because four samples were collected from almost the same depth in the same oil field. Distributions derived with a fixed frequency factor showed consistency and displayed the same E_a value that corresponds to the maximum organic matter conversion, 54 kcal/mol (225,936 J/mol) (**Figure 50**, **Figure 52**, **Figure 54**, and **Figure 57**).

In the samples with mature organic matter at MC₁₋₂ grade (Samples #1, #2, #3 and #4), a part of HC generation capability was utilized, whereas the remaining kerogen will have E_a distribution differing from that of the immature material. **Figure 58** and **Figure 59** illustrate discrete E_a distribution of isolated kerogen obtained by applying two calculating techniques. Notably, the values obtained are consistent with those of Goncharov *et al.* (2016) who analyzed a lot of Bazhenov shale samples from different oil fields.

The activation energy distribution can be reproduced in the following form:

$$Rate = A \cdot \left(e^{-\frac{E_{a1}}{RT}} \cdot S_1 + e^{-\frac{E_{a2}}{RT}} \cdot S_2 + \dots + e^{-\frac{E_{an}}{RT}} \cdot S_n \right) \quad (3.1)$$

where A is the frequency factor ($2 \times 10^{14} \text{ s}^{-1}$), S_n is the relative proportion of each group of the reacting species, and E_{an} is the activation energy for each group of species.

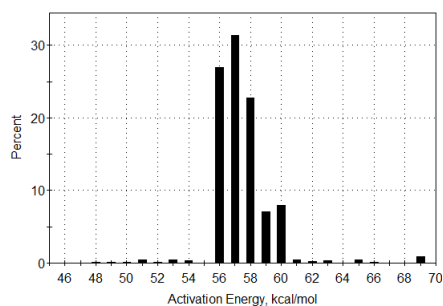


Figure 49. E_a distribution with a spacing of 1 kcal/mole (4,184 J/mol) between groups and $A = 1.1674 \times 10^{15} \text{ s}^{-1}$. Sample #1 (Bondarenko et al., 2017).

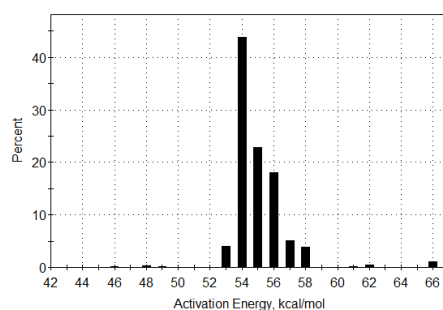


Figure 50. E_a distribution with a spacing of 1 kcal/mole (4,184 J/mol) between groups and fixed $A = 2 \times 10^{14} \text{ s}^{-1}$. Sample #1 (Bondarenko et al., 2017).

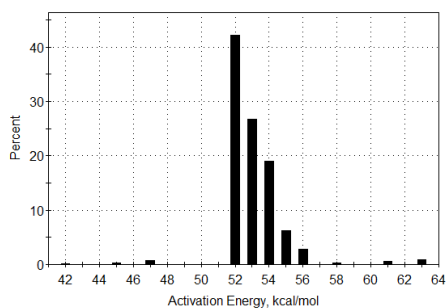


Figure 51. E_a distribution with a spacing of 1 kcal/mole (4,184 J/mol) between groups and $A = 4.8325 \times 10^{13} \text{ s}^{-1}$. Sample #2 (Bondarenko et al., 2017).

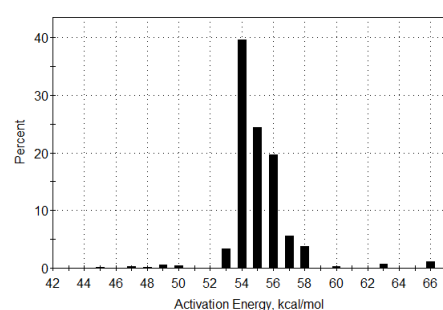


Figure 52. E_a distribution with a spacing of 1 kcal/mole (4,184 J/mol) between groups and fixed $A = 2 \times 10^{14} \text{ s}^{-1}$. Sample #2 (Bondarenko et al., 2017).

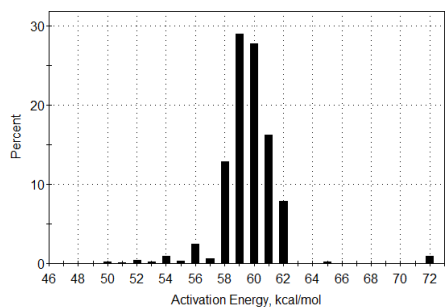


Figure 53. E_a distribution with a spacing of 1 kcal/mole (4,184 J/mol) between groups and $A = 8.3616 \times 10^{15} \text{ s}^{-1}$. Sample #3 (Bondarenko et al., 2017).

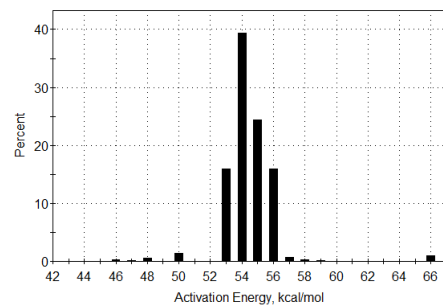


Figure 54. E_a distribution with a spacing of 1 kcal/mole (4,184 J/mol) between groups and fixed $A = 2 \times 10^{14} \text{ s}^{-1}$. Sample #3 (Bondarenko et al., 2017).

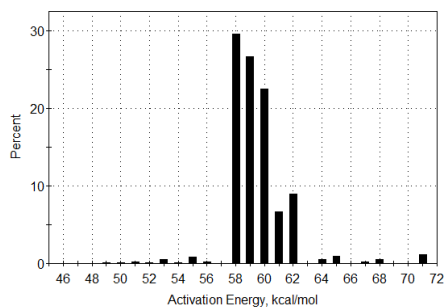


Figure 55. Ea distribution with a spacing of 1 kcal/mole (4,184 J/mol) between groups and $A = 4.5061 \times 10^{15} \text{ s}^{-1}$. Sample #4 (Bondarenko et al., 2017).

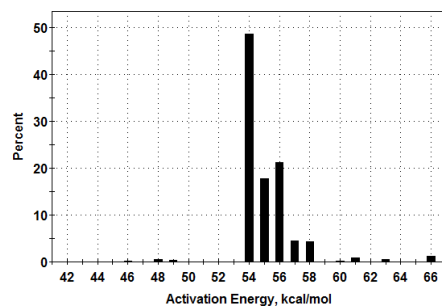


Figure 57. Ea distribution with a spacing of 1 kcal/mole (4,184 J/mol) between groups and fixed $A = 2 \times 10^{14} \text{ s}^{-1}$. Sample #4 (Bondarenko et al., 2017).

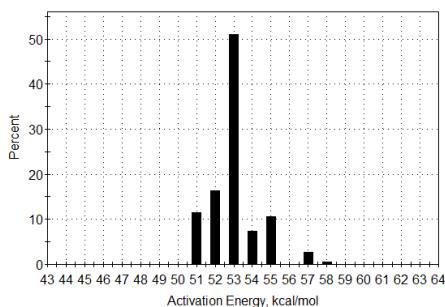


Figure 58. Ea distribution with a spacing of 1 kcal/mole (4,184 J/mol) between groups and $A = 4.5061 \times 10^{15} \text{ s}^{-1}$. Sample #5 (isolated kerogen) (Bondarenko et al., 2017).

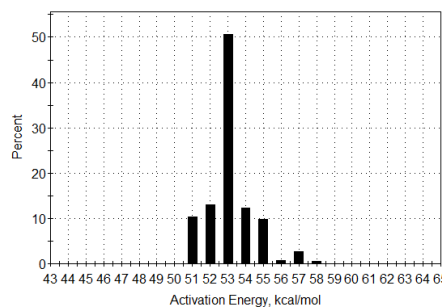


Figure 59. Ea distribution with a spacing of 1 kcal/mole (4,184 J/mol) between groups and fixed $A = 2 \times 10^{14} \text{ s}^{-1}$. Sample #5 (isolated kerogen) (Bondarenko et al., 2017).

3.4.3 Pressurized Differential Scanning Calorimetry (PDSC)

Table 9 features the results of a Rock-Eval pyrolysis study with lithological characterization of the Sample #8. Shown in **Figure 60** is the temperature pyrogram of a rock sample.

Table 9. Open-system pyrolysis experiment data for Sample 8.

Sample	S0, <i>mg HC/g rock</i>	S1, <i>mg HC/g rock</i>	S2, <i>mg HC/g rock</i>	TOC, <i>Total Organic Carbon, wt%</i>	T _{max} , °C	Depth, <i>m</i>	HI	Lithological type
8	0.68	0.68	16.89	3.01	428	2631	560	Kerogen- siliceous

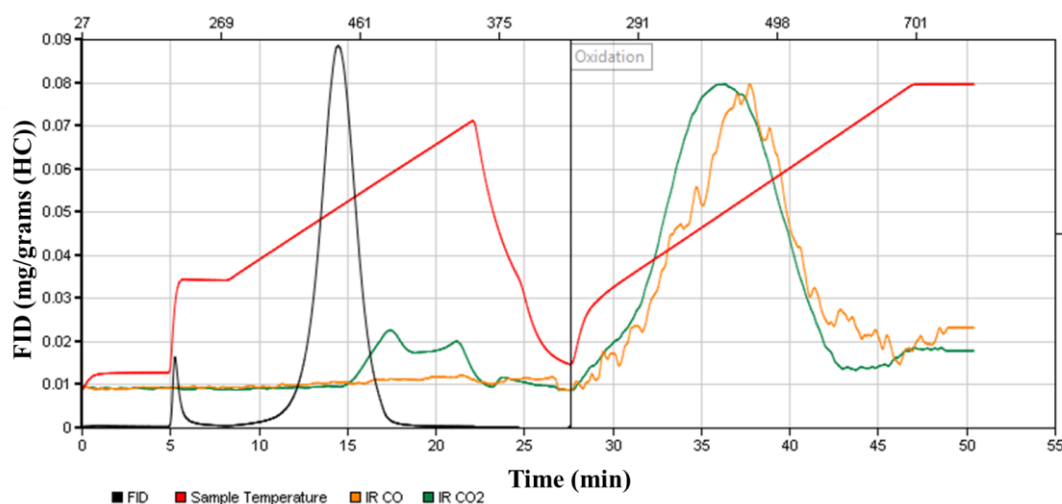


Figure 60. Pyrogram for Sample #8 (Khakimova et al., 2018).

Bazhenov shale oil and rock (< 0.5 mm) were mixed in a ratio of 1 to 9 by weight that mimics saturation in the combustion tube test described in the following Chapter. NETZSCH DSC 204 HP Phoenix differential scanning calorimeter was used to conduct experiments on 4 mg samples at pressures of 8 and 14 MPa with an air flow rate of 60 ml/min from the room temperature up to 600°C. Heating rates of 5, 10, 15, and 20°C/min were used in experiments under 8 MPa, whereas only 10 and 20°C/min were implemented at a pressure of 14 MPa.

PDSC results revealed three exothermic peaks, which repeated the results obtained in Section 3.3.3 (Figure 61). Moreover, Sample #5 and Sample #8 represent oil

shale samples collected from the same well in Oil Field 1 (almost the same depth). From the comparison of **Figure 39** and **Figure 61**, one can conclude that oxidation reactions of light oil that was mixed with the sample prevailed in the low-temperature region. These reactions caused the growth of the first peak, as compared to the kerogen oxidation heat output curve (**Figure 39**). The second peak may correspond to oxidation of kerogen and products of its pyrolysis, which is proved by DSC curve of isolated kerogen. The last peak may correspond to oxidation of the non-generative organic (NGOC) part of kerogen and coke generated in the previous oxidation stage (the second peak). In Chapter 5, this scenario is tested numerically.

NETZSCH Proteus 6.0 tool was used for pre-smoothing DSC curves and NETZSCH Peak Separation 3 software for breaking down DSC curves into individual peaks (**Figure 62**).

Table 10 presents the data derived from the analysis of PDSC individual peaks, namely: onset temperature, $T_{on,i}$, peak temperatures, $T_{peak,i}$, thermal effects of individual peaks, ΔH_i , cumulative thermal effect, ΔH , sample mass losses, and Δm at different heating rates β and under two pressures, 8 and 14 MPa.

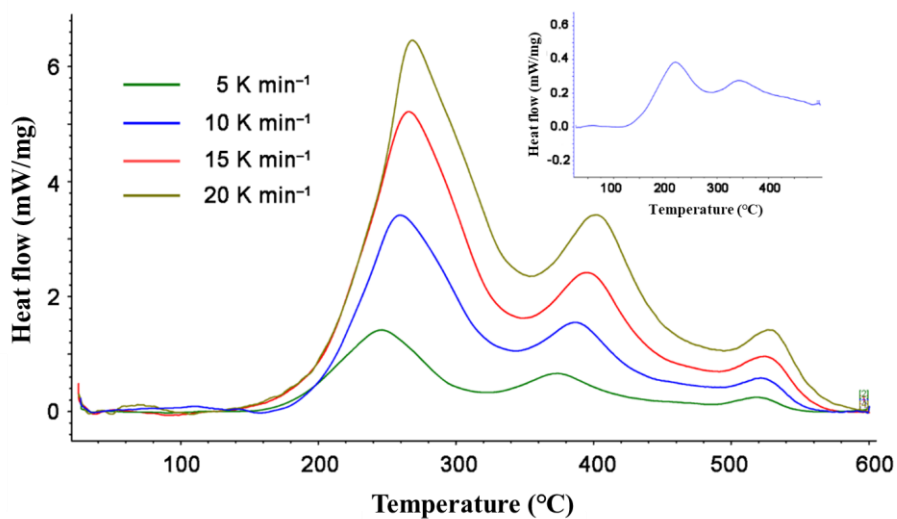


Figure 61. Sample #8. DSC oxidation curves, pressure 8 MPa. Upper right corner curve represents a heating rate of 1°C/min (Khakimova et al., 2018).

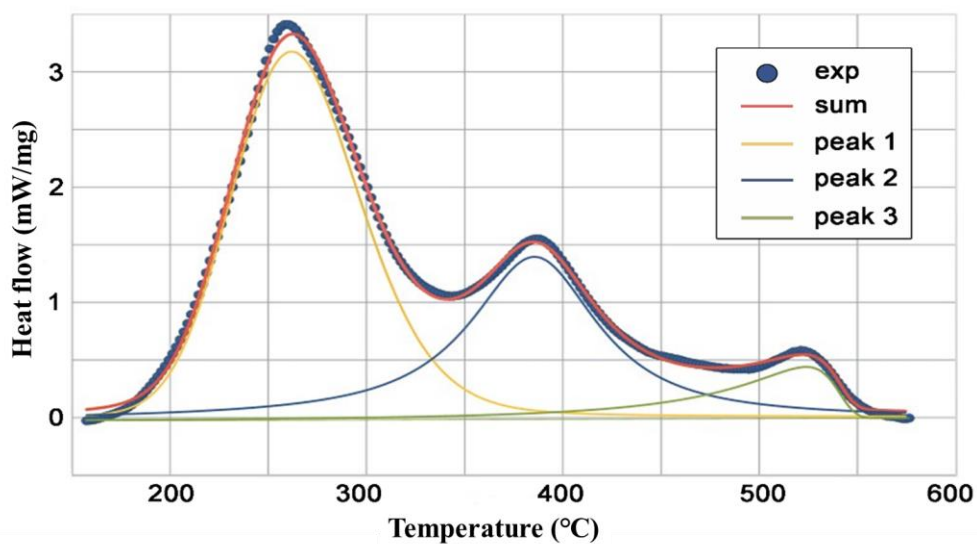


Figure 62. Sample #8. Example of DSC curve breakdown into individual peaks, heating rate 10°C/min (Khakimova et al., 2018).

Table 10. PDSC individual peaks analysis results (Khakimova et al., 2018).

β , K/min	$T_{on, 1}$, °C	$T_{peak, 1}$	ΔH_1^{**} , J/g	$T_{on, 2}$, °C	$T_{peak, 2}$, °C	ΔH_2^{**} , J/g	$T_{on, 3}$, °C	$T_{peak, 3}$, °C	ΔH_3^{**} , J/g	ΔH^{**} , J/g	Δm , %
<i>P = 8 MPa</i>											
1	143.8	217.6			335.2			-		3126	7.0
5	179.6	246.1			373.6			518.5		2183	10.8
10	200.4	259.2			387.6			521.3		2754	11.2
15	204.5	265.7			395.1			524.2		2954	11.3
20	223.0	268.2			402.1			526.6		2955	10.3
1	150.0*	217.6*	1658*	256.2*	340.8*	1328*	469.5*	-	-	3126	7.0
5	184.4*	245.4*	1214*	308.5*	372.9*	697*	469.5*	523.1*	117*	2183	10.8
10	203.0*	262.3*	1568*	321.6*	386.1*	721*	447.3*	523.0*	189*	2754	11.2
15	201.7*	267.8*	1710*	329.7*	395.4*	752*	442.2*	524.8*	229*	2954	11.3
20	209.7*	273.4*	1630*	339.2*	402.9*	698*	449.7*	528.3*	229*	2955	10.3
<i>P = 14 MPa</i>											
10	191.7	259.8			385.9			540.1		2519	11.7
20	220.3	253.7			378.4			534.6		3649	11.3

* Calculated for individual components of DSC curves.

** the thermal effect of the reaction is calculated based on the initial mass of the sample; the linear function was chosen as the baseline.

The kinetic parameters calculated for each exothermic peak by three methods, namely, ASTM, Ozawa-Flynn-Wall and Friedman, are presented in

Table 11. They can be reproduced in Arrhenius form:

$$k_n = A_n \cdot e^{-\frac{E_{an}}{RT}} \quad (3.2)$$

where k_n is the rate constant of reaction at the n^{th} peak, A_n is the frequency factor for the reaction at the n^{th} peak (s^{-1}), E_{an} is the activation energy for the reaction at the n^{th} peak (J/mol), R is the universal gas constant (8.314 J/(mol·K)), and T is the absolute temperature (K).

Table 11. Kinetic characteristics of sample oxidation at 8 MPa.

Peak number	ASTM		Friedman*		Ozawa-Flynn-Wall*	
	$E_a, J/mol$	$\log A, s^{-1}$	$E_a, J/mol$	$\log A, s^{-1}$	$E_a, J/mol$	$\log A, s^{-1}$
1	108,000 ± 10,000	8.4	77,000 ± 7,000	5.0	87,000 ± 9,000	6.1
2	154,000 ± 7,000	9.9	193,000 ± 9,000	12.9	171,000 ± 9,000	11.3
3**	563,000 ± 161,000	35.5	438,000 ± 66,000	27.2	383,000 ± 71,000	24.0

* - The values given correspond to a conversion of 0.5;

** - When processing data for the third peak, the heating rate of 5 K/min was not used.

3.4.4 Accelerating Rate Calorimetry (ARC)

NETZSCH ARC 254 accelerating rate calorimeter was used for this study. The same mixture of oil and rock as that used in PDSC test was packed into a 7 ml stainless steel spherical container. This equipment is able to accurately monitor changes in temperature and also detect fast reactions, so that it can switch into adiabatic regime

when needed (*Bhattacharya et al., 2015*). In this study, the "heat-wait-search" regime was applied, where the sample was heated with a 5°C step, followed by isothermal regime for 30 minutes. If the temperature inside the container grew faster than 0.02°C/min, the equipment automatically switched to the adiabatic regime to follow the exothermic reaction until the self-heating rate dropped below 0.02°C/min or until the temperature reached 500°C. If no self-heating was detected in the samples for 30 minutes, the system started the next 5°C heating step. The initial pressure in the system was 15 MPa. **Figure 63** presents the variations of pressure and temperature during the experiment. One can see from the temperature profile that the oxidation reaction started at 105°C and continued up to 383.6°C for 843 minutes, while the maximum reaction rate was detected at 245.8°C. The results indicated that the oxidation of oil-saturated oil shale is quite intensive, with the maximum pressure change rate of 2020 bar/min and the maximum heating rate of 339.8°C/min. When the self-heating rate was less than 0.02°C/min, the stepwise heating was resumed. Another exothermic reaction was detected at 477°C, followed by self-heating up to 492°C.

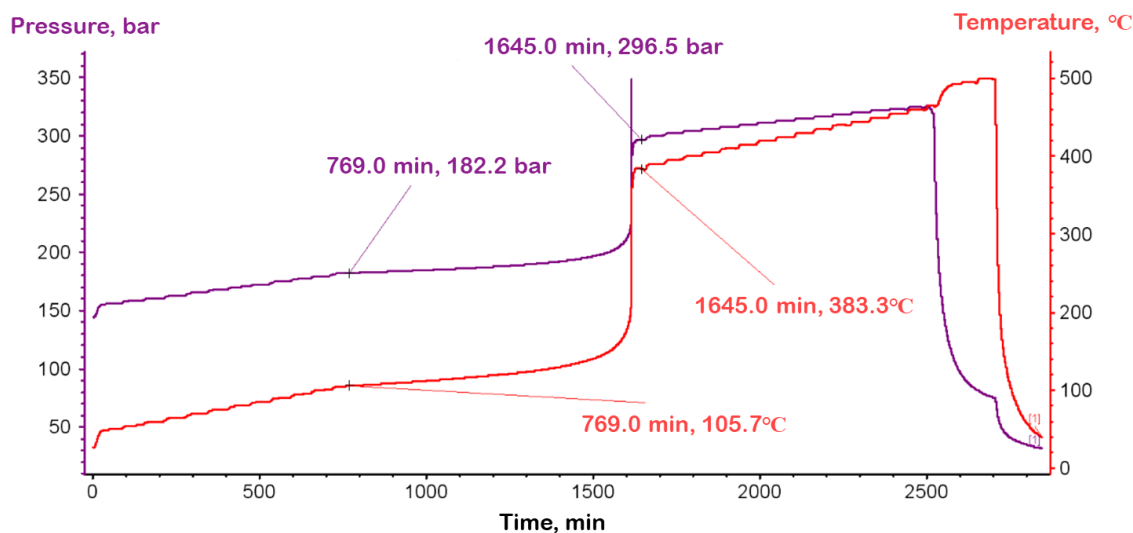


Figure 63. Pressure profile (purple line) and temperature profile (red line) during oxidation (Khakimova et al., 2018).

3.4.5 Ramped-temperature oxidation experiment (RTO)

Ramped temperature oxidation RTO device unit consists of a flow reactor with a pressure monitoring system (Item 4, Figure 64), a gas flow control system (Items 1-3, Figure 64), a temperature control system (Item 5, Figure 64) and oxygen and carbon oxides analyzers (Item 6, Figure 64).

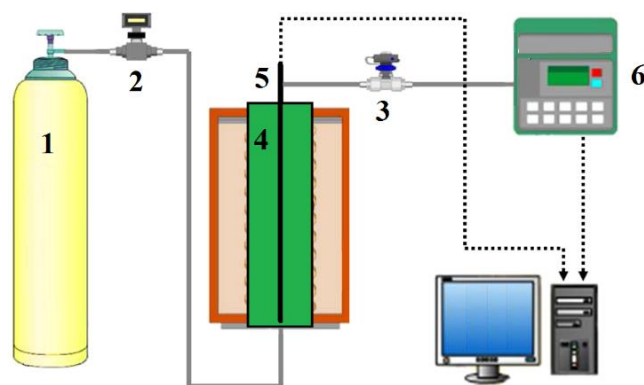


Figure 64. Schematics of RTO set-up (Khakimova et al., 2018).

The same crushed sample (20 g) not subjected to pre-saturation was placed in the reactor with the thermocouple rod in the center. For this study, 1.50, 1.75, 2.00,

2.25°C/min heating rates were applied at 15 l(ST)/h air flow rate. The sample's mass was limited because of the limitation of gas analyzers.

Figure 65 shows the rate of oxygen consumption during heating. **Figure 66** illustrates gas molar composition versus temperature at the minimum heating rate of 1.5°C/min. Two regions were identified, namely: a low-temperature region (LTR) and a high-temperature region (HTR), where oxidation reactions are dominant in LTR (**Table 12**). Two peaks can be identified in HTR, proving the concept of three stages.

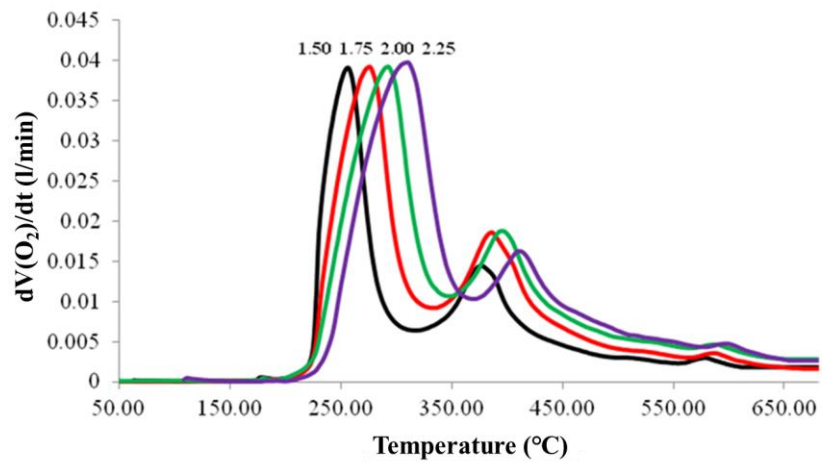


Figure 65. Sample 8. Rate of oxygen uptake (1.50, 1.75, 2.00 and 2.25°C/min) (Khakimova et al., 2018).

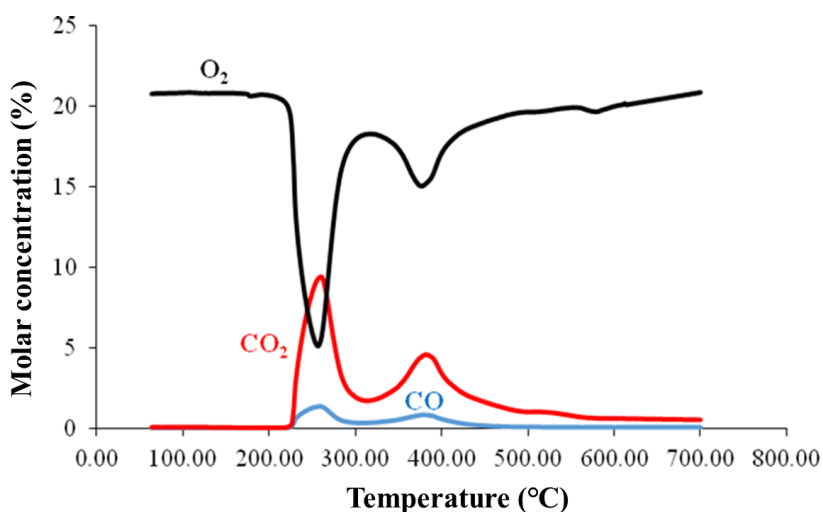


Figure 66. Sample #8. Gas mixture composition versus temperature (1.50°C/min) (Khakimova et al., 2018).

Table 12. Temperature parameters of LTR and HTR (Khakimova et al., 2018).

Heating rate, °C/min	LTR*		HTR**	
	Temperature interval, °C	Peak temperature, °C	Temperature interval, °C	Peak temperature, °C
1.50	225-289	255.6	322-423	377.1
1.75	224-311	276.8	318-446	387.0
2.00	224-332	293.3	325-455	395.3
2.25	234-356	308.9	331-478	410.1

*LTR – low-temperature region

**HTR – high-temperature region

The kinetic parameters for the two peaks were calculated using three methods, namely: ASTM E 698-11 (I), ASTM E 698-11 (II) and Ozawa-Flynn-Wall method. The results are presented in **Table 13**.

Table 13. Kinetic parameters in LTR and HTR (Khakimova et al., 2018).

Heating rate, K/min	LTR*		HTR**	
	E _a , J/mol	A, s ⁻¹	E _a , J/mol	A, s ⁻¹
ASTM E 698 (I)	10,300±500	6.94×10 ⁻²	34,500±5.3	8.87
ASTM E 698 (II)	13,900±400	20.19×10 ⁻²	34,200±4.0	8.58
Ozawa-Flynn-Wall	21,700±1500	1.78×10 ⁻⁴	39,000±2.8	3.82*10 ⁻³

*LTR – low-temperature region

**HTR – high-temperature region

3.4.6 Conclusions

In this section, the oxidation and pyrolysis kinetics data were measured and reported. By means of geochemical analysis, the bulk-kinetic parameters were calculated and two different approaches to determining E_a distribution were studied. The outcomes suggest that fixing the frequency factor rather than letting the frequency vary freely yields more consistent results.

The pressurized differential scanning calorimetry (PDSC) study identified temperature regions where heat generation rates were significant. The kinetic parameters were calculated from the data obtained. By means of the accelerating rate calorimetry (ARC) study, the oxidation starting temperature was determined to be 105°C. Two regions of reactions were identified, namely: 105 - 383.6°C and 477 - 492°C. In both PDSC and ARC studies, samples pre-saturated with oil were used. In the ramped-temperature oxidation (RTO) study, the rock sample used had not been subjected to pre-saturation. It was found from the experiments that the dominant oil and kerogen oxidation

reactions occur in the low-temperature region (LTR), which is indicative of the spontaneous ignition at reservoir conditions. Moreover, the experiments established the negative temperature gradient region (NTGR).

3.5. Oxidation: High-pressure ramped temperature oxidation (HPRTO)

3.5.1 Samples selection and test design strategy

High-pressure ramped temperature oxidation (HPRTO) of non-extracted crushed core without oil flood is a unique study that helps to understand adsorbed hydrocarbons and kerogen oxidation behavior in a porous media at the reservoir pressure of 28 MPa. Core samples from Oil Field 3 (MC₁) were selected for this study. It must be noted that the same experiment conditions and core material are replicated in the nitrogen injection test described in the next section. Comparing the air and inert gas injection tests, one can determine the mass of hydrocarbons that will be burned under these test conditions.

3.5.2 Methodology

HPRTO set-up was chosen as the testing tool for the current study (*Moore et al., 1999; Mallory et al., 2018*). The basic flow schematics is displayed in **Figure 67**. In this experiment, synthetic air (22.38% O₂, 77.62% N₂) was injected top-down at a flow rate of 15.34 l(ST)/h (air flux 40 m³(ST)/m²h), while the controlled non-extracted crushed core (0.1-0.7 mm) heating rate was set to 40°C/h. Crushed and homogenized core samples were packed inside a one-dimensional reactor which was then placed in a high-pressure jacket. The reactor had a 21.1 mm diameter and a 483 mm length. The porosity of the core model was 39.9% and the grains volume was 92 cm³. The crushed core samples were not pre-mixed with oil as is usual in similar cases. Oil was eliminated from the

study in order to understand kerogen and adsorbed HC oxidation behavior, in other words, as many native oil oxidation reactions as possible were excluded from the study. The flow reactor was set to uniform heating along the whole length from room temperature to 500°C, followed by isothermal heating until no heat release and oxygen uptake occurred. Gas composition was measured every 20 min using gas chromatographs directly connected to the system, while liquid samples were collected into four traps according to the heating schedule. The pressure inside the flow reactor was maintained at 28 MPa (reservoir pressure). The annulus pressure was kept 0.3 - 0.6 MPa higher than the reactor pressure. In order to sweep out the trapped gases, the reactor was purged with helium at the same injection rate.

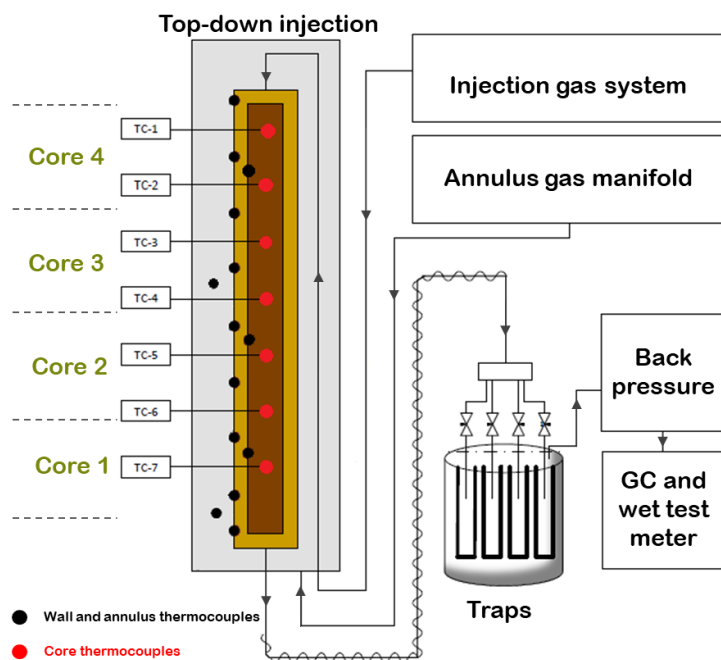


Figure 67. Flow schematics of HPRTO set-up.

The reactor was divided into seven heating intervals. Seven thermocouples were inserted radially at uniform intervals into the center of the reactor at the midpoint of each

of the heating zone sections to monitor the temperatures along the core model (**Table 14**). Comparison of the temperatures from these intervals gives accurate data on the temperature intervals, where significant changes of heat generation or consumption occur. The temperature intervals within which the liquid samples are collected are of critical importance. The traps switching schedule was set based on the temperature intervals of hydrocarbon yields in oil shales, in other words, intervals of S0, S1, and S2 peaks during pyrolysis by Rock-Eval method (*Peters, 1986*). It is known that the exothermic peak is a sum of the exothermic peaks of hydrocarbon oxidation reactions and the endothermic peak of thermal decomposition and distillation reactions.

Table 14. Location of thermocouples (TC) along the HPRTO reactor.

Thermocouple number	Distance between thermocouple and production end, mm
TC 1	445
TC 2	388
TC 3	331
TC 4	274
TC 5	217
TC 6	160
TC 7	103

3.5.3 Results: temperature profiles

Analyzing the temperature profiles illustrated in **Figure 68** and **Figure 69** one can see that the adsorbed hydrocarbons and kerogen oxidation reactions start at about 140°C. Interval seven was not subjected to external heating, which explains its lower peak

temperature. It was done intentionally for safety reasons. Most of the oxygen consumption occurs after the exothermic peak in the second zone. It can be noted that kerogen and the products of its thermal decomposition burn more slowly than oil. This is evident from the shape of the oxygen consumption curve and the exothermic temperature peaks that appear after the temperature reaches 500°C. This may be due to the fact that the thermal decomposition of kerogen occurs at up to 650°C, generating a continuous stream of new oxidative pyrolysis products which consume oxygen from the air injected. The peak temperatures attained in each interval of the reactor are listed in **Table 15**.

Table 15. Peak/maximum temperatures of the reactor intervals.

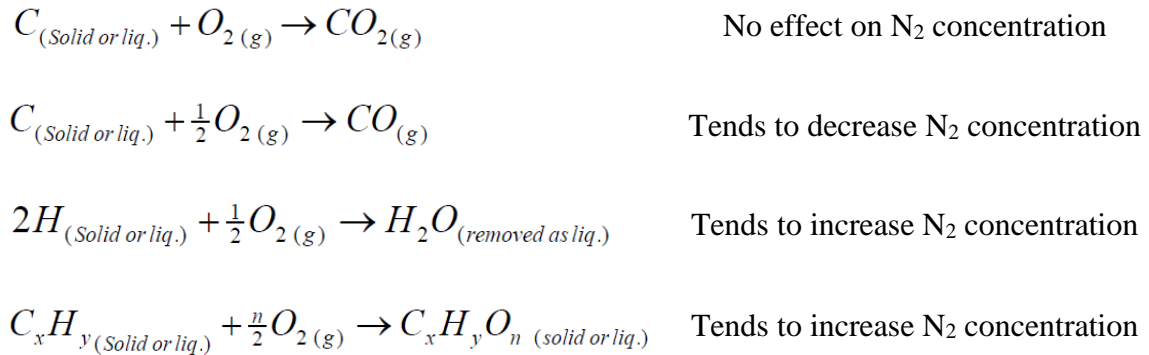
Interval/zone	Peak/maximum temperature, °C
1	500
2	500
3	502
4	549
5	608
6	516
7	562

3.5.4 Results: gas analysis

Table 16 contains total volumes and masses of each gas evolved from the reactor. **Figure 68** illustrates a combined temperature and CO, CO₂, N₂ and O₂ molar composition profile. **Figure 69** gives a combined temperature and hydrocarbon gases molar composition profile. It should be noted that gas composition profiles have been adjusted to reflect the delay associated with the passage of evolved gases from the reactor

outlet to the gas chromatograph. This adjustment was based on the helium identification delay after the start of helium purge. It does not, however, reflect the time it takes the gas to travel from the reaction front to the reactor exit, as this quantity is constantly changing. According to the calculation, GC delay time of 1.47 hours was applied. According to **Figure 69**, the prevailing hydrocarbon gas produced from the reactor was methane, which composition is much lower than flue gases composition.

The molar flow rate of nitrogen into the reactor remained essentially constant during the whole run. Therefore, the observed increase in nitrogen composition shown in **Figure 68** is indicative of the occurrence of oxygen addition and/or water generating reactions during the increased oxygen consumption period. The influence of the different oxidation reactions on nitrogen composition in the produced gases is shown below:



According to the result for the liquid samples, the increase in nitrogen content is attributed to water generation. At the 25th hour of the experiment, gas composition measurements were interrupted due to a technical problem. It must be stressed that during this short period of time no helium was injected into the core model and no gases were

evolved, which means that only isothermal heating occurred. In addition, thermocouple #6 did not show correct value of temperature due to the technical reasons.

Table 16. Total volumes and masses of evolved gases – HPRTO oxidation test.

Parameter	Volume, cc	Mass, g
CH ₄	572.29	0.38
C ₂ H ₆	154.93	0.21
C ₂ H ₄	2.83	0.004
C ₃ H ₈	76.35	0.15
C ₃ H ₆	15.27	0.029
n-C ₄ H ₁₀	36.16	0.098
n-C ₅ H ₁₂	33.58	0.116
CO	416.99	0.52
CO ₂	29,467.22	58.25
H ₂	18.44	0.002
H ₂ S	1174.17	1.81

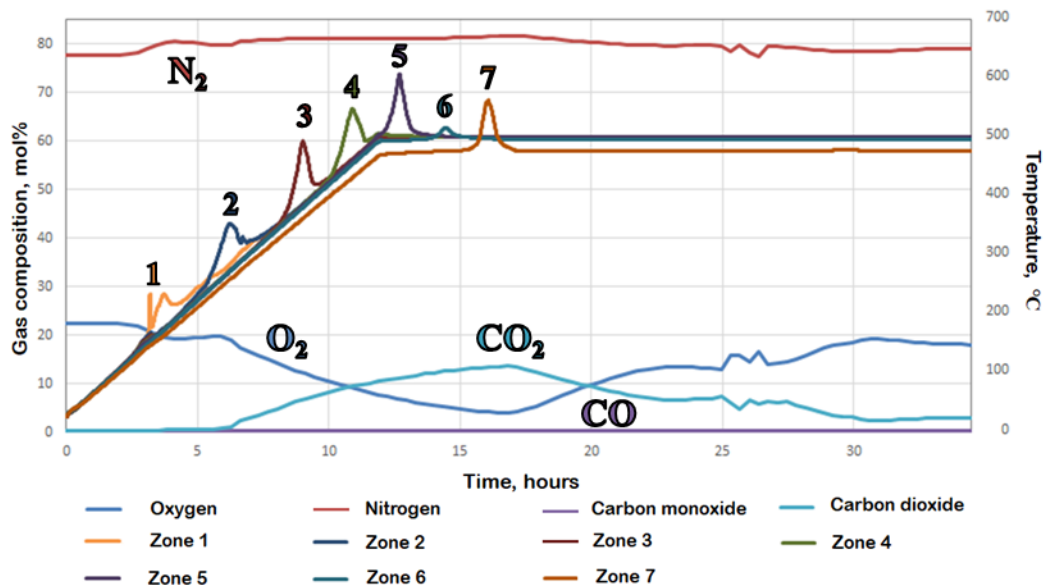


Figure 68. Temperature profiles and gas compositions (CO, CO₂, N₂, O₂). GC delay time – 1.47 hours.

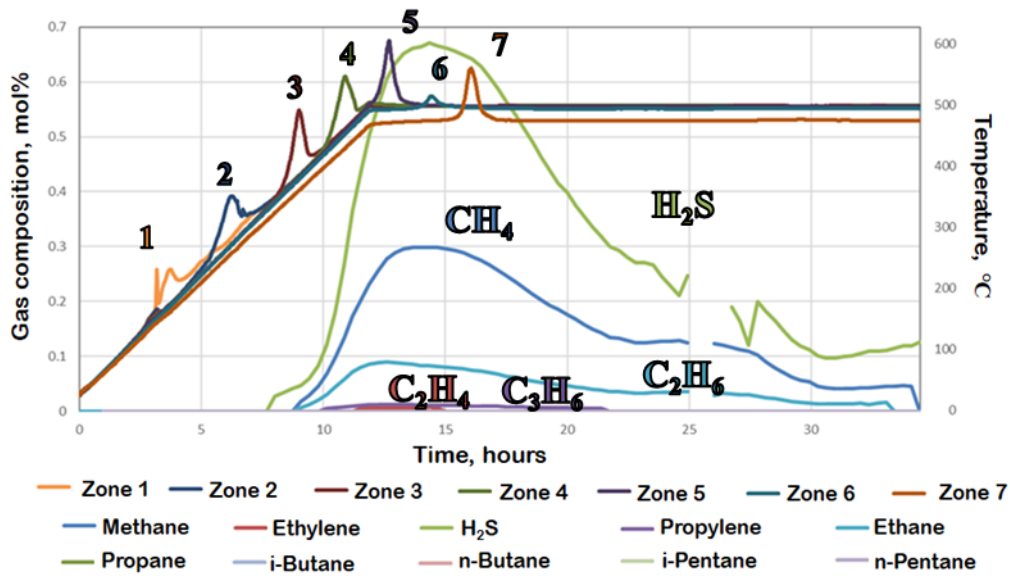


Figure 69. Temperature profiles and hydrocarbon gas compositions. GC delay time –1.47 hours.

The HPRTO analysis is based on O₂ balances inside and outside the reactor. It can be seen from the temperature profiles that the thermal front is moving much slower in the first two zones. Starting with the third zone, the front is moving faster, with a velocity of 39.8 mm/h. It should be noted that this velocity is low compared to the front velocity in heavy oil HPRTO tests. This means that the air requirements are very high. The combustion parameters were calculated from the following relationships (*Moore et al., 1999*):

$$\text{Air requirement} = \frac{\text{Air flux}}{\text{Front velocity}} \quad (3.3)$$

$$\text{Reacted O}_2 / \text{Fuel Ratio} = \frac{23.6445 \left(\frac{[N_2]}{R} \right)}{([CO_2] + [CO])(12.011 + 1.008[H/C])} \quad (3.4)$$

$$AAHCR = \frac{4 \left(\frac{[N_2]}{R} - [CO_2] - \frac{[CO]}{2} - [O_2] \right)}{([CO_2] + [CO])} \quad (3.5)$$

$$\%O_2 \text{ to } COx = \frac{\left([CO_2] + \frac{[CO]}{2} \right) \times 100}{\left(\frac{[N_2]}{R} - [O_2] \right)} \quad (3.6)$$

Table 17 provides the results for the apparent atomic H/C ratio (AAHCR), percentage of reacted oxygen converted to carbon oxides and apparent reacted oxygen/fuel ratio for this test. What's interesting in this table is that the air requirements are very high. However, the combustion parameters calculated from gas composition in HPRT0 tests are different from those obtained in the combustion tube test or in the reservoir. These parameters are presented here for the sake of comparison with other tests (*Moore et al., 1999*). According to the literature review, no such test has been conducted for oil shales so far. Further investigation is needed for testing different oxidation regimes in such a set-up by changing air flux, heating rate and maximum heating ramp temperature.

Wet combustion is commonly used to reduce the requirement for air and increase the front velocity. In the case of oil shale, water is in the supercritical state. By co-injecting water, *in situ* supercritical water generation may be initiated (depending on gas content).

Table 17. Combustion parameters.

Air requirement, m ³ (ST)/m ³ reservoir	1,003.5
Apparent atomic H/C ratio	0.95
Apparent reacted oxygen/fuel ratio, m ³ (ST)/kg	7.58
Reacted oxygen converted to carbon oxides, %	81.38

3.5.5 Results: core analysis

Rock-Eval pyrolysis study

Rock-Eval pyrolysis analysis was applied to crushed rock samples taken from different zones along the length of the reactor to assess the degree of conversion of kerogen to hydrocarbons as a result of thermal and chemical exposure. A photo of the unpacking procedure is shown in **Figure 70**. In total, core samples from for intervals were unpacked (100 mm in length each). **Table 18** presents Rock-Eval pyrolysis results.

The pyrolysis study data suggest that virtually no kerogen remained in the samples: one part served as fuel for combustion and the other was transformed into liquid and hydrocarbon gases. **Figure 71** and **Figure 72** illustrates pyrograms (SO, S1, S2, S4CO₂) of initial core and unpacked core samples.



Figure 70. Unpacking the core from the reactor (Bondarenko et al., 2017b).

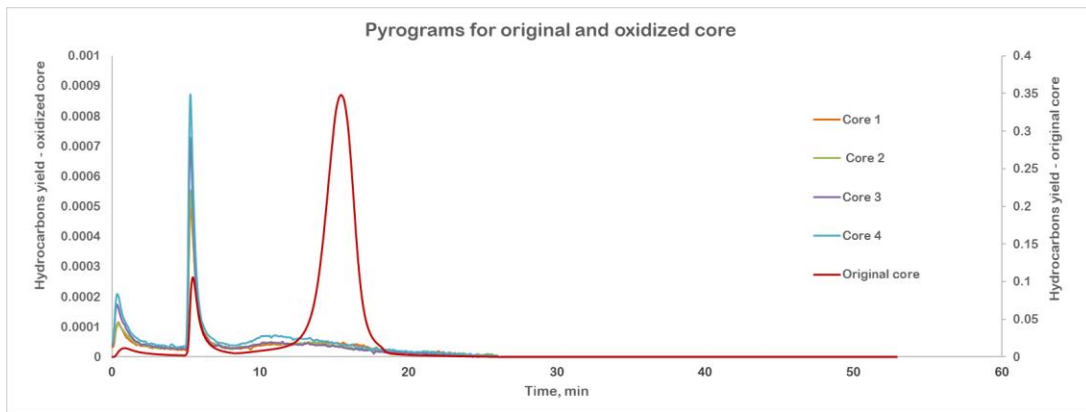


Figure 71. Pyrogram (hydrocarbon yield) of initial core sample and unpacked core samples (HPRTO air injection test).

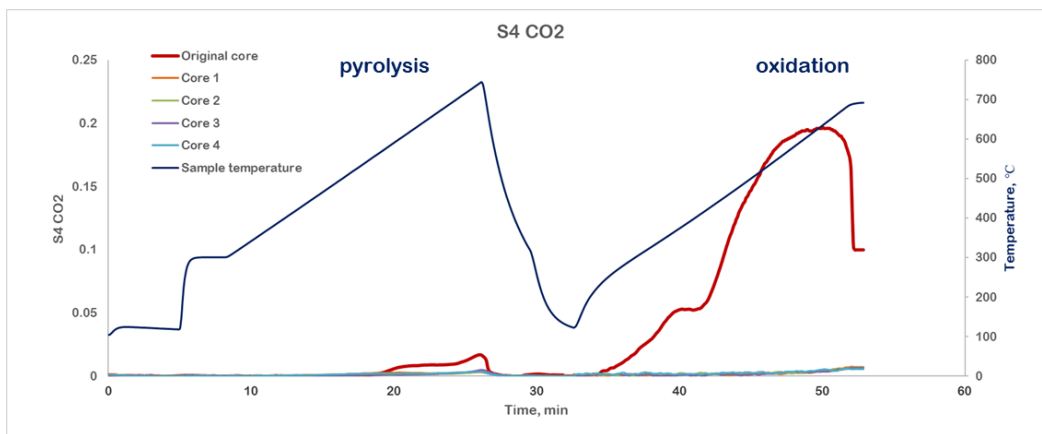


Figure 72. Pyrogram (S4CO2) of initial core sample and unpacked core samples with temperature schedule (HPRTO air injection test).

Table 18. Pyrolysis study results (HPRTO test: oxidation test).

Sample	S0	S1	S2	TOC	T _{max}	HI	OI	PI	S4CO2	S4CO
	<i>mg HC/g rocks</i>	<i>mg HC/g rocks</i>	<i>mg HC/g rocks</i>	<i>Total Organic Carbon, wt%</i>	<i>Maturity, °C</i>	<i>Hydrogen Index, S2/TOC*100</i>	<i>Oxygen Index, S3/TOC*100</i>	<i>Production Index, S1/S1+S2</i>		
Original Core	1.91	6.94	65.74	9.63	438	682	1	0.10	99.41	12.50
Core 1	0.02	0.03	0.04	0.18	383	20	105	0.43	1.46	2.35
Core 2	0.02	0.03	0.04	0.17	321	21	69	0.43	1.91	2.03
Core 3	0.02	0.03	0.03	0.23	340	13	63	0.50	1.29	3.51
Core 4	0.03	0.04	0.05	0.24	328	19	96	0.46	2.42	2.80

Elemental analysis and mineralogy change

Table 19. Results of elemental analysis of crushed core samples before and after exposure (HPRTO test: oxidation test).

Oil Field	Temperature, °C	Sample	N, %	C, %	H, %	S, %
Oil Field 3		Original core	0.23	11.67	1.34	4.23
Oil Field 3	500°C	Core 1 oxidation	0.00	0.00	0.41	2.75
Oil Field 3	549°C	Core 2 oxidation	0.00	0.00	0.18	2.88
Oil Field 3	608°C	Core 3 oxidation	0.00	0.00	0.21	3.19
Oil Field 3	562°C	Core 4 oxidation	0.00	0.00	0.30	3.10

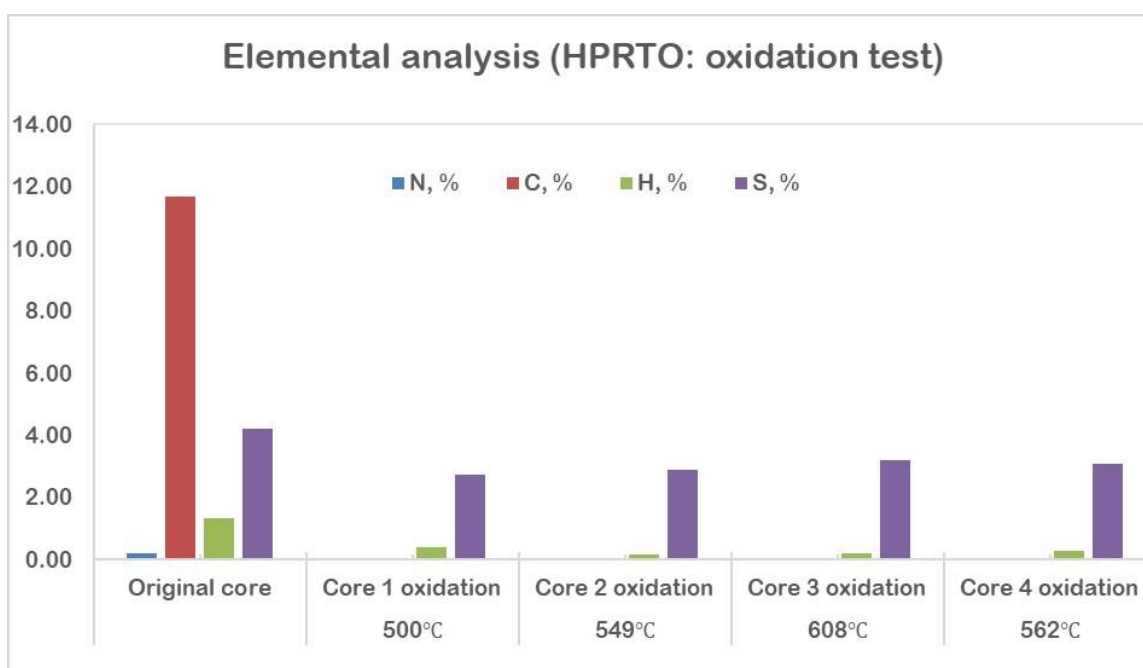


Figure 73. Results of elemental analysis of crushed core samples before and after exposure (HPRTO test: oxidation test).

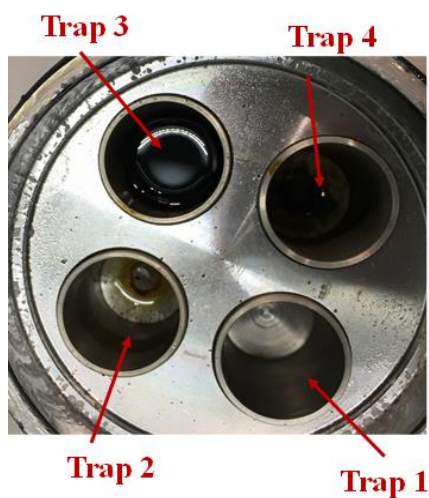
All the carbon elements were oxidized, which reconfirms the conclusion made in the Rock-Eval pyrolysis study. No nitrogen was identified in the elemental analysis. No pyrite minerals were detected during the mineralogy analysis in the core samples after exposure.

3.5.6 Results: oil analysis

Based on the analysis of the masses of the fluids generated from the 92 cm³ of rock as a result of oxidation reactions and reactions of thermal decomposition of kerogen, 24.8 g of water-oil emulsion were generated. The temperature sampling intervals, sample masses and their description are presented in **Table 20**, and the photographs of the traps are given in **Figure 74**.

Table 20. Description of liquid samples in traps – oxidation test.

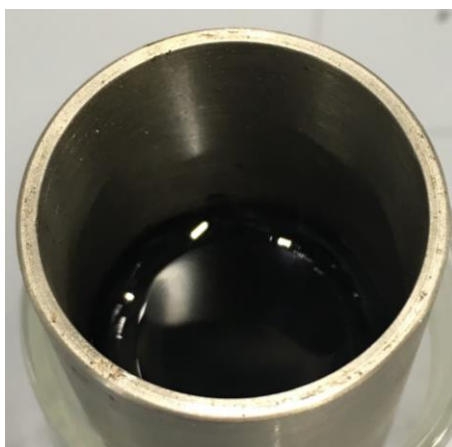
Trap number	Temperature interval of sample collection, °C	Sample weight, g	Sample description
Trap 1	20 - 180	0	No generation of hydrocarbons
Trap 2	180 - 300	0.5	Water with oil film
Trap 3	300 - 500, isothermal at 500	24.1	Water-in-oil emulsion
Trap 4	Helium purge and depressurizing	0.2	Oil traces



a. Four traps.



b. Trap 2 (180 - 300°C)



c. Trap 3 (300 - 500°C)



d. Trap 4 (helium purge and pressure down)

Figure 74. Photos of traps after the experiment – oxidation test.

Stable (hard to break) oil was obtained in the water emulsion, which implies a risk of emulsion being produced during field operations. The oil sample was separated from the water by CHCl_3 extraction. The original oil extract was obtained through toluene extraction of the original core packed into the HPRTO reactor. **Table 21** lists the results of GC×GC-MS analysis and calculated parameters.

Figure 75 shows the position of these two extracts samples on Cannon Cassou diagram (*Connan and Cassou, 1980*). According to the work of *Connan and Cassou (1980)*, pristane to n-C₁₇ and phytane to n-C₁₈ ratios continuously decrease with increasing maturation for crude oils that belong to the same family and, in other words, are of a similar kerogen type. As illustrated by **Figure 75**, CHCl₃ extract from the synthetic oil sample collected during oxidation of non-extracted crushed oil shale has lower values of pristane/n-C₁₇ and phytane/n-C₁₈, which is indicative of increased maturation of oil samples.

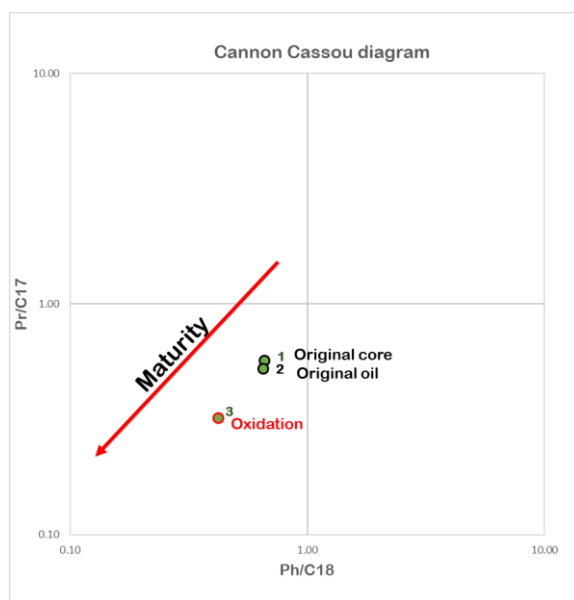


Figure 75. Cannon Cassou diagram – sample after oxidation treatment.

Table 21. GC×GC-MS results of the original core extract and oil sample collected in trap 3.

Sample ID	1	2
Sample description	Original core	HPRTO-oxidation (Trap 3)
Sample preparation details	toluene extract	CHCl ₃ extract from the trap 3 (separation from water)
alkanes	43	39
olefins and naphthenes	23	9
mono-aromatics	19	33
di-aromatics	12	17
tri-aromatics	4	2
Pr/C ₁₇	0.57	0.32
Ph/C ₁₈	0.66	0.42
Pr/Ph	1.06	1.01
Ki	0.61	0.36

3.5.7 Material balance calculation

Table 22. Material balance. Air injection test (HPRTO).

Parameter	Oil, g	Water, g
Trap 1 (20 - 180°C)	0	0
Trap 2 (180 - 300°C)	0	0.5
Trap 3 (300-500°C, isothermal at 500°C)	2.41	21.69
Trap 4 (helium purge and depressurizing)	0.2	0
Washing lines with toluene	0.8	0
Oil and water produced, g	3.41	22.19
Hydrocarbons in the system (S0+S1+S2), g	14.79	
HC gases produced, g	0.99	
CO and CO ₂ produced, g	58.77	
H ₂ S produced, g	1.81	
H ₂ produces, g	0.002	
Percent of hydrocarbons produced (recovery factor), %	29.75	

3.5.8 Conclusions

The percentage of potential hydrocarbons produced was 29.75 wt%. Gas composition was determined. A significant amount of water and carbon dioxide was generated through this process, which indicates that the non-generative part of kerogen was consumed as a fuel. Rock-Eval pyrolysis study showed total kerogen conversion/oxidation of both generative and non-generative parts. Synthetic oil composition and geochemical parameters were obtained. According to Cannon-Cassou diagram, synthetic oil collected was characterized by a high maturity level. Oil was collected in emulsion, which implies a risk of emulsion being produced during field operations. No pyrite minerals were detected during mineralogy analysis in the core

samples after exposure. It is strongly recommended to further investigate and experiment with the air flux effect on oil recovery.

3.6. Pyrolysis: High-pressure ramped temperature cracking (HPRTC)

3.6.1 Samples selection and test design strategy

Crushed rock samples from Oil Field 3 were chosen for this study which duplicates the HPRTO experiment described above except for the injection gas.

3.6.2 Methodology

To make a correct comparison of the results of the two experiments conducted in an atmosphere of air and in a nitrogen atmosphere, the second experiment must replicate the first one, with the exception of the gas used.

3.6.3 Results: core analysis

Rock-Eval pyrolysis study

As can be seen from **Figure 76**, **Figure 77**, and **Table 23**, almost the entire generative organic (GOC) part was converted. Coke-like material that can serve as a fuel for further combustion was generated. It should be noted that T_{\max} of S2 peak associated with this material shifted to higher temperatures. The area below the S4CO2 peak grew larger, which testifies to the fuel lay-down.

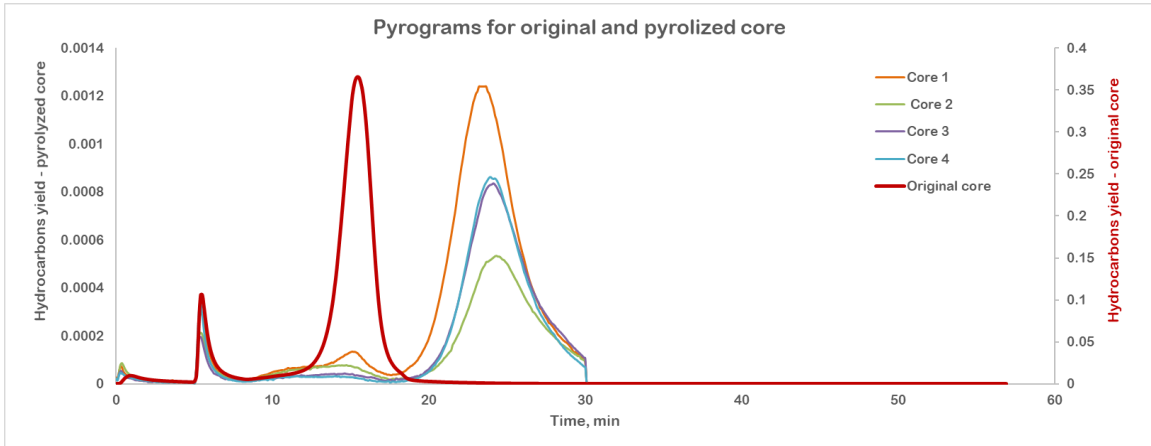


Figure 76. Pyrogram (hydrocarbon yield) of initial core sample and unpacked core samples.

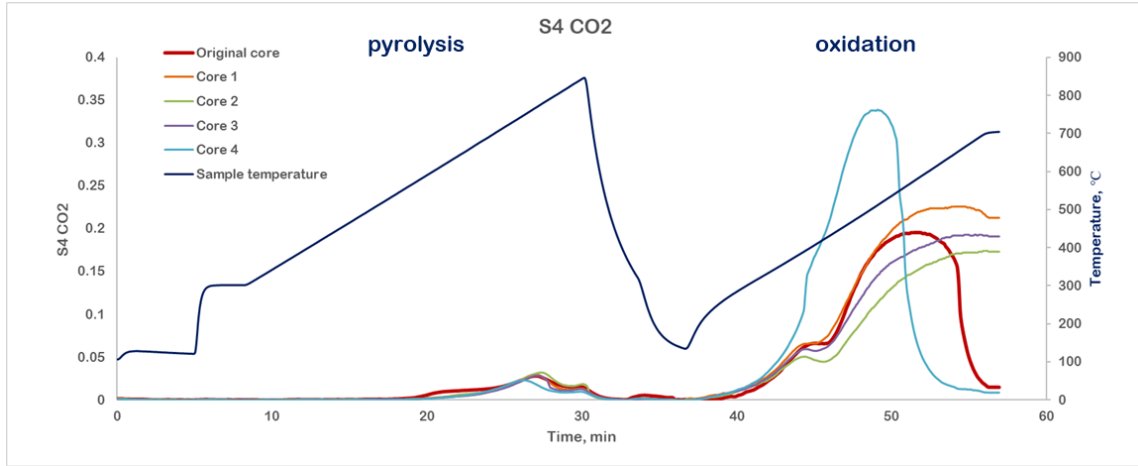


Figure 77. Pyrogram (S4CO2) of initial core sample and unpacked core samples with temperature schedule.

Mineralogy change

No pyrite minerals were detected during the mineralogy analysis in the core samples after exposure.

Table 23. Pyrolysis study results (HPRTC nitrogen injection test).

Sample	S0	S1	S2	TOC	Tmax	HI	OI	PI	S4CO2	S4CO
	<i>mg HC/g rocks</i>	<i>mg HC/g rocks</i>	<i>mg HC/g rocks</i>	<i>Total Organic Carbon, wt%</i>	<i>Maturity, °C</i>	<i>Hydrogen Index, S2/TOC*100</i>	<i>Oxygen Index, S3/TOC*100</i>	<i>Production Index, S1/S1+S2</i>		
Original Core	1.91	6.94	65.74	9.63	438	682	1	0.10	99.41	12.50
Core 1 - pyrolysis test	0.00	0.02	0.51	3.73	640	13	5	0.04	117.38	10.31
Core 2 - pyrolysis test	0.00	0.02	0.25	3.13	660	8	5	0.06	102.49	6.38
Core 3 - pyrolysis test	0.00	0.01	0.33	3.54	656	9	4	0.04	114.38	8.35
Core 4 - pyrolysis test	0.00	0.02	0.32	5.51	651	5	2	0.05	158.27	26.52

Elemental analysis

Table 24. Results of elemental analysis of crushed core samples before and after exposure (HPRTC test: nitrogen injection test).

Oil Field	Temperature, °C	Sample	N, %	C, %	H, %	S, %
Oil Field 3		Original core	0.23	11.67	1.34	4.23
Oil Field 3	500°C	Core 1 pyrolysis	0.21	7.21	0.39	2.43
Oil Field 3	500°C	Core 2 pyrolysis	0.21	7.18	0.34	2.42
Oil Field 3	500°C	Core 3 pyrolysis	0.21	7.25	0.35	2.44
Oil Field 3	500°C	Core 4 pyrolysis	0.20	7.05	0.31	2.40

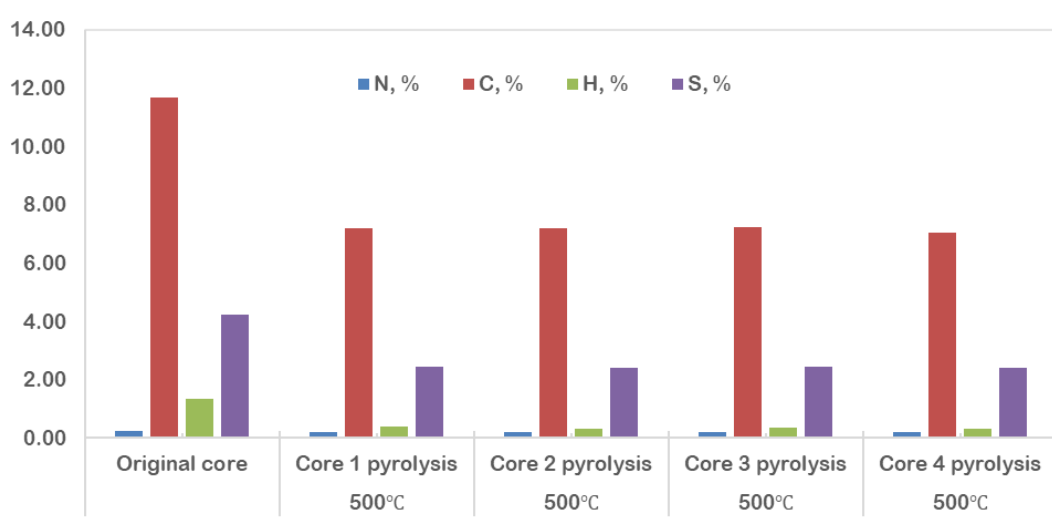


Figure 78. Results of elemental analysis of crushed core samples before and after exposure (HPRTC test: nitrogen injection test).

From elemental analysis one can conclude that the remaining carbon left can be used as fuel for oxidation reactions.

Table 25. Results of elemental analysis of crushed core samples before and after exposure (HPRTO tests: oxidation and pyrolysis).

Oil Field	Temperature, °C	Sample	N, %	C, %	H, %	S, %
Oil Field 3	before exposure	Original core	0.23	11.67	1.34	4.23
Oil Field 3	500°C	Core 1 oxidation	0.00	0.00	0.41	2.75
Oil Field 3	549°C	Core 2 oxidation	0.00	0.00	0.18	2.88
Oil Field 3	608°C	Core 3 oxidation	0.00	0.00	0.21	3.19
Oil Field 3	562°C	Core 4 oxidation	0.00	0.00	0.30	3.10
Oil Field 3	500°C	Core 1 pyrolysis	0.21	7.21	0.39	2.43
Oil Field 3	500°C	Core 2 pyrolysis	0.21	7.18	0.34	2.42
Oil Field 3	500°C	Core 3 pyrolysis	0.21	7.25	0.35	2.44
Oil Field 3	500°C	Core 4 pyrolysis	0.20	7.05	0.31	2.40

3.6.4 Results: oil analysis

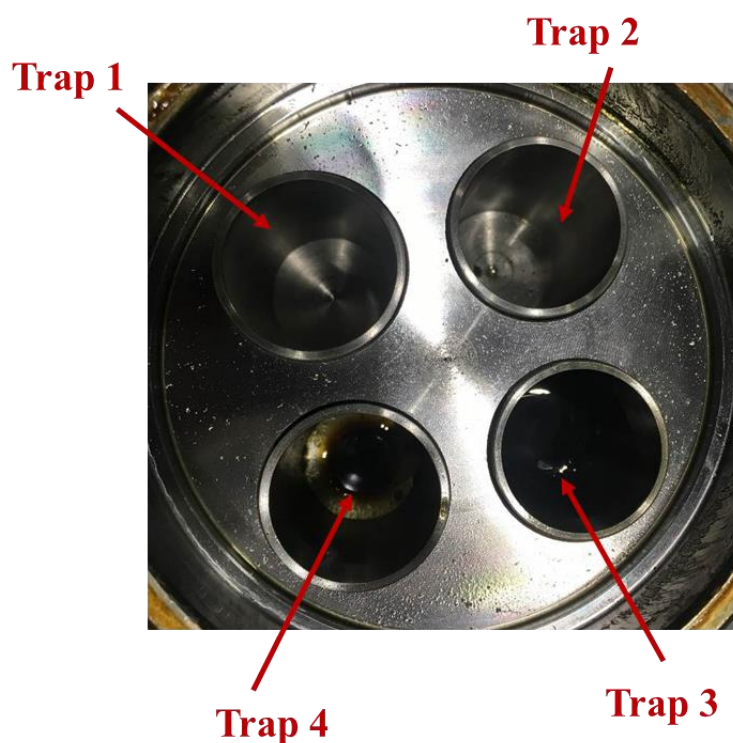


Figure 79. Photos of traps after the experiment – pyrolysis test (HPRTC).

Table 26. Description of liquid samples in traps – pyrolysis test.

Trap number	Temperature interval of sample collection, °C	Sample weight, g	Sample description
Trap 1	20 - 180	0	No generation of hydrocarbons
Trap 2	180 - 300	0	No generation of hydrocarbons
Trap 3	300-500, isothermal at 500	6.8	Oil
Trap 4	Helium purge and depressurizing	0.6	Oil
Lines	Washing lines with toluene	2.2	Oil

Table 27. GC×GC-MS results of the extracts from original core and liquid samples collected.

Sample description	Original core	HPRTC -pyrolysis (Trap 3)
Sample preparation details	toluene extract	oil from the Trap 3
alkanes	43	18
olephins and naphtenes	23	20
mono-aromatics	19	38
di-aromatics	12	23
tri-aromatics	4	1
K_i	0.61	0.27
Pr/C ₁₇	0.57	0.25
Ph/C ₁₈	0.66	0.28
Pr/Ph	1.06	1.24

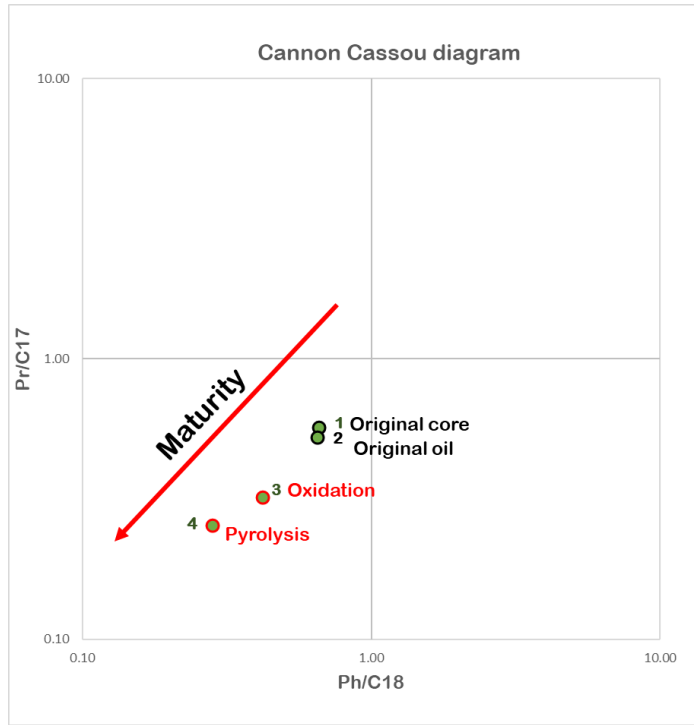


Figure 80. Cannon Cassou diagram – sample after pyrolysis treatment.

3.6.5 Results: gas analysis

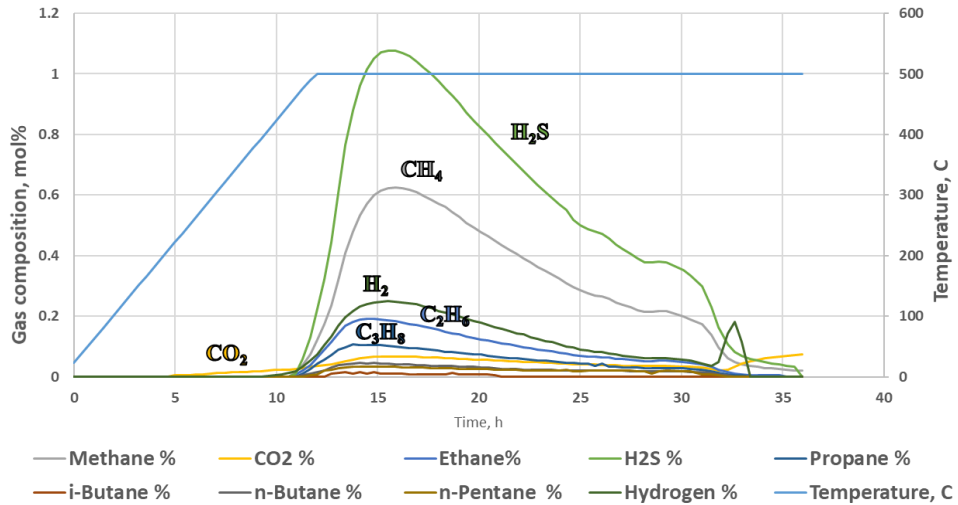


Figure 81. Temperature profiles and gas compositions. GC delay time - 1.47 hours.

Table 28. Total volumes and masses of evolved gases – HPRTC pyrolysis test.

Parameter	Volume, cc	Mass, g
CH ₄	1,239.45	0.828
C ₂ H ₆	319.634	0.429
C ₃ H ₈	177.468	0.356
n-C ₄ H ₁₀	78.788	0.031
i-C ₄ H ₁₀	11.646	0.213
n-C ₅ H ₁₂	76.554	0.265
CO ₂	269.867	0.533
H ₂	494.27	0.044
H ₂ S	1,987.59	3.059

It can be seen from the table above that the amount of hydrocarbon gases generated as a result of pyrolysis is greater as compared to oxidation. This can be explained by the hypothesis about vapor-phase combustion stated in the papers of the University of Calgary (*Barzin et al., 2010; Mallory et al., 2018*). However, further research is needed to prove this statement.

3.6.6 Material balance calculation

Table 29. Material balance. Comparison of oxidation (HPRTO) and pyrolysis (HPRTC) tests.

Parameter	Oxidation		Pyrolysis
	Oil, g	Water, g	Oil, g
Trap 1 (20 - 180°C)	0	0	0
Trap 2 (180 - 300°C)	0	0.5	0
Trap 3 (300 - 500°C, isothermal at 500°C)	2.41	21.69	6.8
Trap 4 (helium purge and depressurizing)	0.2	0	0.6
Washing lines with toluene	0.8	0	2.2
Oil and water produced, g	3.41	22.19	9.6
Hydrocarbons in the system (S0+S1+S2), g	14.79		14.72
HC gases produced, g	0.99		2.12
CO and CO ₂ produced, g	58.77		0.53
H ₂ S produced, g	1.81		3.06
H ₂ produced, g	0.002		0.044
Percent of hydrocarbons produced (recovery factor), %	29.75		79.62

As compared to the HPRTO material balance estimation results, around 50% of potential hydrocarbons were consumed as extra fuel in oxidation, leading to carbon oxides and water generation.

3.6.7 Conclusions

As compared to the air injection experiment, 37.4 wt% (29.75 wt% of 79.62 wt%) of the possible yield of hydrocarbons were extracted during the oxidation. This suggests that the oxidation of kerogen and the products of its reaction led to coking and further combustion under the given experimental conditions. It is necessary to select the optimal

flow rate. Since heating in the presence of air started at room temperature, low-temperature oxidation resulted in the oxidation of an additional part of oil, which resulted in a low displacement coefficient. No unsaturated hydrocarbons were detected in the gases.

3.7. Hydropyrolysis: closed-system test

3.7.1 Samples selection and test design strategy

Four crushed rock samples from Oil Field 3 (MC₁ grade) were chosen for hydropyrolysis experiments to represent the Bazhenov shale. The experiments were conducted at different temperatures of exposure in order to test the effect of temperature on the kerogen conversion degree, change in porosity and permeability, and gas composition and yield. Four temperatures were chosen for the investigation, namely: 300, 350, 400 and 480°C, where exposure at 300°C simulates hot water extraction, 350°C represents sub-critical water extraction, 400 and 480°C allow testing supercritical water exposure. All these temperatures exist during air injection at a different distance from the combustion front. The data obtained can be used for evaluating the hot and SCW injection potential in oil shales, where the heating agent is injected from the surface with down-hole preheating.

3.7.2 Methodology

Closed-system reactors (**Figure 82**) were used to evaluate the effectiveness of sub-critical and supercritical water (SCW) extraction. The selected core samples were crushed and homogenized to the size of 0.5-2 mm, and 55 g were collected for each experiment (**Figure 83**). A set of experiments at 300, 350, 400 and 480°C was conducted

on non-extracted crushed core samples at a pressure of 27 MPa. Heating was performed starting from the room temperature up to the target temperature with a heating rate of 20°C/h, followed by isothermal treatment at the selected temperatures for 30 hours. The cumulative volume of evolved gases was measured by a wet test meter; the gases were then collected for further analysis. Liquid samples were collected into graduated cylinders. The crushed core was removed from the reactor and oven-dried down to constant weight at 105°C.

Kerogen conversion due to thermal exposure was assessed by Rock-Eval open-system pyrolysis method which was conducted on original samples and heated samples in HAWK pyrolysis instrument. Since porosity and permeability cannot be measured by conventional methods due to the extremely low permeability and porosity of Bazhenov oil shale samples, GRI analysis method using CoreLab SMP-200 matrix permeameter was applied. According to this method, the matrix permeameter detects the pressure pulse response in the cell filled with crushed rock samples. Afterwards the permeability value is calculated by analyzing the pressure decay over time. In order to identify gas composition, the samples were collected and analyzed in a gas chromatograph.

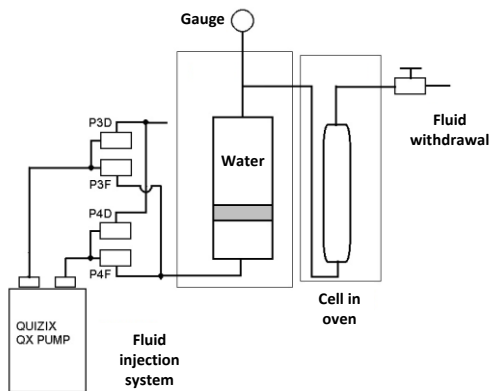


Figure 82. Experimental set-up for closed-system hydrolysis testing (Bondarenko et al., 2016).



Figure 83. A disintegrated core sample of Bazhenov oil shale (Bondarenko et al., 2016).

3.7.3 Results: core analysis

An open-system pyrolysis study using Rock-Eval pyrolysis method was performed and two primary parameters, S1 and S2, were measured in order to identify the degree of kerogen conversion as a result of hydrolysis. As described earlier, S1 is the amount of hydrocarbons thermally released by the temperature of 300°C, while S2 is the amount of hydrocarbons obtained via thermal decomposition of non-volatile organic matter. Therefore, S2 value serves as an indication of hydrocarbons yield that the kerogen has the potential to generate under high temperature and pressure over a long period of time. To investigate the change in those parameters, the core samples were analyzed before and after exposure. **Table 30** reports the results of pyrolysis parameters measurements, which point to nearly total conversion of free oil (S1 parameter) and a 82% decrease in parameter S2 as a result of supercritical water extraction at 480°C.

Table 30. S1 and S2 parameters before and after hydropyrolysis exposure.

Sample	Temperature, °C	Before hydropyrolysis exposure		After hydropyrolysis exposure		Percentage change, %	
		S1, mg HC/g rock	S2, mg HC/g rock	S1, mg HC/g rock	S2, mg HC/g rock	S1, mg HC/g rock	S2, mg HC/g rock
1	300	8.40	78.30	4.70	75.50	-44.0	-3.6
2	350	5.20	66.80	2.93	64.13	-43.7	-4.0
3	400	6.30	107.60	2.52	97.50	-60.0	-9.4
4	480	9.03	77.07	0.29	13.83	-96.8	-82.1

GRI analysis of the crushed samples revealed a minor increase in porosity with a rise in temperature and noticeable growth in permeability at 480°C (**Table 31**).

Table 31. GRI analysis results: porosity and permeability.

Temperature, °C	Before hydropyrolysis exposure		After hydropyrolysis exposure		Percentage change, %	
	Porosity, %	K, nD	Porosity, %	K, nD	Porosity	K
300	1.07	20	1.14	23.3	7	17
350	0.75	14.4	0.97	17.8	29	24
400	1.40	37	1.56	45.2	11	22
480	1.04	28	1.55	244	49	771

3.7.4 Results: gas and oil analysis

Only gases were collected at 300 and 350°C, whereas a small amount of liquid hydrocarbons in the form of oil films was extracted from the organic matter during supercritical water exposure at 400°C. During the hydrous pyrolysis at 480°C, 1,350

cm³(ST) of gas were generated from 55 g of core sample. According to the gas analysis results (**Figure 84**), methane generation increased with temperature. A remarkable amount of methane was identified in the evolved gases at 480°C, which suggests that secondary cracking and associated coke generation occur at about 480°C. The mass of oil extract collected was 0.308 g. The compositional analysis showed 21.0% of the resins and asphaltenes, and 77.5% of saturated HC, unsaturated HC, and aromatics, where n-alkanes (C₁₀-C₃₅) concentration was 3.9%.

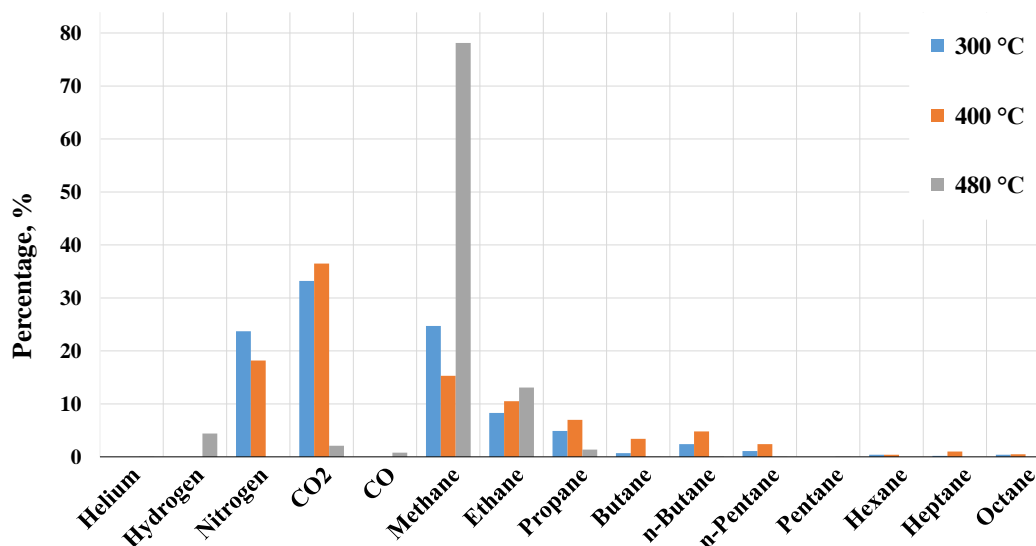


Figure 84. Produced gas compositional analysis.

3.7.5 Conclusions

Kerogen conversion during the hydrolysis process was evaluated. The study identified the “oil generation window” within a temperature range of 400°C to 480°C for the Bazhenov oil shale samples. The compositional analysis of evolved products suggests that secondary cracking and coke generation started at about 480°C. The pyrolysis study results are indicative of kerogen conversion with time, displaying almost total conversion of free oil and a 82% drop in kerogen yield after SCW exposure at 480°C. GRI analysis

of crushed core samples revealed porosity growth with temperature and a noticeable increase in permeability in the samples subjected to hydrolysis above 400°C, which can be explained by microfractures formed through the voids created as a result of kerogen conversion.

3.8. Hydrolysis: open-system test

3.8.1 Samples selection and test design strategy

The primary goals of the test were to assess hydrolysis potential for *in situ* synthetic oil generation from the Bazhenov Formation oil shale and to measure produced gas composition and synthetic oil composition to provide benchmarks for monitoring field operations.

Table 32. Samples selection.

Sample number	Shape	Oil Field	Complementary study
1	Cylinder 30*30mm	Oil Field 2	2D pyrolysis
2	Cylinder 30*30mm	Oil Field 4	2D pyrolysis
3	Cylinder 30*30mm	Oil Field 4	2D pyrolysis
4	Crushed core, 0.1-1 mm	Oil Field 4	Pyrolysis, catalytic effect study

3.8.2 Methodology

The test was conducted in a high-pressure vessel. Consolidated and crushed core samples were distributed in the unsaturated sand. This run was performed at a reservoir pressure of 28 MPa with non-extracted core samples. The test consisted of four stages, namely: 300°C and 350°C hot water injection, 400°C supercritical water injection, followed by 250°C hot water injection. This sequence was chosen to test different kerogen extraction temperatures. However, this sequence replicates the slugs of water

sequence in oil shales during the high-pressure air injection in shales, where SCW slug is moving right ahead of the combustion front. A pyrolysis study was conducted to assess kerogen conversion and pyrite catalytic effect by adding pyrite in the crushed core samples.

3.8.3 Experimental results

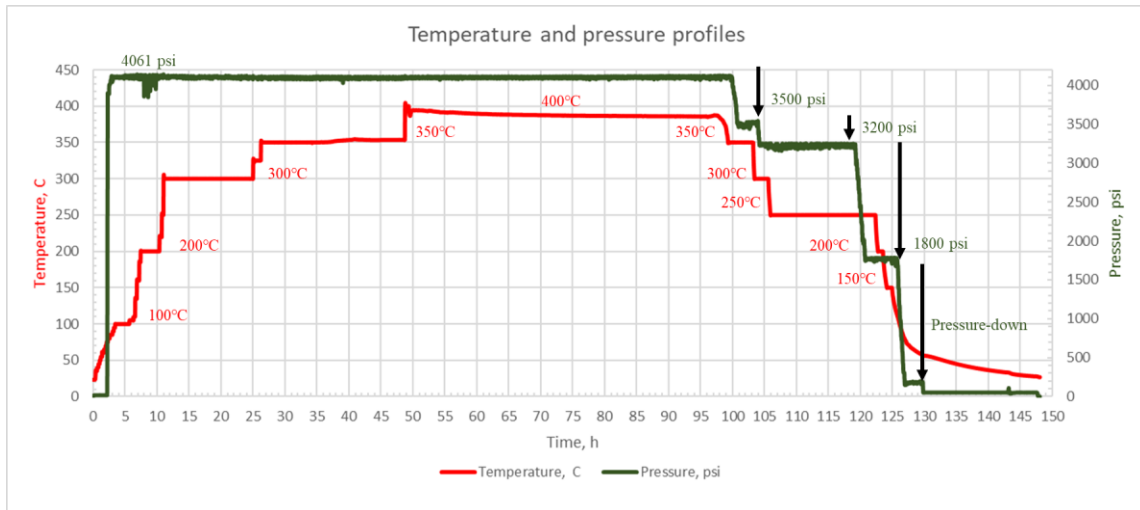


Figure 85. Temperature and pressure profiles.

Figure 84 shows temperature and pressure profiles. Sulfur water samples were produced throughout the test without any drop of oil. At the end of the experiment, a pressure drop was implemented to order to produce oil. Liquid oil samples were collected after the last pressure drop only.

3.8.4 Results: oil analysis

Table 33. GC×GC-MS results for the oil sample extracted from the sand and oil samples collected.

Sample ID	1	4	5
Sample description	Original core	Open-system hydropyrolysis	Open-system hydropyrolysis
Oil Field	Oil Field 2	Oil Field 4	Oil Field 4
Sample preparation details	toluene extract	Oil film from the collected sample	Toluene extract from the sand
alkanes	43	7	7
olephins and naphtenes	23	13	1
mono-aromatics	19	57	17
di-aromatics	12	20	58
tri-aromatics	4	3	17
Ki	0.61	0.29	0.31
Pr/C ₁₇	0.57	0.23	0.25
Ph/C ₁₈	0.66	0.39	0.39
Pr/Ph	1.06	0.94	0.82

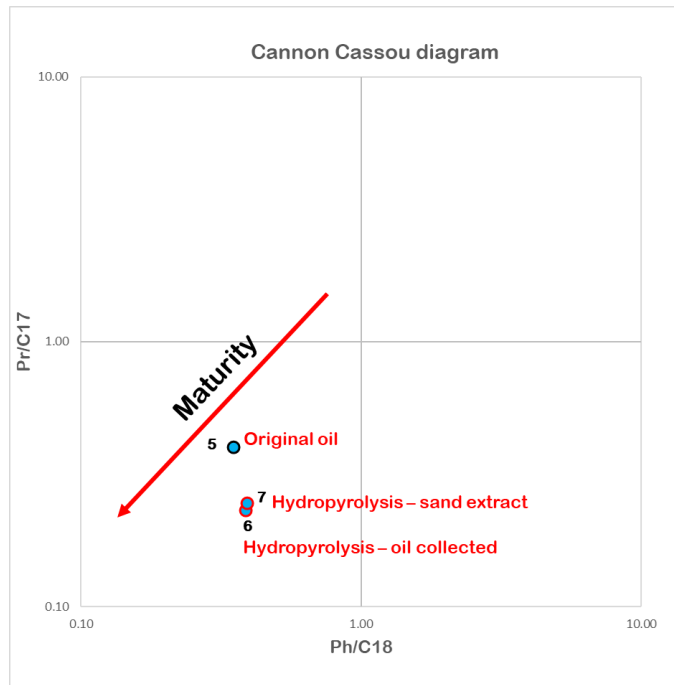


Figure 86. Cannon Cassou diagram – samples after hydrolysis treatment.

3.8.5 Results: core analysis



Figure 87. Photo of the core sample after exposure (Oil Field 4).

The photos in **Figure 87** show the sample fracturing along the bedding plane, which allows supercritical or sub-critical water to extract kerogen. The water bank ahead of the combustion front can displace the generated oil and extract kerogen. Pressure down the system possibly resulted in core-like material coming out. Coke-like material can be

seen on the sample surface. It can be the synthetic oil that got coked and that can serve as a fuel for combustion.

Rock-Eval pyrolysis study

The pyrolysis study was conducted on crushed and consolidated core samples in order to investigate the contact area effect and the possibility to convert kerogen inside the consolidated core (15 mm from the contact area). This study showed almost total kerogen decomposition both in the crushed and consolidated core samples.

In order to evaluate kerogen conversion in consolidated kerogen-bearing rocks after SCW extraction, three cylindrical core samples were cut into two symmetrical parts, and one part was chosen for the investigation. Those cylindrical samples were 30 mm in diameter and 30 mm in length. This kerogen conversion assessment method can be called 2D pyrolysis, meaning that the distribution of geochemical parameters is obtained in two directions, namely, radial and vertical. This technique helps to analyze the effectiveness of thermal exposure in terms of kerogen conversion and the coking effect of thermal exposure in terms of coke distribution along the core sample. The part of the sample is divided into 20 sections. **Figure 88** depicts the 2D pyrolysis technique as applied to a sample divided into sections, where Sections 3, 8, 13 and 18 represent the 3 mm central isothermal radius; Sections 2, 7, 12, 17, 4, 9, 14, 19 represent the 3-9 mm isothermal radius; Sections 1, 6, 11, 16, 5, 10, 15, 20 represent the 9-15 mm outer radius. Each sample is collected from each section by drilling 3 mm deep holes. Then each collected sample undergoes an open-system pyrolysis study by Rock-Eval methodology described in Chapter 3 (Section 3.3.4).

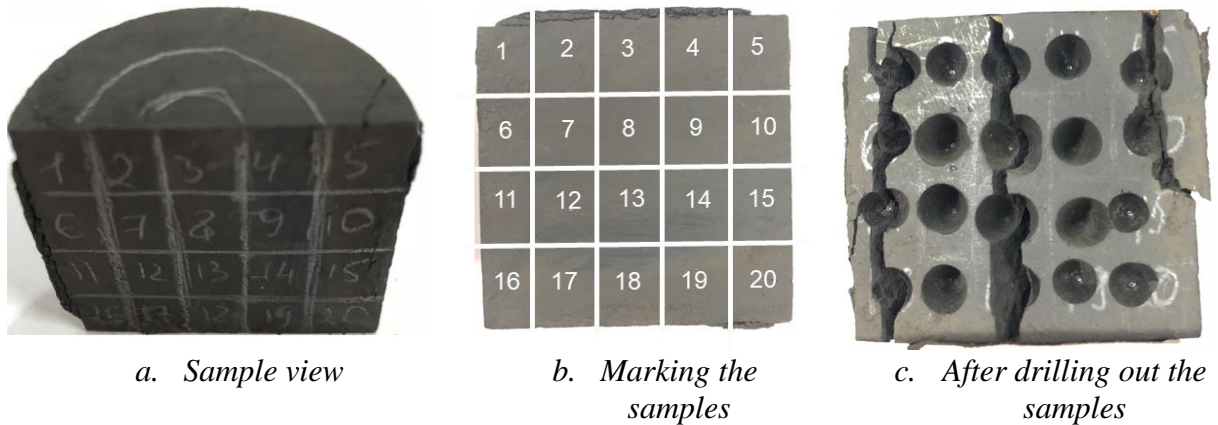


Figure 88. Photo of the sample used for 2D pyrolysis study.

Samples #1, #2 and #3 were chosen for Rock-Eval pyrolysis study. From the 2D maps (Figure 89, Figure 90, Figure 91) homogeneous kerogen conversion was observed.

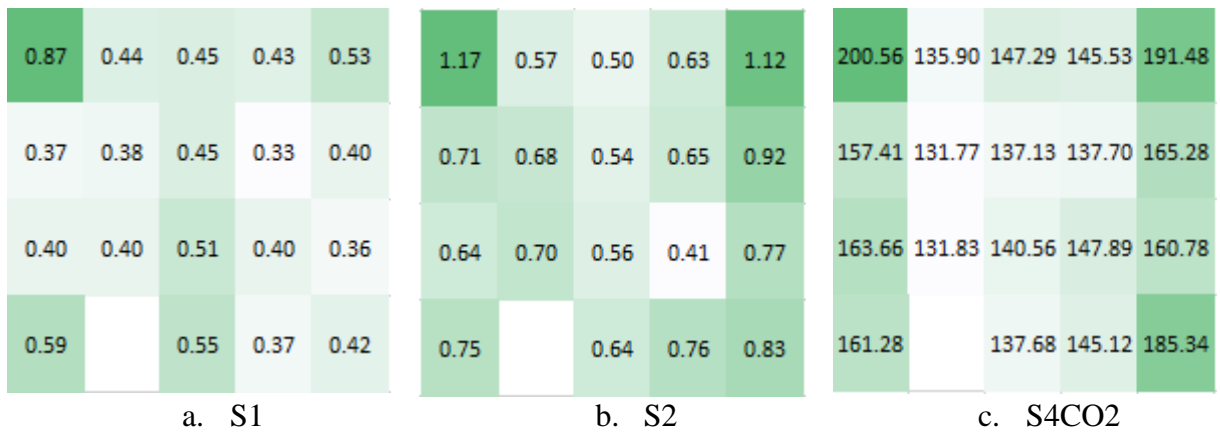


Figure 89. Distribution of S1, S2 and S4CO2 parameters in the consolidated sample (Sample #1, Oil Field 2).

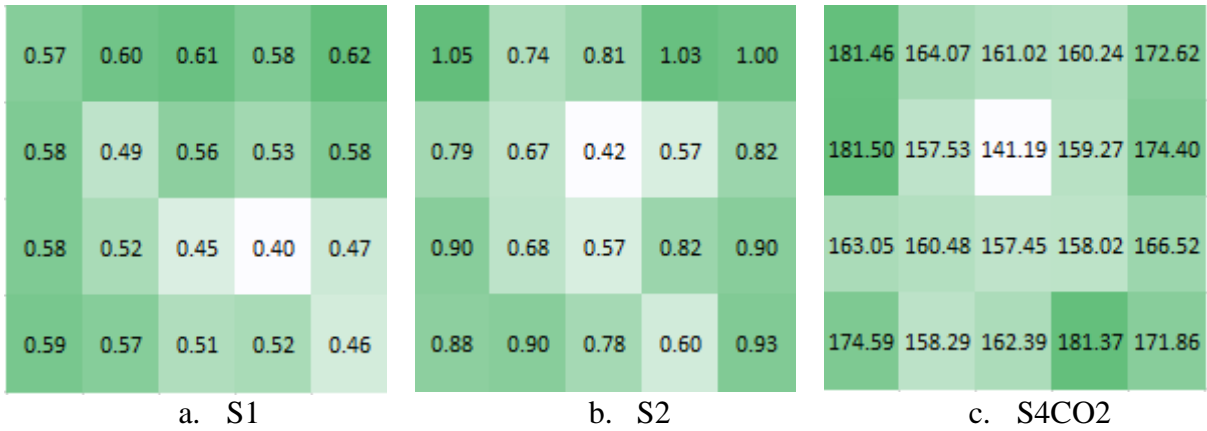


Figure 90. Distribution of S1, S2 and S4CO2 parameters in the consolidated sample (Sample #2, Oil Field 4).

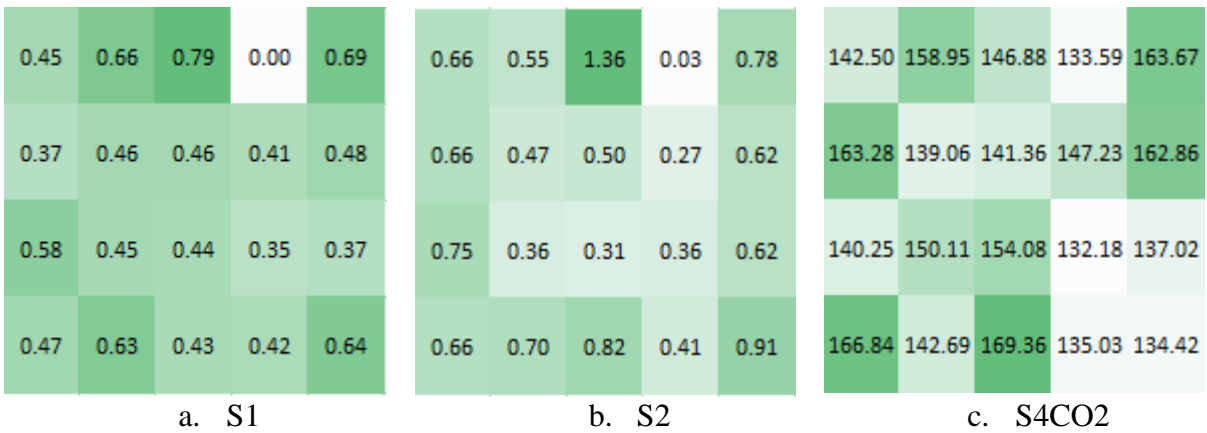


Figure 91. Distribution of S1, S2 and S4CO2 parameters in the consolidated sample (Sample #3, Oil Field 4).

Table 34. Results of Sample #1 Rock-Eval pyrolysis study.

Sample	S0	S1	S2	TOC	Tmax	HI	OI	PI	S4CO2	S4CO
	<i>mg HC/g rocks</i>	<i>mg HC/g rocks</i>	<i>mg HC/g rocks</i>	<i>Total Organic Carbon, wt%</i>	<i>Maturity, °C</i>	<i>Hydrogen Index, S2/TOC*100</i>	<i>Oxygen Index, S3/TOC*100</i>	<i>Production Index, S1/S1+S2</i>	<i>mg CO2/g rocks</i>	<i>mg CO/g rocks</i>
Original	1.81	6.52	30.52	7.98	446	382	1	0.18	126.84	28.29
Sample1_1	0.29	0.87	1.17	9.50	584	12	23	0.42	200.56	74.94
Sample1_2	0.15	0.44	0.57	5.22	599	10	4	0.44	135.90	31.05
Sample1_3	0.14	0.45	0.50	5.73	595	8	3	0.47	147.29	34.80
Sample1_4	0.14	0.43	0.63	5.74	597	10	4	0.41	145.53	36.34
Sample1_5	0.20	0.53	1.12	8.53	583	13	16	0.32	191.48	63.62
Sample1_6	0.14	0.37	0.71	6.78	596	10	7	0.35	157.41	50.17
Sample1_7	0.15	0.38	0.68	5.07	603	13	5	0.36	131.77	29.21
Sample1_8	0.13	0.45	0.54	5.05	607	10	5	0.45	137.13	26.79
Sample1_9	0.17	0.33	0.65	5.28	604	12	5	0.33	137.70	30.89
Sample1_10	0.18	0.40	0.92	6.91	593	13	9	0.30	165.28	46.83
Sample1_11	0.11	0.40	0.64	6.40	599	9	8	0.38	163.66	38.09
Sample1_12	0.12	0.40	0.70	5.17	594	13	7	0.37	131.83	31.73
Sample1_13	0.10	0.51	0.56	5.34	609	10	4	0.48	140.56	29.86
Sample1_14	0.10	0.40	0.41	5.48	603	7	5	0.49	147.89	30.06
Sample1_15	0.13	0.36	0.77	6.52	599	11	6	0.32	160.78	44.02
Sample1_16	0.15	0.59	0.75	6.26	584	11	7	0.44	161.28	36.47
Sample1_18	0.13	0.55	0.64	5.27	601	12	5	0.46	137.68	30.13
Sample1_19	0.18	0.37	0.76	5.72	597	13	3	0.33	145.12	36.01
Sample1_20	0.15	0.42	0.83	7.77	588	10	7	0.33	185.34	52.44

Table 35. Results of Sample #2 Rock-Eval pyrolysis study.

Sample	S0	S1	S2	TOC	Tmax	HI	OI	PI	S4CO2	S4CO
	<i>mg HC/g rocks</i>	<i>mg HC/g rocks</i>	<i>mg HC/g rocks</i>	<i>Total Organic Carbon, wt%</i>	<i>Maturity, °C</i>	<i>Hydrogen Index, S2/TOC*100</i>	<i>Oxygen Index, S3/TOC*100</i>	<i>Production Index, S1/S1+S2</i>	<i>mg CO2/g rocks</i>	<i>mg CO/g rocks</i>
Original	0.55	8.39	27.80	8.07	439	344	2	0.23	141.78	24.27
Sample2_1	0.41	0.57	1.05	20.48	595	5	2	0.35	181.46	44.04
Sample2_2	0.30	0.60	0.74	12.08	599	6	2	0.45	164.07	33.85
Sample2_3	0.29	0.61	0.81	9.30	599	8	3	0.43	161.02	30.89
Sample2_4	0.41	0.58	1.03	9.02	585	11	3	0.36	160.24	30.55
Sample2_5	0.36	0.62	1.00	6.61	586	15	7	0.38	172.62	37.05
Sample2_6	0.29	0.58	0.79	14.18	592	5	2	0.42	181.50	34.23
Sample2_7	0.31	0.49	0.67	10.08	597	6	1	0.43	157.53	32.34
Sample2_8	0.23	0.56	0.42	9.44	614	4	2	0.57	141.19	23.02
Sample2_9	0.29	0.53	0.57	10.87	603	5	2	0.49	159.27	28.88
Sample2_10	0.26	0.58	0.82	9.90	595	8	3	0.41	174.40	34.31
Sample2_11	0.24	0.58	0.90	6.15	593	14	5	0.39	163.05	33.54
Sample2_12	0.21	0.52	0.68	5.81	603	11	4	0.44	160.48	28.21
Sample2_13	0.22	0.45	0.57	5.69	600	10	5	0.44	157.45	28.06
Sample2_14	0.29	0.40	0.82	5.86	601	13	5	0.33	158.02	30.96
Sample2_15	0.23	0.47	0.90	6.28	599	14	5	0.34	166.52	34.98
Sample2_16	0.23	0.59	0.88	6.62	597	13	5	0.40	174.59	36.07
Sample2_17	0.21	0.57	0.90	5.84	594	15	4	0.39	158.29	29.99
Sample2_18	0.22	0.51	0.78	6.01	604	12	4	0.40	162.39	31.37
Sample2_19	0.15	0.52	0.60	6.25	604	9	4	0.47	181.37	24.97
Sample2_20	0.21	0.46	0.93	6.47	589	14	4	0.33	171.86	34.96

Table 36. Results of Sample #3 Rock-Eval pyrolysis study.

Sample	S0	S1	S2	TOC	Tmax	HI	OI	PI	S4CO2	S4CO
	<i>mg HC/g rocks</i>	<i>mg HC/g rocks</i>	<i>mg HC/g rocks</i>	<i>Total Organic Carbon, wt%</i>	<i>Maturity, °C</i>	<i>Hydrogen Index, S2/TOC*100</i>	<i>Oxygen Index, S3/TOC*100</i>	<i>Production Index, S1/S1+S2</i>	<i>mg CO2/g rocks</i>	<i>mg CO/g rocks</i>
Original	0.60	7.80	33.51	7.86	441	426	4	0.19	118.21	23.94
Sample3_1	0.08	0.45	0.66	5.66	597	11	5	0.41	142.50	35.99
Sample3_2	0.08	0.66	0.55	5.53	587	10	5	0.54	158.95	23.31
Sample3_3	0.19	0.79	1.36	6.18	584	21	8	0.37	146.88	40.65
Sample3_4	0.02	0.00	0.03	4.94	469	0	7	0.22	133.59	28.04
Sample3_5	0.11	0.69	0.78	6.51	598	12	7	0.47	163.67	39.20
Sample3_6	0.11	0.37	0.66	7.11	579	9	6	0.36	163.28	53.48
Sample3_7	0.11	0.46	0.47	5.18	600	9	7	0.50	139.06	27.51
Sample3_8	0.11	0.46	0.50	5.30	603	9	6	0.48	141.36	28.49
Sample3_9	0.11	0.41	0.27	5.19	590	5	4	0.60	147.23	22.75
Sample3_10	0.11	0.48	0.62	7.16	572	8	15	0.44	162.86	53.85
Sample3_11	0.11	0.58	0.75	5.49	577	13	4	0.44	140.25	32.90
Sample3_12	0.11	0.45	0.36	5.23	607	6	4	0.55	150.11	23.27
Sample3_13	0.11	0.44	0.31	5.53	604	5	6	0.59	154.08	26.31
Sample3_14	0.11	0.35	0.36	5.04	601	7	3	0.49	132.18	29.66
Sample3_15	0.11	0.37	0.62	5.67	590	10	8	0.38	137.02	38.18
Sample3_16	0.11	0.47	0.66	6.92	559	9	8	0.42	166.84	46.36
Sample3_17	0.11	0.63	0.70	5.66	590	12	5	0.47	142.69	34.98
Sample3_18	0.11	0.43	0.82	7.44	572	10	12	0.35	169.36	53.00
Sample3_19	0.11	0.42	0.41	5.23	602	7	7	0.51	135.03	31.87
Sample3_20	0.11	0.64	0.91	5.23	589	17	6	0.41	134.42	30.45

Figure 92 shows pyrograms of the initial core sample and two sections of the core, where an unusual pyrogram shape was detected, with two peaks corresponding to S2 temperature interval. **Figure 93** shows S4CO₂ pyrograms of the initial core Sample #1 and all the 20 sections. As follows from **Figure 93**, the area below S4CO₂ peak in the sections drilled from the sample after SCW exposure is much bigger, which is suggestive of the coking effect. An extra peak was obtained, which represents wet gases generated through a hydrolysis process. And wet gases might serve as a fuel for further burning.

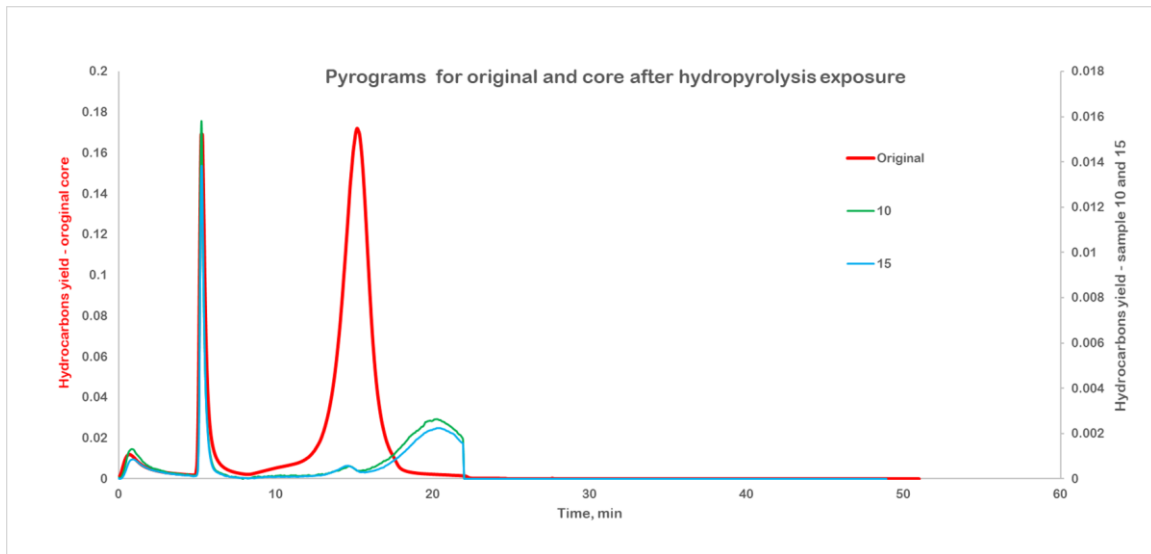


Figure 92. Pyrogram (hydrocarbon yield) of the initial core sample 1 and samples from the Sections 10 and 15.

Comparing the results of the crushed core and consolidated core pyrolysis investigation, one can conclude that the coking process is more intensive in the consolidated core, which may be due to the low permeability of the samples preventing displacement of the generated oil.

The catalytic study showed that pyrite increased the level of kerogen decomposition to some extent and, at the same time increased non-generative organic part content.

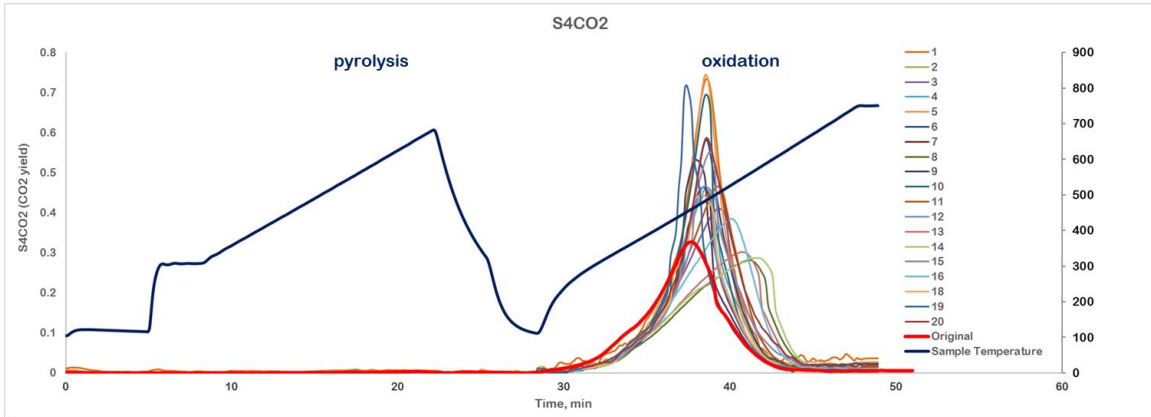


Figure 93. Pyrogram (S4CO₂) of the initial core sample 1 and samples from all the 20 sections.

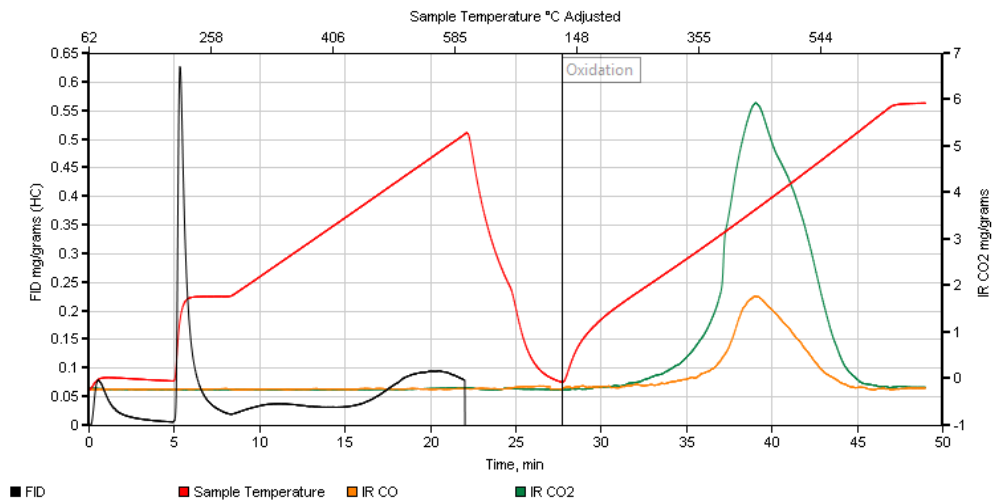


Figure 94. Pyrogram of coke-like material.

The coke-like material from **Figure 87** was collected for Rock-Eval pyrolysis study to understand the nature of this material. Analysis of the data from **Figure 94** and **Table 37** revealed that it is mostly coke or heavy component.

Table 37. Results of Sample 4 (crushed core) pyrolysis study.

Sample	S0	S1	S2	TOC	Tmax	HI	OI	PI	S4CO2	S4CO
	<i>mg HC/g rocks</i>	<i>mg HC/g rocks</i>	<i>mg HC/g rocks</i>	<i>Total Organic Carbon, wt%</i>	<i>Maturity, °C</i>	<i>Hydrogen Index, S2/TOC*100</i>	<i>Oxygen Index, S3/TOC*100</i>	<i>Production Index, S1/S1+S2</i>	<i>mg CO2/g rocks</i>	<i>mg CO/g rocks</i>
Original crushed core sample 4	4.90	16.03	61.75	10.06	442	613	1	0.21	86.48	14.93
Crushed core sample 4 after exposure	1.42	2.47	4.49	3.79	554	118	4	0.36	102.58	5.71
Crushed core sample 4 + pyrite after exposure	1.79	2.38	3.88	4.20	522	92	4	0.38	104.11	15.13

123

Table 38. Results of Sample 4 (crushed core) pyrolysis study.

Sample	S0	S1	S2	S3	TOC	Tmax	HI	OI	PI	S4CO2	S4CO
	<i>mg HC/g rocks</i>	<i>mg HC/g rocks</i>	<i>mg HC/g rocks</i>	<i>mg CO2/g rocks</i>	<i>Total Organic Carbon, wt%</i>	<i>Maturity, °C</i>	<i>Hydrogen Index, S2/TOC*100</i>	<i>Oxygen Index, S3/TOC*100</i>	<i>Production Index, S1/S1+S2</i>	<i>mg CO2/g rocks</i>	<i>mg CO/g rocks</i>
Original core – Sample #3	0.60	7.80	33.51	0.32	7.86	441	426	4	0.19	118.21	23.94
Coke-like material	8.56	31.47	54.60	3.09	103.36	562	52	2	0.37	2351.61	710.23

Elemental analysis

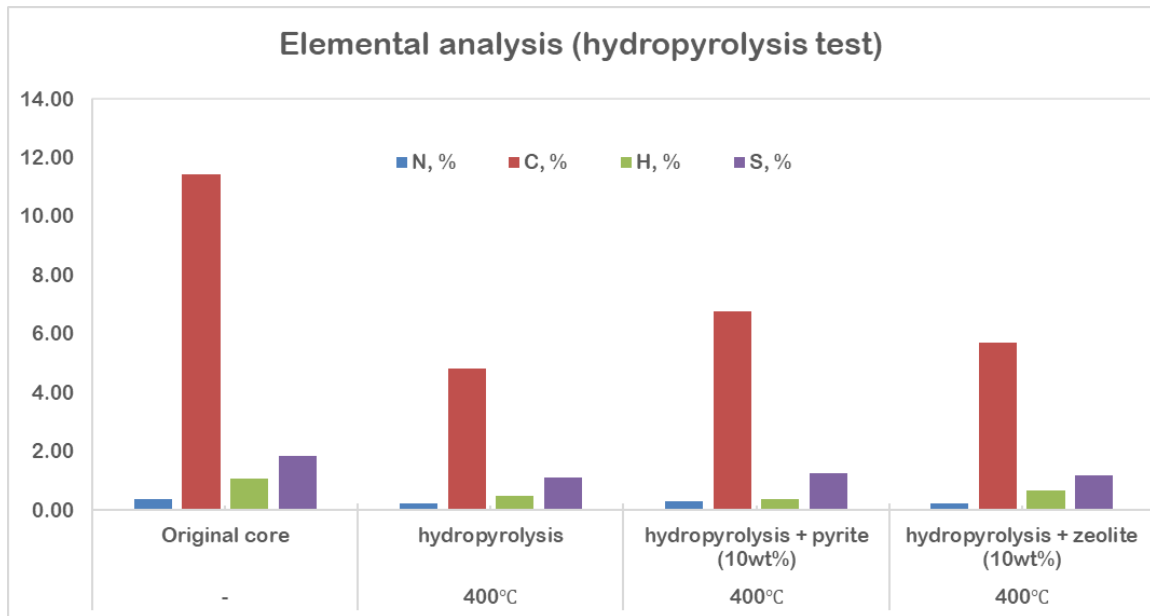


Figure 95. Elemental analysis of the original core sample and samples after exposure.

Table 39. Elemental analysis of the original core sample and samples after exposure.

Oil Field	Temperature, °C	Sample	N, %	C, %	H, %	S, %
Oil Field 4	-	Original core	0.38	11.45	1.07	1.86
Oil Field 4	400°C	hydropyrolysis	0.25	4.84	0.48	1.10
Oil Field 4	400°C	hydropyrolysis + pyrite (10 wt%)	0.29	6.76	0.39	1.25
Oil Field 4	400°C	hydropyrolysis + zeolite (10 wt%)	0.25	5.71	0.68	1.17

3.8.6 Results: gas analysis

The gas composition showed constant carbon dioxide generation, along with an increase in hydrogen sulfide concentration after the start of 350°C hot water flood. A more significant increase in hydrogen sulfide concentration and generation of hydrocarbon gases started at 400°C. Approximately 31 wt% of organic matter decomposed into gas. The gas analysis revealed a high amount of hydrogen sulfide and

carbon dioxide generation, which can overlap with gas generation during high-pressure air injection.

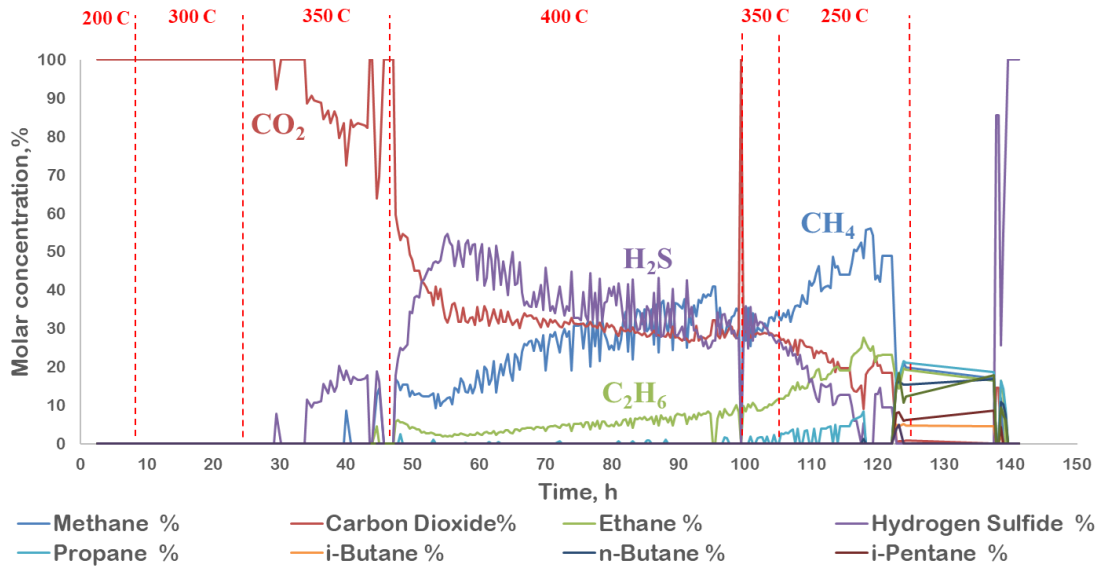


Figure 96. Molar gas composition.

3.8.7 Material balance estimation

Uncertainty of the hydrocarbons initial content is one of the difficulties in the material balance calculation. TOC of the samples chosen for the experiments varied from 8 to 10 wt% due to depth-dependent anisotropy of organic content. The mass of hydrocarbons was calculated assuming that the sum $S_0+S_1+S_2$ is the same along the sample. The mass of free oil was determined by separation of liquid samples collected and by sand extraction. The mass of coke was found by oven-drying the extracted sand samples overnight at 600°C and calculating the weight loss of the dried samples. The mass of gases was established by interpreting the gas chromatography and wet test meter data.

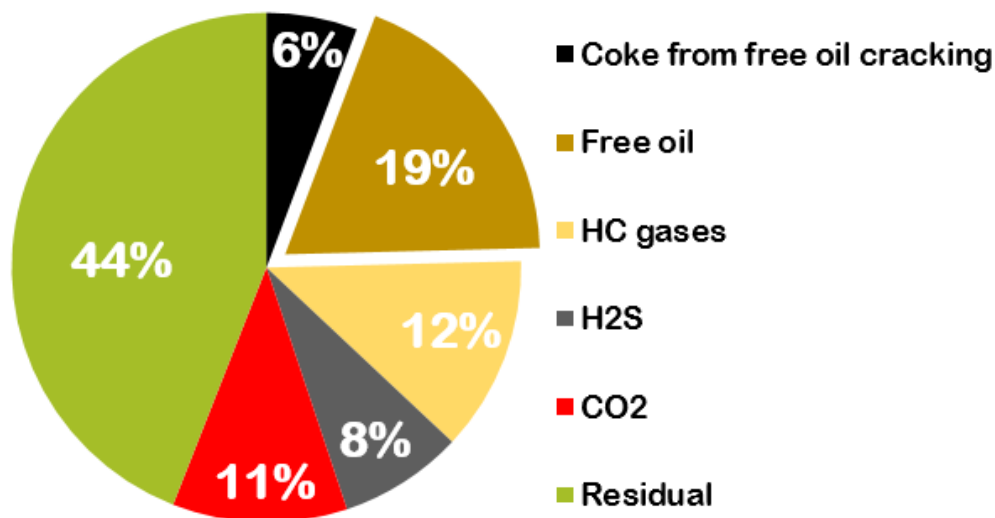


Figure 97. Material balance estimation.

At least 40 % of the generated oil was lost due to coking, the amount of which is difficult to estimate. Approximately 19 wt% of decomposition of organic matter resulted in free oil extraction. This calculation was based on the assumption that the core samples are quite homogeneous and have the same hydrocarbons yield. Synthetic oil was extracted from the sand only and not the surface of consolidated samples which have thin oil film and coke-like material on the surface. The percentage of synthetic oil recovered might have been underestimated. Therefore, these material balance results should be interpreted with caution. However, one can conclude from this study that a part of generated oil was coked inside the sample during rather long exposure.

3.8.8 Conclusions

The open-system hydrolysis experiment was designed to evaluate the role of sub-critical and supercritical water in kerogen conversion and fuel lay-down. The Rock-Eval pyrolysis study showed almost total kerogen decomposition both in the crushed and

consolidated core samples. It was found that the samples subjected to sub-critical and supercritical water exposure contained over-matured kerogen, which indicates that a coking process took place. Coke-like material was visible on the sample surface. It can serve as a fuel for combustion. Approximately 19 wt% of organic matter decomposed into oil that came out from the consolidated core samples. A part of the generated synthetic oil was coked in the consolidated samples due to low permeability. The catalytic study showed that pyrite increased the level of kerogen decomposition to some extent. Microfracturing, expansion perpendicular to the layering and release of coke-like material were observed in the samples after hydrolysis or, in other words, the sub-critical and supercritical water exposure. Sulfur water evolved from the vessel. Liquid hydrocarbons were not produced until a pressure drop was applied in the system. The produced gas and oil compositions can serve as benchmarks for future field implementations. The gas analysis revealed intensive hydrogen sulfide and carbon dioxide generation which can overlap with gas generation during high-pressure air injection. Further research is needed to closely examine the links between the pressure drop and the amount of liquid hydrocarbons displaced. It is important to choose the right regime for the recovery of generated products to prevent the coking process.

3.9. Comparison of three processes: pyrolysis, oxidation, and hydrolysis

This Section compares the results obtained from the experimental analysis of pyrolysis, oxidation and hydrolysis processes in oil shales.

3.9.1 Results: oil analysis

Table 40. GC×GC-MS results for the oil extract and oil samples collected.

Sample ID	1	2	3	4	5
Sample description	Original core	HPRTO-oxidation (trap 3)	HPRTO-pyrolysis (trap 3)	Open-system hydropyrolysis	Open-system hydropyrolysis
Sample preparation details	toluene extract	CHCl ₃ extract from the Trap 3 (separation from water)	Oil from the Trap 3	Oil film from the collected sample	Toluene extract from the sand
Oil Field	Oil Field 3	Oil Field 3	Oil Field 3	Oil Field 4	Oil Field 4
alkanes	43	39	18	7	7
olephins and naphtenes	23	9	20	13	1
mono-aromatics	19	33	38	57	17
di-aromatics	12	17	23	20	58
tri-aromatics	4	2	1	3	17
K _i	0.61	0.36	0.27	0.29	0.31
Pr/C ₁₇	0.57	0.32	0.25	0.23	0.25
Ph/C ₁₈	0.66	0.42	0.28	0.39	0.39
Pr/Ph	1.06	1.01	1.24	0.94	0.82

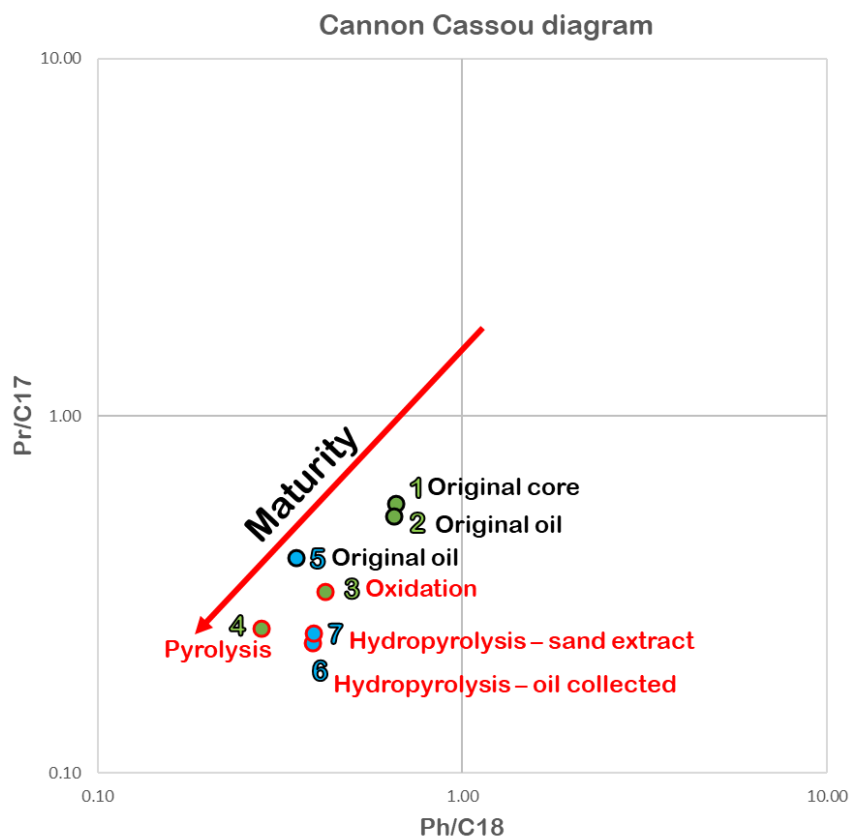


Figure 98. Cannon Cassou diagram – all the collected oil samples and extracts.

As can be seen from **Figure 98**, the samples of synthetic oil obtained after thermal exposure are more mature than the extract from the original core sample. The results presented in this manner can be found in *Kozlova et al. (2018)*. A higher content of aromatics in the oil sample treated by hydrolysis indicates that supercritical water does not only act as an extraction solvent but also reacts with the oil shale kerogen. Analysis of the fractions showed that n-alkanes and olefins were present in HPRTC – pyrolysis test extracts, but not in the SCW extracts, which might be the result of SCW reactions with olefins. The pyrolysis process in the HPRTC reactor was slow due to a low

heating rate of 40°C/hour. Therefore, more aliphatic oil was formed due to the secondary cracking of the kerogen decomposition products.

3.9.2 Results: gas analysis

Unsaturated HC gases were identified in HPRTO – oxidation experiment but not in the pyrolysis and hydropyrolysis processes which suggests that unsaturated hydrocarbon gases are benchmarks for the oxidation process in the field.

The high methane content obtained in HPRTO oxidation test (Chapter 3, Section 3.5) confirmed the data obtained in the experiments performed in closed reactors at various temperatures described in Chapter 3 (Section 3.7). According to the hydropyrolysis results, methane and coke were the main reaction products after exposure to 480°C. Moreover, the methane content kept growing during 400°C open-system hydropyrolysis, indicating that secondary cracking reactions were going on.

Since the gas composition for different coexisting processes, such as oxidation, pyrolysis, and hydropyrolysis, is known, the combustion tube results can be interpreted correctly.

3.9.3 Results: elemental analysis

Figure 99 shows the results of the elemental analysis of the original core (Oil Field 3) and the core after HPRTO oxidation and HPRTC pyrolysis tests from four different locations of the reactor. As illustrated by **Figure 99**, the pyrolysis reactions caused the sulfur content to decrease to a larger extent as compared to oxidation. As for the hydrogen content, it displayed the opposite result.

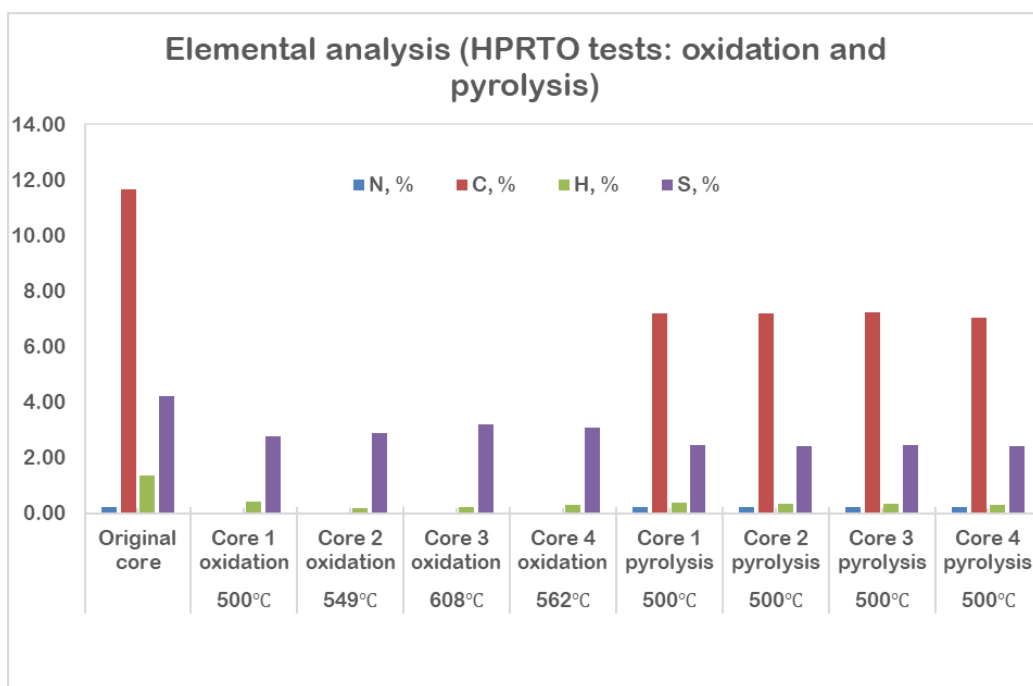


Figure 99. Results of elemental analysis of crushed core samples before and after exposure (HPRTO tests: oxidation and pyrolysis).

3.9.4 Conclusions

The primary goals of this Chapter were to study three different processes that occur during air injection in oil shales, namely: pyrolysis, oxidation, and hydrolysis (hot water, sub-critical water, and supercritical water extraction). These findings enhanced our understanding of mechanisms of kerogen conversion and synthetic oil characteristics as a result of three independent processes.

STA analysis showed a linear relationship between the total organic carbon and heat effect for oil shales with the same grade of catagenesis. Moreover, the grade of catagenesis might play an important role in the oxidation of organic matter. The mass loss and heat effect bear evidence of the Bazhenov shale organic matter oxidation reactions occurring within the temperature range from 240°C to 580°C.

Thermomicroscopy proved that conversion of organic matter due to thermal decomposition and oxidation causes an increase in void space. This analysis revealed the existence of two temperature ranges of intensive oxidation reactions, namely 120 – 200°C and 220 – 570°C. Fracturing started at 450°C and, what is more, fractures induced through the voids formed due to kerogen oxidation. A drastic change in mineralogy was registered at 540°C. It was noticed that pink and red magnetic minerals formed as a result of pyrite oxidation. This analysis yielded the same results as those obtained while analyzing the core drilled from the burnt area in the field pilot (Sredne-Nazymkoye oil field).

PDSC analysis revealed temperature intervals where heat generation rates are significant, and established activation energies corresponding to the different heat generation reactions. ARC test exhibited the temperature corresponding to the start of oxidation, that is 105°C. The absorbed oil and kerogen reactivity with air in the porous medium was investigated during RTO experiment which helped determine the temperature corresponding to the start of oxygen uptake (225°C) and identify the temperature ranges over which oxygen uptake rates are high. Arrhenius kinetics parameters for low and high-temperature regions were established. It was discovered that the dominant oxidation mode corresponds to the low-temperature region, which indicates that oil and kerogen can ignite spontaneously under reservoir temperature. Moreover, these experiments helped to pinpoint the negative temperature gradient region (NTGR).

Bulk-kinetic parameters were obtained through open-system pyrolysis using two approaches to determining the activation energy distribution. It was concluded that fixing

the frequency factor at $2 \times 10^{14} \text{ s}^{-1}$ during the derivation of the kinetic parameters and using a spacing of 1 kcal/mole (4,184 J/mol) in the discrete activation energy distribution gives a more stable solution as compared to the traditional approach.

In HPRTO experiment, 29.75 wt% of potential hydrocarbons were produced. Gas composition was determined, where a big amount of water and carbon dioxide was generated through the process which indicates that the non-generative organic part of kerogen was consumed as a fuel. In addition, Rock-Eval pyrolysis study also showed total conversion/oxidation of both the generative and non-generative organic parts of kerogen. Oil in water emulsion was collected, which means there is a risk of emulsion being produced during field operations. No pyrite minerals were detected during the mineralogy analysis in the core samples after exposure. It is strongly recommended to further investigate and experiment with the air flux effect on oil recovery.

HPRTC experiment revealed that only 37.4 wt% (29.75 wt% of 79.62 wt%) of the possible pyrolysis yield of hydrocarbons were extracted during the oxidation. This suggests that the oxidation of kerogen and the products of its reaction led to coking and further combustion under the given experimental conditions. HPRTO and HPRTC experiments identified the need to select the optimal air flux for balancing coking and oxidation reactions. No unsaturated hydrocarbons were detected in the gases.

The study of kerogen conversion during the closed-system hydrolysis process identified the “oil generation window” within a temperature range of 400°C to 480°C for the Bazhenov oil shale samples. The compositional analysis of evolved products indicated that secondary cracking and coke generation started at about 480°C. The Rock-

Eval pyrolysis study results are indicative of kerogen conversion with time, displaying almost total conversion of free oil and a 82% drop in kerogen yield after SCW exposure at 480°C. GRI analysis of crushed core samples revealed porosity growth with temperature and a noticeable increase in permeability in the samples subjected to hydrolysis exposure above 400°C, which can be explained by micro-fractures formed because of heating.

Rock-Eval pyrolysis study of the core samples following the open-system hydrolysis experiment showed almost total kerogen decomposition both in the crushed and consolidated core samples. It was found that the samples subjected to sub-critical (350°C) and supercritical water exposure (400°C) contained over-matured kerogen, which indicated that a coking process took place. Visible on the sample surface was coke-like material which can serve as a fuel for combustion. Approximately 19 wt% of organic matter decomposed into oil that came out from the consolidated core samples. A part of the generated synthetic oil was coked in the consolidated samples due to low permeability. The catalytic study showed that pyrite increased the level of kerogen decomposition to some extent. Microfracturing, expansion perpendicular to the layering and release of coke-like material were observed in the sample after hydrolysis. In addition, sulfur water evolved from the vessel, which may pose a problem for field operations. Moreover, lengthy treatment in SCW strongly affected the equipment parts made of Inconel steel. Liquid hydrocarbons were not produced until a pressure drop was applied in the system, which means that the process should be tested with different treatment times and pressure drops. The produced gas and oil compositions can serve as

benchmarks for future field operations. The gas analysis revealed intensive hydrogen sulfide and carbon dioxide generation which can overlap with gas generation during high-pressure air injection. The study brought into focus the importance of choosing the right regime for the recovery of generated products to prevent the coking process.

Synthetic oil composition and geochemical parameters of oil generated in HPRTO (oxidation), HPRTC (pyrolysis) and open-system hydrolysis experiments were obtained. It was found that the synthetic oil samples from all the three processes are more mature than the extract from the core prior to exposure. Moreover, supercritical water reacted with kerogen, while pyrolysis reactions resulted in thermal decomposition only, which means that SCW can serve as an extractor *in situ*.

Chapter 4. Laboratory investigation of high-pressure air injection in oil shale via combustion tube test

4.1. Samples selection and test design strategy

Table 41. Sample selection and test design strategy.

Oil Field	Grade of catagenesis	Samples type	Complementary study
1	Protocatagenetic substage (PC ₃ grade)	Consolidated core, cylinders 30*30mm	2D pyrolysis study
		Consolidated core, cylinders 30*30mm	Porosity and permeability measurements
		Consolidated core, cylinders 30*30mm	Thermal properties measurements
		Consolidated core, cylinders 3*58mm	Microtomography
2	Mesocatagenesis substage (MC ₂ grade)	Consolidated core, cylinders 30*30mm	2D pyrolysis study
		Consolidated core, cylinders 30*30mm	Porosity and permeability measurements
		Consolidated core, cylinders 30*30mm	Thermal properties measurements
		Crushed core	Pyrolysis study
3	Mesocatagenesis substage (MC ₁ grade)	Consolidated core, cylinders 30*30mm	2D pyrolysis study
		Consolidated core, cylinders 30*30mm	Porosity and permeability measurements
		Consolidated core, cylinders 30*30mm	Thermal properties measurements
4	Mesocatagenesis substage (MC ₁ – MC ₂ grade)	Crushed core	Pyrolysis study

4.2. Methodology

In order to assess the potential of high-pressure air injection in the Bazhenov kerogen-bearing rocks, a laboratory experiment was conducted in the combustion tube (CT). Combustion tube is technologically sophisticated equipment designed for physical modeling of *in situ* combustion and high-pressure air injection. Structurally, CT is divided into fourteen zones equipped with individual external heaters with continuous monitoring of the temperature both on the zone wall surface and in the core center. Temperature control is ensured by built-in thermocouples. Each zone is thermally insulated to reduce heat losses. Uninsulated zones function as boundaries between the heaters to prevent heat transfer between zones along the tube.

The parameters obtained in the course of the experiment, such as combustion front velocity, peak temperatures, and evolved gases composition, are essential for numerical simulation of the high-pressure air injection process.

The objectives of the experiment were:

- to assess the oil ignition and front propagation;
- to estimate the peak temperatures attained as a result of exothermic oxidation reactions, *i.e.*, the temperatures which can be created in the formation to convert kerogen to liquid and hydrocarbon gases;
- to assess the changes in the properties of oil as a result of thermal and chemical effects;

- to assess the degree of kerogen conversion as a function of temperature and time of heat exposure;
- to evaluate the changes in the rock properties, such as porosity, permeability, and thermal conductivity.

Core samples of the rocks from different oil fields (Oil Field 1, Oil Field 2, Oil Field 3 and Oil Field 4) were used for the core pack. The model was saturated with a low density low-viscosity dead oil sample from Oil Field 4.

CT was packed with crushed (fraction 0.1 - 1 mm, Oil Field 4) and consolidated core samples of various shapes, depending on the complementary experiments that were carried out to assess the change in their properties. The first two zones were packed with sand and BF samples. The following four zones were packed with oil shale material only. The remaining eight zones were packed with sand. A detailed layout of the samples is given in **Figure 100**.

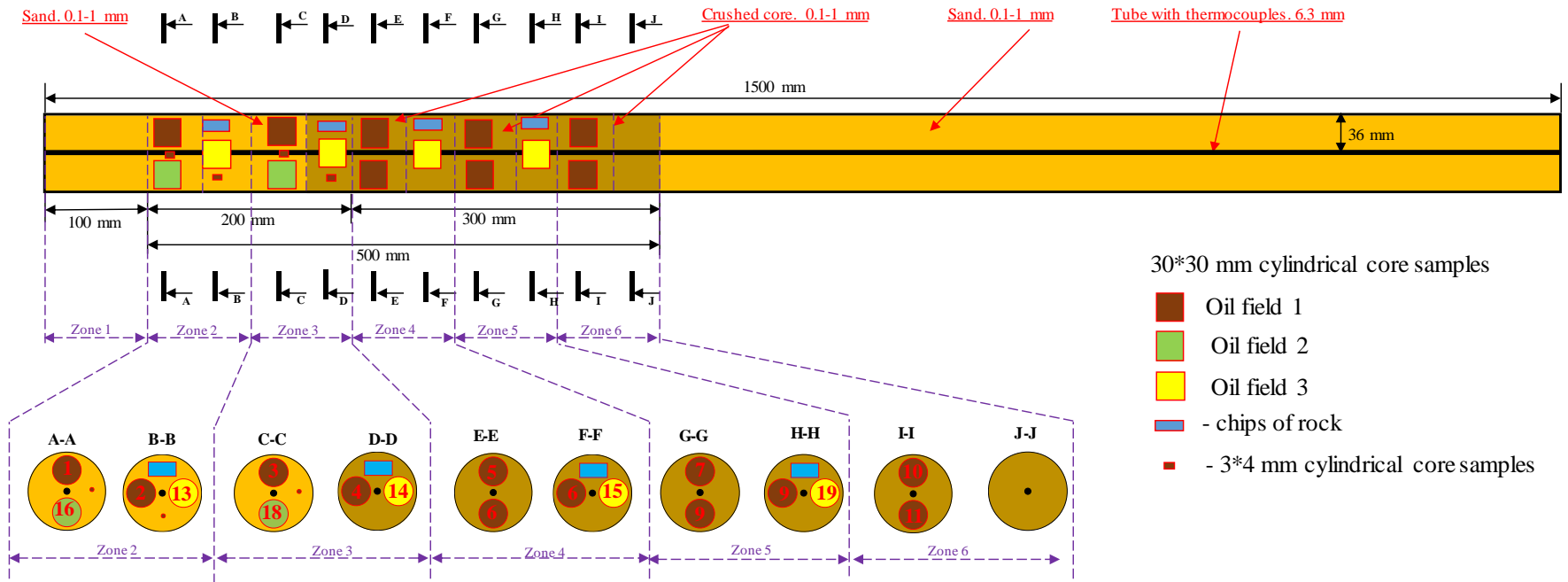


Figure 100. Rock samples packed in CT.

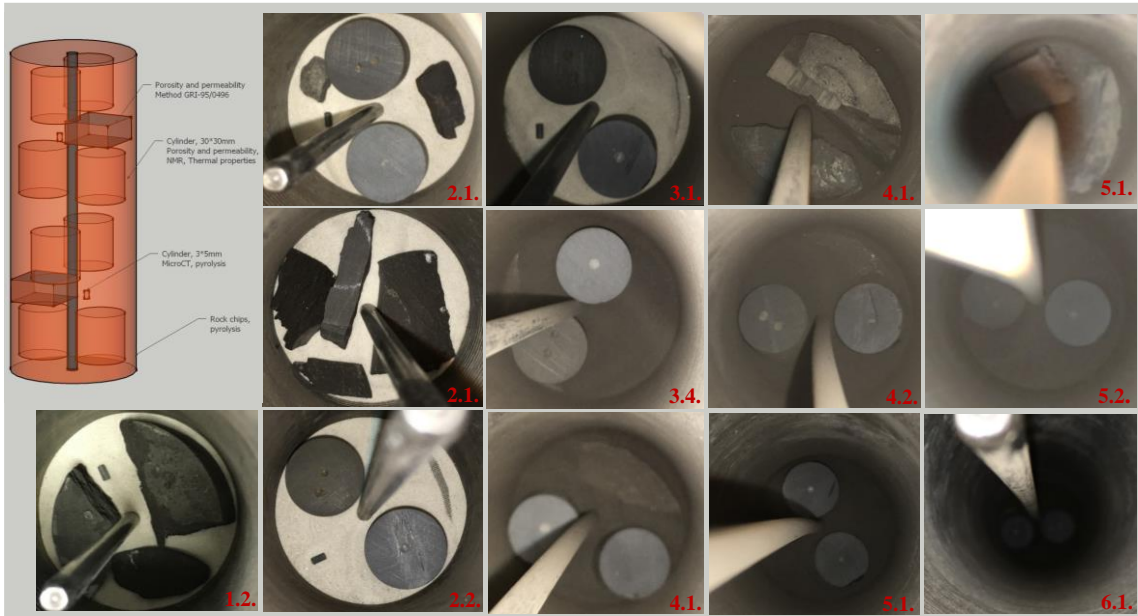


Figure 101. Photos and schematics of core samples packing.

Once the prepared core pack model of CT was pressurized with dry air, the permeability of the model was measured by air at room temperature (22°C) and found to be 2.8 D. Then 5 liters of oil were injected through CT down-top. The volume of CT and the initial oil saturation were determined from the balance of volumes of the injected and collected oil. The pore volume and porosity were 2,138.4 cm³ and 29.8%, respectively, and the initial oil saturation was 100%. The initial permeability of the bulk oil model at room temperature (22°C) was also determined to be 3.3 D. The pressure was set to 8 MPa due to the limitations on the maximum pressure in CT during the experiment. A back pressure unit and a system for collecting liquid and gaseous products, including a condenser, a separator, a gas analyzer, and a gas meter, were connected to the combustion tube outlet. Based on the results of high-pressure differential-scanning calorimetry performed at a pressure of 8 MPa and a heating rate of 1°C/min, it was decided to heat

the first two zones of CT to 200°C to accelerate the ignition and start oxidation in high-temperature oxidation mode. In all the other zones, the formation temperature was set to 100°C.

18 30×30 mm cylinders drilled from the BF rocks were packed into CT. Porosity and permeability were measured for all the samples before and after the experiment to estimate the changes taking place in the rocks during heating. The samples were located along the axis of the entire bulk model, while the experiment was prepared in such a way that different samples were heated to different temperatures. This allowed evaluating the effect of temperature on the change in the samples' characteristics after heating.

The experiment was carried out following the steps below:

- Nitrogen was injected top-down at a rate of 2.4 l(ST)/min. At the same time, CT was heated up to its predetermined temperature. During the nitrogen injection, samples of the displaced fluids were collected from the separator and its volume was measured.
- As soon as the right regime was reached (200°C for Zones 1 and 2 and 100°C for the rest of the zones), air was injected at a flow rate of 2.4 l(ST)/min (air flux: 30 m³(ST)/m²h).
- Samples of the displaced fluid were collected at CT outlet and gas samples were collected to determine the content of carbon dioxide, carbon monoxide, nitrogen, hydrogen sulfide, and hydrocarbon gases on the chromatograph at a given periodicity. The advance of the combustion front along CT was recorded in the form of temperature profiles. To make up for the heat losses, the temperature on CT outer surface was maintained at no more than 10°C below the temperature in the core using sectional electric heaters.

- Air injection was terminated, when combustion front propagated through Zone 4.
- At the end of the experiment, external heating was switched off for the removal and termination of generation of hydrogen sulfide inside CT; the CT pressure was gradually decreased to 2 MPa for 2.5 hours, followed by nitrogen purge at 1.2 l(ST)/min.
- The air supply was stopped as soon as the combustion front reached the fifth zone to check on the degree of kerogen conversion and BF rock properties as a function of exposure duration and temperature. Thus, the samples in the sixth zone were not exposed to such high temperatures.

4.3. Results: temperature profiles

The combustion process was initiated right after the first two zones were additionally heated to 200°C. The formation temperature in all the other zones was maintained at 100°C. The front propagated steadily during the experimental work. Within the framework of the experiment, the zone temperature profile was determined during the oxidation process in CT (**Figure 102**). As a result of the experiment, several exothermic peaks were registered in each zone, which may result from the superposition of successive parallel combustion reactions of the initial oil sample which a bulk model was saturated with, synthetic oil generated as a result of thermal decomposition of kerogen and kerogen oxidation. The analysis of the non-hydrocarbon gas composition at CT outlet leads one to conclude that the reactions were high-temperature oxidation reactions, as evidenced by the high concentration of CO₂. The maximum temperatures of 460°C and

463°C were registered in Zones 3 and 4, respectively. **Table 42** shows peak temperatures for all CT zones.

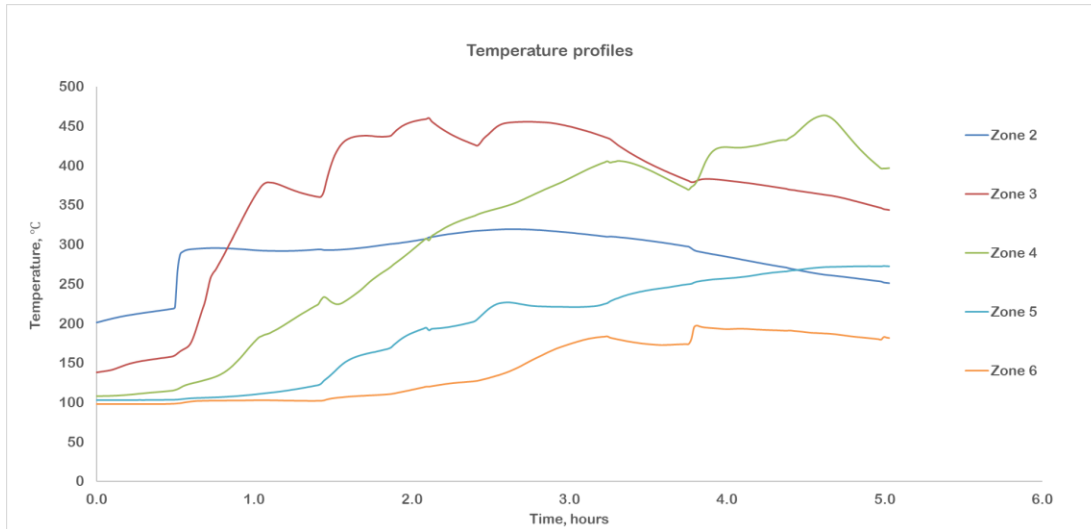


Figure 102. Temperature profiles.

Table 42. Peak temperatures.

Zone number	Location, cm	Peak temperature, °C
1	4*-14.7	237
2	14.7-25.4	319
3	25.4-36.2	460
4	36.2-46.9	463
5	46.9-57.6	273
6	57.6-68.3	197

* flange took 4 cm of CT injection end.

Since CT was packed with core material from various BF oil fields and samples with different degrees of consolidation, and since the combustion front propagated

through one third of the model only, the combustion front velocity estimation problem is ill-posed. However, it was decided to use the data on differential high-pressure differential calorimetry (8 MPa) at a heating rate of 1°C/min, namely the oil combustion onset temperature (146°C), the maximum low-temperature combustion interval temperature (219°C) and the negative temperature gradient interval end temperature (263°C), in order to plot the estimation of rate at which these temperatures were reached in CT (**Figure 103**). As it is obvious from **Figure 103**, the oil combustion reaction in Zones 3 - 6 begins at regular intervals. The rate of initiation of oil combustion in CT zones was 12.7 cm/h. The oil burning initiation front was moving steadily, which is proved by the linear dependence in **Figure 103**. The same can be said about the temperature of 219°C. The oil combustion front moved through Zones 3 - 5 with a velocity of 11.6 cm/h. The velocity of the 263°C temperature front was 5.8 cm/h, which can be explained by several reasons. First, the rise in temperature falls within the negative temperature gradient range. Second, several reactions, such as synthetic oil and kerogen oxidation, are superimposed at a given temperature. As the high-temperature front moves from Zone 2 to Zone 3, the velocity drops substantially, which is due to the change in packed material. Zones 1 and 2 were packed mainly with sand, and Zones 3 - 6 were packed with crushed and consolidated shale core samples. Core material has more fuel to be burn, hence it burns slower.

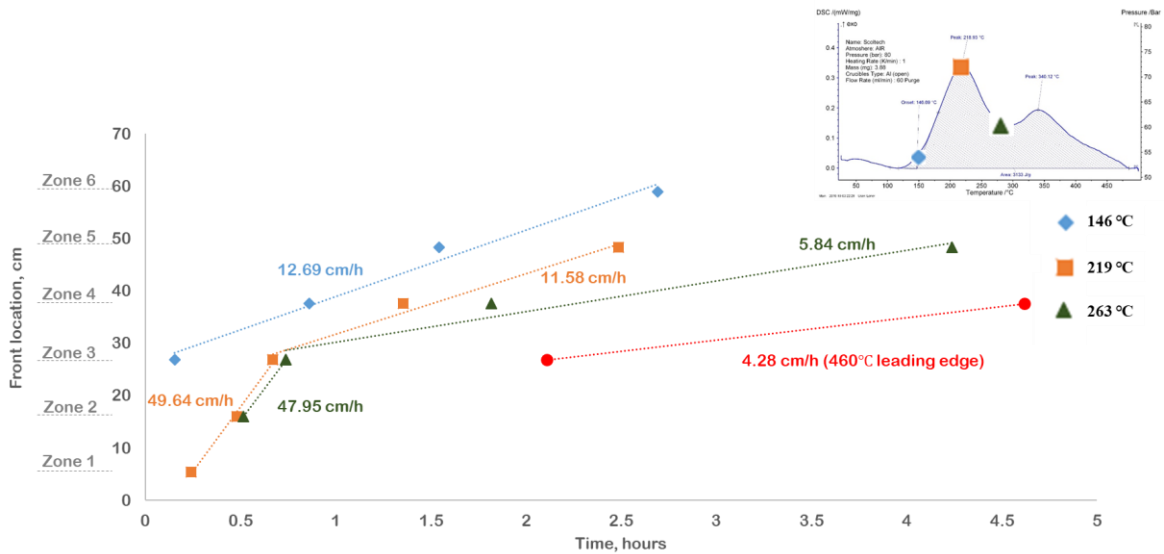


Figure 103. Combustion front locations.

4.4. Results: oil analysis

Table 43, Table 44 and Table 45 present data on the physicochemical analysis of the original oil sample and the oil samples collected during the experiment. Growth in resins and sulfur content can be observed. Cannon Cassou diagram (Figure 104) shows that oil extracts (#9, #10, #11) from core fall closely to the original oil sample (#8), however, they are less mature due to the fact that they were extracted from the core with resins and asphaltenes. Nevertheless, the location of extracts on the diagram is in the area with synthetic oil from HPRTC test.

Table 43. Original and produced oil composition.

Component	Composition									
	Original oil sample		0.95*, h		2.35*, h		4.95*, h		22.3*, h	
	mol%	wt%	mol%	wt%	mol%	wt.%	mol%	wt%	mol%	wt%
i-pentane	6.57	3.48	4.9	2.8	4.65	2.79	3.03	1.73	0.42	0.22
n-pentane	7.3	3.87	6.68	3.83	6.81	4.1	7.1	4.07	2.2	1.15
i-hexane	7	4.44	6.85	4.68	7.29	5.24	7.64	5.22	6.87	4.29
n-hexane	9.59	6.08	9.45	6.46	10.07	7.23	10.34	7.07	10	6.24
i-heptane	16.62	12.25	16.87	13.41	16.34	13.64	16.84	13.39	16.8	12.2
n-heptane	8.92	6.57	8.52	6.78	8.38	6.99	8.78	6.98	9.22	6.7
n-octane	6.25	5.25	5.64	5.11	5.13	4.88	5.55	5.03	6.77	5.6
n-nonane	5.22	4.92	4.54	4.62	3.97	4.24	4.36	4.43	5.92	5.5
n-decane	3.53	3.69	3.02	3.41	2.55	3.02	2.85	3.22	4.08	4.21
n-hendacane	2.08	2.39	1.76	2.19	1.46	1.9	1.67	2.07	2.42	2.74
C ₁₂₊	26.94	47.07	31.77	46.7	33.36	45.96	31.85	46.78	35.29	51.14
Molecular weight	136		126		120		126		138	

*time from the start of air injection.

Table 44. Original and produced oil properties.

Item	Original oil sample	0.95*h	2.35*h	4.95*h	22.3*h
Density at 20°C, kg/m ³	762,07	780.94	757.02	761.62	776.98
Kinematic viscosity at 20°C, mm ² /s	1.39	1.36	1.26	1.35	1.67
Molecular weight	136	126	120	126	138
Water, wt%	0.80	0	0	0	0
Sulfur, wt%	0.062	0.058	0.058	0.119	0.205
Ashphaltenes, wt%	0.04	-	-	-	-
Resins, wt%	1.16	0.42	0.36	2.22	12.35
Wax, wt%	0.43	0.69	0.59	0.70	0.65

*time from the start of air injection.

Table 45. GC×GC-MS results for the oil sample extracted from the sand and core and original oil.

Sample ID	8	9	10	11
Sample description	CT - original oil	Extract from Zones 4 and 5	Extract from Zone 6	Extract from the sand (7-14 zones)
Sample preparation details	Original oil	CHCl ₃ extract from the core	CHCl ₃ extract from the core	CHCl ₃ extract from the sand
Ki	0.28	0.30	0.31	0.31
Pr/C ₁₇	0.26	0.28	0.30	0.30
Ph/C ₁₈	0.30	0.32	0.34	0.31
Pr/Ph	1.11	1.58	1.76	1.45

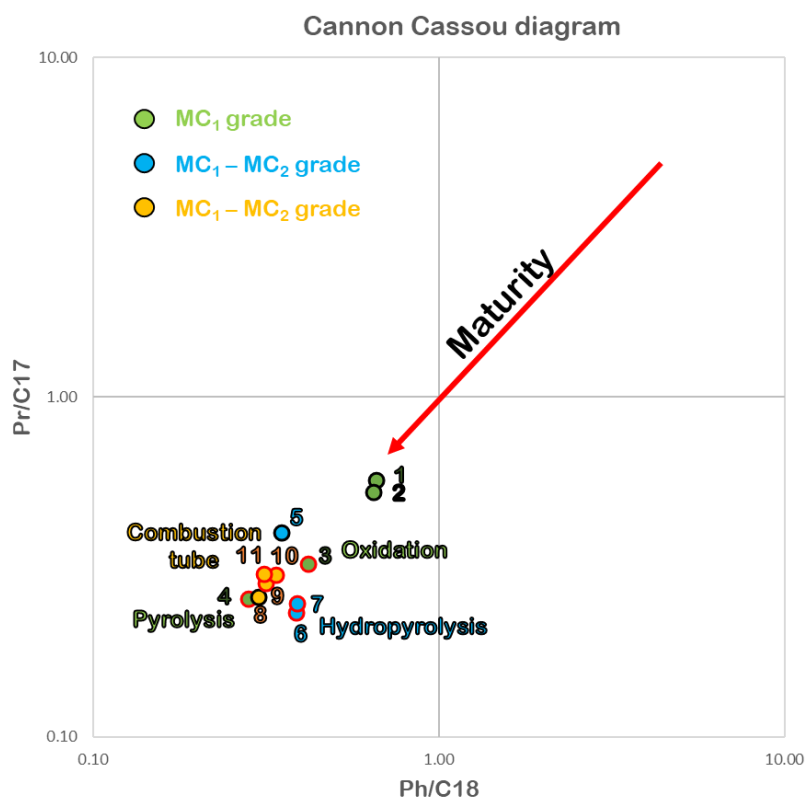


Figure 104. Cannon Cassou diagram – extracted oil samples and original oil.

4.5. Results: gas analysis

Table 46 shows the composition of hydrocarbon and non-hydrocarbon gases. In the first two hours, there is an increase in the concentration of carbon monoxide. Then there is an increase in the amount of carbon dioxide in the evolved gases, which indicates that combustion process is going on, especially in Zones 3 and 4. Carbon dioxide has higher solubility in oil than carbon monoxide, which explains the delay in the release of carbon dioxide from CT. After initiation of the combustion front, the formation of hydrogen sulfide in the gas phase is observed, along with an increase in its content of up to 750 ppm during the test. Oxygen composition is 100%, which is indicative of its complete consumption in the oxidation process.

Table 46. Evolved gas composition.

Component	Gas molar composition, mol. %									
	1.13 h	1.47 h	1.60 h	2.10 h	2.63 h	3.25 h	3.67 h	4.13 h	5.08 h	5.55 h
H ₂ S	-	n/a	n/a	n/a	traces	0.059	n/a	n/a	0,075	n/a
CH ₄	0.006	n/a	n/a	n/a	0.214	0.283	n/a	n/a	0,152	n/a
C ₂ H ₆	0.009	n/a	n/a	n/a	0.023	0.076	n/a	n/a	0,044	n/a
C ₃ H ₈	0.153	n/a	n/a	n/a	0.012	0.017	n/a	n/a	0,031	n/a
i-C ₄ H ₁₀	0.07	n/a	n/a	n/a	0.026	0.008	n/a	n/a	0,005	n/a
n-C ₄ H ₁₀	0.195	n/a	n/a	n/a	0.094	0.048	n/a	n/a	0,036	n/a
O ₂	0	0	0	0	0	0	0	0	0	0
CO	1.24	1.98	1.71	0.89	0.35	0.08	0.23	0.04	0.07	0.05
CO ₂	0.18	2.2	4.67	8.19	11.65	8.06	12.18	11.65	9.08	16.7
N ₂	98.15	95.49	93.27	90.48	87.63	91.37	87.22	87.97	90.51	82.85

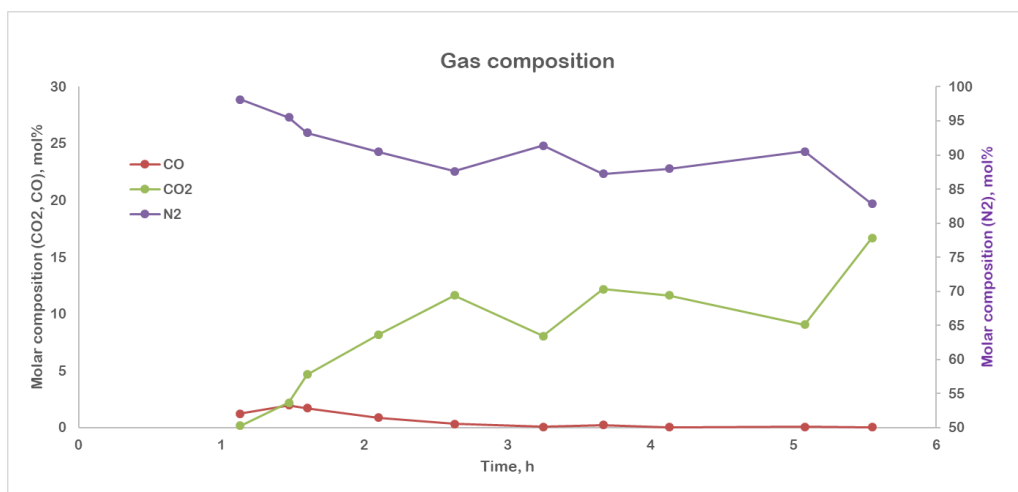


Figure 105. Evolved gas composition (N₂, CO, CO₂).

It is likely that the high amount of CO₂ is a result of the non-generative organic part of kerogen producing extra fuel. High concentrations of methane and hydrogen sulfide were observed. It is known that methane is the product of oil cracking, kerogen pyrolysis and secondary cracking of generated products. Hydrogen sulfide is also a product of oil cracking and kerogen pyrolysis. The presence of these gases in the evolved gases composition indicates that kerogen conversion takes place ahead of the front. Pyrite may also contribute to the hydrogen sulfide generation. The core elemental analysis results revealed a decrease in sulfur content, which explains the high concentration of H₂S.

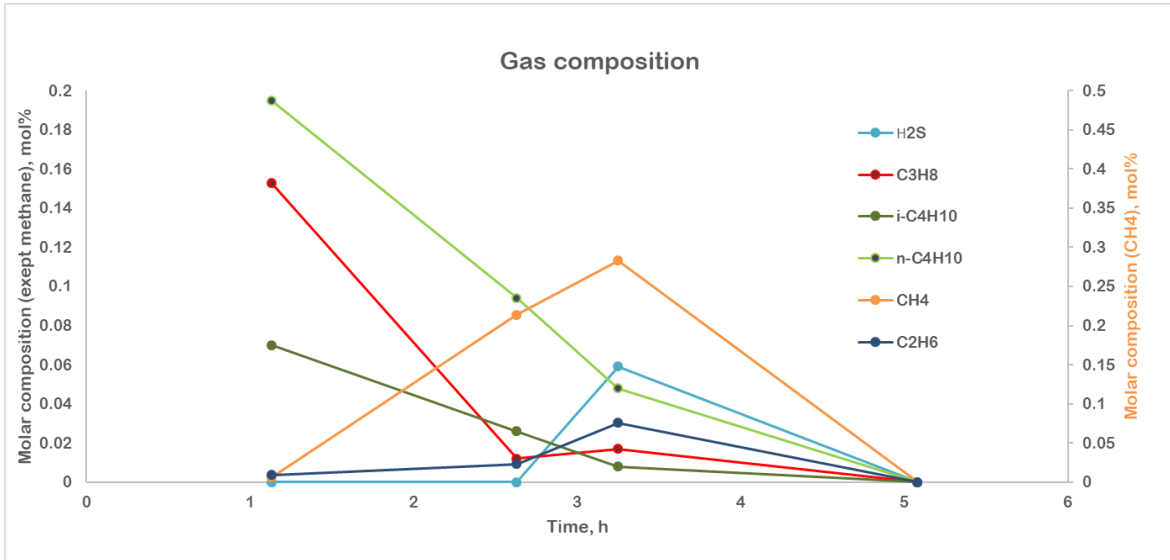


Figure 106. Evolved gas composition (hydrocarbon gases and hydrogen sulfide).

4.6. Results: core analysis

4.6.1 Core samples appearance after the test

Figure 107 shows photographs of the cylindrical core samples unpacked from CT. The photos are grouped according to the zones the samples were taken from. The deposits, materials, peak zone temperatures and ordinal numbers are specified in the legend. It can be seen that two samples (#2 and #3) from Oil Field 1 changed color to reddish-red, which may be due to the higher pyrite content in the samples. Bitumen is found in Samples #16 and #18 from Oil Field 2. However, all these assumptions must be confirmed by an analysis of the mineralogical composition in the future. In the Sample #14 from Oil Field 3, the formation of cracks is clearly observed.

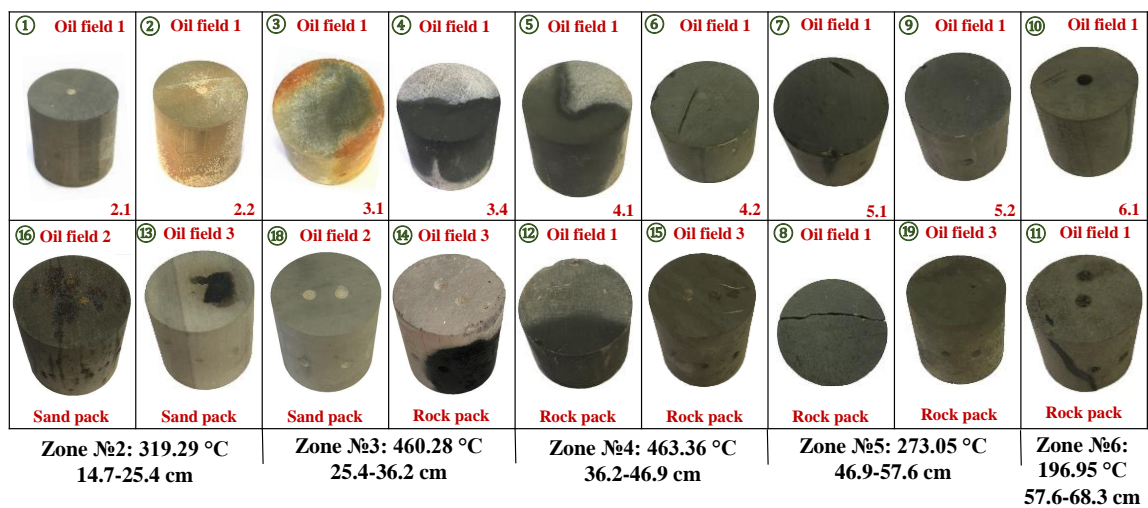


Figure 107. Photos of core samples after exposure.

4.6.2 Pyrolysis study of crushed core

A Rock-Eval pyrolysis study of crushed core samples from Oil Field 4 taken from different zones along the length of the tube was carried out to assess the degree of conversion of kerogen to hydrocarbons as a result of thermal and chemical effects in CT. The samples were subjected to thermal and chemical effects of various degrees. The pyrograms of crushed samples from different CT intervals differ from the pyrogram of the initial sample exposed to thermal and chemical effects (**Figure 108**). It can be seen from the pyrograms of crushed core taken from CT zones where the high-temperature combustion front passed through that the peak S2 disappears, which testifies to complete conversion and/or oxidation of kerogen. In the region in front of the high-temperature front where the maximum temperatures are lower, the S2 peak steadily increases, which attests to incomplete conversion and/or oxidation of kerogen. These data confirm the theory that in the region behind the combustion front there are no hydrocarbon compounds, and in the region ahead of the combustion front, pyrolysis reactions of

kerogen occur. At a greater distance from the high-temperature combustion front, the temperatures do not reach values high enough to trigger significant chemical transformations. The gases and liquid hydrocarbons displaced from the previous zones and generated as a result of pyrolysis of kerogen flow through this region, and evaporation and condensation of light oil fractions occur sequentially. In support of the above, the pyrograms show that a significant peak S1 and even a peak S0 appear in the last zones packed with the BF crushed samples. The pyrograms show how the S2 peaks of samples unpacked from CT are shifted toward higher temperatures (as compared to the peak S2 of the original sample). Presumably, this phenomenon is associated with the primary process of asphaltenes cracking, which are released at approximately the same temperatures as the products of kerogen cracking in the BF. However, the existing difference in evaporation or decomposition temperatures with the predominance of one or another component in the mixture will result in a difference in the values of the T_{\max} parameter. **Table 47** presents the results of Rock-Eval pyrolysis study of crushed samples from three oil fields that were packed into CT. The high-temperature combustion front passed through Zones 3.2 - 4.1, which is confirmed by the absence of hydrocarbons in these zones.

Table 47. Crushed rock samples open-system pyrolysis results.

Oil Field number	CT Zone	S0	S1	S2	TOC	T _{max}	HI	OI	PI	S4CO2	S4CO
		<i>mg HC/g rock</i>	<i>mg HC/g rock</i>	<i>mg HC/g rock</i>	<i>Total Organic Carbon, wt%</i>	<i>Maturity, °C</i>	<i>Hydrogen Index, mg HC/g TOC</i>	<i>Oxygen Index, mg CO2/g TOC</i>	<i>Production Index, S1/(S1+S2)</i>	<i>mgCO2/g rock</i>	<i>mgCO/g rock</i>
Before exposure											
2	3.2.	1.81	6.52	30.52	7.98	446	382	1	0.18	126.84	28.29
1	3.3.	0.16	0.68	16.89	3.01	428	560	5	0.04	41.08	8.84
4	3.4.-6.2.	1.3	4.42	50.57	11.08	445	456	1	0.08	186.42	27.98
After exposure											
2	3.2.	0.08	0.06	0.17	0.27	88	64	67	0.28	2.64	3.72
1	3.3.	0.08	0.08	0.18	0.19	88	96	75	0.30	2.32	2.06
4	3.4.	0.21	0.23	0.18	1.06	89	17	11	0.56	26.33	6.5
	4.1.	0.48	0.49	0.67	3.04	458	22	10	0.42	79.93	16.4
	4.2.	0.8	2.13	22.56	7.28	443	310	3	0.09	141.1	29.01
	5.1.	0.8	5.97	35.44	7.73	447	458	1	0.14	135.77	10.21
	5.2.	1.84	11.62	25.75	7.43	447	347	3	0.31	116.27	21.26
	6.1.	6.17	11.72	38.00	10.48	445	362	2	0.24	164.41	28.95
	6.2.	11.14	4.95	40.70	10.90	443	374	3	0.11	173.32	30.95

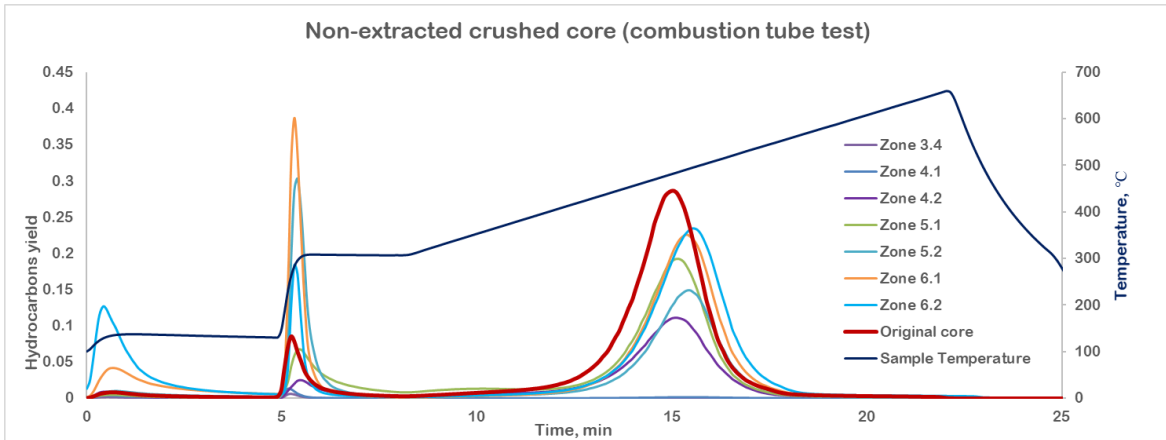


Figure 108. Pyrograms of non-extracted crushed core samples from different zones (combustion tube test). Oil Field 4.

It should be noted that the difference between the pyrograms is more significant right ahead of the combustion front than in the zones located farther from the front. **Figures 108-113** show pyrograms of extracted and non-extracted samples after the combustion tube test. The area highlighted in yellow indicates potential hydrocarbons that were converted from kerogen into pyrobitumen, but also oxidized, therefore their mobility decreased. They will burn if they are not displaced out of the tube.

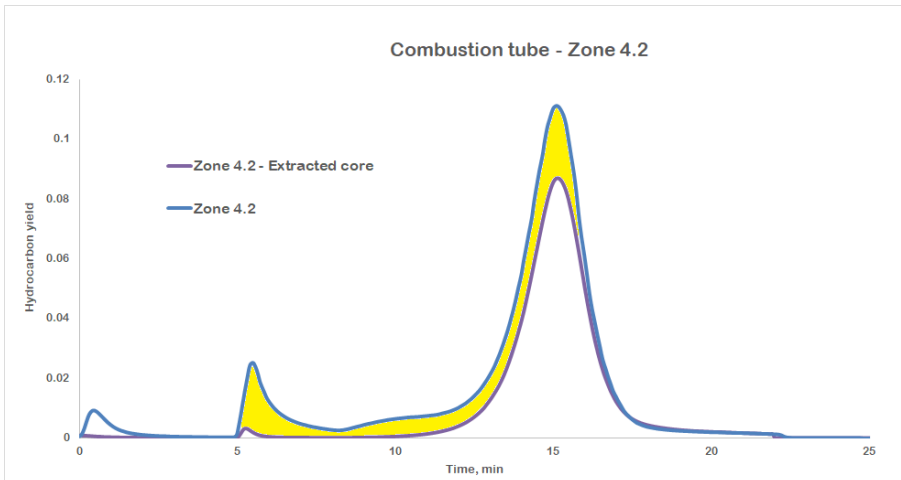


Figure 109. Comparison of pyrograms of extracted core and non-extracted core from Zone 4.2 (combustion tube test).

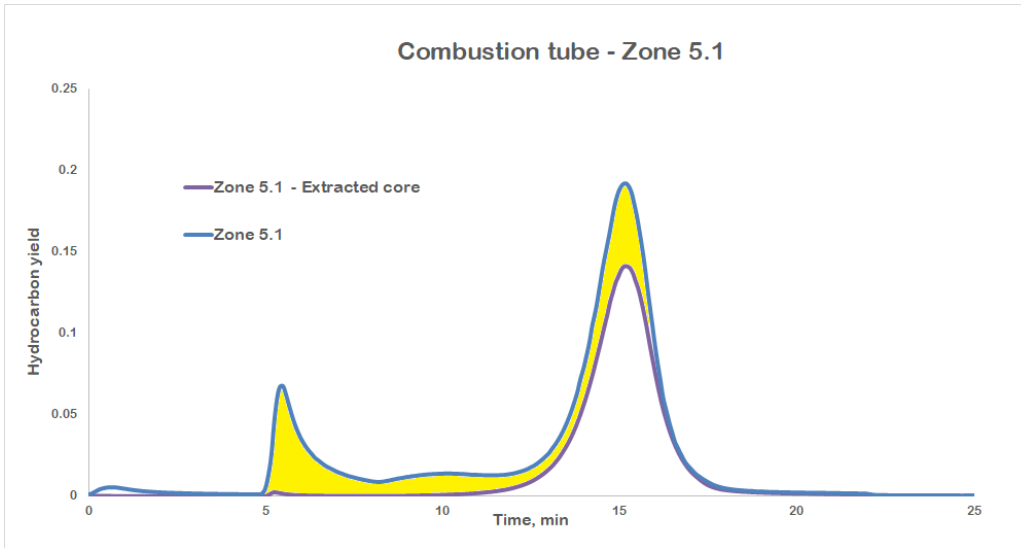


Figure 110. Comparison of pyrograms of extracted core and non-extracted core from Zone 5.1 (combustion tube test).

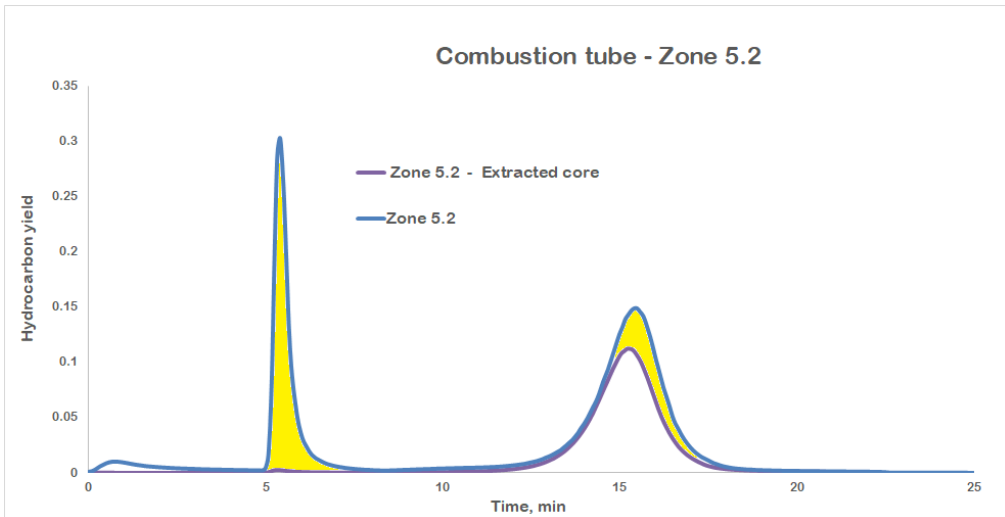


Figure 111. Comparison of pyrograms of extracted core and non-extracted core from Zone 5.2 (combustion tube test).

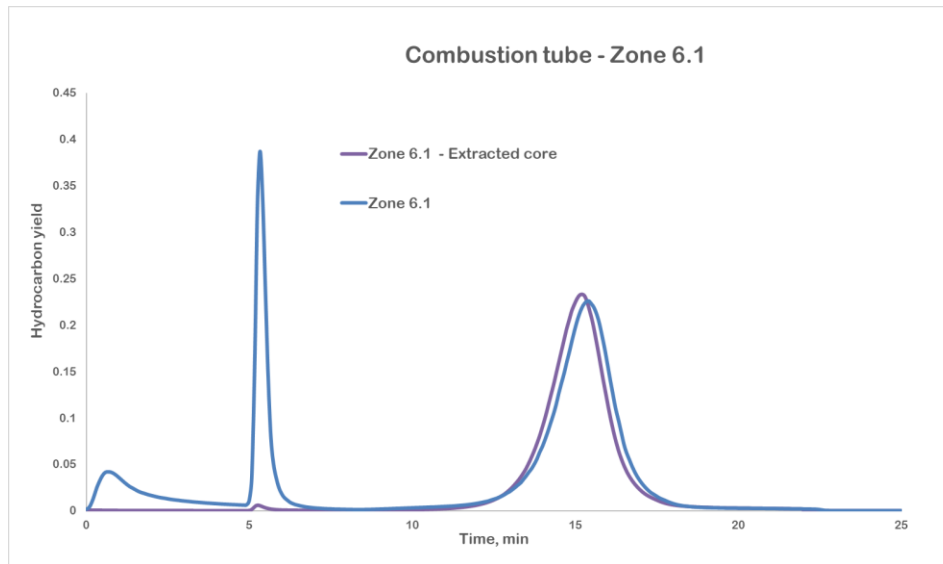


Figure 112. Comparison of pyrograms of extracted core and non-extracted core from Zone 6.1 (combustion tube test).

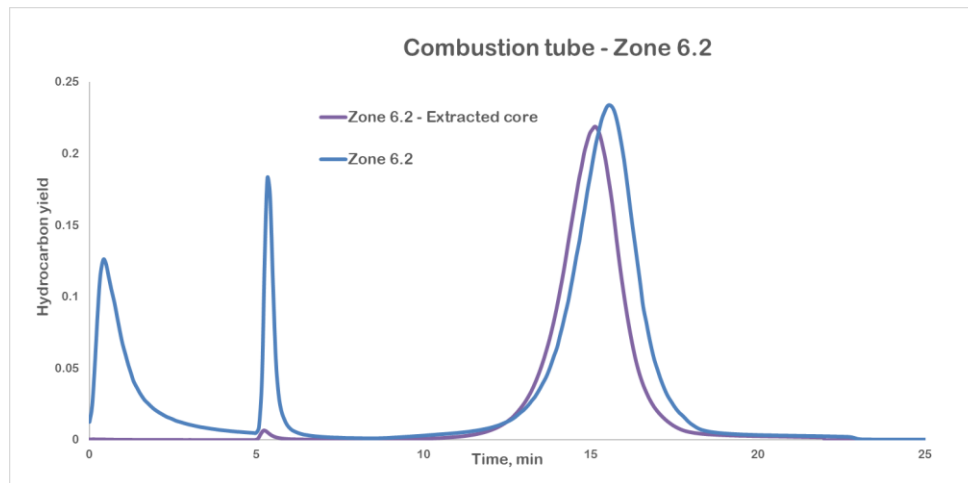


Figure 113. Comparison of pyrograms of extracted core and non-extracted core from Zone 6.2 (combustion tube test).

As can be seen from the pyrogram in **Figure 114**, Zone 4.1 is transitional due to formation of the coke-like material (fuel for combustion).

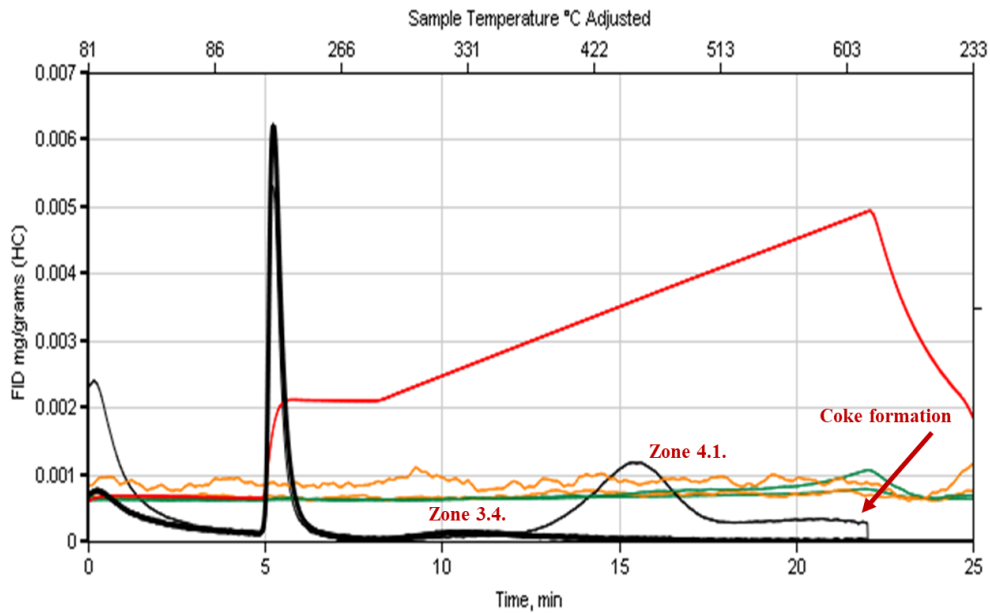


Figure 114. Comparison of core from Zone 3.4 (bold line) and Zone 4.1.

4.6.3 2D pyrolysis of consolidated samples

The 2D pyrolysis methodology was described in Chapter 3 (3.7.5). Distribution (**Figure 115**) is homogeneous along the core. There are no higher values of geochemical parameters in the center of the core.



a. Drilled holes location

2.54	2.60	2.87	2.87	2.87
2.52	2.57	2.58	2.41	3.12
3.13	2.72	2.69	2.65	2.69
2.39	2.85	3.57	2.96	2.93

b. S1 parameter distribution

27.96	26.44	29.25	29.75	28.42
25.55	27.42	28.53	27.48	32.62
35.08	29.22	26.42	27.83	26.43
26.60	31.64	31.37	29.68	30.11

c. S2 parameter distribution

77.73	69.59	74.28	71.86	86.82
66.60	67.49	91.46	62.80	83.31
85.22	69.81	68.46	67.87	66.07
68.86	77.34	75.78	74.34	71.48

d. S4CO2

Figure 115. Results of 2D pyrolysis study – Sample #15 (consolidated core).



a. Drilled holes location

0.28		0.34	0.33	0.29
0.22	0.45	0.21	0.26	0.29
0.32	0.32	0.12	0.29	0.44
0.35	0.35	0.46	0.34	0.34

b. S1 parameter distribution

4.86		5.26	5.24	4.96
4.27	4.86	5.26	4.52	4.62
4.68	4.07	3.33	3.61	5.14
5.48	5.02	5.16	4.66	4.89

c. S2 parameter distribution

36.50		33.08	32.93	34.92
40.95	37.18	30.01	40.49	39.19
37.59	43.17	39.50	43.51	35.74
34.67	32.40	34.04	35.75	31.85

d. S4CO2

Figure 116. Results of 2D pyrolysis study – Sample #10 (consolidated core).

Table 48. Results of 2D pyrolysis study – Sample #15 (consolidated core).

Sample	S0	S1	S2	TOC	T _{max}	HI	OI	PI	S4CO2	S4CO
	<i>mg HC/g rocks</i>	<i>mg HC/g rocks</i>	<i>mg HC/g rocks</i>	<i>Total Organic Carbon, wt%</i>	<i>Maturity, °C</i>	<i>Hydrogen Index, S2/TOC*100</i>	<i>Oxygen Index, S3/TOC*100</i>	<i>Production Index, S1/S1+S2</i>	<i>mg CO2/g rocks</i>	<i>mg CO/g rocks</i>
Original sample 15	1.91	6.70	72.66	11.37	437	639.00	1.00	0.08	130.42	24.53
1	1.22	2.54	27.96	5.60	431	498	6	0.08	77.73	17.59
2	1.79	2.60	26.44	5.38	431	491	7	0.09	69.59	19.21
3	1.67	2.87	29.25	5.72	432	511	4	0.09	74.28	18.35
4	1.79	2.87	29.75	5.76	431	516	5	0.09	71.86	19.58
5	1.18	2.87	28.42	5.77	435	492	6	0.09	86.82	14.00
6	1.57	2.52	25.55	5.20	431	491	4	0.09	66.60	19.46
7	1.94	2.57	27.42	5.40	431	508	5	0.09	67.49	18.86
8	1.69	2.58	28.53	6.41	432	444	8	0.08	91.46	25.04
9	2.10	2.41	27.48	5.28	430	520	4	0.08	62.80	19.18
10	1.56	3.12	32.62	6.22	433	524	3	0.09	83.31	17.18
11	1.80	3.13	35.08	6.67	430	525	4	0.08	85.22	21.43
12	1.92	2.72	29.22	5.59	433	523	5	0.09	69.81	17.99
13	2.20	2.69	26.42	5.30	434	498	4	0.09	68.46	17.38
14	1.98	2.65	27.83	5.40	430	515	4	0.09	67.87	17.49
15	1.34	2.69	26.43	5.10	432	517	5	0.09	66.07	15.95
16	1.93	2.39	26.60	5.29	430	502	5	0.08	68.86	17.39
17	2.03	2.85	31.64	6.22	430	508	5	0.08	77.34	22.76
18	1.31	3.57	31.37	6.01	430	522	4	0.10	75.78	19.37
19	1.77	2.96	29.68	5.79	432	512	4	0.09	74.34	18.78
20	1.47	2.93	30.11	5.75	432	523	6	0.09	71.48	19.63

Table 49. Results of 2D pyrolysis study – Sample #10 (consolidated core).

Sample	S0	S1	S2	TOC	T _{max}	HI	OI	PI	S4CO ₂	S4CO
	<i>mg HC/g rocks</i>	<i>mg HC/g rocks</i>	<i>mg HC/g rocks</i>	<i>Total Organic Carbon, wt%</i>	<i>Maturity, °C</i>	<i>Hydrogen Index, S2/TOC*100</i>	<i>Oxygen Index, S3/TOC*100</i>	<i>Production Index, S1/S1+S2</i>	<i>mg CO₂/g rocks</i>	<i>mg CO/g rocks</i>
Original Sample #10	0.16	0.68	16.89	3.01	428	560	5	0.04	41.08	8.84
1	0.27	0.28	4.86	1.84	429	264	47	0.05	36.50	7.61
3	0.18	0.34	5.26	1.68	430	313	56	0.06	33.08	5.23
4	0.20	0.33	5.24	1.66	430	316	43	0.06	32.93	5.20
5	0.20	0.29	4.96	1.80	430	276	70	0.06	34.92	7.51
6	0.09	0.22	4.27	1.88	432	226	69	0.05	40.95	7.30
7	0.23	0.45	4.86	1.83	429	264	54	0.08	37.18	6.96
8	0.15	0.21	5.26	1.58	431	333	35	0.04	30.01	5.80
9	0.06	0.26	4.52	1.80	430	251	56	0.05	40.49	5.39
10	0.11	0.29	4.62	1.89	432	244	53	0.06	39.19	8.06
11	0.15	0.32	4.68	1.81	432	258	71	0.06	37.59	6.48
12	0.12	0.32	4.07	1.87	429	217	110	0.07	43.17	5.13
13	0.04	0.12	3.33	1.67	433	198	79	0.04	39.50	5.20
14	0.12	0.29	3.61	1.88	429	192	126	0.07	43.51	5.71
15	0.15	0.44	5.14	1.84	430	279	72	0.08	35.74	7.15
16	0.18	0.35	5.48	1.86	430	294	50	0.06	34.67	8.18
17	0.29	0.35	5.02	1.64	429	305	46	0.07	32.40	5.30
18	0.19	0.46	5.16	1.66	432	310	55	0.08	34.04	4.50
19	0.21	0.34	4.66	1.71	429	273	64	0.07	35.75	5.40
20	0.17	0.34	4.89	1.72	431	285	48	0.06	31.85	8.00

Table 50. Consolidated rock samples open-system pyrolysis results (15 mm from the contact area).

CT Zone	Oil Field	Sample	S0	S1	S2	TOC	Tmax	HI	OI	PI	S4CO2	S4CO	S2 decrease, %
			<i>mg HC/g rocks</i>	<i>mg HC/g rocks</i>	<i>mg HC/g rocks</i>	<i>Total Organic Carbon, wt%</i>	<i>Maturity, °C</i>	<i>Hydrogen Index, S2/TOC*100</i>	<i>Oxygen Index, S3/TOC*100</i>	<i>Production Index, S1/S1+S2</i>	<i>mg CO2/g rocks</i>	<i>mg CO/g rocks</i>	
	1	Original	0.16	0.68	16.89	3.01	428	560	5	0.04	41.08	8.84	
2.1	1	1	0.05	0.13	4.56	1.55	425	294	45	0.03	32.21	5.29	73.00
2.2	1	2	0.30	0.55	3.25	1.43	430	227	34	0.15	28.08	6.48	80.76
3.1	1	3	0.04	0.10	0.44	1.41	457	31	26	0.19	37.35	7.42	97.39
6.1	1	10	0.04	0.12	3.33	1.67	433.00	198.00	79.00	0.04	39.50	5.20	80.28
2.2	3	13 – original	1.91	6.30	107.60	16.98	433.00	633.00	1.00	0.06	212.66	34.53	78.63
2.2	3	13	4.20	17.14	22.99	10.88	439	211	1	0.43	195.52	40.86	
4.2	3	15 – original	1.91	6.70	72.66	11.37	437.00	639.00	1.00	0.08	130.42	24.53	63.64
4.2	3	15	2.20	2.69	26.42	5.30	434	498	4	0.09	68.46	17.38	
3.1	2	18 – original	1.81	6.52	30.52	7.98	446	382	1	0.18	126.84	28.29	95.64
3.1	2	18	0.19	0.69	1.33	4.86	586	27	3	0.34	118.61	33.01	

4.6.4 Kerogen thermal decomposition kinetics after the exposure

Figure 118, Figure 119, Figure 120, Figure 121, Figure 122, Figure 123 and Figure 124 illustrate discrete activation energy distributions with a fixed frequency factor $A = 2 \times 10^{14} \text{ s}^{-1}$ and a spacing of 1 kcal/mole (4,184 J/mol) between the groups for samples from different CT zones. Figure 117 shows discrete activation energy distribution for the original sample. The original core pyrolysis yields an activation energy distribution value of 53 kcal/mol (221,752 J/mol) corresponding to the maximum organic matter conversion, while in the zones ahead of the front this value increases to 54 kcal/mol (225,936 J/mol). This observation can be explained by partial conversion of kerogen. High activation energy is needed for further decomposition. Zone 3.4 does not contain much kerogen due to the combustion front propagation, but the remaining organic matter has low activation energy as compared to the original core.

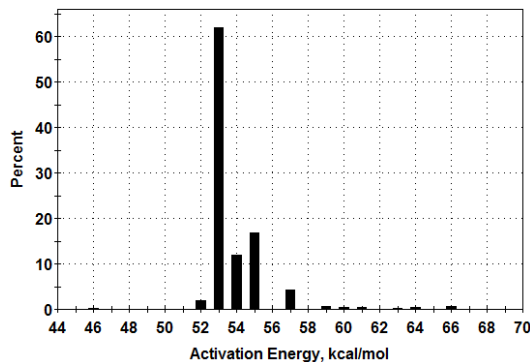


Figure 117. E_a distribution with a spacing of 1 kcal/mole (4,184 J/mol) between groups and fixed $A = 2 \times 10^{14} \text{ s}^{-1}$. Original core.

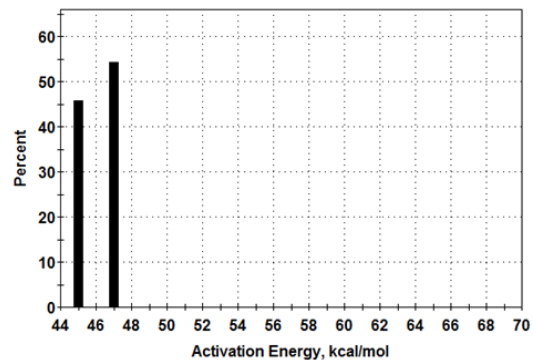


Figure 118. E_a distribution with a spacing of 1 kcal/mole (4,184 J/mol) between groups and fixed $A = 2 \times 10^{14} \text{ s}^{-1}$. Core from Zone 3.4.

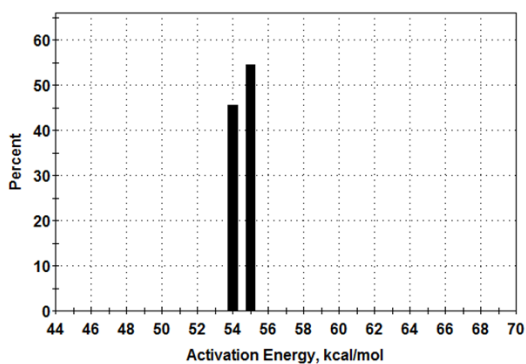


Figure 119. E_a distribution with a spacing of 1 kcal/mole (4,184 J/mol) between groups and fixed $A = 2 \times 10^{14} \text{ s}^{-1}$. Core from Zone 4.1.

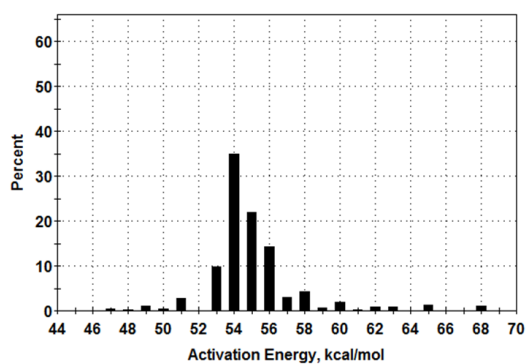


Figure 120. E_a distribution with a spacing of 1 kcal/mole (4,184 J/mol) between groups and fixed $A = 2 \times 10^{14} \text{ s}^{-1}$. Core from Zone 4.2.

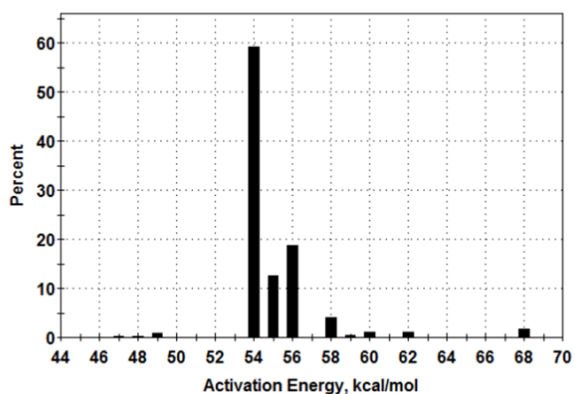


Figure 121. E_a distribution with a spacing of 1 kcal/mole (4,184 J/mol) between groups and fixed $A = 2 \times 10^{14} \text{ s}^{-1}$. Core from Zone 5.1.

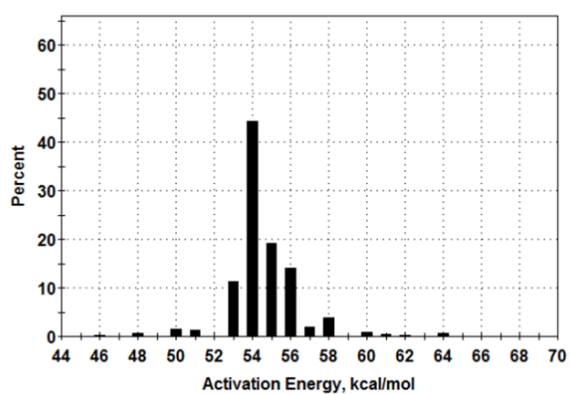


Figure 122. E_a distribution with a spacing of 1 kcal/mole (4,184 J/mol) between groups and fixed $A = 2 \times 10^{14} \text{ s}^{-1}$. Core from Zone 5.2.

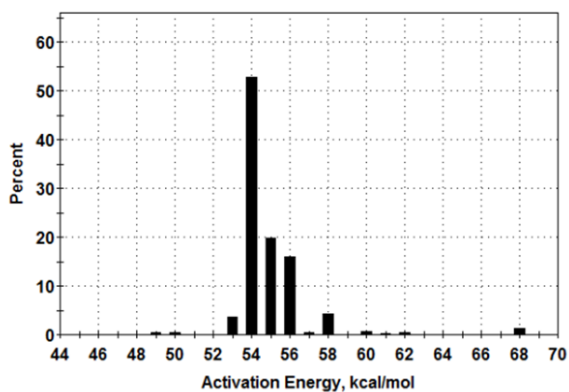


Figure 123. E_a distribution with a spacing of 1 kcal/mole (4,184 J/mol) between groups and fixed $A = 2 \times 10^{14} \text{ s}^{-1}$. Core from Zone 6.1.

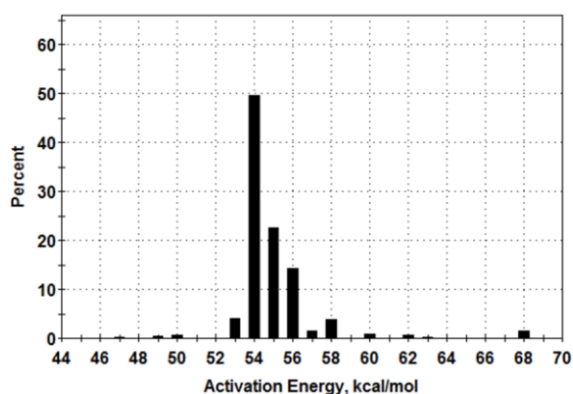


Figure 124. E_a distribution with a spacing of 1 kcal/mole (4,184 J/mol) between groups and fixed $A = 2 \times 10^{14} \text{ s}^{-1}$. Core from Zone 6.2.

4.6.5 Elemental analysis of crushed core samples from different combustion tube zones

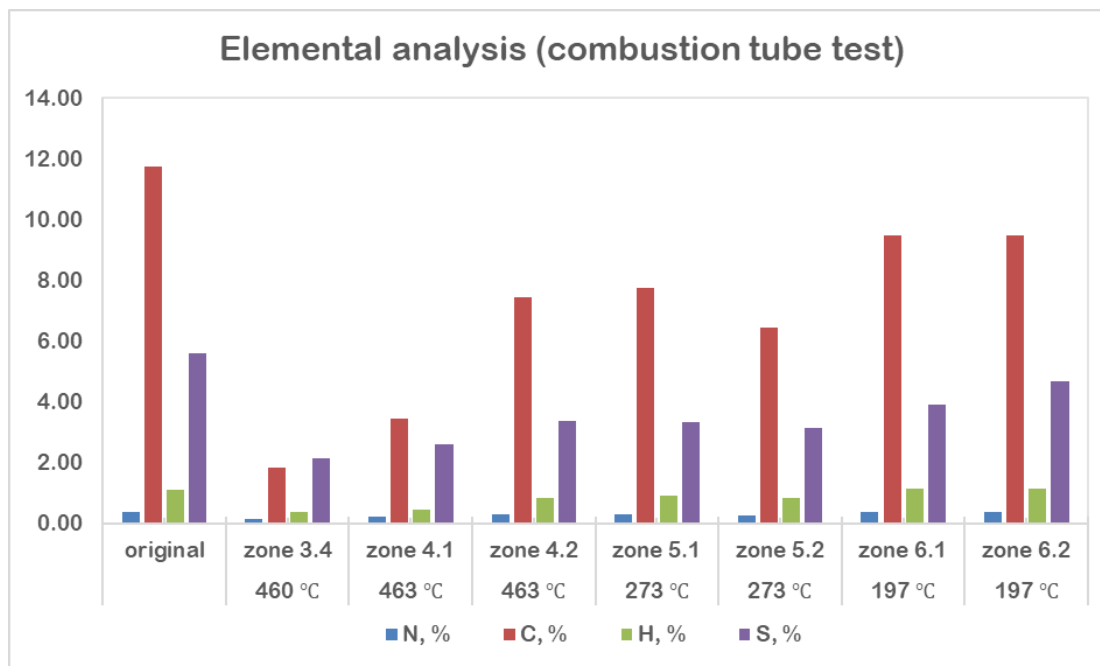


Figure 125. Results of elemental analysis of crushed core samples after exposure (combustion tube test).

Table 51. Results of elemental analysis of crushed core samples after exposure (combustion tube test).

Temperature, °C	Oil Field	Tube zone	N, %	C, %	H, %	S, %
-	Oil Field 4	Original core	0.36	11.74	1.11	5.58
460°C	Oil Field 4	Zone 3.4	0.12	1.81	0.37	2.12
463°C	Oil Field 4	Zone 4.1	0.20	3.44	0.43	2.58
463°C	Oil Field 4	Zone 4.2	0.31	7.44	0.83	3.37
273°C	Oil Field 4	Zone 5.1	0.29	7.73	0.91	3.33
273°C	Oil Field 4	Zone 5.2	0.25	6.44	0.83	3.13
197°C	Oil Field 4	Zone 6.1	0.37	9.47	1.13	3.89
197°C	Oil Field 4	Zone 6.2	0.38	9.47	1.13	4.66

4.6.6 Permeability and porosity of consolidated core samples from different combustion tube zones

The porosity and permeability measurements taken before and after the experiment are given in **Table 52**, which also contains the maximum temperatures the cylinders are heated to, assuming that the maximum temperatures at each point changed linearly along the core-pack model axis and neglecting the thermal losses in the radial direction.

Figure 126 shows the dependence of the change in permeability from the mass loss of the samples. It can be seen from the graph that an increase in the permeability of the samples is proportional to the mass loss. The exception is Sample #4 where fracturing might have occurred due to the increased temperature and layering. No such changes were observed in Sample #5 at a similar temperature. It can be concluded that when studying the effect of CT temperature on fractures formation, special attention should be given to the texture and homogeneity of the samples. It should be noted that to confirm the type of dependence of permeability on mass loss, it is necessary to conduct additional experiments and increase the statistical samples number.

On the other hand, a possible additional factor affecting the characteristics of the samples is the time of thermal exposure in the air environment. Thus, Sample #4 (Zone 3.4.) was subjected to a longer exposure than Sample #5 (Zone 4.1.), although both samples were subjected to practically the same maximum exposure temperature (461°C and 462°C, respectively). Another proof of the influence of the time of action on the change in permeability is provided by Sample #6 (Zone 4.2.) which was exposed to a maximum temperature of 414°C but showed a less change in permeability in contrast to the changes in Samples #1 and #2 heated for a longer time and located in Zones 2.1 and 2.2, respectively. However, further analysis is required to confirm this trends.

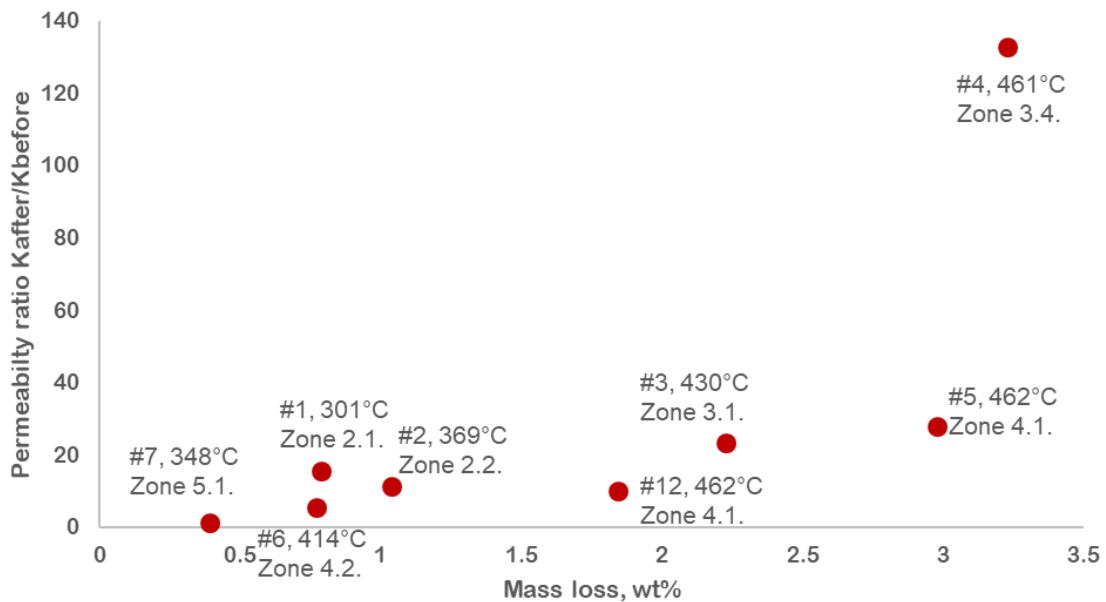


Figure 126. Relationship between sample mass loss and increase in permeability (Oil Field 1).

Table 52. Core samples porosity and permeability measured before and after exposure.

Zone number	Sample number	Peak temperature, °C	Before exposure			After exposure		
			Pore volume, cc	ϕ , %	k, mD	Pore volume, cc	ϕ , %	k, mD
2.1.	1	300	0.226	1.067	0.004	0.857	4.04	0.062
2.1.	16	300	0.618	2.808	0.053	0.730	3.30	1.591
2.2.	13	368	0.12	0.576	0.024	5.690	26.07	5.768
2.2.	2	369	0.272	1.284	0.003	0.406	1.91	0.034
3.1.	3	430	0.114	0.538	0.033	1.768	8.27	0.769
3.1.	18	430	0.519	2.433	0.065	3.944	18.39	0.577
3.4.	14	461	0.103	0.467	0.012	7.299	31.92	4.277
3.4.	4	461	0.165	0.781	0.004	2.568	12.10	0.531
4.1.	5	462	0.168	0.8	0.004	2.381	11.25	0.111
4.1.	12	462	0.244	1.412	0.003	1.260	7.24	0.030
4.2.	15	422	0.141	0.624	0.007	0.287	1.27	0.085
4.2.	6	413	0.196	1.203	0.003	0.231	1.42	0.016
5.1.	7	348	0.106	0.502	0.756	0.421	1.99	0.964
5.2.	9	257	0.073	0.347	0.003	0.157	0.75	0.014
5.2.	19	257	0.173	0.817	0.016	0.318	1.50	0.033
6.1.	10	207	0.201	0.948	0.003	0.176	0.84	0.014
6.1.	11	207	0.091	0.433	0.005	0.246	1.16	0.044

As mentioned above, the change in porosity is as essential as permeability which plays an important role in studying the heat transfer, advancing the front and assessing the possibility of removing formed hydrocarbons from the formation. The change in porosity as a function of the heating temperature is shown in **Figure 127**. The tendency

towards increased porosity with an increase in exposure temperature is obvious from the graphs. The highest temperatures were registered in Zones 3 and 4 and, as a result, a significant change in porosity occurred in the samples located in these CT zones.

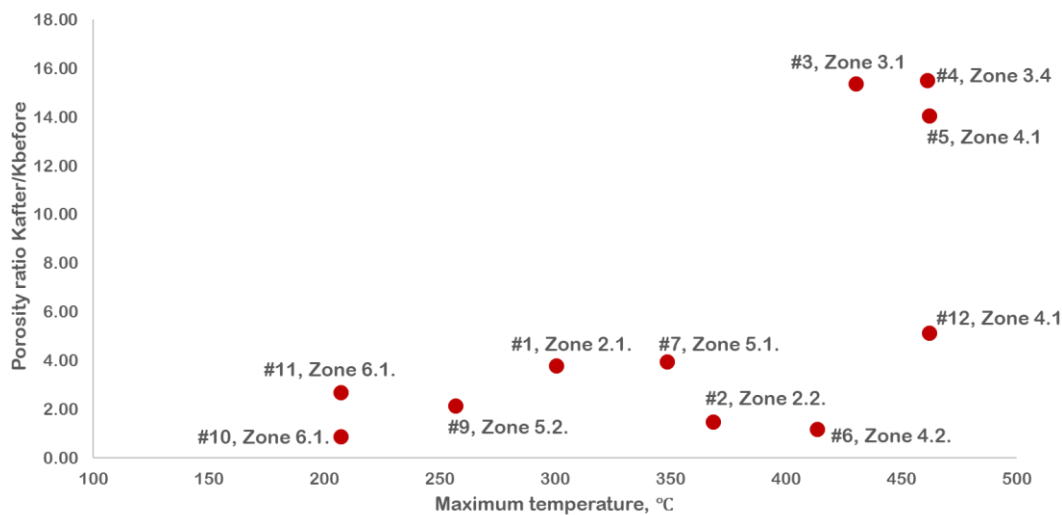


Figure 127. Relationship between maximum temperatures reached at the sample location and increase in porosity (Oil Field 1).

4.6.7 Thermal properties of consolidated core samples from different combustion tube zones

The thermal properties of 16 BF rock samples were measured in parallel and perpendicular to the bedding and the anisotropy coefficient was determined before and after the experiment in order to assess the changes in the rock structure after heating in CT. The measurement results are shown in **Table 53**. The change in the thermal conductivity for the samples studied are visually illustrated on the graph (**Figure 128**). The results show that the thermal conductivity of the samples exposed by the combustion front is significantly altered, primarily by conversion and combustion of organic matter (OM) contained in the sample and filling the volume previously occupied by the OM

with air. At the same time, the graph indicates that the most significant changes occur primarily in thermal conductivity perpendicular to the bedding. It can be said that changes in the core affect both parameters in a similar way. There was no direct relationship between the change in thermal conductivity and the change in porosity. This trend is absent in the presented collection of samples, since all the samples were subjected to high-temperature effects of varying degrees, both at the maximum temperature and in time.

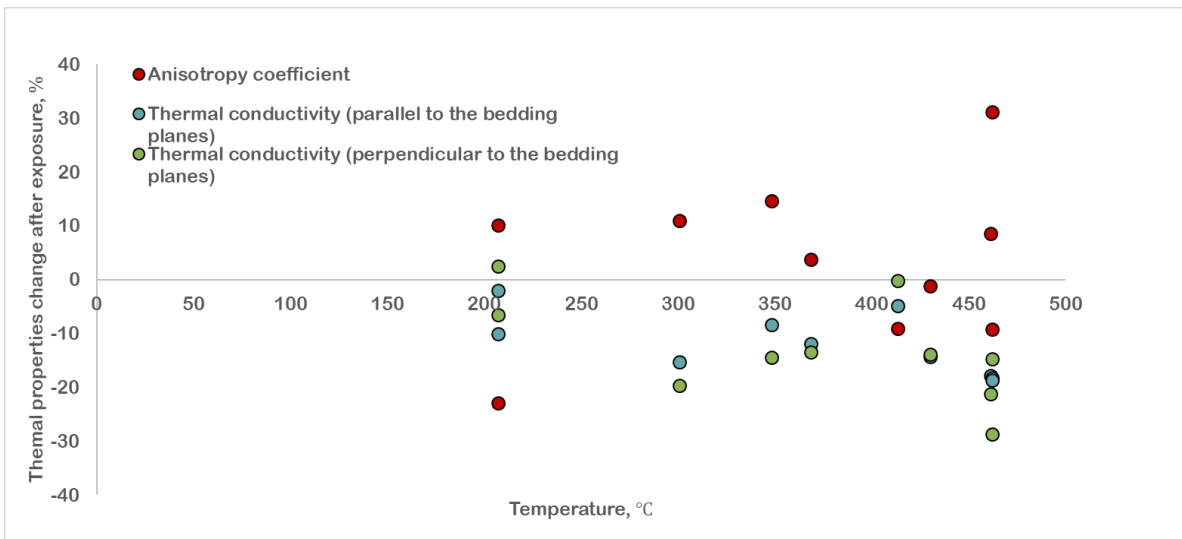


Figure 128. Changes in thermal conductivity and anisotropy coefficient as a result of exposure.

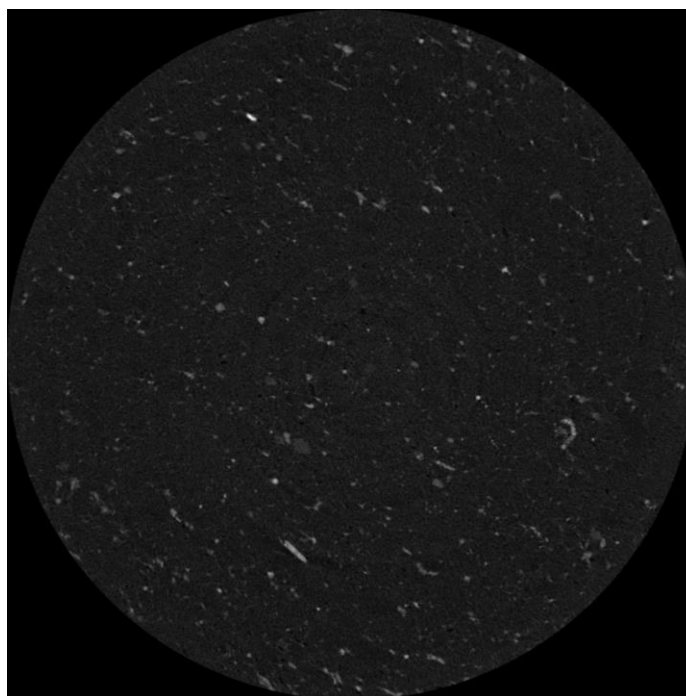
Table 53. Thermal conductivity and anisotropy coefficient data before and after exposure.

CT zone	Sample number	Peak temperature, °C	Before exposure			After exposure		
			Thermal conductivity (parallel to the bedding plane) λ_{\parallel} W/(m·K)	Thermal conductivity (perpendicular to the bedding plane) λ_{\perp} W/(m·K)	Anisotropy coefficient	Thermal conductivity (parallel to the bedding plane) λ_{\parallel} W/(m·K)	Thermal conductivity (perpendicular to the bedding plane) λ_{\perp} W/(m·K)	Anisotropy coefficient
2.1	1	300	2.63	2.44	1.17	2.23	1.96	1.3
2.1	16	300	1.93	1.87	1.07	2.03	1.71	1.42
2.2	13	368	1.55	1.28	1.48	1.1	0.71	2.39
2.2	2	369	2.47	2.42	1.05	2.18	2.09	1.09
3.1	3	430	2.23	2.13	1.1	1.91	1.83	1.09
3.1	18	430	2.02	1.85	1.19	1.92	1.62	1.4
3.4	14	461	1.59	1.36	1.38	1.16	0.84	1.92
3.4	4	461	2.11	1.95	1.17	1.73	1.53	1.27
4.1	5	462	2.09	2.08	1.01	1.7	1.48	1.32
4.1	12	462	2.37	2.29	1.08	1.93	1.95	0.98
4.2	15	422	2.27	2.11	1.16	2.14	1.82	1.37
4.2	6	413	2.38	2.28	1.09	2.27	2.28	0.99
5.1	7	348	2.23	2.17	1.05	2.04	1.86	1.2
5.2	19	257	2.18	1.97	1.23	2.19	2.01	1.19
6.1	10	207	2.45	2.16	1.29	2.21	2.21	1
6.1	11	207	1.88	1.68	1.25	1.84	1.57	1.37

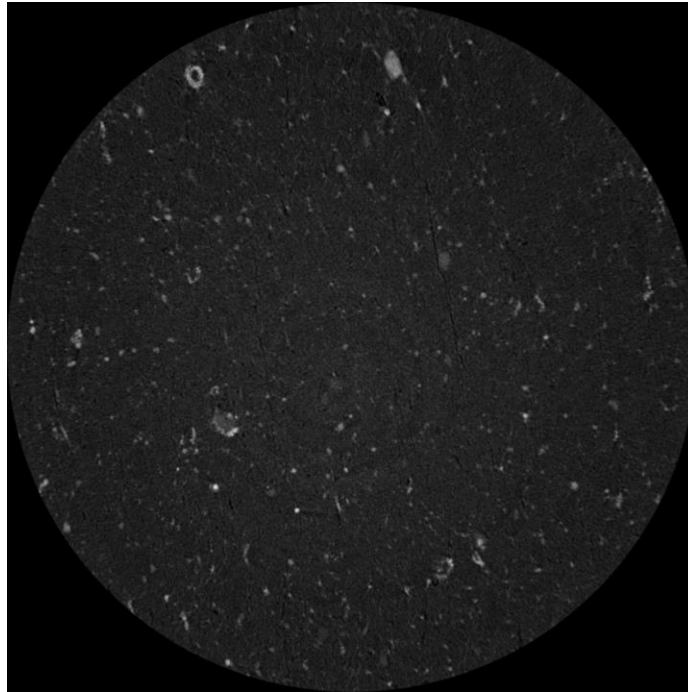
4.6.8 Microtomography of samples from different combustion tube zones

Table 54. Microtomography results

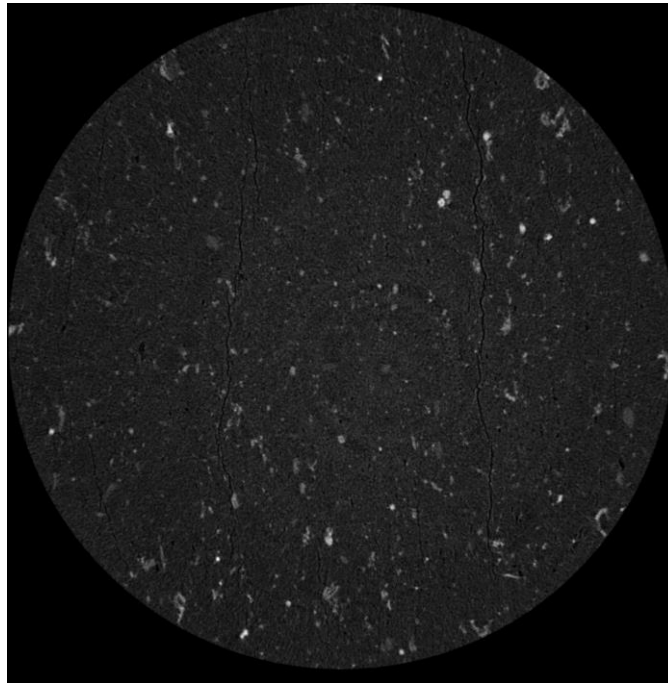
Initial porosity		Max. porosity (after)		Min. porosity (after)	
Total	Open	Total	Open	Total	Open
1.253	0.026	2.589	0.182	1.171	0.052



a. Before exposure



b. 319°C



c. 460°C

Figure 129. Microtomography results (samples from different zones).

It is evident from the above that cracking and porosity increase with temperature.

4.7. Conclusions

A unique laboratory experiment was carried out to test air injection into a heterogeneous core-pack model that consisted of a crushed core and consolidated core samples distributed along the combustion tube. As a result of the experiment, the parameters required for numerical simulation, such as temperature profiles and gas compositions, were obtained. These data were used to simulate the combustion tube experiment and adapt the chemical reaction model that was used for full-field model simulation (*Khakimova et al., 2017; Bondarenko et al., 2017a*).

With additional heating of the first zones of the combustion tube up to 200°C, the oil combustion process was initiated rapidly, and stable propagation of the combustion front was observed. The maximum temperature attained as a result of the exothermic combustion reaction was 463°C. Note that heat losses in the combustion tube caused a decrease in temperature.

As a result of the combustion front propagation, the total residual oil saturation by the bulk model was 2%. The minimum residual oil saturation corresponds to the zones swept by the combustion front and equals 0%; the maximum oil saturation characterizes the zone ahead of the combustion front and is equal to 11.1%.

Rock-Eval pyrolysis method was used for understanding the kerogen conversion mechanisms during air injection at a different distance from the combustion front. The results revealed the conversion of kerogen ahead of the combustion front. A new useful technique, 2D-pyrolysis, was applied to estimate kerogen conversion occurring inside the consolidated samples as a result of the combustion front propagation. The results

revealed a homogeneous distribution of geochemical parameters along the core and showed that kerogen was decomposed and oxidized (decrease in S₄CO₂ parameter).

Consolidated core micro-fracturing increased with the temperature of exposure. The increase in the samples' permeability is directly proportional to mass loss and influenced by both the temperature and the time of thermal exposure; the maximum permeability obtained was 5.8 mD. Porosity was found to increase with exposure temperature, and the maximum porosity registered was around 32%. These data are consistent with the permeability and porosity measurements of the core samples drilled from the heated zone in ICP field pilot (*Kibodeaux, 2014*).

The high-temperature combustion front velocity was much slower than in typical light or heavy oil combustion tube tests, which confirms the complex oxidation behavior of the oil shale and higher air requirements. The measured compositions of produced gas and the properties of produced oil can serve as benchmarks for monitoring field operations.

Chapter 5. An integrated approach to developing a HPAI kinetic model for the oil shale

This Chapter discusses the important aspects of developing a high-pressure air injection kinetic model for the oil shale. According to the complex oxidation behavior of kerogen, a number of pseudo-components are proposed.

5.1. Aspects of an air injection kinetic model development

First of all, the purpose of constructing a field-scale air injection simulation model is to predict the processes that occur *in situ* and to select the right air injection regime for oil production maximization. Running the simulation helps oil companies to test different scenarios and design the field pilot.

Gutierrez et al., (2011) define a kinetic model as “a heart and soul of a good *in situ* combustion model”. The authors give guidance on how to build a kinetic model and offer a review of relevant works. The kinetic model comprises a set of chemical reactions and corresponding kinetic parameters and simulates the oxidation behavior of the components. It should be pointed out that a badly tuned kinetic model would cause poor predictability of a simulation model, or, in other words, it won't be able to capture different temperature regions, model the transition between oxidation modes and predict the conditions leading to ineffective displacement and mobilizing oil.

Another aspect is a choice of laboratory experiments, based on which the kinetic model is developed and tuned. Laboratory tests must model the relevant oxidation behaviors. For example, low-temperature oxidation (LTO) reactions must be developed

based on the test that simulates conditions, where LTO reactions are dominant. A good example of such an experiment would be a ramped temperature oxidation test, where slow heating takes place from room temperature in air purge. Combustion tube tests, in turn, are designed to operate in the effective oxidation mode and can be used to tune high-temperature oxidation (HTO) reactions.

The first step in the kinetic model development is choosing pseudo-components and chemical reactions. Then quantitative kinetic studies, such as TGA, DSC, and other thermal analysis techniques, are conducted to determine an initial guess for kinetic parameters of the selected reactions for further iterative history matching process using a thermal simulator.

High-pressure ramped temperature oxidation tests are usually history-matched to back-calculate the kinetic parameters (*Sequera et al., 2010; Dechelette et al., 2006*). History matching of combustion tube tests is performed to validate the developed kinetic model. However, further validation is needed even after a good match has been found.

5.2. Complex nature of oil shale and oxygen and pyrolysis behavior of its components

As was stated before, constructing a kinetic model is one of the most important and difficult steps in the air injection numerical simulation process. This is especially true for oil shales, because the model must predict the oxidation and pyrolysis behavior of oil and solid kerogen. In order to do that, the kinetic model should be validated against the experiments that represent a complex oxidation and pyrolysis behavior of the components in a hybrid system, such as the oil shale.

First of all, let us list the oil shale components that should be considered in this process. **Figure 28** in Chapter 3 illustrates the complexity of the Bazhenov Formation system in microscale (*Manuilova et al., 2017*). Free oil, adsorbed oil, resins and asphaltenes, and kerogen form the hybrid system.

In order to compare the oxidation behavior of these components separately and together, DSC curves were plotted in the same graph. **Figure 130** shows two DSC curves obtained in this work, namely DSC curve of an oil shale sample saturated with oil and DSC curve of its isolated kerogen in air environment. Both curves comprise three peaks. Many researchers have shown that DSC curves of different oils contain two peaks. The difference in the peaks lies in the nature of oil. For light oils, the first peak is higher because high-temperature oxidation (HTO) reactions are dominant in the low-temperature range (LTR). For heavy oils, the second peak is higher due to the dominance of HTO reactions in the high-temperature range (HTR) (*Li et al., 2006*). It should be noted that three peaks were observed in both DSC curves, which means that the source of that third peak might be related to kerogen oxidation. To facilitate further description, DSC curves were divided into three temperature ranges, namely: LTR (up to 300°C), HTR1 (300-450°C), and HTR2 (from 450°C). Those ranges were chosen based on the heat output peaks and temperature ranges of kerogen pyrolysis. **Figure 131** illustrates DSC curves of samples with a different grade of maturity, namely: PC₃ and MC₁₋₂. Kerogen is known to consist of two parts: generative organic carbon (GOC) and non-generative organic carbon (NGOC). As the maturity increases, GOC decreases and NGOC increases. *Bogdanovich et al. (2017)* present Rock-Eval open-system pyrolysis

pyrograms of non-extracted and extracted Bazhenov oil shale samples, where the delay in oxidation of NGOC was detected in the non-extracted sample, which can be explained by the fact that the NGOC part oxidized after the GOC pyrolysis. So one can speculate that the third peak can correspond to NGOC combustion. GOC will be pyrolyzed within LTR and generated coke and oil will burn within HTR1 (second peak).

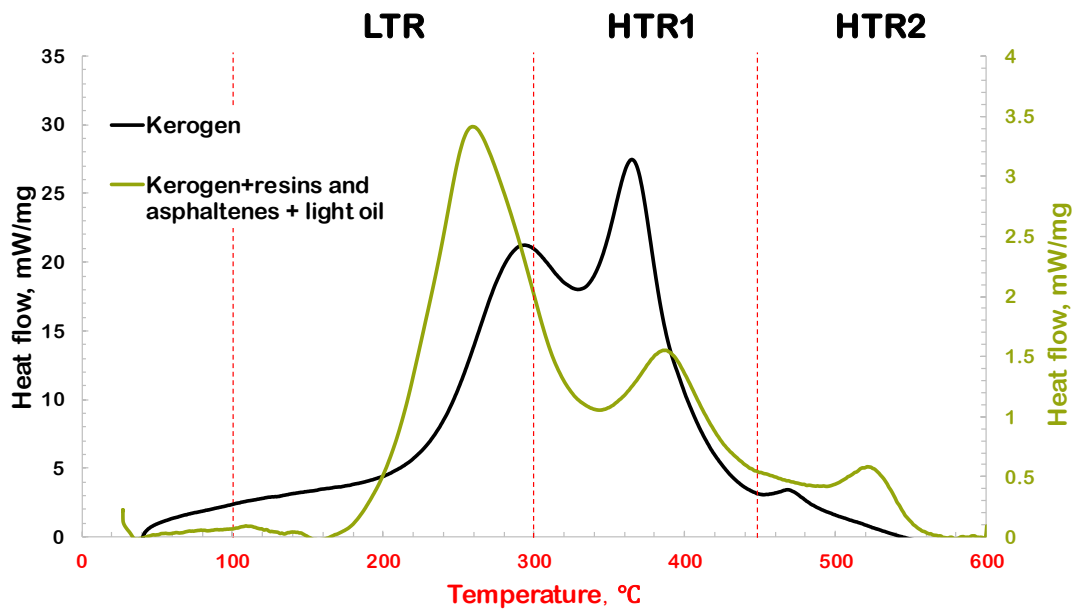


Figure 130. Comparison of two DSC curves of isolated kerogen and oil shale sample saturated with oil.

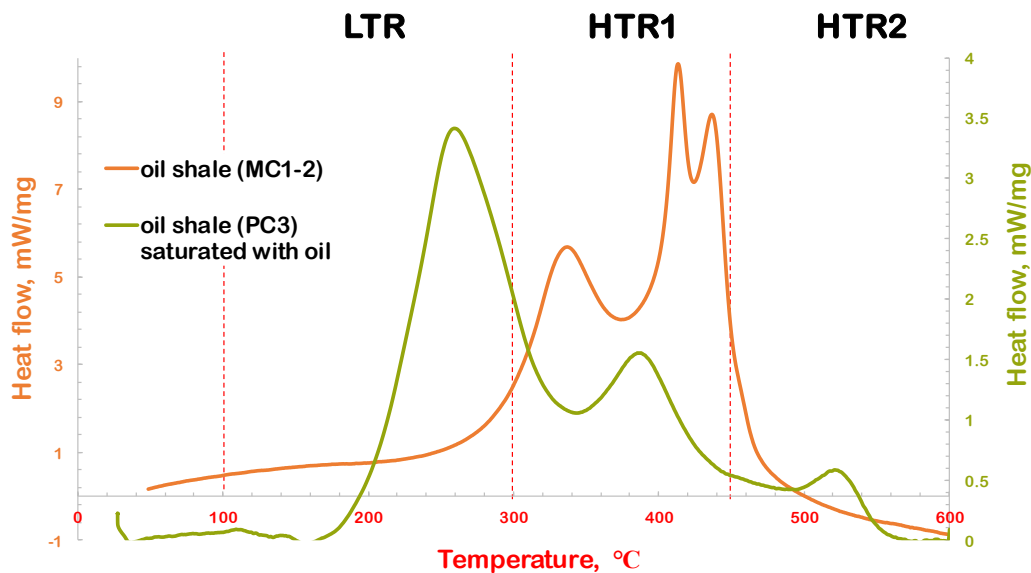


Figure 131. Comparison of two DSC curves of oil shale samples with different degrees of maturity.

It can be concluded from **Figure 131** that the higher the content of non-generative organic (NGOC) in the sample, the higher the heat output during the third DSC peak. Moreover, the third peak is shifted to the left or, in other words, NGOC burns earlier at lower temperatures. A possible reason is the complex nature of oxygen consumption and the complex structure of kerogen. At first, GOC part and its pyrolysis products will be pyrolyzed and oxidized, and then NGOC part will be opened to oxidation.

5.3. Choice of pseudo-components and schematic representation of the reactions

While proposing pseudo-components, one must keep in mind that the calculation time in numerical simulation increases whenever new components are added. Therefore, it is essential to find the optimal number that can truly represent the oxidation and pyrolysis behavior of the oil shale.

Using RTO experiment data described in Section 3.4.6, a set of kerogen pseudo-components was proposed. RTO study was performed using a non-extracted oil shale sample without pre-saturation with oil, which means that kerogen pseudo-components can be tested against this experiment.

It is important to reflect the complex structure of kerogen that can be represented by more than one component. Pseudo-components must help to describe the oxidation and pyrolysis behavior of kerogen parts, namely: non-generative organic carbon (NGOC) and generative organic carbon (GOC). **KER_COKE** pseudo-component can represent NGOC and can be involved in the oxidation process only. GOC can be pyrolyzed and oxidized, that is why two other components can be chosen to represent this part of kerogen. **Kerogen_solid1** will react with oxygen and **Kerogen_solid2** will thermally decompose.

All these processes are illustrated in **Figure 132**. Grey lettering means that although the reactions were not described in the model, they are important for process description and further research. For example, low-temperature oxidation or oxygen addition reactions were omitted, which is admittedly a weak spot in the model. This was done for simplification only. Two sets of experiments, such as PDSC and RTO, are not enough to qualitatively and quantitatively study all the processes and answer all the questions that arise in abundance. Another missing component in this model is hydrocarbon gases that should also be taken into account in the pyrolysis description.

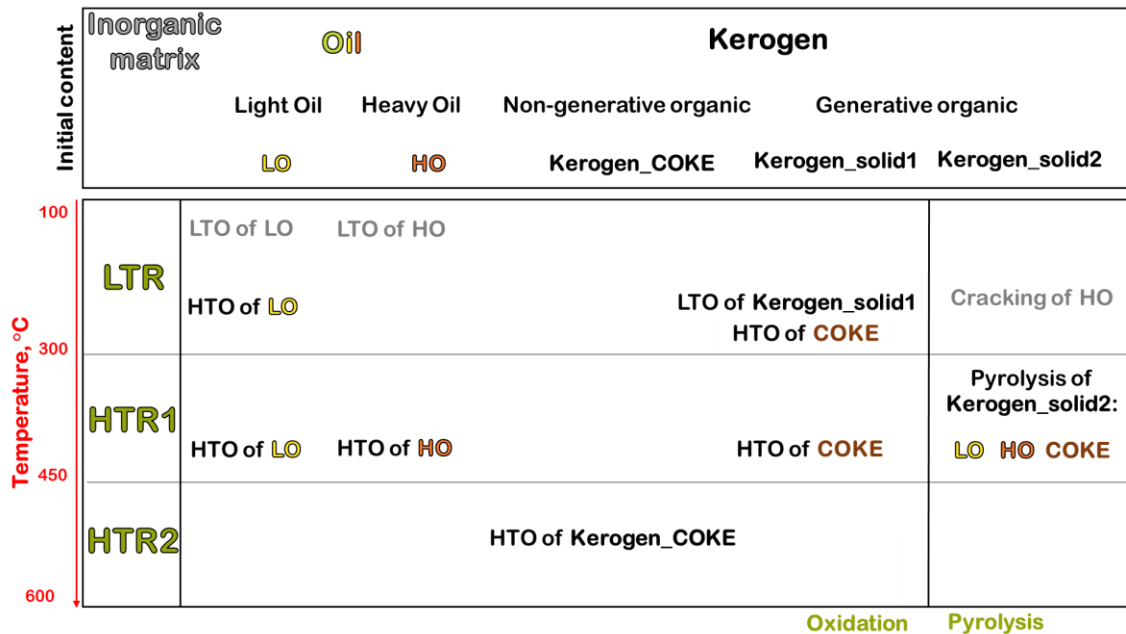


Figure 132. Schematic model of oxidation and thermal decomposition processes during HPAI (modified from *Khakimova et al. (2018)*).

The heavy oil cracking reaction and oxygen-addition reaction or the low-temperature oxidation (LTO) reaction were not added because of the small content of heavy fractions in Bazhenov free oil. Resins and asphaltenes were covered by the GOC part of kerogen. Light oil oxygen-addition reactions were not included either, but they should be taken into account in further research.

5.4. Results of history matching of conducted experiments and proposed kinetic model

The model was built using CMG STARSTTM thermal simulator. An integrated approach to building such a model with a complete description of the history matching procedure was presented in the work of *Khakimova et al. (2018)*.

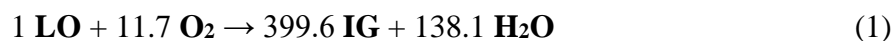
Table 55 presents the selected pseudo-components of Bazhenov oil.

Table 55. Pseudo-components of the original oil (Khakimova et al., 2018).

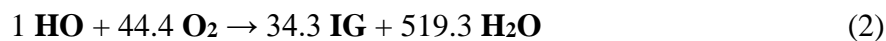
Pseudo-component	LO	HO
Description	Light oil	Heavy oil
Composition	C ₅ -C ₁₁	C ₁₂₊
Molecular weight, g/mol	132	500
Mole fraction	0.98	0.02

A modified model of *Smith et al. (1973)* was used to represent oil oxidation (IG represents CO and CO₂ with 20/80).

Bond-scission reaction for Light Oil in LTR:



Bond-scission reaction for Heavy Oil in HTR:



The model was tested using oxygen consumption data. The simulation result is presented in **Figure 133**. Kerogen was represented as a solid and impermeable component of complex nature that converts through pyrolysis. (**Table 56**).

Table 56. Pseudo-components of kerogen (Khakimova et al., 2018).

Pseudo-component	Kerogen_COKE	Kerogen_solid1	Kerogen_solid2
Description	Non-generative organic carbon	Generative organic carbon	
Mass fraction	0.05	0.45	0.4

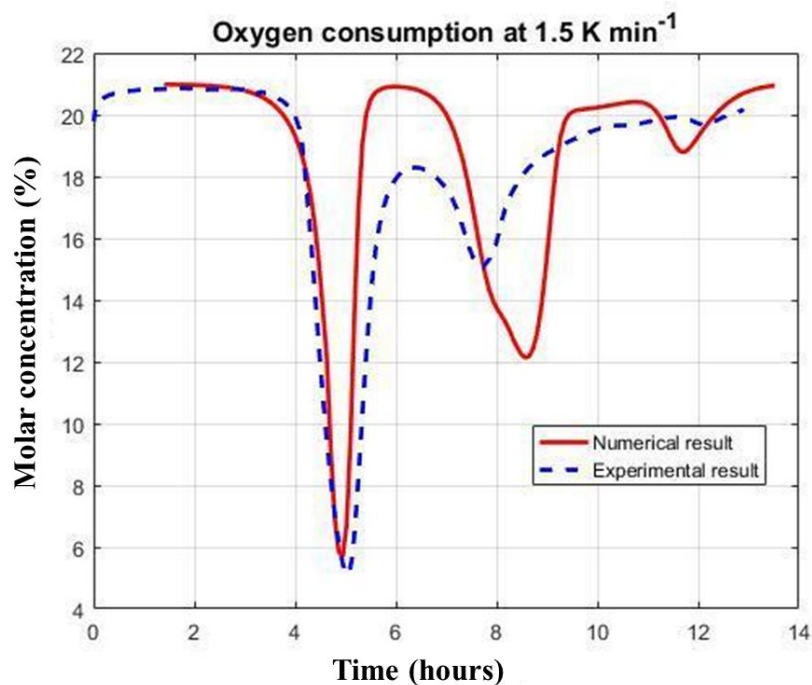
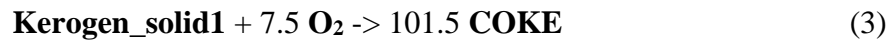


Figure 133. Experimental and numerical oxygen uptake in RTO test (*Khakimova et al., 2018*)

Kerogen_solid1 and **Kerogen_solid2** were represented by an asphaltene-like material, so that the open-source reactions model could be used (*Belgrave et al., 1990*). For simplicity, synthetic oil composition was assumed to be the same as in the original Bazhenov shale oil, which means that the same pseudo-components were used in all the reactions. As a result, the following model of chemical reactions was proposed:

Oxidation of generative organic part of Kerogen in LTR:



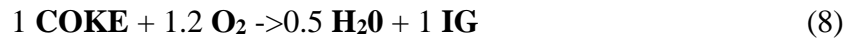
Pyrolysis of generative organic part of Kerogen:



Oxidation of non-generative organic part of Kerogen in HTR:



Oxidation of Coke:



The proposed model is a combination of two sets of reactions described previously. Their temperature intervals are illustrated in **Figure 134**.

In this reactions model, the kinetic parameters were tuned by applying history matching to PDSC experiment described in detail in Chapter 3 (3.3.1). The results are illustrated in **Figure 123** and the corresponding kinetic parameters are listed in **Table 57**.

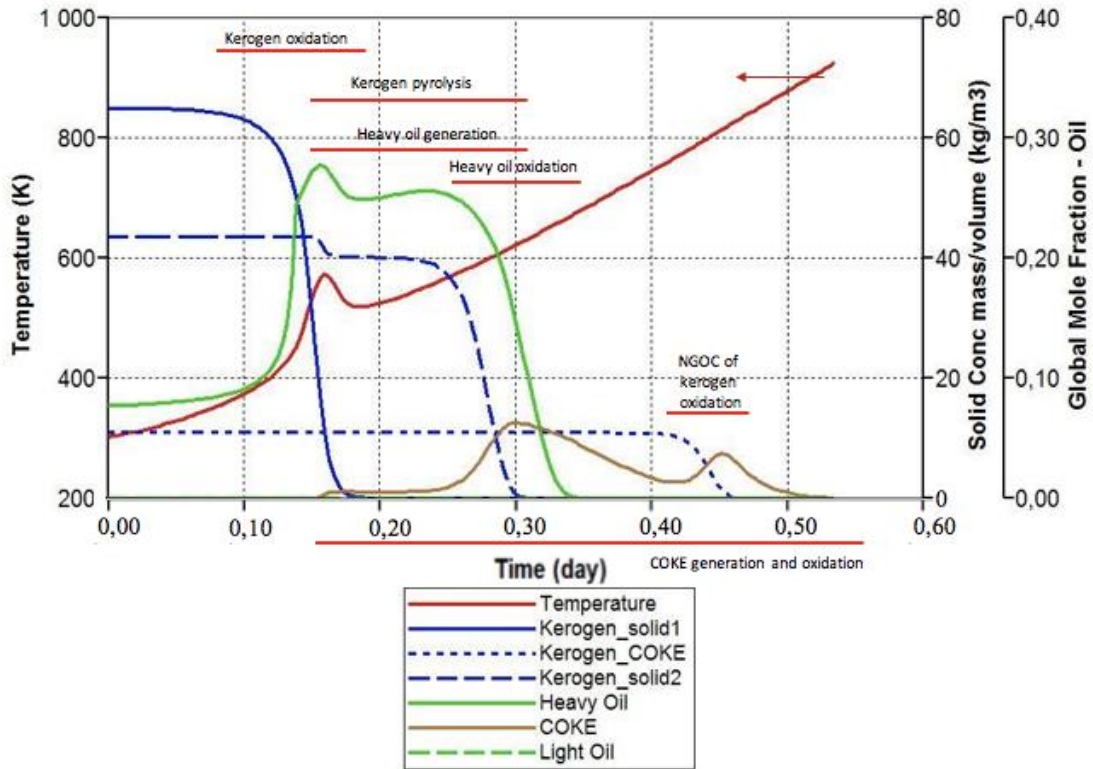


Figure 134. Kerogen and coke components conversion representation (*Khakimova et al., 2018*).

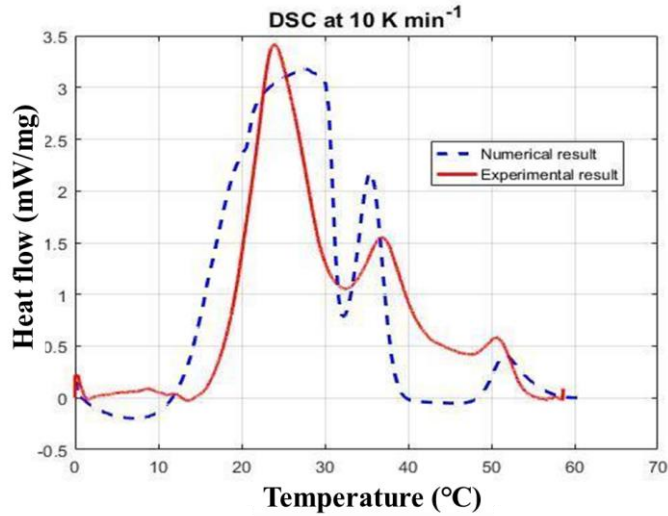


Figure 135. Experimental and numerical results of PDSC test (*Khakimova et al., 2018*).

Table 57. Kinetic data for proposed chemical reaction model (Khakimova et al., 2018).

№	Reaction	A, s⁻¹	E_a (J/mol)	H_r (J/mol)
1	Bond-scission reaction for Light Oil in LTR	8.1*10 ⁷	7.7*10 ⁴	3*10 ⁶
2	Bond-scission reaction for Heavy Oil in HTR	5*10 ¹⁴	1.8*10 ⁴	3*10 ⁷
3	Oxidation of generative organic part of Kerogen in LTR	8.1*10 ⁴	5*10 ⁴	4.3*10 ⁵
4	Pyrolysis of generative organic part of Kerogen	9*10 ²¹	2.3*10 ⁵	0
5	Pyrolysis of generative organic part of Kerogen	9*10 ²¹	2.3*10 ⁵	0
6	Pyrolysis of generative organic part of Kerogen	9*10 ²¹	2.3*10 ⁵	0
7	Oxidation of non-generative organic part of Kerogen in HTR	1*10 ²⁷	4.2*10 ⁵	8.3*10 ⁶

5.5. Recommendations for multistage development and validation of HPAI kinetic model for oil shales

In this work, all the experiments were conducted using Bazhenov oil shale samples, which means that the model should be used with caution for any other oil shales. This model should be tuned by history matching of HPRTO experiments and validated by CT tests. The detailed approach is presented in **Figure 136**. It is proposed to develop-and validate the kinetic model in three main stages.

The first stage is devoted to determining the starting kinetic parameters or, in other words, making the first guess regarding further iterative tuning and validation process. However, it should be noted that even this stage requires a substantial laboratory work. As was stated in the recommended laboratory plan (Chapter 3, Section 3.1), the kinetic studies must be conducted on different fractions of the complex oil shale system

in order to characterize the oxidation behavior of light oil, resins and asphaltenes, and GOC and NGOC parts of kerogen. This Chapter gives a partial description of this stage in the understanding that further oil fractionation is needed.

The second stage consists of history matching of high-pressure ramped temperature oxidation and cracking experiments. The stage starts with identical experiments at three different air fluxes to determine the optimal one in terms of oil generation and production. In comparison with HPRTO tests conducted in this work, the listed tests should be conducted on extracted oil shale samples to eliminate the effect of resins and asphaltenes, to tune the kinetic parameters of GOC and NGOC burning, and to enhance the understanding of the kerogen oxidation behavior. The high-pressure ramped temperature cracking (HPRTC) test at optimal nitrogen (inert gas) flux will help to tune GOC pyrolysis reactions. The goal is to make the process effective and maximize oil generation and production. However, to attain the goal, one must overcome some obvious obstacles, the low mobility of the pyrolysis products, such as pyrobitumen or heavy oil, being the biggest one. Kerogen thermally decomposes into gases and pyrobitumen, with a portion of pyrobitumen oxidized. Pyrobitumen, or heavy oil (HO), is characterized by low mobility, resulting in low recovery of pyrolysis products and lower effectiveness of the air injection method. Therefore, it is crucial to find the optimal air flux to decrease fuel requirements for the process.

Once the experiments with extracted oil shale samples are complete, components of the hybrid system must be added sequentially. Oxidation of resins and asphaltenes will be tested through HPRTO experiment with non-extracted oil shale samples. Light oil

oxidation, in turn, will be tested in HPRTO test where the core model is prepared by oil and core premixing. The kinetic parameters of the proposed reactions will then be back-calculated by applying history matching to these experiments.

The third stage purports to validate the developed model against CT tests. History matching of the wet combustion tube test would help to develop the hydrolysis reaction.

A PDSC study of NGOC part of kerogen must be added to the described approach in order to evaluate the effect of NGOC value on the oxidation behavior (shape of PDSC curves and heat effects). This effect should be studied by coupling the PDSC study with Rock-Eval pyrolysis method.

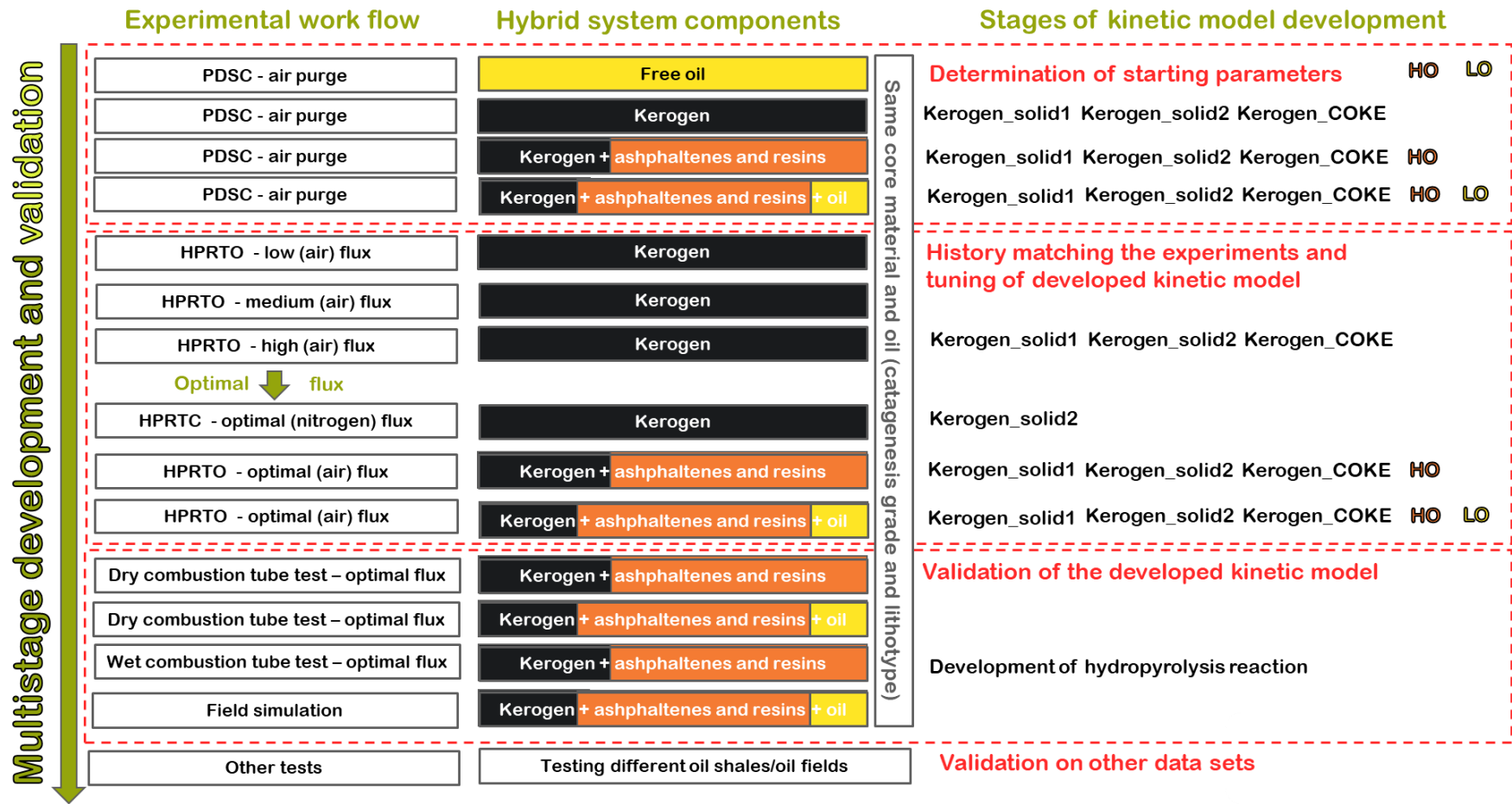


Figure 136. Proposed schematics of multistage development and validation of HPAI kinetic model for oil shale.

5.6. Conclusions

A minimal set of pseudo-components was proposed by analyzing the laboratory data obtained, and the history matching over kinetics studies described in Chapter 3, namely: pressurized differential scanning calorimetry (PDSC) and ramped temperature oxidation (RTO) experiments. A kinetic model of high-pressure air injection (HPAI) for oil shales was proposed, along with a detailed multistage development and validation procedure subject to further investigation. In the kinetic model, kerogen was described by three pseudo-components that reflect the oxidation and pyrolysis behavior.

Chapter 6. Summary, conclusions and recommendations

6.1. Summary

In this work, an integrated approach was used to study the high-pressure air injection in oil shales, during which oxidation, pyrolysis and hydrolysis of oil and organic matter coexist. These processes should be investigated separately and jointly in order to understand the mechanisms of synthetic oil generation and displacement during high-pressure air injection in oil shales.

As a result of this study, a schematic of high-pressure air injection process, specifically in oil shales, was constructed, showing the temperature profile, kerogen conversion and various zones in the reservoir (**Figure 137**). Note that this schematic chart is not drawn to scale. After conducting series of experiments, the pseudo-components were proposed for numerical simulation and were arranged according to the reaction temperature intervals (**Figure 132**).

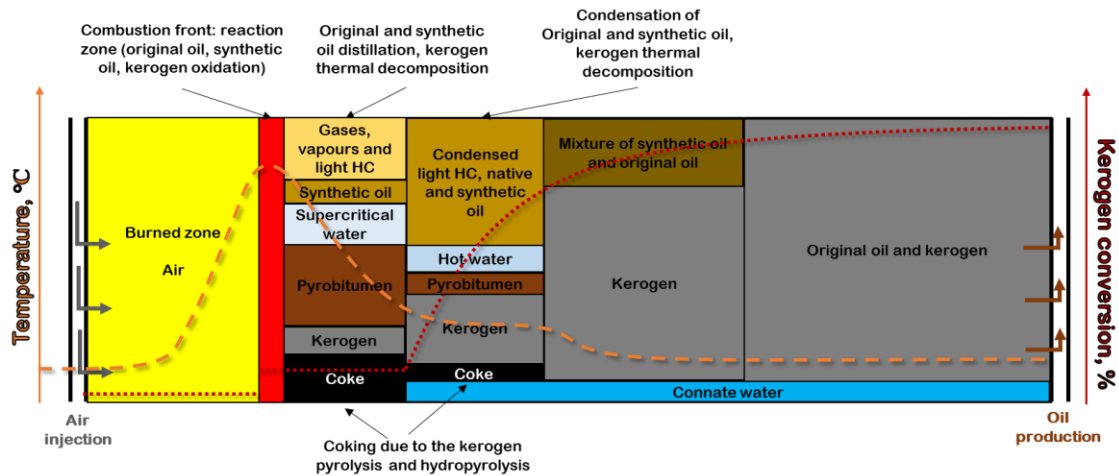


Figure 137. Schematics of high-pressure air injection in the oil shale (modified from John Belgrave Skoltech Thermal EOR lecture notes, 2016)

The shale oil oxidation process differs from light and heavy oils oxidation in fuel lay-down and complex nature of kerogen. In the case of light and heavy oils, low-temperature oxidation reactions play an important role in fuel generation, whereas oil shales have an extra component, i.e. the non-generative part of kerogen, that causes combustion at high temperatures and generation of a significant amount of carbon dioxide. On the other hand, the generated water which might be in supercritical state will react with kerogen and extract the generated oil ahead of the combustion front. It was shown in this study that supercritical water can serve as a good extractor.

The results of this study evaluated the effectiveness of the promising enhanced oil recovery method that is used for different types of reservoirs. Unique and specialized laboratory experiments eliminated the gaps associated with limited knowledge of the oxidation process in oil shales and made a significant step forward in the Bazhenov Formation development.

This study demonstrated the advantages and risks associated with air injection in oil shales, underscoring the need for a thorough investigation of the proper injection regimes and oxidation modes. There are several approaches to implementing air injection in the Bazhenov Formation. The first approach used by RITEK oil company involves air injection into the relatively permeable layer and initiating exothermic reactions which can heat the overburden kerogen-rich layer. However, the lab tests indicate that there is a risk of heating the overburden kerogen in the presence of air without extracting the generated synthetic oil, which leads to coking of the formation. That is why displacement techniques must be investigated in future. One can use another approach which involves cyclic air injection that will lead to the production of generated synthetic oil before coking occurs. However, this method might be potentially hazardous due to the uncertainty of the end of oxidation reactions in oil shales and, as a consequence, the risk of explosion. The high air requirements that transpired in this research can be optimized by implementing cyclic wet combustion, which will help to extract the generated oil, use the heat of combustion for generating supercritical water *in situ* and, as a result, heat the formation at a bigger distance from the well. Water injection may also quench the oxidation reactions before production starts.

The work performed and the results obtained in this study are summarized below:

- The potential of high-pressure air injection for generating synthetic oil in oil shales based on the Bazhenov Formation was evaluated by assessing kerogen conversion degree and hydrocarbon yields during three coexisting processes, such as oxidation, pyrolysis, and hydropyrolysis. The oxidation of crushed core

samples enabled recovering 23.7 wt% of organic matter that can be pyrolyzed into hydrocarbons, versus 79.6 wt% for pyrolysis. Treating the consolidated samples by hydrolysis resulted in a 31 wt% recovery which can be higher if the treatment time is shortened and the generated hydrocarbons are forced from the sample by pressure-down.

- A new experimental methodology for testing HPAI in oil shales was designed and tested. It is based on the investigation of kerogen thermal decomposition, oxidation and hydrolysis processes that coexist during air injection in the oil shale.
- Benchmarks for monitoring future field operations, such as produced gas composition and produced oil properties, were provided for HPAI application and for three separate processes: pyrolysis, oxidation, and hydrolysis.
- Valuable data were obtained for the numerical simulation of high-pressure air injection field project in oil shales, such as chemical reactions and their kinetics, peak temperatures, rock properties changes with temperature, gas and synthetic oil compositions. The experimental data obtained were used to predict the potential of the field project.
- Recommendations were made on how to move on to the oil production field pilot using high-pressure air injection in oil shales. Cyclic wet combustion was proposed for optimizing the coking process and synthetic oil extraction and lowering the air requirements.

6.2. Conclusions

- Air injection caused *in situ* synthetic oil generation from oil shales. Oxidation of crushed oil shale samples resulted in 23.7 wt% recovery of organic matter that can be pyrolyzed into hydrocarbons, while pyrolysis resulted in 79.6 wt% recovery. Synthetic oil generation occurred in the temperature range of 300 - 500°C. It is necessary to design the optimal air flux and oxidation mode for maximization of synthetic oil recovery.
- Hydropyrolysis treatment of consolidated oil shale samples caused 31 wt% recovery, which might be higher if the time of treatment is decreased and generated hydrocarbons are forced from the sample by draw-down. Oil generation window from crushed samples was at a temperature range of 400°C and 480°C. Coke-like material stayed at the sample's surface. Due to the low permeability, part of the generated synthetic oil was coked in the consolidated samples. Higher aromatics content in the oil sample from hydropyrolysis treatment indicated that supercritical water does not only act as an extraction solvent but also reacts with the oil shale kerogen.
- Three oxidation regions were identified, while high-temperature oxidation reactions are dominant in low-temperature range. The non-generative organic part of kerogen is an extra fuel for the stable combustion process. The self-ignition potential at reservoir conditions was justified.
- Oxidation of oil shale hybrid system showed light oil oxidation behavior by rapid ignition after preheating up to 200°C and then showed heavy oil oxidation

behavior with a peak combustion temperature of 463°C. High-temperature combustion front velocity was much slower than in typical light or heavy oil combustion tube tests, which showed the complex oxidation behavior of oil shale and higher air requirements.

- The conversion of kerogen ahead of the combustion front was revealed. The new 2D-pyrolysis technique showed the combustion front propagation through consolidated samples.
- Modification of reservoir properties and an increase of the contact area with the reservoir were revealed. Conversion of organic matter due to thermal decomposition and oxidation caused an increase in void space, while fracturing occurred through voids formed due to kerogen oxidation. Due to the combustion front propagation, maximum permeability of 5.8 mD was reached. Porosity increased with increasing of exposure temperature. Maximum porosity of 32% was reached.
- Kerogen can be described by three pseudo-components for the air injection kinetic model in terms of generative and non-generative organic parts. A grade of catagenesis might play an important role in the oxidation of organic matter.

6.3. Contributions to Knowledge

New experimental methodology for testing HPAI in oil shales based on an investigation of kerogen thermal decomposition, oxidation and hydrolysis processes that coexist during air injection in oil shale was designed. Synthetic oil and gas yields as a result of oxidation, pyrolysis, and hydrolysis were obtained. Benchmarks for

monitoring future field operations, such as produced gas composition and produced oil properties were determined for air injection application and for three processes separately: pyrolysis, oxidation, and hydrolysis. Valuable data for numerical simulation of high-pressure air injection field project in oil shales were obtained, i.e., chemical reactions and their kinetics, peak temperatures, rock properties changes with temperature, gas and synthetic oil compositions. A minimal set of pseudo-components that reflect oxidation and pyrolysis behavior of oil shale was proposed and organized in terms of temperature intervals of reactions. Mechanisms of the air injection process, specifically in oil shales, were proposed, where the temperature profile, kerogen conversion and various zones in the reservoir are marked.

6.4. Recommendations

This research has thrown up many questions in need to further investigation:

- A natural progression of this work is to follow the recommended laboratory plan, described in Chapter 3 (Section 3.1), on the samples from one oil field of interest. It will help to fill the gaps in our understanding of mechanisms of air injection in oil shales and to test this methodology on another object.
- In this work, HPRTO test was conducted at high air flux and showed a high content of hydrocarbons burnt. Therefore, considerably more work will need to be done to determine an optimal regime for oxidation of oil shale for maximization of the synthetic oil generation and recovery. A number of possible future studies using the same experimental set-up are apparent. At least three high-pressure ramped temperature oxidation tests at different air fluxes are strongly

recommended. We need to find the balance between the coking process and displacement of generated synthetic fluids to minimize hydrocarbons burnt. The precise mechanism of kerogen oxidation remains to be elucidated. Therefore, listed experiments need to be carried out on extracted crushed oil shale samples to eliminate the effect of resins and asphaltenes on the oxidation process.

- Combustion tube test conducted in this work was performed on heterogeneous core pack at 8 MPa, which is lower than reservoir pressure. The next step would be to run a combustion tube test with homogeneous crushed core pack at reservoir conditions. It will provide relevant combustion parameters. Wet combustion tube run will help to test the possible increase of combustion front velocity. Other types of physical simulation might also help to evaluate the efficiency of wet combustion.
- More research is needed to evaluate the feasibility of ignition in low permeable oil shales. Combustion tube run or another type of physical simulation tests with an artificial fracture in a consolidated core model will test the ability of oil shale ignition after the multi-stage hydraulic fracturing performed.
- The multistage validation process is essential for improving the proposed air injection kinetic model for oil shales. The detailed approach is presented in Chapter 5 (Section 5.5) and consists of three main stages, i.e., the determination of starting kinetic parameters using PDSC tests; history matching of HPRTO/HPRTC experiments and tuning of the developed kinetic model, and validation of it through history matching of combustion tube tests. Each stage

involves a set of experiments, where components of the hybrid oil shale system, such as kerogen, resins/asphaltenes, and light oil, must be added sequentially. Kerogen oxidation should be investigated on extracted core pack. Resins and asphaltenes oxidation might be tested through HPRTTO experiment on non-extracted oil shale samples. Light oil oxidation, in turn, might be tested in HPRTTO test where the core pack is prepared using oil and core premixing. Addition of low-temperature oxidation reactions of light oil and heavy oil components in the low-temperature range is needed. In addition, hydrocarbon gases pseudo-component is an essential part of the model and must be added.

- Further research is needed to examine more closely the links between catagenesis grade and oxidation mechanism. In this research, it was shown that the higher content of non-generative organic carbon (NGOC) in the sample, the higher the heat output during the third DSC peak. Moreover, NGOC burning occurred earlier at lower temperatures. Therefore PDSC study on oil shale samples of different catagenesis grade is essential to establish the difference in the oxidation mechanism of different oil shales.
- Future research should assess the impact of compaction and coking on the permeability of oil shale.

References

- Abdurrahman, M., 2016. Using oil shale as alternative raw material for energy production and potentiality of Turkey. *Energy policy Turkey* 104–115.
- Akin, S., Kok, M. V., Bagci, S., Karacan, O., 2000. Oxidation of heavy oil and their SARA fractions: its role in modeling *in situ* combustion. *Proc. - SPE Annu. Tech. Conf. Exhib. SIGMA*, 757–768. <https://doi.org/10.2523/63230-MS>.
- Alexander, J.D., 1962. Factors Affecting Fuel Availability and Composition During In Situ Combustion, in: *SPE Production Research Symposium*. Tulsa, Oklahoma, USA.
- Alfarge, D., Wei, M., Bai, B., 2017. IOR Methods in Unconventional Reservoirs of North America: Comprehensive Review. *SPE West. Reg. Meet.* <https://doi.org/10.2118/185640-MS>.
- Allix, P., Burnham, A., Fowler, T., Herron, M., 2010. Coaxing Oil from Shale. *Oilf. Rev.* 22, 4–15.
- Barzin, Y., Moore, R.G., Mehta, S.A., Ursenbach, M.G., Tabasinejad, F., 2010. Impact of Distillation on the Combustion Kinetics of High Pressure Air Injection (HPAI).
- Behar, F., Beaumont, V., De, H.L., Pentead, B., 2001. Rock-Eval 6 Technology: Performances and Developments. *Oil Gas Sci. Technol. – Rev. IFP* 56, 111–134. <https://doi.org/10.2516/ogst:2001013>.
- Behar, F., Roy, S., Jarvie, D., 2010. Artificial maturation of a Type I kerogen in closed system: Mass balance and kinetic modelling. *Org. Geochem.* 41, 1235–1247. <https://doi.org/10.1016/j.orggeochem.2010.08.005>.
- Bhattacharya, S., Belgrave, J.D., Oil, B., Corporation, G., Mallory, D.G., Moore, R.G., Ursenbach, M.G., Mehta, S.A., 2015. Investigation of Thermal Finger Print in Accelerating Rate Calorimetry for Air-Injection Enhanced Oil Recovery Processes.
- Bhattacharya, S., Mallory, D.G., Moore, R.G., Ursenbach, M.G., Mehta, S.A., 2016. Vapor Phase Combustion in Accelerating Rate Calorimetry for Air-Injection EOR Processes. *SPE West. Reg. Meet.* <https://doi.org/10.2118/180451-MS>.
- Bogdanovich, N.N., Borisenko, S.A., Kozlova, E. V, Spasennykh, M.Y., Rudakovskaya, S.Y., 2017. Mosaic Hydrophobization of the Surface of Organic-Mineral Matrix from Rocks of Bazhenov Formation. *SPE Russ. Pet. Technol. Conf.* <https://doi.org/10.2118/187873-MS>.
- Bokserman, A.A., Kokorev, V.I., 2013. Thermogas method of developing hard-to-

recover and unconventional hydrocarbon reserves, in: “Enercon-2013.” Moscow, Russia.

- Bondarenko, T., Cheremisin, A., Kozlova, E., Zvereva, I., Chislov, M., Myshenkov, M., Novakowski, V., 2017. Experimental investigation of thermal decomposition of Bazhenov formation kerogen: Mechanism and application for thermal enhanced oil recovery. *J. Pet. Sci. Eng.* 150, 288–296. <https://doi.org/10.1016/j.petrol.2016.12.011>.
- Bondarenko, T., Khakimova, L., Cheremisin, A., Spasennykh, M., 2017a. SPE-187849-MS High-Pressure Air Injection Laboratory and Numerical Modelling in Bazhenov Source Rocks Key aspects of building a HPAI model , sensitivity analysis.
- Bondarenko, T., Khakimova, L., Cheremisin, A., Spasennykh, M., 2017b. High-Pressure Air Injection Laboratory and Numerical Modelling in Bazhenov Source Rocks. SPE Russ. Pet. Technol. Conf. <https://doi.org/10.2118/187849-MS>.
- Bondarenko, T., Popov, E., Cheremisin, A., Karpov, I., Morozov, N., 2016. Experimental assessment of the hydrocarbons yeilds from Bazhenov shale formation by kerogen conversion in the presence of supercritical water. *Int. Symp. Soc. Core Anal.* 1–6.
- Chen, X., Chen, Z., Moore, R.G., Mehta, S.A., Ursenbach, M.G., Harding, T.G., 2014. Kinetic Modeling of the In Situ Combustion Process for Athabasca Ramped Temperature Oxidation (RTO) Experiments and Pseudo Component Modeling Process. SPE Heavy Oil Conf. 1–19. <https://doi.org/10.2118/170150-MS>.
- Connan, J., Cassou, A.M., 1980. Properties of gases and petroleum liquids derived from terrestrial kerogen at various maturation levels. *Geochim. Cosmochim. Acta* 44, 1–23. [https://doi.org/10.1016/0016-7037\(80\)90173-8](https://doi.org/10.1016/0016-7037(80)90173-8).
- Darischev, V.I., Delia, S.V., Karpov, V.B., Shadchnev, A.N., 2017. RITEK - 25 Years of Innovation, Volume 2. Moscow, Russia.
- Dechelette, B., Heugas, O., Quenault, G., Bothua, J., Christensen, J.R., 2006. Air Injection-Improved Determination of the Reaction Scheme With Ramped Temperature Experiment and Numerical Simulation. *J. Can. Pet. Technol.* 45, 7. <https://doi.org/10.2118/06-01-03>.
- Deng, S., Wang, Z., Gu, Q., Meng, F., Li, J., Wang, H., 2011. Extracting hydrocarbons from Huadian oil shale by sub-critical water. *Fuel Process. Technol.* 92, 1062–1067. <https://doi.org/10.1016/J.FUPROC.2011.01.001>.
- E. Kozlova, E. Leushina, A. Voropaev, M.S., 2018. Identification of shale oils from the Bazhenov Formation using GCxGCx-MS, in: *Petromass 2018*.

- Fassihi, M.R., Yannimaras, D.V., Westfall, E.E., Gillham, T.H., 1996. Economics of Light Oil Air Injection Projects. SPE/DOE Improv. Oil Recover. Symp.
- Fowler, T.D., Vinegar, H.J., 2009. Oil Shale ICP – Colorado Field Pilots, in: SPE Western Regional Meeting. San Jose, California, pp. 24–26.
- Gjini, D., Buzi, X., Mastmann, M., Tare, S., 2013. Experience With Cyclic In Situ Combustion In Albania. Annu. Tech. Meet. <https://doi.org/10.2118/99-51>.
- Glandt, C.A., Pieterston, R., Dombrowski, A., Balzarini, M.A., E, S.W., 1999. SPE 52198 Coral Creek Field Study : A Comprehensive Assessment of the Potential of High-Pressure Air Injection in a Mature Waterflood Project 1–11.
- Goncharov, I. V, Samoilenko, V. V, Oblasov, N. V, Fadeeva, S. V, Veklich, M.A., Kashapov, R.S., Trushkov, P. V, Bahtina, E.S., 2016. Types of organic matter and catagenesis of the Bazhenov formation and its same-aged analogues (Russian). Oil Ind. J. 2016, 20–25.
- Gutierrez, D., Moore, R., Mehta, S., Ursenbach, M., Skoreyko, F., 2009. The Challenge of Predicting Field Performance of Air Injection Projects Based on Laboratory and Numerical Modelling 48.
- Gutierrez, D., Moore, R.G., Ursenbach, M.G., Mehta, S.A., 2011. The ABCs of In Situ Combustion Simulations: From Laboratory Experiments to the Field Scale. Can. Unconv. Resour. Conf. <https://doi.org/10.2118/148754-MS>.
- Gutierrez, D., Taylor, A.R., Kumar, V., Ursenbach, M.G., Moore, R.G., Mehta, S.A., 2008. Recovery Factors in High-Pressure Air Injection Projects Revisited. SPE Reserv. Eval. Eng. 11, 1097–1106. <https://doi.org/10.2118/108429-PA>.
- Harry R. Johnson, Peter M. Crawford, J.W.B., 2004. Strategic Significance of America ' s Oil Shale Resource II.
- INTEK, 2011. Secure fuels from Domestic Resources. Profiles of companies engaged in domestic oil shale and tar sands resource and technology development.
- Jia, H., Sheng, J.J., 2017. Discussion of the feasibility of air injection for enhanced oil recovery in shale oil reservoirs. Petroleum 3, 249–257. <https://doi.org/10.1016/j.petlm.2016.12.003>.
- Kar, T., Hascakir, B., 2017. In situ kerogen extraction via combustion and pyrolysis. J. Pet. Sci. Eng. 154, 502–512. <https://doi.org/10.1016/j.petrol.2017.01.051>.

- Khakimova, L., Bondarenko, T., Cheremisin, A., Myasnikov, A., Varfolomeev, M., 2018. High pressure air injection kinetic model for Bazhenov Shale Formation based on a set of oxidation studies. *J. Pet. Sci. Eng.* <https://doi.org/10.1016/J.PETROL.2018.09.021>.
- Khakimova, L.A., Myasnikov, A. V, Bondarenko, T.M., Popov, E.Y., Cheremisin, A.N., Karpov, I.A., 2017. Validation of computational model of high-pressure air injection for Bazhenov formations by laboratory modelling results (Russian). *Oil Ind. J.* 2017, 85–89.
- Khlebnikov, V.N., Zobov, P.M., Antonov, S. V., Bakulin, D.A., Guschina, J.F., Vinokurov, V.A., 2011. The study of hydrothermal influence on the Bazhenov formation breed. *Bashkir Chem. J.* 18, 2–7.
- Kibodeaux, K.R., 2014. Evolution of Porosity , Permeability , and Fluid Saturations During Thermal Reservoir Engineering Ramifications of Oil-Shale ICP Physics. *SPE Annu. Tech. Conf. Exhib.*
- Kobchenko, M., Panahi, H., Renard, F., Dysthe, D.K., Malthe-Srensens, A., Mazzini, A., Scheibert, J., Jamtveit, B., Meakin, P., 2011. 4D imaging of fracturing in organic-rich shales during heating. *J. Geophys. Res. Solid Earth* 116, 1–9. <https://doi.org/10.1029/2011JB008565>.
- Kök, M. V., Guner, G., Bage, S., 2008a. Application of EOR techniques for oil shale fields (in situ combustion approach). *Oil Shale* 25, 217–225. <https://doi.org/10.3176/oil.2008.2.04>
- Kök, M. V., Guner, G., Bage, S., 2008b. Application of EOR techniques for oil shale fields (in-situ combustion approach). *Oil Shale* 25, 217–225. <https://doi.org/10.3176/oil.2008.2.04>.
- Kokorev, V.I., Darishchev, V.I., Akhmadeishin, I.A., Shchekoldin, K.A., Boksernam, A.A., 2014. The Results of the Field Tests and Prospects of Termogas Development of Bazhenov Formation in OJSC RITEK. *SPE-171172-MS* 1–12.
- Kozlowski, M.L., Punase, A., Hascakir, B., Texas, A., 2015. The Catalytic Effect of Clay on In Situ Combustion Performance, in: *SPE Latin American and Caribbean Petroleum Engineering Conference*. Quito, Ecuador, pp. 18–20.
- Lee, K., Moridis, G.J., Ehlig-Economides, C.A., 2015. A Comprehensive Simulation Model of Kerogen Pyrolysis for the In situ Upgrading of Oil Shales. *SPE Reserv. Simul. Symp.* <https://doi.org/10.2118/173299-MS>.
- Li, J., Mehta, S.A., Moore, R.G., Zalewski, E., Ursenbach, M.G., Van Fraassen, K., 2006.

Investigation of the oxidation behaviour of pure hydrocarbon components and crude oils utilizing PDSC thermal technique. *J. Can. Pet. Technol.* 45, 48–53. <https://doi.org/10.2118/06-01-04>.

Mallory, D.G., Moore, R.G., Mehta, S.A., 2018. Ramped Temperature Oxidation Testing and in Situ Combustion Projects. *Energy and Fuels* 32, 8040–8056. <https://doi.org/10.1021/acs.energyfuels.8b00760>.

Manrique, E., Gurfinkel, M., Muci, V., 2004. Enhanced Oil Recovery Field Experiences in Carbonate Reservoirs in the United States EOR in U . S . Carbonate Reservoirs. 25th Annu. Work. Symp. Collab. Proj. Enhanc. Oil Recover. Int. Energy Agency 1–32.

Manuilova, E.A., Kalmykov, A.G., Kalmykov, G.A., Bogdanovich, N.N., Karpov, I.A., Mamyashev, T. V, 2017. Complex method for core samples investigations to determine the parameters of the natural reservoirs and the main characteristics of high-carbon formations (Russian). *Oil Ind. J.* 2017, 44–47.

McGee, R., Fraim, M., Hagen, S., 2011. Combined Miscible Drive Enhances Pleito Creek Oil Production. *Oil Gas Jour.*

Moore, R.G., Mehta, S.A., Ursenbach, M.G., 2002. A Guide to High Pressure Air Injection (HPAI) Based Oil Recovery. *SPE/DOE Improv. Oil Recover. Symp.* 1–7. <https://doi.org/10.2523/75207-MS>.

Moore, R.G., Ursenbach, M.G., Laureshen, C.J., Belgrave, J.D.M., Mehta, S.A., 1999. Ramped temperature oxidation analysis of Athabasca Oil Sands bitumen. *J. Can. Pet. Technol.* 38, 52. <https://doi.org/10.2118/99-13-40>.

Pan, Y., Xiao, L., Chen, C., Yang, S., 2012. Development of Radio Frequency Heating Technology for Shale Oil Extraction. *Open J. Appl. Sci.* 02, 66–69. <https://doi.org/10.4236/ojapps.2012.22008>.

Peters, K.E., Burnham, A.K., Walters, C.C., Schlumberger, K.E.P., 2015. Petroleum generation kinetics : Single versus multiple heating- ramp open-system pyrolysis 4, 591–616. <https://doi.org/10.1306/11141414080>.

Raimondi, 1975. A Field Test of Underground Combustion Of Coal 35–41.

Sarathi, P.S., 1999. In Situ Combustion Handbook - Principles and Practices 424.

Sequera, B., Moore, R.G., Mehta, S.A., Ursenbach, M.G., 2010. Numerical Simulation of In Situ Combustion Experiments Operated Under Low Temperature Conditions. *J. Can. Pet. Technol.* 49, 55–64. <https://doi.org/10.2118/132486-PA>.

- Shchekoldin, K.A., 2016. Justification of the technological regimes of thermogas impact on the deposits of the Bazhenov Formation. Russian State University of oil and gas.
- Speight, J.G., 2012. Chapter 4 - Mining and Retorting, in: James G. Speight (Ed.), *Shale Oil Production Processes*. Gulf Professional Publishing, Oxford, pp. 93–122. <https://doi.org/10.1016/B978-0-12-401721-4.00004-7>.
- Spiro, B., 1991. Effects of minerals on Rock Eval pyrolysis of kerogen. *J. Therm. Anal.* 37, 1513–1522. <https://doi.org/10.1007/BF01913484>.
- Symington, W.A., Burns, J.S., El-Rabaa, A.M., Otten, G.A., Pokutyłowicz, N., Spiecker, P.M., Williamson, R.W., Yeakel, J.D., 2009. Field Testing of Electrofrac™ Process Elements at ExxonMobil's Colony Mine, in: 29th Oil Shale Symposium. Golden Colorado, pp. 1–13.
- Team USGS World Energy Assessment, 2000. U.S. Geological survey world petroleum assessment 2000 - Description and results, Assessment.
- Tiwari, P., Deo, M., Lin, C.L., Miller, J.D., 2013. Characterization of oil shale pore structure before and after pyrolysis by using X-ray micro CT. *Fuel* 107, 547–554. <https://doi.org/10.1016/J.FUEL.2013.01.006>
- Waples, D., Nowaczewski, V.S., 2014. Source-rock kinetics. *Encycl. Pet. Geosci.* 1–25.
- Yan, J., Jiang, X., Han, X., Liu, J., 2013. A TG – FTIR investigation to the catalytic effect of mineral matrix in oil shale on the pyrolysis and combustion of kerogen. *Fuel* 104, 307–317. <https://doi.org/10.1016/j.fuel.2012.10.024>.
- Yanik, J., Yüksel, M., Sağlam, M., Olukçu, N., Bartle, K., Frere, B., 1995. Characterization of the oil fractions of shale oil obtained by pyrolysis and supercritical water extraction. *Fuel* 74, 46–50. [https://doi.org/10.1016/0016-2361\(94\)P4329-Z](https://doi.org/10.1016/0016-2361(94)P4329-Z).
- Yannimaras, D.V., Tiffin, D.L., 1995. Screening of Oils for In Situ Combustion at Reservoir Conditions by Accelerating-Rate Calorimetry. *SPE Reserv. Eng.* 36–39.
- Zhang, K., 2016. Experimental and Numerical Investigation of Oil Recovery from Bakken Formation by Miscible CO₂ Injection. *SPE Annu. Tech. Conf. Exhib.* 1, 1–23. <https://doi.org/10.2118/184486-STU>.
- Zheng, H., Shi, W., Ding, D., Zhang, C., 2017. Numerical Simulation of In Situ Combustion of Oil Shale 2017.

Appendix A: Photographs of samples after combustion tube test



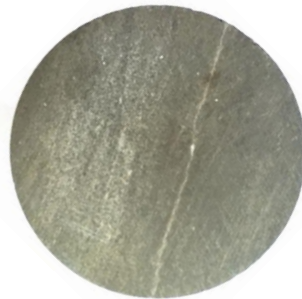
a. before exposure



b. after exposure



c. before exposure



d. after exposure



e. sample location view during the packing process



f. sample location view during the unpacking process

Figure 138. Sample #1 (Zone 2.1). Peak temperature: 319°C.



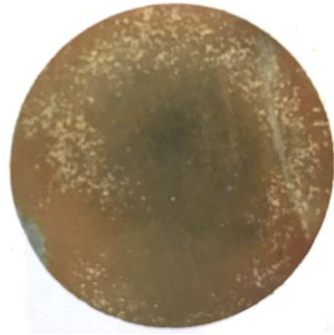
a. before exposure



b. after exposure



c. before exposure



d. after exposure

Figure 139. Sample #2 (Zone 2.2). Peak temperature: 319°C.



a. before exposure



b. after exposure



c. before exposure



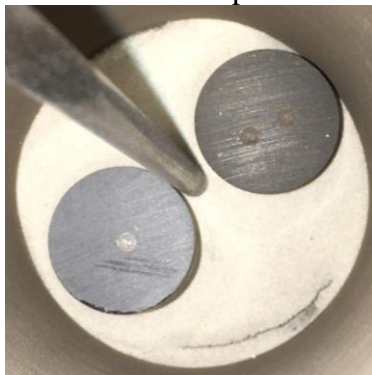
d. after exposure



e. before exposure



f. after exposure



g. sample location view during the packing process



h. sample location view during the unpacking process

Figure 140. Sample #3 (Zone 3.1). Peak temperature: 460°C.



a. before exposure



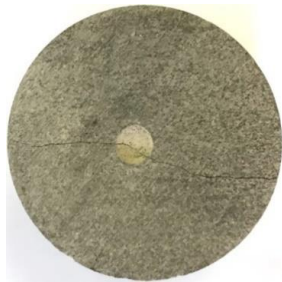
b. after exposure



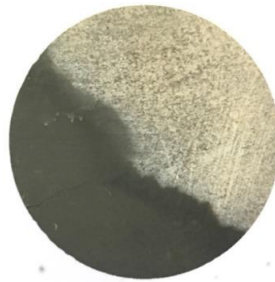
c. before exposure



d. after exposure



e. after exposure



f. after exposure



g. sample location view during the packing process



h. sample location view during the unpacking process

Figure 141. Sample #4 (Zone 3.4). Peak temperature: 460°C.



a. before exposure



b. after exposure



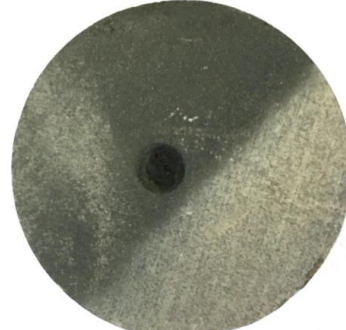
c. before exposure



d. after exposure



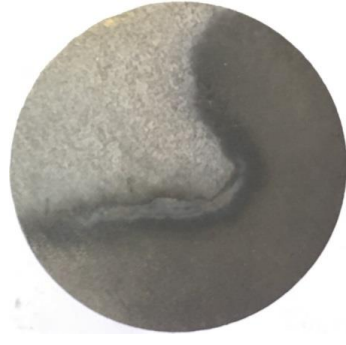
e. before exposure



f. after exposure



g. before exposure



h. after exposure

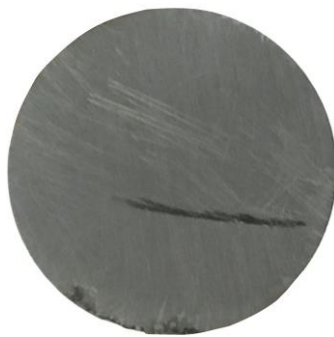
Figure 142. Sample #5 (Zone 4.1). Peak temperature: 463°C.



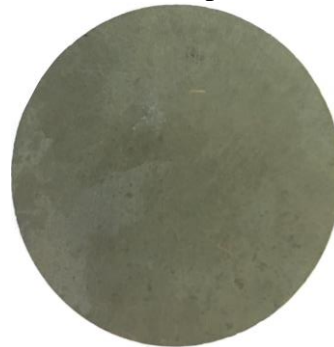
a. before exposure



b. after exposure



c. before exposure



d. after exposure

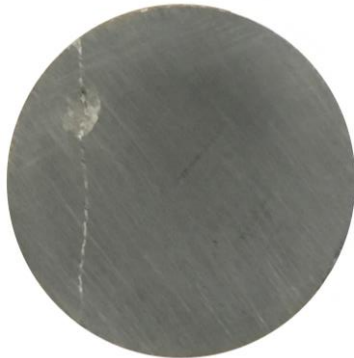
Figure 143. Sample 6 (Zone 4.2). Peak temperature: 463°C.



a. before exposure



b. after exposure



c. before exposure

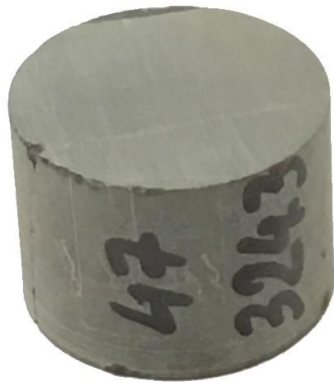


d. after exposure



e. Sample's location view during the unpacking process

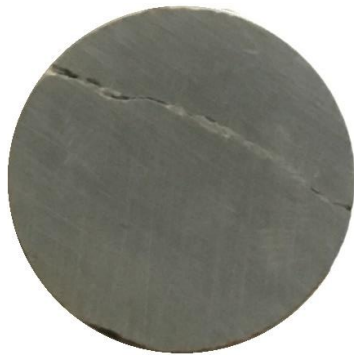
Figure 144. Sample #7 (Zone 5.1). Peak temperature: 273°C.



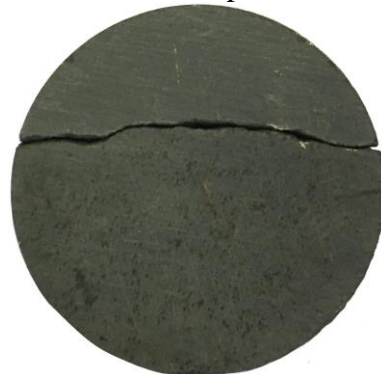
a. before exposure



b. after exposure



c. before exposure



d. after exposure

Figure 145. Sample #8 (Zone 5.1). Peak temperature: 273°C.



a. before exposure



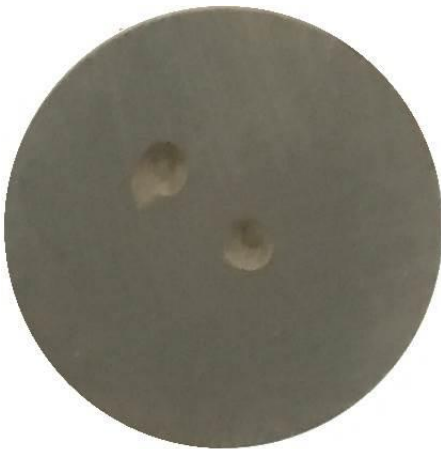
b. after exposure



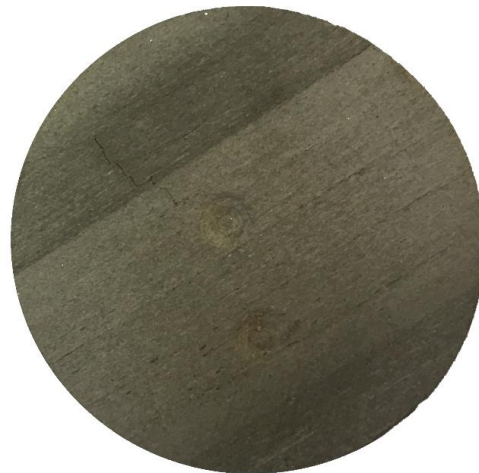
c. before exposure



d. after exposure



e. before exposure



f. after exposure

Figure 146. Sample #13 (Zone 2.2). Peak temperature: 319°C. Oil Field 3.



a. before exposure



b. after exposure



c. before exposure



d. after exposure



e. before exposure



f. after exposure



g. before exposure



h. after exposure



i. before exposure



j. after exposure

Figure 147. Sample #14 (Zone 3.4). Peak temperature: 460°C. Oil Field 3.



a. before exposure



b. after exposure



c. before exposure



d. after exposure

Figure 148. Sample #16 (Zone 2.1). Peak temperature: 319°C. Oil Field 2.



Figure 149. Sample #18 (Zone 3.1). Peak temperature: 460°C. Oil Field 2.